

**Transverse Momentum Distributions of
Hadrons Produced in Au+Au Collisions at 130
GeV Measured by the PHENIX Experiment
at RHIC BNL**

A Dissertation Presented

by

Jane Muriel Burward-Hoy

to

The Graduate School

in Partial Fulfillment of the Requirements

for the Degree of

Doctor of Philosophy

in

Physics

State University of New York

at

Stony Brook

December 2001

Copyright © by
Jane Muriel Burward-Hoy
2001

State University of New York
at Stony Brook

The Graduate School

Jane Muriel Burward-Hoy

We, the dissertation committee for the above candidate for the Doctor of Philosophy degree, hereby recommend acceptance of the dissertation.

Barbara V. Jacak (Advisor)

Professor, Department of Astronomy and Physics

Madappa Prakash (Chair)

Professor, Department of Astronomy and Physics

Thomas K. Hemmick

Professor, Department of Astronomy and Physics

Roy Lacey

Professor, Nuclear Chemistry, Department of Chemistry

This dissertation is accepted by the Graduate School.

Graduate School

Abstract of the Dissertation

Transverse Momentum Distributions of Hadrons Produced in Au+Au Collisions at 130 GeV Measured by the PHENIX Experiment at RHIC BNL

by

Jane Muriel Burward-Hoy

Doctor of Philosophy

in

Physics

State University of New York at Stony Brook

2001

The transverse momentum (p_t) distributions of hadrons produced in Au+Au collisions at 130 GeV are measured at midrapidity, from the most central to the most peripheral collisions, by the PHENIX Experiment at RHIC BNL. The spectra are measured by highly segmented Time-of-Flight, Pad Chamber, and Drift Chamber detectors. The events are triggered, and the event centrality is determined by the Beam-Beam Counters and Zero Degree Calorimeters.

Already after the first year of RHIC running, the data show both hard and soft physics. A feature unpredicted by perturbative QCD calculations is the crossing of proton and pion spectra at $1.5 - 2$ GeV/ c in p_t . A plausible explanation is the jet-quenching of high p_t pions and the broadening of low p_t (anti)protons due to strong radial expansion.

The pion yield varies linearly with the number of participant nucleons. The kaon and (anti)proton yields may also depend on the number of nucleon-nucleon binary collisions. The total hadron yield agrees with published results. In central collisions, the average initial energy density is $4.9 \text{ GeV}/\text{fm}^3$, 70% higher than in Pb+Pb collisions at CERN. The average transverse momentum increases with participant number, indicative of radial expansion.

A hydrodynamics parameterization is fit simultaneously to the hadron spectra in a p_t range that minimizes contributions from hard processes. The resonance and weak decay contribution is excluded in the fit to the pion spectra. In central events, the radial velocity of the expanding surface is $0.70 \pm 0.01 c$, with hadrons decoupling at a temperature of $121 \pm 4 \text{ MeV}$. A hydrodynamics model with an equation of state that simulates a mixed phase transition between a hadron gas and a relativistic gas of quarks and gluons describes the hadron spectra.

The extrapolated spectrum from radial flow contributions is compared to the charged spectrum measured out to $5 \text{ GeV}/c$. The transition region between soft and hard processes is $2.5 - 3 \text{ GeV}/c$ in p_t . In order to measure jet-quenching the spectra need to be measured for $p_t > 3 \text{ GeV}/c$. At CERN SPS energies, the high p_t pion spectra are described by hydrodynamics and need to be measured up to $5 \text{ GeV}/c$ in p_t .

The radial expansion is stronger than at CERN, yet the particle-emitting sources are the same size. This is in contradiction to hydrodynamic predictions and further analysis is necessary in order to understand this discrepancy.

To my family

Contents

List of Figures	xviii
List of Tables	xxv
Acknowledgements	xxvi
1 Introduction	1
1.1 Relativistic Heavy-Ion Collisions	3
1.1.1 Observables	3
1.2 Kinematic Quantities and Definitions	5
1.2.1 Centrality	5
1.2.2 Kinematic Variables	5
1.2.3 Initial Energy Density	7
1.2.4 Hydrodynamic Expansion	7
1.3 Organization of the Thesis	10
2 The Relativistic Heavy Ion Collider Facility	11
3 The PHENIX Detector	14
3.1 Vertex and Trigger Detectors	18
3.1.1 Zero Degree Calorimeters	18
3.1.2 Beam-Beam Counters	19
3.1.3 Multiplicity Vertex Detector	19
3.2 Muon spectrometers (north and south)	19
3.3 Central Arm Spectrometers	21
3.3.1 Central Magnet	21
3.3.2 Charged Particle Acceptance	22
3.3.3 Identified Hadron Acceptance	22
3.3.4 Drift Chambers	23
3.3.5 Track Reconstruction	26
3.3.6 Pad Chamber Detectors	30

3.3.7	Time Expansion Chamber	30
3.3.8	Time-of-Flight Hodoscope	31
3.3.9	Ring Imaging Cherenkov Hodoscopes	33
3.3.10	Electromagnetic Calorimeters.	33
3.4	Detector Alignment	34
3.5	Momentum Reconstruction and the Track Model	35
3.6	Subsystems Used For This Analysis	36
4	Data Reduction	39
4.1	Event Selection	40
4.1.1	Event Centrality	40
4.1.2	Number of Participants	44
4.2	Global Track Selection	45
4.2.1	Track Reconstruction and Quality in the Drift Chambers	45
4.2.2	Matching Global Tracks to the Time-of-Flight	47
4.3	Particle Identification	49
4.3.1	Time-of-Flight Measurement	49
4.3.2	Momentum Measurement	51
4.3.3	The Mass-Squared Distribution	60
4.4	Background and Other Uncertainties in Data Reduction	69
4.4.1	Other Sources of Uncertainty	73
4.5	Raw Transverse Momentum Distributions	74
5	Corrections from Single Particle Monte Carlo	77
5.1	Matching Monte Carlo and Data	78
5.1.1	Drift Chamber	78
5.1.2	Time-of-Flight	86
5.1.3	Matching Global Tracks to TOF Hits	86
5.1.4	Fiducial Cuts	89
5.2	Correcting for Geometrical Acceptance, Decays in Flight, and Detector Response	97
5.2.1	How much Monte Carlo statistics is enough ?	97
5.2.2	Corrections	98
5.3	High Track-Density Efficiency Correction	102
5.3.1	Drift Chamber Efficiency	108
5.3.2	Time-of-Flight Efficiency	108
5.3.3	Efficiency Correction	109
5.4	Systematic Uncertainties from the Corrections	110
5.5	The Identified Particle Spectra	112
5.5.1	Systematic Uncertainties in the Spectra	112

5.5.2	Truncated Mean Transverse Momentum and Yield . . .	112
6	Results	120
6.1	Particle Spectra	121
6.1.1	Static Thermal Source	123
6.1.2	Effective Temperature	127
6.1.3	Resonances	135
6.1.4	A Boosted Thermal Source	135
6.1.5	Measuring β_t and T_{fo} from the Data	137
6.2	Measured Yields and Average Transverse Momentum	150
6.2.1	Systematic Uncertainties	157
6.3	Particle Yields	159
6.3.1	Estimating the Initial Energy Density	160
6.3.2	Particle Ratios	163
6.4	Mean Transverse Momentum	166
7	Discussion and Conclusion	169
7.1	Radial Flow	169
7.2	What is Measured at CERN-SPS Energies?	170
7.2.1	Effective Temperatures	170
7.3	Comparison to High p_t Hadron Spectra	177
7.4	HIJING: pQCD Model Prediction at RHIC Energies	180
7.5	Multiplicity Dependence on Centrality	181
7.6	Hydrodynamic Model Comparison	185
7.6.1	Initial Parameter Tuning	185
7.6.2	The Comparison	187
7.7	Particle Yields and Ratios	190
7.8	Conclusion and Outlook	191
A	Tables of Invariant Cross Sections	200
B	Parabolic Velocity Profile	214
C	Background from Albedo and Decays	218
D	Tables of Extrapolated Yields and $\langle p_t \rangle$	222

List of Figures

1.1	The hydrodynamic evolution of a system produced by two relativistic heavy ions colliding at the point $t = 0$ and $z = 0$ with (right) and without (left) a Quark-Gluon Plasma phase transition.[16]	9
2.1	The RHIC complex at Brookhaven National Laboratory in Upton, New York (left) [22] and a diagram with the experiments operating in Year-1 (right) [23].	12
3.1	The PHENIX acceptance for hadrons and leptons. The vertical axis is azimuthal angle ϕ and the horizontal is the pseudorapidity η	15
3.2	The first Au+Au event as recorded in the PHENIX detector (left) [28]. The PHENIX event display with subsystems used in Year-1 (right) [29].	15
3.3	The experimental setup in PHENIX for the central arm spectrometer. The top picture is the cross-sectional view of PHENIX transverse to the beam axis while the bottom shows the beam-axis subsystems.	17
3.4	The PHENIX Data Acquisition System, triggered by an event in the Zero Degree Calorimeters (left in diagram).[32]	18
3.5	The total number of triggers recorded in PHENIX during the Summer 2000 run (runs 8000-12468) [26, 37].	20
3.6	The BBC event display showing one Au+Au collision event as recorded in the PHENIX BBC detectors [37, 54].	21
3.7	The magnet bends positive and negative particles in opposite senses into the PHENIX acceptance.	22
3.8	The Central arm spectrometer acceptance in rapidity and transverse momentum for protons, kaons, and pions.	23
3.9	The Au-plated tungsten wires inside one of the drift chambers [27].	24
3.10	The wire configuration in a Drift Cell.	25

3.11	The electric field lines that result in a drift cell wire configuration from a GARFIELD simulation [53].	25
3.12	The illustration of a charged track entering one of the Drift Chambers and the Hough transform parameters ϕ and α . The drift chamber hits are shown as open circles that fall along the particle's trajectory in the xy plane. The North beam direction is pointing out of the page [42].	27
3.13	The left plot shows the simulated hits from a central Au+Au collision in a small region of the drift chamber in the xy plane. The right plot is the resulting Hough transform feature space for this region. The tracks appear as peaks in this plot [42].	28
3.14	The geometrical representation of the UV stereo wires (at $\pm 5^\circ$ with tilt angle and the hits of a track on these wires (bottom) as it enters the drift chamber volume (upper plot). The angle β is the angle of inclination of the track with respect to the z axis.	29
3.15	The TOF detector and its 10 panels (left) as it sits at the bottom of the East spectrometer arm of PHENIX. On the right, an illustration of a panel and its slat components is shown. [55]	32
3.16	The PHENIX particle identification setup in Run 2000. The beams are perpendicular to the page. See description in the text.	37
4.1	Event centrality selections using the ZDC energy fraction and BBC fraction counts (left). The charged multiplicity distributions for each centrality selection (right).	42
4.2	Quality variable for tracks reconstructed in run 9666, sequence 0. Three groupings are possible. See text for bit definitions.	47
4.3	The offset in the measured initial time in the BBC detectors as a function of run number [53].	50
4.4	Measured initial time in the BBC detectors as a function of hit density in the Pad Chamber 1 [53].	50
4.5	Extracting the time-of-flight scale factor by fitting a straight line to the expected total time-of-flight and the measured time-of-flight in the TOF detector [53].	52
4.6	The difference of the measured and expected time for high momentum pions. The width of this residual, 115 ps, is the TOF detector resolution [55].	53

4.7	The 1σ contours for each particle species determined separately (left) and simultaneously (right). The pions are excluded in the simultaneous fit. The negative particles correspond to the dashed lines (left). The vertical axis is the time-of-flight offset and the horizontal is the momentum scale. [58]	55
4.8	The global tracks and PC3 hit residuals in ϕ (vertical axis) as a function of momentum (horizontal) for different Drift Chamber track qualities [59].	57
4.9	The momentum resolution using measured particle identification. The protons are more sensitive to the multiple scattering term (upper curve), while the pions are less sensitive (lower curve).	59
4.10	PHENIX high resolution particle identification of light hadrons (left)[56]. Particle identification bands to select pions, kaons, and protons (right) [60].	61
4.11	The extracted means and sigmas after fitting gaussians to the mass-squared distribution for pions, kaons, and protons in each momentum slice.	63
4.12	The mass-squared distribution [58].	64
4.13	The n-sigma distribution of positive pions [57].	65
4.14	The n-sigma distribution of negative pions [57].	66
4.15	The ΔE of particles in the TOF versus β . Faster particles are to the right. Both the straight threshold cut and the new approximate Bethe-Bloch are shown. [60]	68
4.16	The raw dN/dp_t distribution of kaons (left) and protons (right), illustrating the effect of the two types of energy loss cuts [60].	68
4.17	The mass-squared distribution (symbols) and the estimated random contribution (histogram). The 2σ particle-identification cuts are shown as dashed lines.	70
4.18	Estimating the random background contamination under the pion peaks in three different p_t ranges. Positive pions are the top row and negative pions are the bottom.	71
4.19	Estimating the random background contamination under the kaon peaks in three different p_t ranges.	72
4.20	Estimating the random background contamination under the combined protons and anti-proton peaks in three different p_t ranges.	73
4.21	Minimum bias raw transverse momentum distributions of pions, kaons, and protons. Positive particles are plotted (left) and negative (right).	74

4.22	Centrality selected raw transverse momentum distributions of positive pions (left) and negative pions (right).	75
4.23	Centrality selected raw transverse momentum distributions of positive kaons (left) and negative kaons (right).	76
4.24	Centrality selected raw transverse momentum distributions of protons (left) and anti-protons (right).	76
5.1	Simulation of electron drift distances (full lines) and isochrones (dashed) in one drift cell in the drift chamber. The spacing between isochrones is $0.01\mu\text{s}$. The gas mixture is 50% Ar and 50% C_2H_6 . [53].	79
5.2	Geometrical description of a drift cell, modeled after a GARFIELD simulation of electron drift distances. A track enters the drift cell and the drift distance is calculated. [53].	80
5.3	The time distribution for a pulse of electrons in a single drift cell in the drift chamber as measured in the West arm. The hit time is determined by the leading edge of the pulse (here it is 112.9). The time bin size is 0.822368 ns/bin.[61]	81
5.4	Measured and simulated distributions of the drift distances for all X1 (left) and X2 (right) wire nets in the drift chamber.[53]	83
5.5	The width of the time distribution (pulse width) depends on the angle α both in data (points) and, after tuning, in simulation (histogram).[53].	83
5.6	The width of the time distribution (pulse width) as a function of the drift distance in the drift cell.[53]	84
5.7	The hit resolution depends on the drift distance as measured in the data (left) and parameterized in the simulation (right).[53]	85
5.8	The single wire efficiency as measured in the data (left) and as mapped in the simulation (right) for the drift chamber in the East arm.[53]	85
5.9	The simulated mass after smearing the TOF GEANT time (left) compared to data (right two plots). The data plots correspond to before and after the $2\sigma_{m^2}$ PID cuts, respectively.	87
5.10	Comparison of the momentum-dependent residuals of DC tracks matched to TOF hits in ϕ (left) and z (right) between data (dashed) and simulation (line). (The residuals in the data were determined by F. Messer of the PHENIX Collaboration.) . . .	88
5.11	The TOF sector spacing in simulation (left) is too small when compared to data (right). The arrow indicates the gap which is the geometrical space between the sectors in the TOF.	90

5.12	The ϕ distribution of tracks with $p_t > 1.5$ GeV/c in the each drift chamber for both Monte Carlo and data. The dead channel region in the south (left) is well describe while the north (right) Monte Carlo is too small.	93
5.13	The North East dead channel region in the Drift Chamber (left). The lines indicate an example of a p-dependent fiducial cut in the $q/p-\phi_{DC}$ space (left). An example of a larger fidiucial cut is also shown (right).	93
5.14	The edge in the Monte Carlo that is approximately 1/2 a key-stone short of the data (left). The line indicates the p-dependent fiducial cut in the $q/p-\phi_{DC}$ space (right) and is applied both in the Monte Carlo and in the raw data.	94
5.15	The known hole in the South East part of the Drift Chamber (left). The lines indicate an example of a p-dependent fiducial cut in the $q/p-\phi_{DC}$ space. The figure on the right is the same region, but with a wider cut that excludes the triangular region on the lower left-hand side that is not well described by the Monte Carlo.	94
5.16	A study of how the negative to positive pion ratio changes as a fraction of drift chamber tracks cut in each fiducial cut in $q/p - \phi_{DC}$ space.	95
5.17	Relative error comparison of Monte Carlo and raw data for π^+ (solid) and π^- (open). The relative error in the data dominates above 1 GeV/c and is comparable to the simulation at low p_t	98
5.18	The phase space coverage for the single protons. The vertical axis is p_t and the horizontal is y . The top panel are the EXODUS input particles, the middle are the protons in the drift chamber acceptance, and the bottom are the protons reconstructed with x, y, and z information in coordinate space. [53]	101
5.19	The pion, kaon, and proton dN/dp_t input (top three curves in each panel as labeled) and output (bottom three curves in each panel as labeled) distributions for positive (left panel) and negative (right panel) single particle Monte Carlo.	103
5.20	Corrections for positive (left) and negative (right) particles using single particle Monte Carlo.	104
5.21	The resulting mass-squared distribution of anti-protons reconstructed after embedding into peripheral events (left) and central events (right), before the 2σ particle identification cut. The circle shows the region where particles have the wrong mass reconstructed in the higher track density environment. [57]	109

5.22	Final efficiency correction as a function of centrality for pions (left) and anti-protons (right). The centrality is expressed in increments of 5% in bin number. The most central and peripheral bins are labeled accordingly. The fully (X1&X2) and partially (X1 X2) reconstructed track corrections are different and labeled accordingly. [57]	111
5.23	The spectra of positive particles (left) and negative (right) in minimum bias events at 130 GeV.	113
5.24	The spectra of π^+ (left) and π^- (right) for five centralities from the most central 0-5% to the most peripheral 60-92% at 130 GeV.	114
5.25	The spectra of K^+ (left) and K^- (right) for five centralities from the most central 0-5% to the most peripheral 60-92% at 130 GeV.	115
5.26	The spectra of p (left) and \bar{p} (right) for five centralities from the most central 0-5% to the most peripheral 60-92% at 130 GeV.	116
6.1	The transverse momentum spectra of pions, kaons, protons and antiprotons for the most central (top), mid-central (center), and most peripheral (bottom) collisions. In both the positive particles (left) and negative particles (right) the crossing point of nucleons and pions decreases with increasing impact parameter [68].	122
6.2	Transverse mass distributions of π^+ , K^+ , and p (left) in minimum bias events and the equivalent for negative particles (right).	126
6.3	The transverse energy spectra of positive pions (left) and negative pions (right). Thermal fits in the range $(m_t - m_0) < 1$ GeV are extrapolated over the entire transverse kinetic energy range for comparison to the data. The pions are not exponential over the measured range.	128
6.4	The transverse energy spectra of positive kaons (left) and negative kaons (right). Thermal fits in the range $(m_t - m_0) < 1$ GeV are extrapolated over the entire transverse kinetic energy range for comparison to the data. The kaons are exponential over the measured range.	129
6.5	The transverse energy spectra of protons (left) and antiprotons (right). Thermal fits in the range $(m_t - m_0) < 1$ GeV are extrapolated over the entire transverse kinetic energy range for comparison to the data. The protons are exponential over the measured range, while the thermal extrapolation diverges slightly from the measured antiproton data.	130

6.6	The effective temperature in each centrality is plotted against the average number of participants for each particle. Positive particles are plotted (left) and negative (right). The errors are statistical only from the thermal fit to the particle transverse energy spectra in the range $(m_t - m_0) < 1$ GeV.	132
6.7	T_{eff} versus m_0 for the most central and most peripheral data.	133
6.8	The resonance contribution in the pion and anti-proton spectra at RHIC energies [73].	136
6.9	Transverse velocity profiles as a function of ξ	137
6.10	Individual particle contours of the parameter space T_{fo} and β_t for pions (top), kaons (middle), and protons (bottom). The left column are positive particles and the right are negative particles.	139
6.11	The χ^2 contours in the parameter space T_{fo} and β_t that result after simultaneously fitting pions, kaons, and (anti)protons for 0–5% centrality. The minimum χ^2/dof is 34.0/40 with parameters corresponding to the point as shown. The n-sigma contours are labeled accordingly.	140
6.12	The χ^2 contours in the parameter space T_{fo} (vertical axis) and β_t (horizontal) that result after simultaneously fitting pions, kaons, and protons for 5–15% centrality. The minimum χ^2/dof is 34.7/40 with parameters corresponding to the point as shown.	141
6.13	The χ^2 contours in the parameter space T_{fo} and β_t that result after simultaneously fitting pions, kaons, and (anti)protons for 15–30% centrality. The minimum χ^2/dof is 36.2/40 with parameters corresponding to the point as shown.	142
6.14	The χ^2 contours in the parameter space T_{fo} and β_t that result after simultaneously fitting pions, kaons, and (anti)protons for 30–60% centrality. The minimum χ^2/dof is 68.9/40 with parameters corresponding to the point as shown.	143
6.15	The χ^2 contours in the parameter space T_{fo} and β_t that result after simultaneously fitting pions, kaons, and (anti)protons for 60–92% centrality. The minimum χ^2/dof is 36.3/40 with parameters corresponding to the point as shown.	144
6.16	The parameterization and the π^+ (left) and π^- (right) data for all five centrality selections.	145
6.17	The parameterization and the K^+ (left) and K^- (right) data for all five centrality selections.	146
6.18	The parameterization and the proton (left) and anti-proton (right) data for all five centrality selections.	147

6.19	The expansion parameters T_{fo} and β_t as a function of the number of participants.	148
6.20	The velocity profiles as generated by hydrodynamics [75]. The vertical axis is the velocity of a fluid element and the horizontal axis is the radial position on the expanding surface. Each contour represents a different proper time in the expansion. The inset shows the velocity profiles when the system undergoes a QGP phase transition.	149
6.21	The 5% central events. Pions are the top row, kaons the middle, and protons the bottom. Positive particles are left and negative right.	152
6.22	The 5-15% event centrality selection. Pions are the top row, kaons the middle, and protons the bottom. Positive particles are left and negative right.	153
6.23	The 15-30% event centrality selection. Pions are the top row, kaons the middle, and protons the bottom. Positive particles are left and negative right.	154
6.24	The 30-60% event centrality selection. Pions are the top row, kaons the middle, and protons the bottom. Positive particles are left and negative right.	155
6.25	The 60-92% event centrality selection. Pions are the top row, kaons the middle, and protons the bottom. Positive particles are left and negative right.	156
6.26	The particle yield dN/dy for positive particles (left) and negative particles (right) as a function of the average number of participants N_p . The errors on the points include both statistical errors from the measured data and systematic errors. . . .	161
6.27	The particle yield dN/dy per participant nucleon pair for positive particles (left) and negative particles (right) as a function of the average number of participants N_p . The errors on the points include both statistical errors from the measured data and systematic errors. The dashed lines about the pions are the systematic errors in determining N_p from the Glauber calculation. The yields for kaons, protons, and antiprotons are scaled by a factor of 2 for clarity.[68]	162
6.28	Negative pions divided by positive pions in each p_t bin. The fit is a constant fit and results in 0.94.	163
6.29	The K^-/K^+ ratio is independent of p_t in the measured range [54].	164
6.30	The \bar{p}/p ratio is independent of p_t in the measured range [54].	164

6.31	The π^-/π^+ ratio does not depend on the number of participants [54].	165
6.32	The K^-/K^+ ratio plotted against the number of participants [54].	165
6.33	The \bar{p}/p ratio plotted against the number of participants [54].	166
6.34	The p/π^+ and $\bar{p}\pi^-$ ratios plotted against the number of participants [54].	167
6.35	The K^+/π^+ and K^-/π^- ratios plotted against the number of participants [54].	167
6.36	Average transverse momentum for positive (left) and negative (right) particles corresponding to the number of participating nucleons N_p in each event centrality [68].	168
7.1	The effective temperatures are plotted against particle mass for positive particles produced in symmetric (A+A) collisions (left) and asymmetric (p+A and A+B) collisions (right) at CERN energies. Error bars are statistical only.	173
7.2	The freeze-out temperature T_{fo} (top) and radial flow velocity $\langle \beta_t \rangle$ (bottom) plotted for each system in terms of system size AB at CERN energies.	174
7.3	Results of calculating the p_t distribution using a hydrodynamics based parameterization for pions measured out to ≈ 3 GeV produced in a variety of collision systems.	175
7.4	The phase space boundaries for pions, kaons, and protons. The vertical axis is p_t and the horizontal axis is y . The vertical lines correspond to the acceptance in η . On the right panel, the factor y/η (vertical) is plotted for each value of p_t	178
7.5	The high p_t hadron spectra in Reference [81] compared to the fit results assuming radial flow from the π Kp spectra in the most central events.	179
7.6	The multiplicity distribution of charged particles produced in HIJING.	181
7.7	The p_t distributions of hadrons in HIJING events for the 10% central (left) and 85% centrality (right). The proton spectra cross the kaon spectra and not the pion spectra as is observed in data.	182
7.8	The $m_t - m_0$ distributions of pions, kaons, and protons in 10% central HIJING events at RHIC energies. The dotted lines are simple exponential fits in the range $m_t - m_0 < 1$ GeV.	183

7.9	The effective temperatures of pions, kaons, and protons at $m_t - m_0 < m_0$ are independent of particle mass in both central and peripheral HIJING events at RHIC energies.	183
7.10	Both the total charged multiplicity (open) in References [80, 83, 84] and the total identified charged multiplicity (closed) scaled by the number of participant pairs are plotted together as a function of the number of participants.	184
7.11	The hydrodynamics calculation with initial parameters tuned to match the most central spectra in the p_t range 0.3 – 2.0 GeV/c.188	
7.12	The hydrodynamics calculation with initial parameters tuned to match the most central spectra.	189
7.13	The K^+/π^+ ratio for different center of mass energies.	191
B.1	The χ^2 contours of β_t versus T_{fo} after a simultaneous fit to the 0-5% particle spectra. A parabolic profile is used.	215
B.2	The χ^2 contours of β_t versus T_{fo} after a simultaneous fit to the 5-15% particle spectra. A parabolic profile is used.	215
B.3	The χ^2 contours of β_t versus T_{fo} after a simultaneous fit to the 15-30% particle spectra. A parabolic profile is used.	216
B.4	The χ^2 contours of β_t versus T_{fo} after a simultaneous fit to the 30-60% particle spectra. A parabolic profile is used.	216
B.5	The χ^2 contours of β_t versus T_{fo} after a simultaneous fit to the 60-92% particle spectra. A parabolic profile is used.	217
C.1	Monte Carlo (left) and reconstructed Monte Carlo (right) p_t distributions.	219
C.2	Monte Carlo input distribution of charged primary particles (before reconstruction, left) compared to the reconstructed distribution (right).	220
C.3	Same as in Figure C.2 but with decay vertex cut (exclude all decays and albedo outside of 70 and 110 degrees theta). Decays and albedo excluded in the cut are shown as black stars.	221

List of Tables

3.1	The wire plane arrangement in each Drift Chamber in increasing radial position r . The radius R is the drift chamber reference radius. The tilt angle is measured with respect to the z -axis. .	26
3.2	Resolution and positions in r , ϕ , and η of PHENIX subsystems. Detectors not used in Year 1 have a line.	34
4.1	The number of events in each centrality class between 0 and 50% of the total measured cross section.	42
4.2	The number of events in each centrality class between 50 and 92% of the total measured cross section.	43
4.3	The centrality selections and the corresponding number of events as used in this analysis.	43
4.4	The number of participants for the centrality selections used in the analysis [80, 51, 52].	45
4.5	Quality bit definitions	46
4.6	Angular resolutions σ_α for partially (X1 or X2) and fully (X1 and X2) reconstructed tracks in the ideal case, in simulation, and in data. [59, 58]	58
4.7	Materials positioned at radial positions r up to the drift chambers, with thicknesses Δr , and their contribution to σ_α [59]. . .	60
4.8	The offset A and factor B necessary to avoid cutting into the distribution of pions [57].	67
4.9	Positive and negative particles before and after the β -dependent energy loss cut described in the text for $p_t < 4$ GeV/ c [60]. . .	69
4.10	The background contribution for different p_t ranges in the pion, kaon, and (anti)proton spectra.	73
5.1	The simulated matching sigmas depend on momentum in both ϕ and z	89
5.2	Positive and negative particles before and after fiducial cuts are made in the TOF detector. The fraction of tracks cut is greatest for positive Monte Carlo tracks.	91

5.3	The three main momentum-dependent fiducial cuts that are made using the Drift Chamber ϕ variable. These cuts are used in both the simulation and in the raw data are defined according to TOF Sector and DC Side accordingly.	96
5.4	Pion correction factors from single particle Monte Carlo.	105
5.5	Kaon correction factors from single particle Monte Carlo.	106
5.6	Proton and anti-proton correction factors from single particle Monte Carlo.	107
5.7	The $\langle p_t \rangle$ and yield as measured from the data for positive pions. The measured ranges in p_t are indicated.	117
5.8	The $\langle p_t \rangle$ and yield as measured from the data for negative pions. The measured ranges in p_t are indicated.	117
5.9	The $\langle p_t \rangle$ and yield as measured from the data for positive kaons. The measured ranges in p_t are indicated.	118
5.10	The $\langle p_t \rangle$ and yield as measured from the data for negative kaons. The measured ranges in p_t are indicated.	118
5.11	The $\langle p_t \rangle$ and yield as measured from the data for protons. The measured ranges in p_t are indicated.	118
5.12	The $\langle p_t \rangle$ and yield as measured from the data for anti-protons. The measured ranges in p_t are indicated.	119
6.1	The resulting effective temperatures of positive pions after fitting a thermal function to $m_t - m_0 < 1$ GeV in all centralities.	128
6.2	The resulting effective temperatures of negative pions after fitting a thermal function to $m_t - m_0 < 1$ GeV in all centralities.	129
6.3	The resulting effective temperatures of positive kaons after fitting a thermal function to $m_t - m_0 < 1$ GeV in all centralities.	130
6.4	The resulting effective temperatures of negative kaons after fitting a thermal function to $m_t - m_0 < 1$ GeV in all centralities.	131
6.5	The resulting effective temperatures of protons after fitting a thermal function to $m_t - m_0 < 1$ GeV in all centralities.	131
6.6	The resulting effective temperatures of antiprotons after fitting a thermal function to $m_t - m_0 < 1$ GeV in all centralities.	131
6.7	The fitted freeze-out temperature T_{fo} and averaged transverse flow velocity $\langle \beta_t \rangle$ for three different centralities: most central, mid-central, and most peripheral using the empirical expression Equation 6.1.2 as is done in [99]. The first line in each centrality corresponds to positive particles and the second to negative.	134

6.8	The minimum χ^2 and the parameters T_{fo} and β_t for each of the five centrality selections. The best fit parameters are determined by averaging all parameter pairs within the 1σ contour. The errors correspond to the standard deviation of the parameter pairs within the 1σ χ^2 contour.	141
6.9	The 5% central dN/dy and $\langle p_t \rangle$ for all measured particles. .	157
6.10	The 5-15% central dN/dy and $\langle p_t \rangle$ for all measured particles.	158
6.11	The 15-30% central dN/dy and $\langle p_t \rangle$ for all measured particles.	158
6.12	The 30-60% central dN/dy and $\langle p_t \rangle$ for all measured particles.	159
6.13	The 60-92% central dN/dy and $\langle p_t \rangle$ for all measured particles.	159
6.14	The sources of systematic uncertainties in $\langle p_t \rangle$ and dN/dy [57].	160
7.1	The effective temperature of hadrons for S+S, S+Pb, Pb+Pb colliding systems at CERN energies. Errors are statistical only.	171
7.2	The effective temperatures of hadrons produced in p+p and p+nucleus colliding systems at CERN and ISR energies. Errors are statistical only.	172
7.3	The freeze-out temperature T_{fo} and radial flow velocity $\langle \beta_t \rangle$ for both positive and negative hadrons produced at CERN energies in a variety of collision systems.	172
7.4	The $dN_{ch}/d\eta$ as determined from summing the yields for π , K, and $(\bar{p})p$ respectively. Published values that are measured in the 0-5% centrality are shown as a comparison. The errors include both statistical and systematic uncertainties.	185
7.5	Peter Kolb's calculated maximum initial energy density and maximum temperature for a variety of impact parameters in the transverse plane. The initial energy density is determined using both wounded nucleons and the number of binary collisions.	187
7.6	The $\langle \beta_t \rangle$ as measured from the data compared to the hydrodynamics values. The values are within 5%. The $\langle p_t \rangle$ are also compared for negative pions.	188
A.1	Invariant cross section for positive and negative pions produced in minimum bias events. The errors include the statistical error from the data and the systematic uncertainty from the bin correction.	201

A.2	Invariant cross section for positive and negative kaons produced in minimum bias events. The errors include the statistical error from the data and the systematic uncertainty from the bin correction.	202
A.3	Invariant cross section for protons and antiprotons produced in minimum bias events. The errors include the statistical error from the data and the systematic uncertainty from the bin correction.	203
A.4	Invariant cross section for positive and negative pions produced in the 0-5% centrality. The errors include the statistical error from the data and the systematic uncertainty from the bin correction.	204
A.5	Invariant cross section for positive and negative kaons produced in the 0-5% centrality. The errors include the statistical error from the data and the systematic uncertainty from the bin correction.	204
A.6	Invariant cross section for protons and antiprotons produced in the 0-5% centrality. The errors include the statistical error from the data and the systematic uncertainty from the bin correction.	205
A.7	Invariant cross section for positive and negative pions produced in the 5-15% centrality. The errors include the statistical error from the data and the systematic uncertainty from the bin correction.	206
A.8	Invariant cross section for positive and negative kaons produced in the 5-15% centrality. The errors include the statistical error from the data and the systematic uncertainty from the bin correction.	206
A.9	Invariant cross section for protons and antiprotons produced in the 5-15% centrality. The errors include the statistical error from the data and the systematic uncertainty from the bin correction.	207
A.10	Invariant cross section for positive and negative pions produced in the 15-30% centrality. The errors include the statistical error from the data and the systematic uncertainty from the bin correction.	208
A.11	Invariant cross section for positive and negative kaons produced in the 15-30% centrality. The errors include the statistical error from the data and the systematic uncertainty from the bin correction.	208

A.12	Invariant cross section for protons and antiprotons produced in the 15-30% centrality. The errors include the statistical error from the data and the systematic uncertainty from the bin correction.	209
A.13	Invariant cross section for positive and negative pions produced in the 30-60% centrality. The errors include the statistical error from the data and the systematic uncertainty from the bin correction.	210
A.14	Invariant cross section for positive and negative kaons produced in the 30-60% centrality. The errors include the statistical error from the data and the systematic uncertainty from the bin correction.	210
A.15	Invariant cross section for protons and antiprotons produced in the 30-60% centrality. The errors include the statistical error from the data and the systematic uncertainty from the bin correction.	211
A.16	Invariant cross section for positive and negative pions produced in the 60-92% centrality. The errors include the statistical error from the data and the systematic uncertainty from the bin correction.	212
A.17	Invariant cross section for positive and negative kaons produced in the 60-92% centrality. The errors include the statistical error from the data and the systematic uncertainty from the bin correction.	212
A.18	Invariant cross section for protons and antiprotons produced in the 60-92% centrality. The errors include the statistical error from the data and the systematic uncertainty from the bin correction.	213
B.1	The T_{fo} and β_t that result after fitting the hydrodynamic parameterization to the particle spectra simultaneously. A parabolic velocity profile is used.	214
D.1	Extrapolated yield and average transverse momentum after fitting functions to the 0-5% positive pion spectra. The power-law is Equation 6.22 and the m_t exponential is Equation 6.12. . .	222
D.2	Extrapolated yield and average transverse momentum after fitting functions to the 0-5% negative pion spectra. The power-law is Equation 6.22 and the m_t exponential is Equation 6.12. . .	223

D.3	Extrapolated yield and average transverse momentum after fitting functions to the 0-5% positive kaon spectra. The p_t exponential is Equation 6.23 and the m_t exponential is Equation 6.12.	223
D.4	Extrapolated yield and average transverse momentum after fitting functions to the 0-5% negative kaon spectra. The p_t exponential is Equation 6.23 and the m_t exponential is Equation 6.12.	223
D.5	Extrapolated yield and average transverse momentum after fitting functions to the 0-5% proton spectra. The p_t exponential is Equation 6.23 and the m_t exponential is Equation 6.12. . .	224
D.6	Extrapolated yield and average transverse momentum after fitting functions to the 0-5% antiproton spectra. The p_t exponential is Equation 6.23 and the m_t exponential is Equation 6.12.	224
D.7	Extrapolated yield and average transverse momentum after fitting functions to the 5-15% pion spectra. The power-law is Equation 6.22 and the m_t exponential is Equation 6.12. . . .	225
D.8	Extrapolated yield and average transverse momentum after fitting functions to the 5-15% kaon spectra. The p_t exponential is Equation 6.23 and the m_t exponential is Equation 6.12. . . .	226
D.9	Extrapolated yield and average transverse momentum after fitting functions to the 5-15% (anti)proton spectra. The p_t exponential is Equation 6.23 and the m_t exponential is Equation 6.12.	227
D.10	Extrapolated yield and average transverse momentum after fitting functions to the 15-30% pion spectra. The power-law is Equation 6.22 and the m_t exponential is Equation 6.12. . . .	228
D.11	Extrapolated yield and average transverse momentum after fitting functions to the 15-30% kaon spectra. The p_t exponential is Equation 6.23 and the m_t exponential is Equation 6.12. . . .	229
D.12	Extrapolated yield and average transverse momentum after fitting functions to the 15-30% (anti)proton spectra. The p_t exponential is Equation 6.23 and the m_t exponential is Equation 6.12.	230
D.13	Extrapolated yield and average transverse momentum after fitting functions to the 30-60% pion spectra. The power-law is Equation 6.22 and the m_t exponential is Equation 6.12. . . .	231

D.14 Extrapolated yield and average transverse momentum after fitting functions to the 30-60% kaon spectra. The p_t exponential is Equation 6.23 and the m_t exponential is Equation 6.12. . . .	232
D.15 Extrapolated yield and average transverse momentum after fitting functions to the 30-60% (anti)proton spectra. The p_t exponential is Equation 6.23 and the m_t exponential is Equation 6.12.	233
D.16 Extrapolated yield and average transverse momentum after fitting functions to the 60-92% pion spectra. The power-law is Equation 6.22 and the m_t exponential is Equation 6.12. . . .	234
D.17 Extrapolated yield and average transverse momentum after fitting functions to the 60-92% kaon spectra. The p_t exponential is Equation 6.23 and the m_t exponential is Equation 6.12. . . .	235
D.18 Extrapolated yield and average transverse momentum after fitting functions to the 60-92% (anti)proton spectra. The p_t exponential is Equation 6.23 and the m_t exponential is Equation 6.12.	236

Acknowledgements

I would like to first gratefully acknowledge my advisor, Professor B.V. Jacak, for her guidance and support in the work leading up to this dissertation. From the very beginning, Barbara encouraged me to get involved in the physics of relativistic heavy ion collisions, while PHENIX was still in the hardware stage. It was challenging to balance hardware, software, and analysis, but in the end I found the experience and knowledge I obtained essential for Year-1 physics at RHIC. Her questions and observations guided the analysis presented here. I thank Barbara for giving me the opportunity to analyze Year-1 physics at RHIC, for encouraging me to work with theorists, and for nominating me for the Gertrude Goldhaber Prize.

I acknowledge the dissertation committee for their contribution to the preparation of this manuscript. I also give special thanks to U. Heinz and P. Kolb for their hydrodynamics model contribution and the most useful discussions.

I thank Tom Hemmick, Axel Drees, Vlad Pantuev, and Michael Marx for their support and encouragement in addition to their many suggestions related to this study. I acknowledge the contributions to this work, either directly or indirectly, from: Julia Velkovska, Federica Messer, Steve Johnson, Ralf Averbeck, Jiangyoung Jia, Yasuyuki Akiba, Momchil Velkovsky, Johann Heuser, Sergey Butsyk, PNPI, David Morrison, Jeff Mitchell, Hiroaki Ohnishi, Tatsuya Chujo, Mikhail Kopytine, Derek Teaney, Mike Miller, Frank Muehlbacher, and Akiyo Kiyomichi. I especially thank Jennifer Thomas, Richard Hutter, and the SUNY Stony Brook undergraduates who worked on the RICH and Drift Chamber detectors.

This work would not be possible without the help and support from the PHENIX Collaboration. At Brookhaven National Laboratory (BNL), I thank those who worked in the Counting House during the Summer 2000 Run. In particular: Mickey Chiu, Jamie Nagle, Steve Adler, Craig Woody, Achim Franz, and Martin Purshke. I thank the Global and Hadron Physics Working Groups; in particular, Bill Zajc, Glenn Young, Sam Aronson, Craig Ogilvie, John Sullivan, Roy Lacey, and Mike Tannenbaum for the useful comments and

suggestions they made during my presentations.

At SUNY Stony Brook, I acknowledge the Nuclear Theory Group for the valuable physics discussions; in particular, Edward Shuryak, Jerry Brown, Madappa Prakash, Thomas Shaefer, and Ralf Rapp. In the Graduate Program, I thank Peter Koch, Laslo Mihaly, Chris Jacobsen, Janos Kirz, Peter Stephens, and Peter Kahn for their advice and guidance. I especially thank Patricia Peiliker, Diane Siegel, Socoro Delquaglio, and Pamela Burris for their administrative support.

I acknowledge Steve Kahn, Fritz Paerels, Alex Zetzl, Seamus Davis, and Richard Packard of the University of California (UC) at Berkeley for giving me the opportunity to advance my research experience prior to graduate study. I especially thank Walter Knight for his guidance during my undergraduate years while at UC Berkeley, and David Newton of De Anza College who was most influential in my decision to continue with physics.

On a personal note, I am most grateful for my kindred spirit, Scott Fiscus, who was most supportive of this pursuit. Without his patience and understanding this work would not have been possible. The encouragement and discipline I received from my uncles Graeme and Trevor was most crucial during my undergraduate studies, and I cannot thank them enough. Finally, I must thank my brother Andrew, sister Rachel, and my parents, Ken and Virginia, who all inspired me to pursue my dreams without accepting limitation. This work is dedicated to them.

Chapter 1

Introduction

It is predicted by theoretical calculations that highly excited and dense hadronic matter undergoes a phase transition from a hadronic gas to a deconfined state of quarks and gluons, a plasma of quarks and gluons called a Quark Gluon Plasma (QGP)[8].

Matter is made up of hadrons and leptons. The hadrons include the baryons which consist of three quarks and mesons with a quark (q) and antiquark (\bar{q}) pair. As there are quarks and antiquarks, there are baryons and antibaryons. Hadrons are color neutral combinations of the fundamental particles called quarks and gluons as defined in the standard model¹.

Before nuclei and atoms were formed, the very hot and baryon free² early universe may have existed in such a state of deconfinement, a few μs after the Big Bang[14]. The initial state of the Universe is a hot and dense plasma made up of relativistic quarks, leptons, gauge bosons, and Higgs bosons. As the universe expanded and cooled, it evolved through phase transitions that spontaneously broke various symmetries. These phase transitions can be extrapolated backward in time to 10^{-34}s after the Big Bang[5]:

- $< 10^{-34}\text{s}$: All the fundamental forces are unified according to the Grand Unified Theory (GUT).
- 10^{-34}s : The strong force separates from the weak and electromagnetic forces.
- 10^{-11}s : The weak force breaks away from the electromagnetic force.

¹The u, c, and t all have an electrical charge of $+2/3$, while the d, s, and b have $-1/3$. All the quarks are fermions (1/2 spin) with baryon number $1/3$, while the gluons are massless bosons (spin 1).[7]

²Baryon free means the net baryon number is 0.

- 10^{-5} s: Quarks condensed into hadrons (QGP phase transition).
- $10^{-5} < t < 10^{-2}$ s: Pair production and annihilation of baryons. The stable hadrons (baryons and nucleons) survive.
- $10^{-2} < t < 10^2$ s: Nucleosynthesis until light elements freeze-out at a particular temperature.

The quark-hadron phase transition can affect the baryon number density distribution in the universe which affects the distribution of the light elements (in addition to generating magnetic fields)[4].

At the other extreme, a QGP can exist in matter with a large baryon density. Theoretical calculations predict that a QGP may also exist in cold neutron stars where the pressure gradients and density of baryons are many times larger than normal nuclear matter mass density³. At such densities different phases of superdense matter may be reached. Models with equations of states map out the phase transition region in terms of the conserved quantities, electric charge, and baryon number. Such phases include a nucleon star which has a either a kaon or pion condensate; a hyperon star where it has hyperons in its core⁴; or a strange star which has in its core stable quark matter that is made up of the u, d, and s quarks. The challenge is to find the appropriate experimental observables that verify such phase transitions. One such observable is the rotational frequency of pulsars, where the decreasing moment of inertia may be caused by a phase transition between hadronic and quark matter [15].

The quark-hadron phase transition is the predicted first-order phase transition in the theory called Quantum Chromodynamics (QCD). This theory describes the strong interactions of quarks and gluons. As Quantum Electrodynamics (QED) is to electromagnetic interactions, QCD is to strong interactions. The electromagnetic force (or coupling) between two charged particles decreases with the inverse square of their relative distance, while the strong force between quarks and gluons decreases logarithmically at small relative distances (called asymptotic freedom). A small distance in space-time is equivalent to a large momentum transfer between quarks (q) and gluons (g). In this energy regime, the force that binds quarks and gluons together (QCD coupling) becomes small and perturbation theory, called perturbative QCD (pQCD) can be used. As the energy decreases, the distances in space-time increase and the relative momenta between the quarks and gluons decrease. In

³Normal nuclear matter mass density is $140 \text{ MeV}/\text{fm}^3$

⁴Some of the hyperons include Σ , Λ , and Δ .

this limit, the QCD coupling increases and the quarks and gluons are confined into bound states of hadrons.[6, 7, 8]

1.1 Relativistic Heavy-Ion Collisions

The objective of relativistic heavy-ion physics is to produce an energy density in a region of overlap between two colliding ions that is high enough that quarks initially confined as hadrons can move freely as in a relativistic gas. The large energy density produces particles that are focused into detectors where each particle's momentum, time-of-flight, and energy are measured.

1.1.1 Observables

The collisions of relativistic Au nuclei probe the phase transition between hadronic matter and quark matter. If the collision can be described as an expanding, relativistic fluid, hydrodynamic models with various equations of state can be used to predict the hadron spectra. The expansion evolves according to an equation of state and initial conditions appropriate for the collision energy studied are tuned. The predicted spectra are then compared to the measured spectra [86, 87, 9].

The quarks and gluons coexisting in this plasma state cannot be measured directly. Therefore, the challenge experimentally is to study a suite of observables that are sensitive to the collision dynamics. Such observables are still controversial as they are indirect probes of plasma formation.

The observable that is measured and discussed in this work is the transverse momentum spectra of produced hadrons; namely, pions, kaons, and (anti)protons. Hadrons are sensitive to the dynamics of the hadronic system. The shape of the momentum spectra are sensitive to the freeze-out hypersurface of the expanding system; the strength of the expansion and its duration can be extracted from the data assuming hydrodynamic behavior. The rising and falling ratios of measured particle yields studied over a variety of collision anisotropies may signal the onset of an increase in particle production. The total yield of particles produced is proportional to the initial energy density. Hydrodynamic calculations model the system as an expanding hadronic fluid given an equation of state that relates the energy density and pressure as a function of proper time.

Observables discussed in Reference [10] include the following measurements that are only briefly described here.

Jet Quenching

The momentum of hadrons produced by high p_t jets can decrease if the plasma has formed. The jets lose more energy in quark matter than in hadronic matter [1, 78]. The observable is the momentum dependence of the cross section of hadrons at high momenta for collisions where the phase transition is expected to occur.

Hanbury-Brown and Twiss Interferometry

The size of the particle emitting source in the hadronic system can be determined by measuring the interference between produced hadrons using a technique called Hanbury-Brown and Twiss (HBT) interferometry [11]. This technique has already worked well at CERN SPS energies and first results at RHIC energies are comparable to the CERN source radii [12].

Dileptons

Photons and dielectrons that are emitted directly from the plasma can be measured. The processes include quark-antiquark annihilation and Compton scattering of a gluon and a quark.

The invariant mass distribution of dileptons produced in the decays of vector mesons such as the ρ , the ω , and the ϕ in a QGP medium is another dilepton measurement. Changing masses would probe whether or not Chiral symmetry in QCD is restored. There is a competing process called Brown-Rho scaling[13] which can also change the mass of the ρ .

Hadron Production Cross Sections

Two more independent observables are the yields of the J/ψ and strange hadrons. The number of produced J/ψ mesons, which are bound charm-anticharm quarks may be reduced due to Debye screening in the QGP plasma. The potential can reduce the force of attraction between a $c\bar{c}$ and the probability for a bound state (the production cross section) decreases.

The number of produced hadrons containing the s or \bar{s} quark is an observable. In a QGP, the process is $q\bar{q} \rightarrow s\bar{s}$ or by two gluons fusing together to form an s and \bar{s} pair. Another one is difference in the ratios of K^+/π^+ and K^-/π^- .

1.2 Kinematic Quantities and Definitions

The relevant kinematic quantities and definitions are described. These include the definition of collision centrality, the kinematic variables used in the analysis, and hydrodynamic expansion.

1.2.1 Centrality

There are two types of nucleons in the early stage of the collision: spectator and participant nucleons. The impact parameter of each collision, or event, varies during the experiment. The collection of all possible impact parameters is called a minimum bias sample. Large impact parameter collisions are called peripheral events, while small impact parameter collisions are called central. The variation of impact parameter is called centrality. The participant nucleons N_p are those baryons that interact and suffer multiple collisions as the ions pass through each other. The spectator nucleons do not participate in the collision and travel at their initial energy toward detectors positioned along the beam axis.

1.2.2 Kinematic Variables

Momentum and Energy

The transverse momentum p_t is the projection of the particle's 3-momentum onto the plane that is transverse to the collision axis z : $p_t = p \sin \theta_0$, where θ_0 is the initial polar angle of the particle with respect to the event vertex position along the collision axis z .

The transverse energy of the particle with rest mass m_0 is

$$m_t = \sqrt{p_t^2 + m_0^2}. \quad (1.1)$$

Along the beam axis z , a quantity called rapidity y defines the longitudinal motion scale for a particle with a known mass m_0 :

$$y = \frac{1}{2} \log \left(\frac{E + p_z}{E - p_z} \right) \quad (1.2)$$

where $p_z = m_t \sinh(y)$.

The four-momentum of a particle can be described in terms of its transverse momentum p_t , its rapidity y , and transverse energy m_t

$$p^\mu = (m_t \cosh y, p_t \cos \phi_0, p_t \sin \phi_0, m_t \sinh y) \quad (1.3)$$

Center of Mass Energy

For two colliding nuclei with four-momentum p_i^μ and rest mass m_i , the center of mass energy is calculated from the Lorentz invariant s variable:

$$s = (p_1 + p_2)^\mu \cdot (p_1 + p_2)_\mu \quad (1.4)$$

where $p_i^\mu = (E_i, \mathbf{p}_i)$ and E_i is the energy of each nucleus. The momentum vectors \mathbf{p}_i are three-dimensional. The center of mass energy is the square-root of s .

$$\sqrt{s} = \sqrt{m_1^2 + 2E_1E_2 - 2\mathbf{p}_1 \cdot \mathbf{p}_2 + m_2^2} \quad (1.5)$$

At relativistic energies, $E_i = \gamma m_i$, where $1/\gamma = \sqrt{1 - \beta^2}$ and β is the speed of each nucleus⁵. In a collider, the momentum vectors are antiparallel along the beam axis. At RHIC energies, studied here, the center of mass energy is $\sqrt{s} = 130$ GeV.

Invariant Momentum Distribution

The invariant differential cross section of a particle is the probability of measuring d^3N particles (out of the number of events N_{evt}) with momenta dp^3/E in a differential phase space volume

$$\frac{1}{N_{evt}} E \frac{d^3N}{dp^3} = \frac{d^3N}{N_{evt} p_t dp_t d\phi dy} \quad (1.6)$$

where $dp^3 = dp_x dp_y dp_z = p_t dp_t d\phi m_t \cosh y dy$ in cylindrical coordinates. The quantities dp^3/E , N , $d\phi$, and dy are all Lorentz invariant.

Because of azimuthal symmetry there is no ϕ dependence and a factor of $1/2\pi$ results in the final form

$$\frac{1}{N_{evt}} E \frac{d^2N_i}{dp^2} = \frac{d^2N_i}{2\pi N_{evt} p_t dp_t dy} \quad (1.7)$$

Pseudorapidity

When the mass of a measured particle is unknown, the pseudorapidity variable η is used and is defined as

$$\eta = -\ln \left(\tan \frac{\theta}{2} \right) \quad (1.8)$$

The difference between pseudorapidity and rapidity is important when comparing single particle to unidentified charged particle spectra.

⁵Units where $c = \hbar = k = 1$ are used

1.2.3 Initial Energy Density

The region of overlap between the participant nucleons is called the deconfinement region where quarks and gluons are predicted to decouple from each other. Bjorken's approximation is used to calculate the energy density from the measured particle yield dN/dy (determined by integrating Equation 1.2.2 over p_t) [14].

In cylindrical coordinates, the volume of the overlap region between two colliding nuclei depends on the collision centrality. For the most central collisions, the impact parameter is zero and the volume is $\pi R^2 \Delta z$, where $\Delta z = c\tau$, and τ is the time that elapses for hadronization (typically taken to be 1 fm/c). If the average energy per particle is $\langle E \rangle$, and the number of particles produced is dN/dy , then

$$dE/dy \approx \langle E \rangle dN/dy \quad (1.9)$$

and the average initial energy density $\langle \epsilon_0 \rangle$ is

$$\langle \epsilon_0 \rangle = \frac{\langle E \rangle dN}{V dy} \quad (1.10)$$

where V is the volume of the overlap region that depends on the collision centrality and the radius R of the nucleus is

$$R = r_0 A^{1/3} \quad (1.11)$$

where $r_0 = 1.2\text{fm}$ is the nucleon radius. At RHIC energies, $\langle \epsilon_0 \rangle$ is 5.0 GeV/fm³ [76]. The predicted $\langle \epsilon_0 \rangle$ threshold for QGP formation is 2 – 3 GeV/fm³ [14].

1.2.4 Hydrodynamic Expansion

Modern cosmological models are used to determine the expansion rate of the Universe and the energy density in it[4]. So too in heavy-ion collisions, where hydrodynamic models are used to extract the collective expansion of hadrons until they freeze-out at a temperature T_{fo} [86, 87, 9].

In a collision between two nuclei traveling relativistically, Lorentz contraction causes the nuclear shapes to flatten in the direction of motion. In the space-time diagram of the collision, in Figure 1.1, the two relativistic nuclei travel toward each other close to the speed of light along a collision axis called z in time t . They collide at $z=0$ and $t=0$. The hyperbola are constant proper-time⁶ curves where c is 1 and z is the longitudinal position of the fluid element

⁶The proper-time $\tau = \sqrt{t^2 - z^2}$.

along the beam axis z . On each curve, the energy density, entropy density, and temperature are constant. The left diagram is the evolution of the system if no QGP phase transition occurs. The temperature is a maximum at the time of hadron formation. After hadronization in time τ_h , the hadronic fluid expands until it reaches a freeze-out temperature at time τ_f . The arrows indicate the decoupling of the hadrons on the freeze-out hypersurface as they stream freely toward the detectors. The diagram on the right shows the evolution of the system in the mixed phase between a hadron gas and a QGP.

The longitudinal expansion velocity is z/t so that a piece of fluid positioned at $z = 0$ does not move longitudinally and observes other fluid elements receding away from it in either direction. Instead of the beam axis position coordinate z and time t , the variables η and τ , respectively, are used where η is defined as the space-time rapidity variable written in terms of t and z in Equation 1.12.

$$\eta = \frac{1}{2} \ln \left(\frac{t+z}{t-z} \right) \quad (1.12)$$

There are different types of EOS in hydrodynamic models and the one used to compare to the data is a combination of a hadron gas and a relativistic gas by U. Heinz and P. Kolb. The EOS was originally developed by R. Venugopalan and M. Prakash [18]. The relativistic gas represents the deconfined QGP phase.

The system evolves according to the following equation of state [87]:

- Hadron resonance gas. All the known resonances are incorporated up to 2 GeV in mass.
- Mixed phase between a hadron resonance gas and a QGP phase.
- QGP phase: $p = \epsilon/3$. The QGP is modeled as an ideal relativistic gas of massless quarks and gluons. The phase transition occurs at temperature $T = 164$ MeV.

All calculations relativistic hydrodynamics use conservation of entropy density and baryon number density[9].

During the expansion, fluid elements that are positioned far away from the overlap region of the nuclei and transverse to the collision axis cool faster than fluid elements in the interior. This is due to the shock wave that travels at the speed of sound in the hadronic fluid from the edge of the nuclei toward the interior. This makes the hydrodynamic calculations difficult[87].

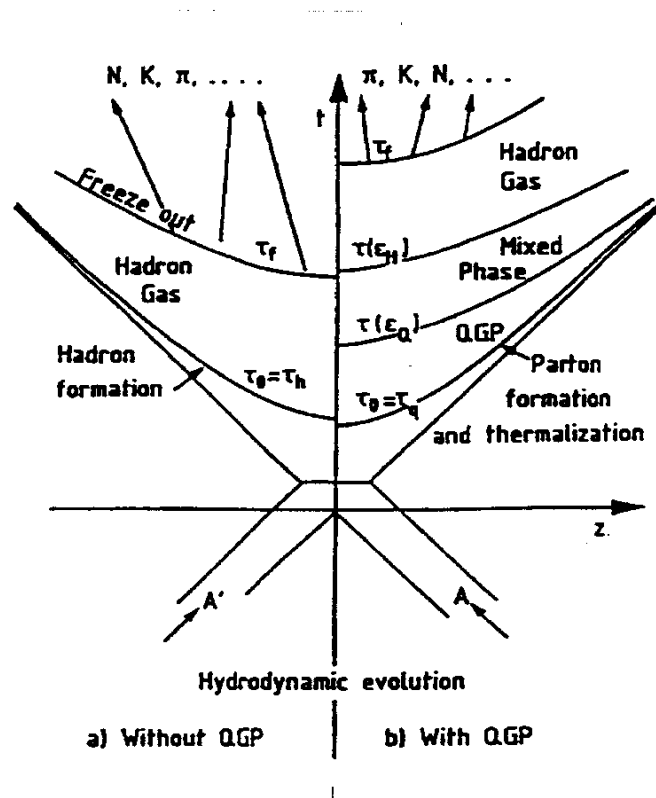


Figure 1.1: The hydrodynamic evolution of a system produced by two relativistic heavy ions colliding at the point $t = 0$ and $z = 0$ with (right) and without (left) a Quark-Gluon Plasma phase transition.[16]

1.3 Organization of the Thesis

The results of the first PHENIX measured transverse momenta of identified hadrons as produced in Au-Au collisions at $\sqrt{s_{NN}} = 130$ GeV are presented. The analysis is based on the data taken during the first year's run in Summer 2000 by the PHENIX Collaboration at RHIC at BNL.

In Chapter 2, the Relativistic Heavy Ion Collider facility at Brookhaven National Laboratory is introduced. In Chapter 3, the detectors that measure the hadrons and leptons produced in such a high particle density environment are discussed in more detail.

The data reduction techniques using the Time-of-Flight and Drift Chamber detectors are described in Chapter 4. The event and track selection criteria are defined, applied, and discussed. The steps involved in reducing the data to raw, uncorrected spectra for pions, kaons, protons, and antiprotons are discussed in detail.

In Chapter 5, the corrections that are applied to the raw spectra are described in detail. Inherent in the raw spectra are detector and track reconstruction effects. These effects include the detector acceptance and resolution, decays in flight, and track reconstruction inefficiencies. The corrections for these effects are determined using single particle Monte Carlo and the GEANT simulation of the detector response. The particle spectra, yields, and truncated average momentum in the measured range in p_t are determined.

In Chapter 6, the results are presented. Functions that describe the shape of the spectra are used to extrapolate the unmeasured portion in order to determine the total average momentum and particle yield for each particle. In each centrality, a hydrodynamic parameterization is fit simultaneously to the spectra and the χ^2 contours are produced for the expansion parameters. The overall systematic uncertainties in the spectra are discussed.

In Chapter 7, a discussion of the results is presented. Comparisons are made to similar measurements made at lower center of mass energies. First, a radial flow analysis for collisions produced at lower energies for different nuclei is described and discussed. The goal of the analysis is to determine the transition region in p_t between hard and soft physics. A similar analysis is repeated for RHIC energies. A full hydrodynamics model calculation by U. Heinz and P. Kolb with an equation of state that simulates a mixed phase comprised of a hadron gas and a relativistic gas of quarks and gluons (QGP) is tuned to RHIC energies and is compared to the data. Finally, an outlook to Year-2 physics at RHIC is discussed.

Chapter 2

The Relativistic Heavy Ion Collider Facility

Experimentalists use high-energy colliders and accelerators to propel heavy ions to the highest achievable energies in order to study nuclear matter under extreme conditions, where an energy density is at least a few GeV/fm^3 .

Accelerators include the Super Proton Synchrotron (SPS) at CERN and the Alternating Gradient Synchrotron (AGS) at the Brookhaven National Laboratory (BNL). The largest produced center-of-mass energies at the CERN SPS are 20 GeV for S+S and 17 GeV for Pb+Pb. At the AGS, center of mass energies ranged from 2.5 to 4.5 GeV. The maximum beam energy at the AGS is 11.5 GeV/A, while for CERN 160 GeV/A. These accelerators provide a beam of nuclei that is incident on a fixed-target of material. For example, at the CERN SPS, the beam is proton (p), sulfur (S), or lead (Pb), with target materials depending on the experiment. The spectrometers are positioned downstream with a small angular displacement from the accelerator beam line. At the CERN SPS and AGS BNL, a beam is incident on a stationary target material. The reference frame in the lab is not equal to the center-of-mass frame. In the lab frame, the showers of particles produced in the collision are focused by magnets into tracking spectrometers that measure the momentum and energy.

In a collider, the lab and center of mass frames are equal. The most recent collider which produces the highest energy density is RHIC at Brookhaven National Laboratory (BNL) located in Upton, New York. Both an aerial photograph and a diagram of the RHIC complex are shown in Figure 2.1.

RHIC is capable of colliding a wide variety of particle species from Au+Au to polarized p+p. During the first year of running, RHIC collided Au ions at $\sqrt{s_{NN}} = 130 \text{ GeV}$. Before the collisions can occur in RHIC, the ions travel through various stages from production to collisions. Each beam consists of 60 Au ion bunches within μs apart that are:

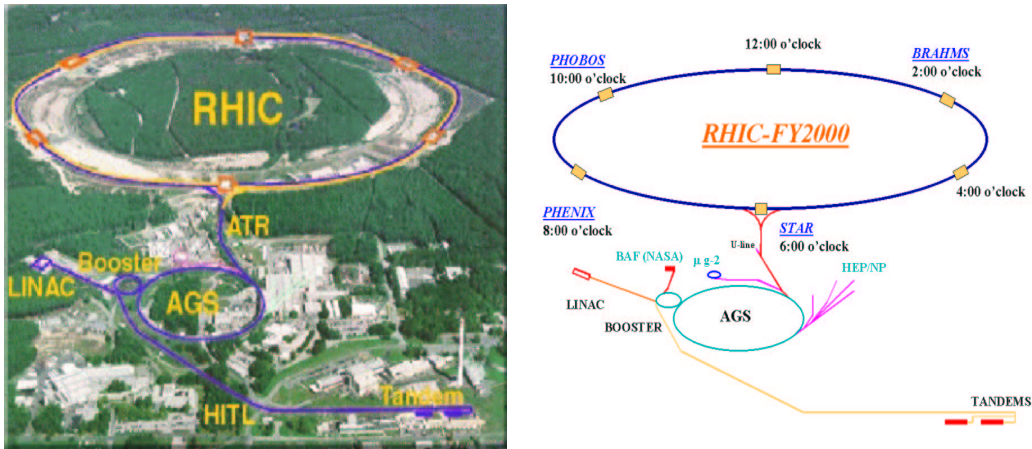


Figure 2.1: The RHIC complex at Brookhaven National Laboratory in Upton, New York (left) [22] and a diagram with the experiments operating in Year-1 (right) [23].

- ionized by two 15 MeV electrostatic accelerators in the Tandem Van de Graff¹,
- propelled by magnets in the Heavy Ion Transport Line (HITL) at $\gamma = 1$ in vacuum,
- injected by a circular Booster synchrotron² into the AGS ring and accelerated to $\gamma = 13$,
- divided by sorting magnets into two beams left and right (called yellow and blue),
- injected into the RHIC ring,
- guided by dipole magnets to travel in a nearly circular orbit, and
- accelerated by a pulse of radio waves (RF) to $\gamma = 70$.

¹The Tandem can provide 40 different types of ion species from hydrogen to uranium [21, 22].

²The magnetic field in the synchrotron increases in strength with each revolution [21, 22].

Dipole magnets then steer the counter-rotating beams to produce collisions at the center of each detector [21, 22]. More detail on colliders can be found in Reference [20].

In the first year of running at the Relativistic Heavy Ion Collider (RHIC), a center-of-mass energy of 130 GeV was obtained for Au+Au collisions. This is ≈ 7 times higher than at the CERN SPS and 30 times higher than at the AGS BNL. The design value is 100 GeV for each Au beam, equivalent to $\sqrt{s} = 200$ GeV. Once this beam energy is obtained, the \sqrt{s} will increase 1.5 times.

Four of the six interaction points house the experiments at RHIC: PHOBOS, BRAHMS, STAR, and PHENIX. The two largest experiments are STAR and PHENIX and the smallest are BRAHMS and PHOBOS (see Figure 2.1). In Year-1, RHIC produced collisions along 120 cm on the beam axis, at the center of each detector.

Common to all experiments at RHIC are two Zero-Degree Calorimeters (ZDC) positioned along the beam axis. The ZDCs measure the event rate produced in RHIC [39]. They also serve as event triggers for the experiments.

Each experiment is designed to measure observables as highlighted in Chapter 1. All the experiments are complimentary in the overall physics objective: to experimentally measure the hadron-quark phase transition. The details on each experiment can be found in Reference [24]. PHENIX measures both electromagnetic and hadronic probes with its four spectrometer arms which are discussed in the next chapter.

Chapter 3

The PHENIX Detector

The PHENIX detector is specifically designed for the measurement of dileptons yet it also has the capability for hadron identification over a large momentum range with its Time-of-Flight (TOF) system in the PHENIX East arm and its two types of Electromagnetic Calorimeters [35]. The baseline detector systems in PHENIX are shown in Figure 3.3. PHENIX has four spectrometer arms, two that are positioned about midrapidity (the Central Arms) and two at more forward rapidities (the Muon Arms). The PHENIX acceptance is illustrated in Figure 3.1.

The first Au+Au event recorded in PHENIX is displayed in the left panel in Figure 3.2. The East central arm is shown with hits recorded in the drift chamber [28]. The event display¹ on the right shows the tracks and hits as recorded by the PHENIX subsystems.

There are three magnets: the Central Magnet provides an axial magnetic field for the Central Arms while the Muon Magnets produce a radial field for the Muon Arms. The coordinate system in PHENIX is defined relative to the beam axis which passes through the center called z. The xyz axes follow the right-hand rule with the positive x axis pointing into the West arm and the positive z axis pointing toward North. The origin in PHENIX is the event vertex position which does not precisely coincide with the symmetry axis of the central arm detectors.

In what follows, the detectors are described in detail, with an emphasis on the Drift Chambers and Time-of-Flight detectors. In general, the detectors (called subsystems) can be grouped as follows:

1. Vertex and Trigger detectors: Zero-Degree Calorimeters (ZDC), Beam-Beam Counters (BBC) , Multiplicity/Vertex Detector (MVD). These detectors are positioned along the collision axis.

¹Jiangyoung Jia of SUNY Stony Brook wrote the PHENIX event display.

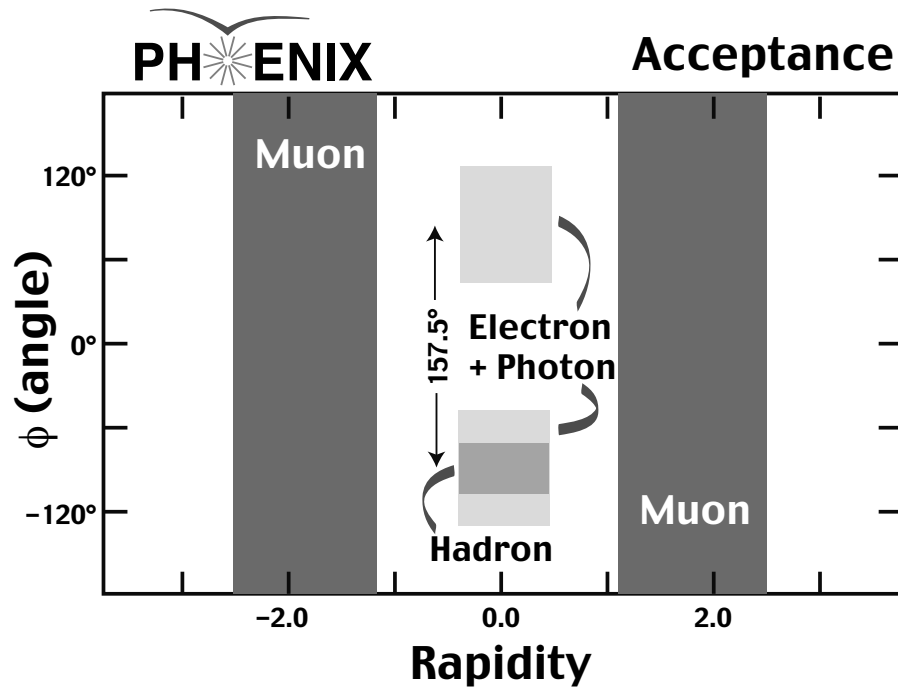


Figure 3.1: The PHENIX acceptance for hadrons and leptons. The vertical axis is azimuthal angle ϕ and the horizontal is the pseudorapidity η .

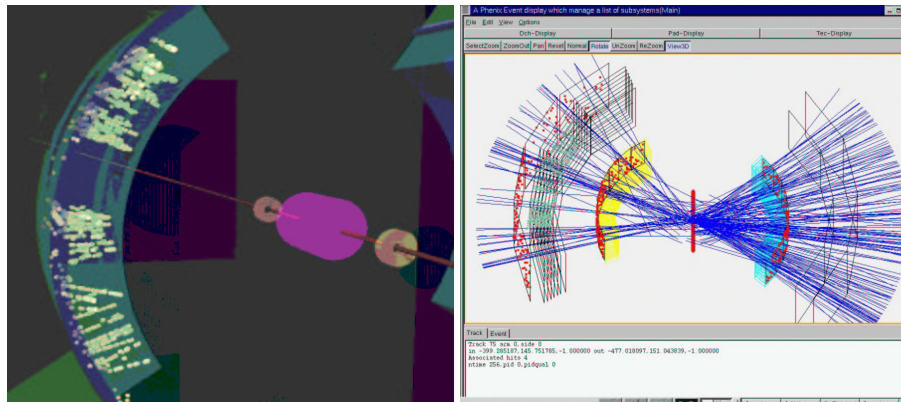


Figure 3.2: The first Au+Au event as recorded in the PHENIX detector (left) [28]. The PHENIX event display with subsystems used in Year-1 (right) [29].

2. Central Arm Detectors. These detectors are all positioned radially about the collision axis, extending from 2 m to 5 m.
 - (a) Central Magnet. The North and South poles of the Central Magnet are positioned on the collision axis at 0.45 m and -0.45 m respectively.
 - (b) Charged Tracking system: Drift Chambers (DC), Pad Chambers (PC), Time Expansion Chambers (TEC). There are two DCs, three PCs, and one TEC positioned radially from the collision axis about midrapidity.
 - (c) Ring Imaging Cherenkov Detector (RICH). There are two RICH detectors.
 - (d) Time-of-Flight System (TOF). The TOF is positioned in one arm only (the East) and has half the acceptance in azimuth as the Drift Chambers.
 - (e) Electromagnetic Calorimetry (PbGl and PbSc).
3. Muon Arm (tracking and particle identification).

The Au beams cross in PHENIX at a rate of 9.4 MHz, and all the PHENIX subsystems are clocked with this frequency. The vertex and trigger detectors measure the start time for the event. The 20 MB/s bandwidth data acquisition system (see Figure 3.4) pipes the data from the detectors when the vertex and trigger subsystems are triggered (Level-1 triggers). The Level-1 triggers are designed to select potentially interesting events while beams cross in PHENIX and to reduce the data rate to the acceptable levels. [25]

The data acquisition in PHENIX is as follows. All the subsystems are equipped with timing modules called Granular Timing Modules (GTM). The Master Timing Module (MTM) is the RHIC clock. The event is to the left in Figure 3.4 and occurs in the interaction region. The ZDC GTM and the MTM both trigger an event, called the Level-1 trigger (L1). The clock, trigger, and mode bits are then transported over optical fibers to the electronics of each detector, the Front End Module (FEM)². The detector records the data in raw digitized format and transports the data packets over fiber optics to the Data Collection Module (DCM). Finally, the data are transported for quality checks to Online Monitoring in the PHENIX control room. The data are then transferred to the end user where data calibration, track reconstruction, and analysis software is run, called Offline Computing.[32]

²For more information on the electronics, please refer to Reference [33, 34].

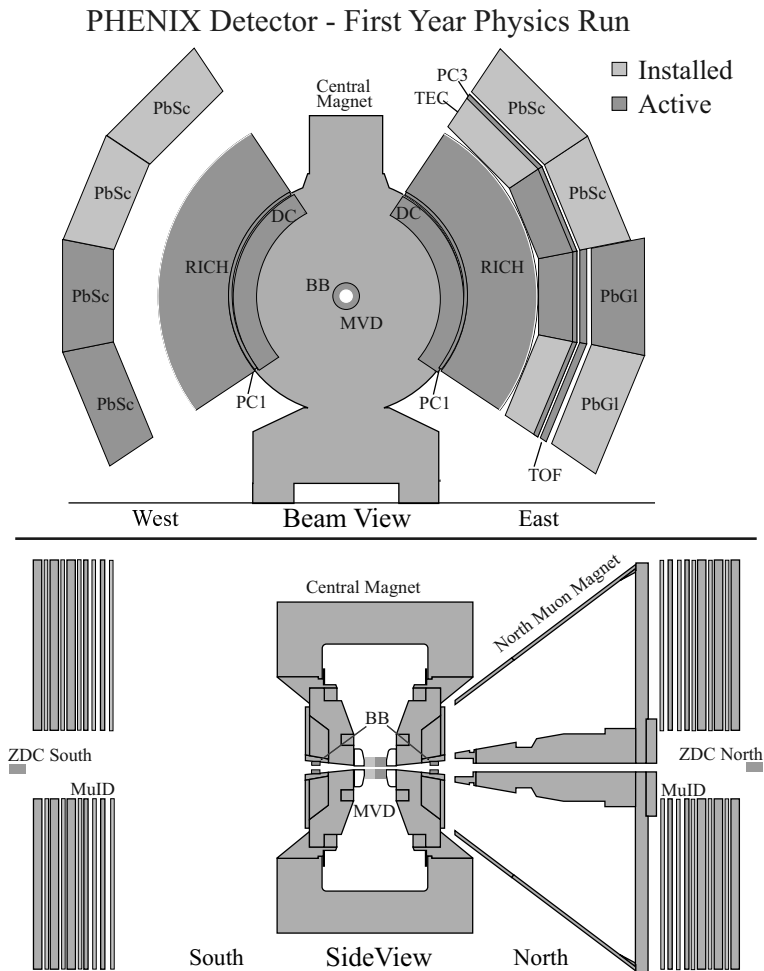


Figure 3.3: The experimental setup in PHENIX for the central arm spectrometer. The top picture is the cross-sectional view of PHENIX transverse to the beam axis while the bottom shows the beam-axis subsystems.

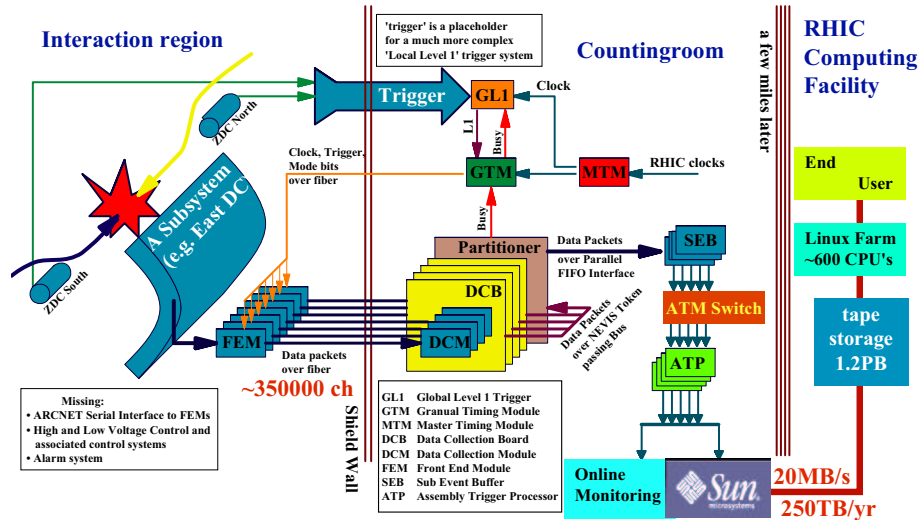


Figure 3.4: The PHENIX Data Acquisition System, triggered by an event in the Zero Degree Calorimeters (left in diagram).[32]

The Time-of-Flight (TOF) System measures the stop time for hadrons entering the TOF acceptance at roughly 5 m from the event vertex. The Drift Chambers and the Electromagnetic Calorimeters are calibrated with respect to the initial time as measured in the Beam-Beam Counters.

3.1 Vertex and Trigger Detectors

There are dedicated subsystems that determine the vertex of each collision in PHENIX. These include the Zero Degree Calorimeters, the Beam-beam Counters, and the Multiplicity Vertex Detector (the collision axis detectors as shown schematically in Figure 3.3).

3.1.1 Zero Degree Calorimeters

The ZDCs are RHIC standard detectors that measure the fraction of the energy deposited by spectator neutrons during the collisions and serve as an event trigger for each RHIC experiment. In PHENIX, two ZDCs are positioned North and South close to the Muon Spectrometers along the beam axis subtending the polar angle $\theta < 4$ mrad. Using the measured time difference

between ZDC North and ZDC South when neutrons are triggered in each detector respectively, the known distance between the two detectors, and the measured energy fraction deposited by the neutrons, the vertex position of the event along the collision axis is determined (between the ZDCs) [39]. Each ZDC is positioned 18 meters up and downstream from the interaction point along the beam axis. The calorimeters are positioned on platforms which support them between the beam pipes from the DX magnet to the D0 magnet. For the Summer 2000 runs, the total number of triggers recorded in the ZDCs are shown in Figure 3.5. A total of 5M events were recorded at $\sqrt{s_{NN}} = 130$ GeV.

3.1.2 Beam-Beam Counters

There are two Beam-beam counters each positioned 1.4 meters from the interaction point just behind the central magnet poles along the beam axis. Each Counter consists of 64 Cherekov telescopes, arranged radially about the collision axis and situated north and south of the Multiplicity Vertex Detector. The BBCs measure the fast particles produced in each collision at these forward angles. The particles measured in the Beam-beam counters along the beam axis from a Au+Au collision in PHENIX are shown in Figure 3.6. More detailed information on the BBCs can be found in Reference [38].

3.1.3 Multiplicity Vertex Detector

The MVD is composed of concentric barrels of silicon strip detectors and end-caps of silican pad detectors. It measures the multiplicity of charged particles produced close to the beam axis in each event. The MVD was not used in Year-1 but it will be used to reconstruct the event vertex in all three spatial coordinates in addition to measuring the $dN_{ch}/d\eta$.

3.2 Muon spectrometers (north and south)

The muon spectrometers identify and track muons that are produced in the high energy collisions. The charge deposited by muons in cathode strip chambers provide the space points of the tracks used in the muon tracking. The muon particle detector is comprised of interleaved layers of iron and Iarocci tubes. The muons are identified by energy loss of the muon via radiation after it traverses each layer of iron; the Iarocci tubes measure the amount of radiation produced. Pions lose energy via bremstrahlung (“braking radiation”)

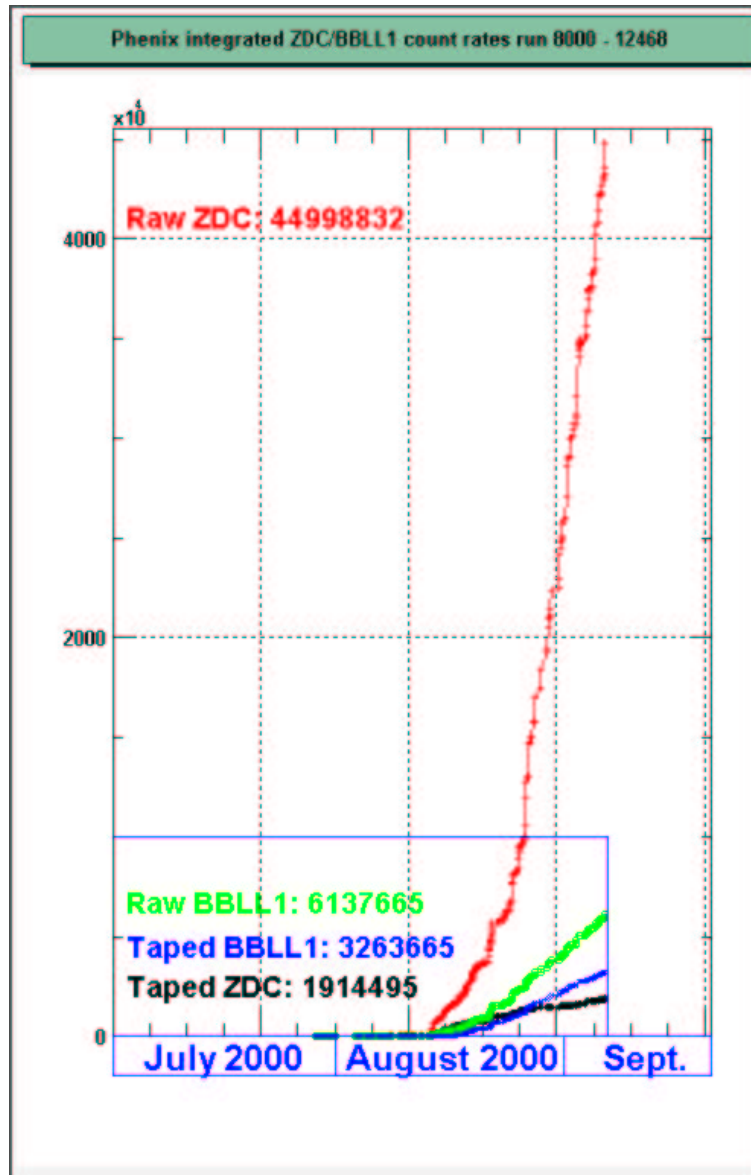


Figure 3.5: The total number of triggers recorded in PHENIX during the Summer 2000 run (runs 8000-12468) [26, 37].

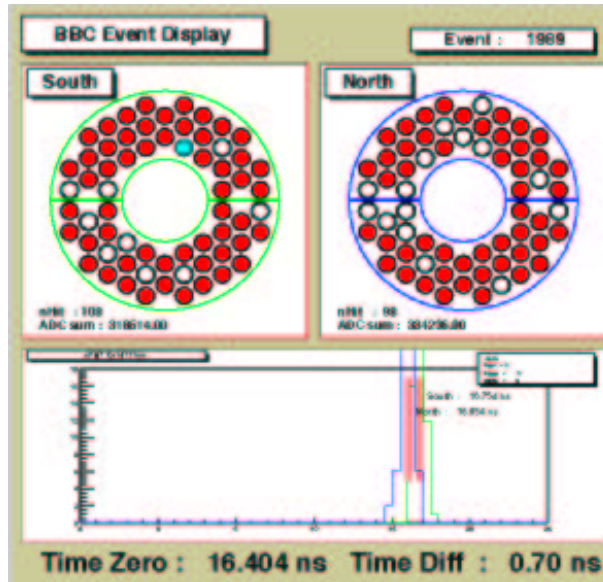


Figure 3.6: The BBC event display showing one Au+Au collision event as recorded in the PHENIX BBC detectors [37, 54].

and are stopped in the iron. The muon spectrometers were not used in Year-1, but will be used in Year-2. The muon tracking and particle identification system will measure J/ψ and ψ' .

3.3 Central Arm Spectrometers

3.3.1 Central Magnet

The central arm spectrometers use a central magnet that produces an approximately axially symmetric field that focusses the tracks into the detector acceptance. (The magnet for the muon spectrometers provides a radial field). The Central Magnet (CM) weighs approximately 500 tons and provides a total field integral of 0.78 T·m at 90 degrees in polar angle from the beam axis. This results in a single particle momentum resolution of 0.5% between 200 MeV/c and 1 GeV/c in momentum as measured in the Drift Chambers. The Year-1 measured resolution is described in more detail in Chapter 4.

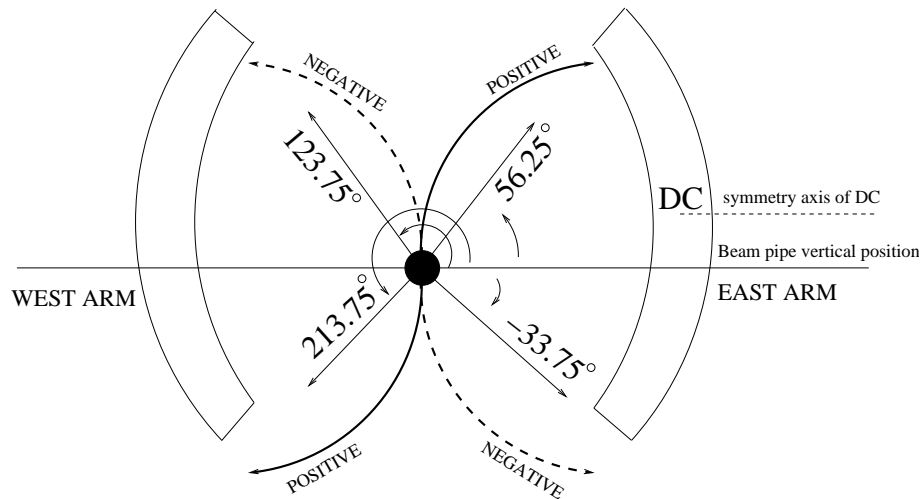


Figure 3.7: The magnet bends positive and negative particles in opposite senses into the PHENIX acceptance.

3.3.2 Charged Particle Acceptance

The central magnet bends positive particles clockwise and negative particles counter-clockwise into the PHENIX central arms (East and West) as illustrated in Figure 3.7. If the drift chambers have dead regions, then an asymmetric number of positive and negative tracks can occur, as was the case in Year-1.

To ensure symmetry between charges, data should be taken with both polarities in the Central Magnet. During the Year-1 run, this was not done due to the difficulty of switching the magnet cables. In order to correct for the asymmetry between the positive and negative charges, the detector acceptance in the simulation is closely matched to the data for both positive and negative charged particles. The resulting acceptance corrections are discussed in more detail in Chapter 4.

3.3.3 Identified Hadron Acceptance

The identified hadron acceptance is illustrated in Figure 3.8 where the transverse momentum is plotted as a function of the particle rapidity (the phase space) within the central arm acceptance subtending the polar angle θ from 70 to 110 degrees for pions, kaons, and protons. The vertical lines are

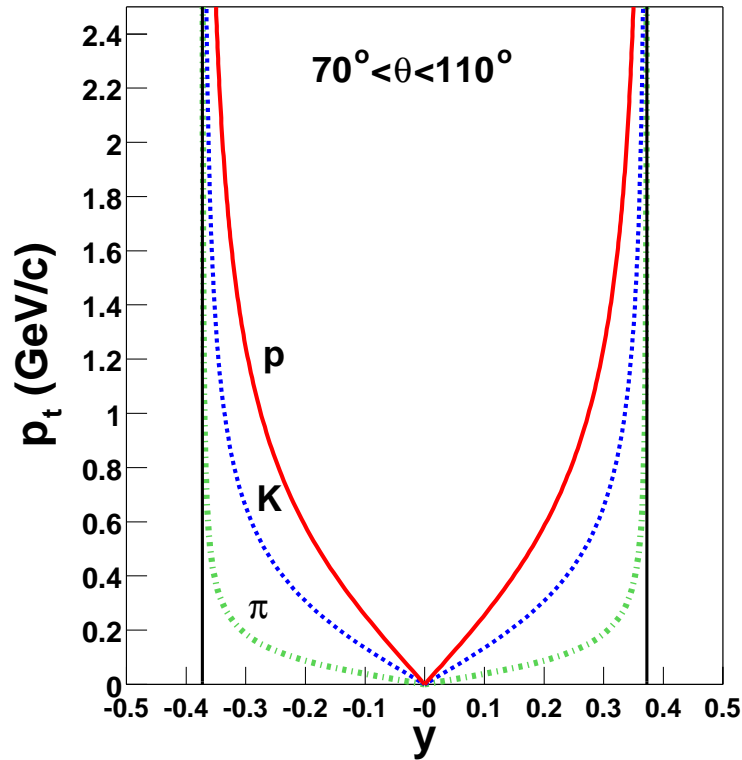


Figure 3.8: The Central arm spectrometer acceptance in rapidity and transverse momentum for protons, kaons, and pions.

the equivalent pseudorapidity edges. For lighter masses, $y \approx \eta$, as is observed for the pions.

3.3.4 Drift Chambers

Most of the field which provides the force necessary to bend the trajectories of charged particles occurs inside the Central Magnet aperture; however, there are residual magnetic field lines within the drift chamber. This residual field causes an additional deflection of $< 1^\circ$ in the xy -plane and negligible deflection in the rz plane (excluding those tracks that have very low momentum or are produced very close to the magnet poles).[49]

The drift chambers³ are the first tracking detectors charged particles en-

³The drift chambers were designed by PNPI in Russia and built by the Relativistic Heavy Ion Group at SUNY Stony Brook.



Figure 3.9: The Au-plated tungsten wires inside one of the drift chambers [27].

counter as they traverse through the central arms. Each subtends 90° in azimuth about the beam axis and measures the track curvature between 2.02 and 2.46 meters radially, from which the momentum is determined. The chambers extend in length to a total of 1.8 meters along the beam axis.

The interior of each DC is composed of 40 planes of wires that are arranged into 160 drift cells (see Figure 3.9 for a picture of the interior of one of the Drift Chambers). A drift cell contains 6 types of wires and subtends $\Delta\phi \approx 1^\circ$ in azimuthal angle and $\Delta r = 6$ mm in radius, where r is the radial coordinate position in the Drift Chamber. The wire configuration in each cell is illustrated in Figure 3.10.

A neighboring drift cell would have its gate and back wires in the opposite configuration as illustrated here. When a charged track passes through a drift cell, it ionizes the gas mixture. The produced electrons are accelerated toward the sense wire and follow the field lines as shown in Figure 3.11. The maximum distance charge can drift toward the sense wire is half the width of a drift cell (a drift cell arclength is $\approx 3.8 - 4.3$ cm from 2.02 – 2.46 m in radius). This is because the back wire in each cell prevents the drift of charge toward the sense wire. This back and gate wire configuration eliminates the left-right ambiguity, and the track charge is localized on either side of the drift cell.

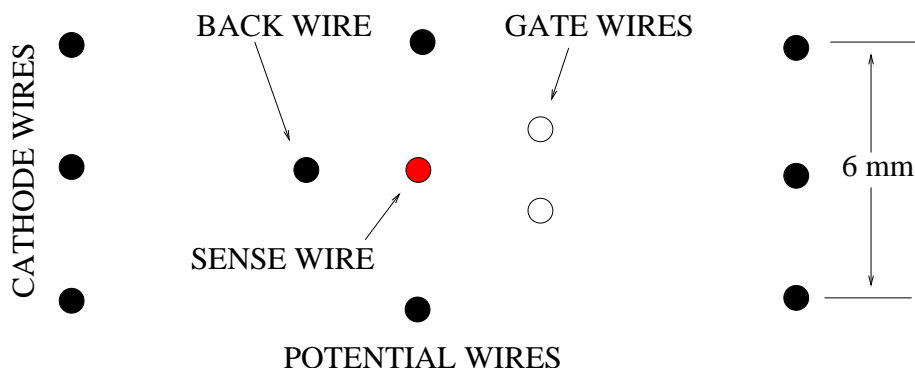


Figure 3.10: The wire configuration in a Drift Cell.

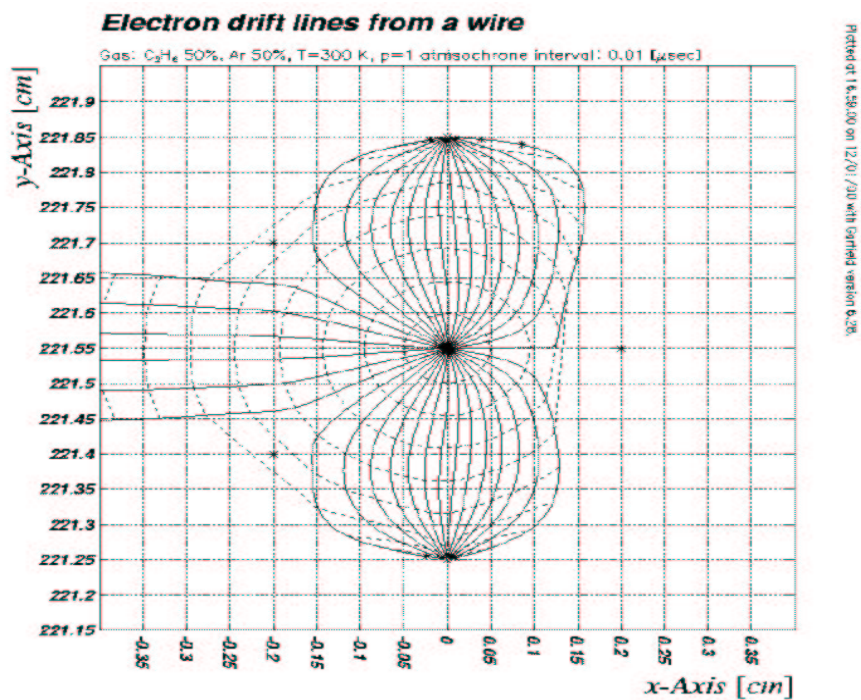


Figure 3.11: The electric field lines that result in a drift cell wire configuration from a GARFIELD simulation [53].

r (m)	Tilt Angle ($^{\circ}$)	Plane	Total	Coord.
2.02	0	X (X1)	12	xy
	5.376	U (U1)	4	z
	-5.5120	V (V1)	4	z
2.20	0	–	0	R
	0	X (X2)	12	xy
	5.90	U (U2)	4	z
2.46	-6.040	V (V2)	4	z

Table 3.1: The wire plane arrangement in each Drift Chamber in increasing radial position r . The radius R is the drift chamber reference radius. The tilt angle is measured with respect to the z -axis.

In Table 3.1, the three different types of wire planes are ordered in increasing radius (first column). The three types of wires are X, U, and V. The X wires provide the track position in the xy -plane transverse to the collision axis in the bend plane z . The UV wires are called stereo wires, and are tilted with respect to the z axis. The UV wires provide z information for the track, while the X wires locate the track’s projection in the xy plane.

The radius R is located in between the two sets of XUV wires and is defined as the reference radius for the track (all angle quantities are determined with respect to this radial position). A straight line is drawn radially from the beam axis to the drift chamber reference radius R of 2.20 m (refer to Table 3.1) and is the trajectory of an infinite momentum particle. The angular deflection of the track from this infinite momentum track is called α . This measured angle α , called the bend angle, is inversely proportional to the particle’s momentum (see Figure 3.12). The bend angle α and the measured track points in the Drift Chamber detector are used in the momentum reconstruction and Drift Chamber Track Model (see Section 3.5).

3.3.5 Track Reconstruction

Track reconstruction within the drift chamber is performed using a combinatorial Hough transform (CHT) technique. In this technique, the drift chamber hits are mapped into a space defined by the azimuthal angle ϕ at the intersection of the track with a reference radius R, and the track’s angular deflection from a straight line, α as schematically shown in Figure 3.12.

In this coordinate space hits from one track have the same values, therefore

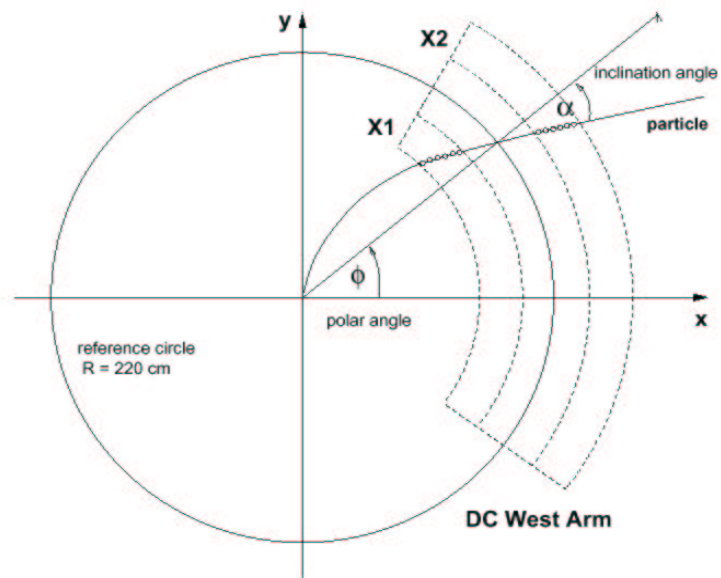


Figure 3.12: The illustration of a charged track entering one of the Drift Chambers and the Hough transform parameters ϕ and α . The drift chamber hits are shown as open circles that fall along the particle's trajectory in the xy plane. The North beam direction is pointing out of the page [42].

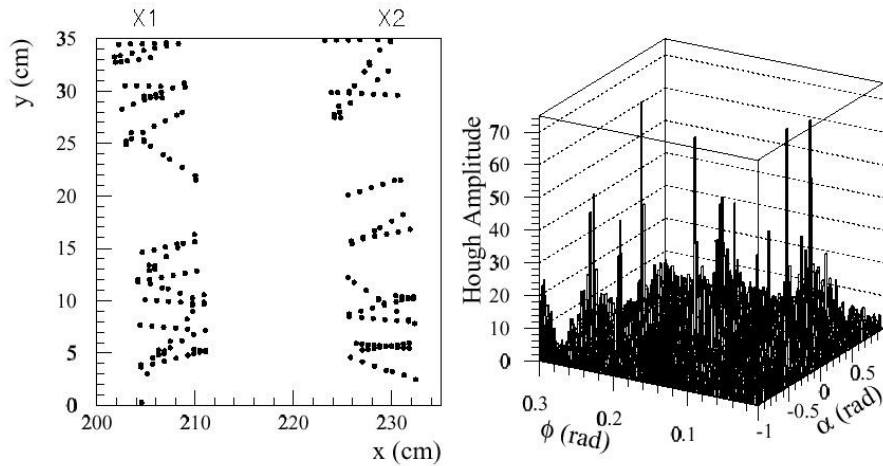


Figure 3.13: The left plot shows the simulated hits from a central Au+Au collision in a small region of the drift chamber in the xy plane. The right plot is the resulting Hough transform feature space for this region. The tracks appear as peaks in this plot [42].

the tracking signal to noise ratio can be greatly enhanced. If a track has n points, then the signal height is $n(n-1)/2$. The granularity in this $\phi\alpha$ space is chosen to be consistent with the inherent resolution of the Drift Chamber. In Figure 3.13, a small region of the drift chamber in y versus x shows the hit pattern that results when particles produced in a central Au+Au collision traverse the volume. The resulting Hough space for this region is displayed on the right. The three dimensional plot shows the Hough amplitude for each ϕ and α pair. The peaks correspond to the tracks.

A track is represented as a local maximum in the Hough space. The position of this maximum in the ϕ - α space is the direction of the track. The measured charge points in the drift chamber are called hits. All the hits that are consistent with the Hough ϕ and α are then grouped together and associated to the track. The track is now two-dimensional. The z information is obtained in two independent ways: the measured charge points in the stereo wires can be used to define the z coordinate of the track, as is illustrated in Figure 3.14. The angle β is the angle of inclination of the track relative to the z axis.

To get the z coordinate of the track, the track reconstruction currently uses information from Pad Chamber reconstructed clusters which contain z

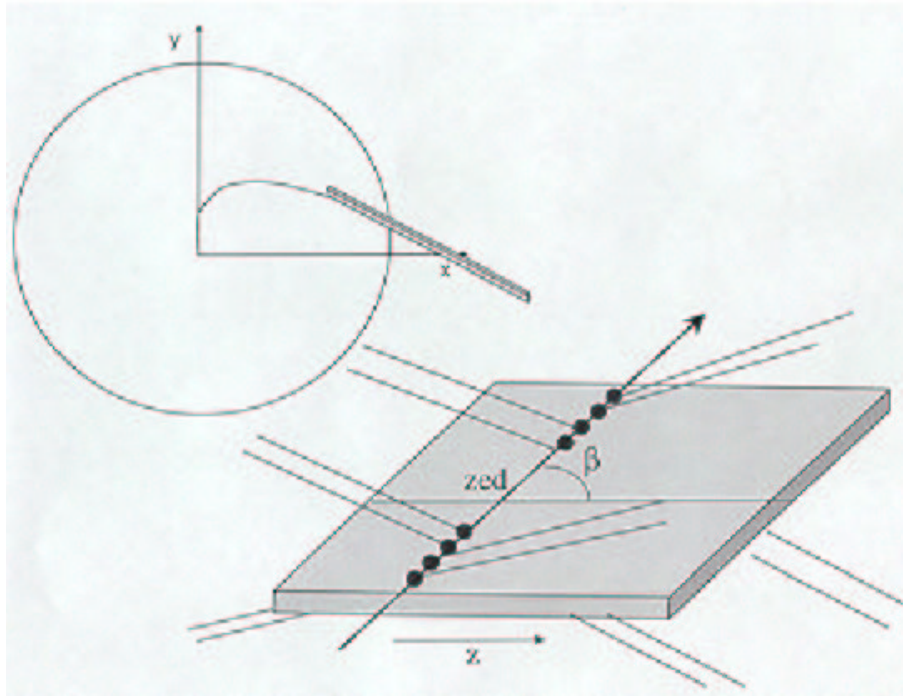


Figure 3.14: The geometrical representation of the UV stereo wires (at $\pm 5^\circ$ with tilt angle and the hits of a track on these wires (bottom) as it enters the drift chamber volume (upper plot). The angle β is the angle of inclination of the track with respect to the z axis.

information with a resolution of 1.89 mm. In Year-2, the stereo (U/V) wires will provide a resolution in the z direction of 2 mm.

With the Year-1 calibration of the hit distributions, the single-wire resolution in the bend plane is 160 microns. The single-wire resolution is 150 microns in r - ϕ if the wires are correctly placed perpendicular to the bend plane. The UV single wire resolution is worse because the wires are nearly parallel to the z axis. The single track wire efficiency is $\approx 99\%$ and the two track separation is less than 1.5 mm. The drift chamber is designed to provide a high resolution transverse momentum measurement of $\sigma_p/p = 0.5\%$ at 0.5 GeV/c. With the current calibration, wire alignment, and active fiducial volume, the Year-1 drift chamber resolution is $\sigma_p/p = 1\% \oplus 3.5\%p$. For more details on why this measurement is larger than the design value, please refer to Chapter 4 where the momentum resolution is measured from the data. For more detail on the drift chambers, please refer to References [41, 33].

3.3.6 Pad Chamber Detectors

Each pad chamber in PHENIX measures a three-dimensional space point of a charged track to within a few millimeters. The pad chamber detectors are used in the global track reconstruction to determine the polar angle of the track and to minimize the background contribution of albedo and non-vertex decay particles (see Appendix C. The Pad Chambers are also used in the no-field runs to determine the total charged particle multiplicity distribution. A charged track entering the Pad Chamber deposits charge on small, rectangular-shaped pixels made of silicon board and etched copper. Anode and field wires are positioned on the top and bottom of each pad. A pixel is a square-shaped copper electrode. Nine pixels are connected together electronically to form a pad, the basic element of the detector. The field wires generate an electric field across the pad, and all the charge deposited in the pad are readout by a single preamplifier and discriminator. The pads are positioned in an interleaved pattern to complete the Pad Chamber volume. In Year-1, three Pad Chambers were positioned in PHENIX. Two were located in the East Arm: PC1 is mounted to Drift Chamber and PC3 was positioned directly behind the Time Expansion Chamber and in front of the Time-of-Flight Hodoscope. For more detail on the pad chambers, please refer to Reference [43].

3.3.7 Time Expansion Chamber

The Time Expansion Chamber (TEC) is located in the East arm. It is designed primarily for e/π separation and tracking in front of the EM Calorime-

ter. The TEC also has particle identification capabilities using energy loss (dE/dx) and momentum reconstruction for high transverse momentum particles. The TEC is composed of 4 sectors, with 6 X-type wire planes per sector. It is also possible to determine whether the track enters the North or South side of the chamber. The TEC tracks all charged particles that travel in between the RICH and the EMCal. For more detail on the TEC, please refer to Reference [44].

3.3.8 Time-of-Flight Hodoscope

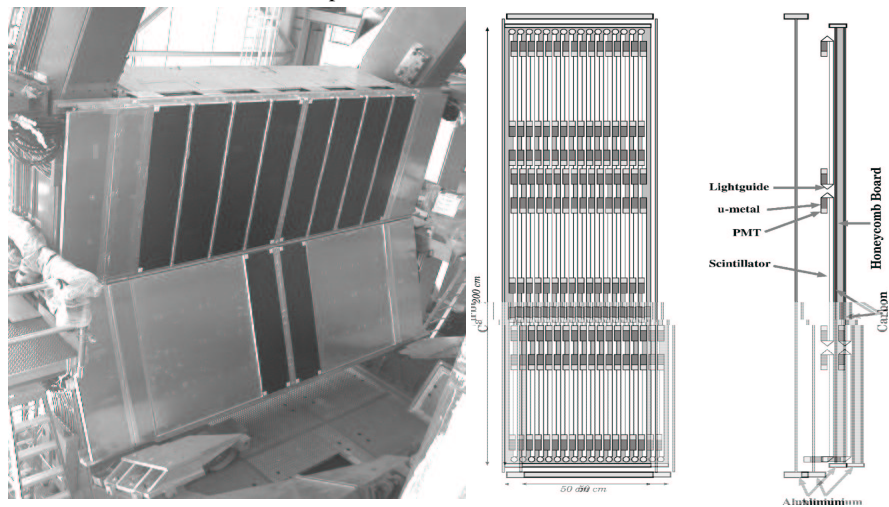
The Time-of-Flight (TOF) hodoscope subtends 45° in azimuth in the East arm (see the left picture in Figure 3.15). There are two sectors in the TOF detector. Each sector is finely segmented due to the high detector occupancy that results after each Au+Au collision. The TOF sectors are comprised of 10 panels. The top sector has 8 panels and the bottom sector has 2 panels. The panels have a total of 960 plastic scintillation counters and 1920 channels of Photomultiplier tubes (PMTs), collectively called slats. Each slat has PMTs at either end, a light guide, and support. A single TOF panel and the slats are illustrated in Figure 3.15. The time, PMT gain, and geometrical position of each slat is calibrated. The total time offset is calibrated slat-by-slat. A particle hit in the scintillator is defined by a measured pulse height. The pulse height is also used to correct the time recorded at each end of the slat (called a slewing correction).

After calibration, the average of the times at either end of the slat is the measured time for a particle. The azimuthal position is proportional to the time difference measured across the slat and the known velocity of light propagation in the scintillator (for Bicorn BC404 this is 14 cm/ns). The reconstruction algorithms determine the time, energy loss in the scintillator, and geometrical position of each particle. The total time of flight is measured relative to the beam-beam counter initial time, the measured time in the Time-of-Flight detector (TOF), and a global time offset from the RHIC clock.

The TOF has a design resolution of 85 ps. In Year-1, the measured TOF resolution was between 110 and 120 ps. The TOF resolution can be measured from the width of the measured time and the expected time for high momentum pions, typically greater than 1 GeV/c in momentum. The expected time is determined from the path length as calculated in the track model (see Section 3.5), and the known mass of pions. For more detail on the measured resolution, please refer to Chapter 4.

The information here is summarized from Reference [47]. More information on particle identification by time of flight techniques can be obtained in

The two TOF sectors with its 10 panels



A PANEL in the TOF

Figure 3.15: The TOF detector and its 10 panels (left) as it sits at the bottom of the East spectrometer arm of PHENIX. On the right, an illustration of a panel and its slat components is shown. [55]

Reference [48].

3.3.9 Ring Imaging Cherenkov Hodoscopes

The RICH detectors measure the Cherenkov radiation emitted by charged particles as they traverse the gas with velocities greater than c/n , where n is the index of refraction of the gas and $1/n$ is the threshold velocity for a particular particle species (either electrons or pions). The radiation is emitted along a cone, where the opening angle of the cone with respect to the apex is $\theta_c = \cos^{-1}(1/n\beta)$. The spherical mirrors are aligned with respect to the collision axis and reflect the photons onto arrays of Photomultiplier Tubes (PMT). At least three PMTs in the RICH, an energy shower in the Electromagnetic calorimeter, and a measured momentum in the Drift Chamber is necessary for the particle to be identified as an electron where $E/p \approx 1$.

The alignment of the spherical mirrors was done using a MANCAT system of three theodolite survey instruments that were used to align the dipole magnets in the RHIC collider [45]. Alignment targets attached to vinyl backings were positioned onto a soft Aluminum plated mirror segment in five positions with four targets in each corner and one in the center⁴. Using a manlift, a person sits behind the mirror once it is positioned in the RICH detector while the MANCAT system of theodolites measures the radial position of the mirror in spherical coordinates. Using adjustment knobs, the person tilts each mirror accordingly until the radial position of each target is within a few μm of the optimum radial position for the spherical array. This procedure was repeated for all 80 mirrors in both the RICHs. For detail on the RICH electronics, please refer to Reference [46].

3.3.10 Electromagnetic Calorimeters.

The purpose of the Electromagnetic Calorimeters in PHENIX is to measure photons and dileptons. There are a total of 8 sectors (4 in each arm). There are two types of Electromagnetic Calorimeters in PHENIX: lead scintillator (6 sectors of PbSc) and lead glass (2 sectors of PbGl)⁵. The calorimeters are positioned in the outer layers of PHENIX ≈ 5 meters radially from the collision axis. The timing resolution of the PbSc results in the identification

⁴The author developed the mirror alignment MANCAT solution with T.K. Hemmick and the RICH group during the Summer of 1998.

⁵The PbGl detector was used in the WA98 experiment at the CERN SPS

Det.	Year-1 Reso.	$\Delta\phi$ (rad)	η
ZDC	$\sigma_E/E < 20\%$ at $E_n = 100\text{GeV}$	10.0cm square	$ \eta < 6$
BBC	$\sigma_z = 1.5\text{cm}$, $\sigma_t = 70\text{ps}$	2π	$3.0 < \eta < 3.9$
MVD	—	2π	$ \eta < 0.43$
DC	$160\mu\text{m}$	$\pi/2$	$ \eta < 0.35$
PC I	$\sigma_y = 1.62\text{mm}$ $\sigma_z = 2.3\text{mm}$	$\pi/2$	$ \eta < 0.35$
PC II	—	$\pi/2$	$ \eta < 0.35$
PC III	$\sigma_y = 3.2\text{mm}$ $\sigma_z = 4.8\text{mm}$	$\pi/2$	$ \eta < 0.35$
TEC	$380\mu\text{m}$	$\pi/2$	$ \eta < 0.35$
TOF	115 ps	$\pi/4$	$ \eta < 0.35$
RICH	—	$\pi/2$	$ \eta < 0.35$
PbGl	$\sigma_E/\sqrt{E}(\%) = 5.8\%/\sqrt{E(\text{GeV})} \oplus 1.0$ $\sigma_t(\text{ps}) = 70/\sqrt{E(\text{GeV})} \oplus 70$	$\pi/4$	$ \eta < 0.38$
PbSc	$8\%/\sqrt{E(\text{GeV})} \oplus 1.9\%$ $\sigma_t(\text{ps}) = 143/\sqrt{E(\text{GeV})} \oplus 75$	$\pi/4$	$ \eta < 0.38$
μ Spect	—	—	$1.1 < \eta < 2.4$

Table 3.2: Resolution and positions in r , ϕ , and η of PHENIX subsystems. Detectors not used in Year 1 have a line.

of pions and kaons out to 1.4 GeV/c in transverse momentum. Recent results of π^0 spectra measured in the PbSc detector are in Reference [81].

3.4 Detector Alignment

The no-field runs and a linear track projection are used to align the detectors⁶. All of the detectors are aligned with respect to the drift chambers. The drift chambers are aligned with respect to the event vertex. The projections and the measured points use the same geometry, so any observed offset is due to misalignment of the coordinate frame that we used in the track reconstruction. The observables used to align the drift chamber to the vertex are in the plane α versus ϕ . In this plane, because the tracks are straight the measured α distribution from the Hough Transform should be centered about zero. The drift chamber geometry is adjusted until this distribution across ϕ is

⁶Julia Velkovska of SUNY Stony Brook aligned the PHENIX subsystems in the offline software.

centered accordingly. Once this is done, each drift chamber track is projected to the outer detectors and the global tracking searches in a road both in ϕ and z for the corresponding measured points. The mean of the residuals are centered to within 1 cm in each coordinate in x , y , and z .

3.5 Momentum Reconstruction and the Track Model

Due to the complicated, non-uniform shape of the focusing magnetic field along the flight path of charged particles traversing the PHENIX central arm spectrometers, an analytic solution for the momentum of the particles cannot be determined. Therefore, other approaches such as look-up tables, must be used. For Run 2000, a four-dimensional field-integral grid was constructed for momentum reconstruction using the drift chamber. The same grid was used to define the track trajectories within the entire radial extent of the central arms. The variables in the field-integral grid are the z coordinate of the event vertex; the polar angle θ_0 , of the particle at the vertex; the total momentum of the particle, p ; and the radius, r , at which the field-integral $f(p, r, \theta_0, z)$ is calculated. The field-integral grid is generated by explicitly swimming particles through the measured magnetic field map and numerically integrating to obtain $f(p, r, \theta_0, z)$ for each grid point.

An iterative procedure is used to reconstruct the momentum of a reconstructed track, utilizing the fact that $f(p, r, \theta_0, z)$ varies linearly with the ϕ angle of the track at a given radius. This can be expressed as

$$\phi = \phi_0 + q \cdot f(p, r, \theta_0, z) / p. \quad (3.1)$$

Each track is assumed to be a primary track originating from the event vertex as determined by the BBC. An initial estimate of the track momentum and charge is made from the reconstructed bend angle α , of the track in the drift chamber. The measured polar angle θ , of the track in the rz plane at the drift chamber reference radius R is used as an initial estimate of θ_0 . Then, using the radial position of each reconstructed hit associated to the track, a four-dimensional polynomial interpolation of the field-integral grid is performed to extract a value of $f(p, r, \theta_0, z)$ for the drift chamber hit. Once this is done for all hits, a robust⁷ fit in ϕ and $f(p, r, \theta_0, z)$ is performed to extract the

⁷A hit that is positioned further away in ϕ relative to the other hits is given a smaller weight in the least-squares linear fit. This is for the case when a hit does not belong to a track. The algorithm used is based on Reference [50].

quantities ϕ_0 and q/p for the track. The extracted values are then fed back into the above equation. The initial polar angle, θ_0 , is also determined using an iterative procedure using the equation

$$\theta = \theta_0 + \delta(p, r = R, \theta_0, z) - g(p, r = R, \theta_0, z)/p, \quad (3.2)$$

where δ is the bend angle of the particle trajectory relative to the straight-line trajectory of an infinite-momentum particle in the rz plane. Typically, less than four iterations are necessary for convergence on these quantities.

This procedure has an additional advantage in that it can be used to define the shape of the track within the central arm magnetic field, which can then be used to determine the track intersections with each detector in order to facilitate inter-detector hit association. After determining the total momentum and the original azimuthal and polar angles, ϕ_0 and θ_0 respectively, this track model⁸ determines the position of the particle at any point in the PHENIX Central Arms (called projection points).

This is done by storing the coordinates of the particle in radial steps as additional entries in the field-integral grid. Line segments connecting the interpolated grid coordinates for a track are intersected with the geometry objects describing the position of each detector in order to estimate the projection of the track on each detector. These projection points are then matched to measured points in the Central Arm detectors. Finally, the length of the interpolated line segments from the event vertex to a given detector can be summed in order to provide an estimate of the flight distance of the particle to that detector. This quantity is used to facilitate particle identification using the TOF. Residual calculations both in ϕ and z between the measured and projected points at each momentum are used to reject background in the data reduction (see Appendix C). [49]

3.6 Subsystems Used For This Analysis

The PHENIX subsystems used for the identification of charged hadrons are schematically shown in Figure 3.16. The subsystems include: TOF, PC1, DC East, BBC and ZDC detectors. The TOF subsystem allows one to measure the light hadrons in a small acceptance corresponding to 0.7 units in pseudo-rapidity and 45° in azimuth (see Table 3.2). The ZDC and BBC detectors are used together to determine the event centrality. The trigger efficiency of the

⁸The drift-chamber based track model used in the Year-1 analysis was written by the author and S.C. Johnson.

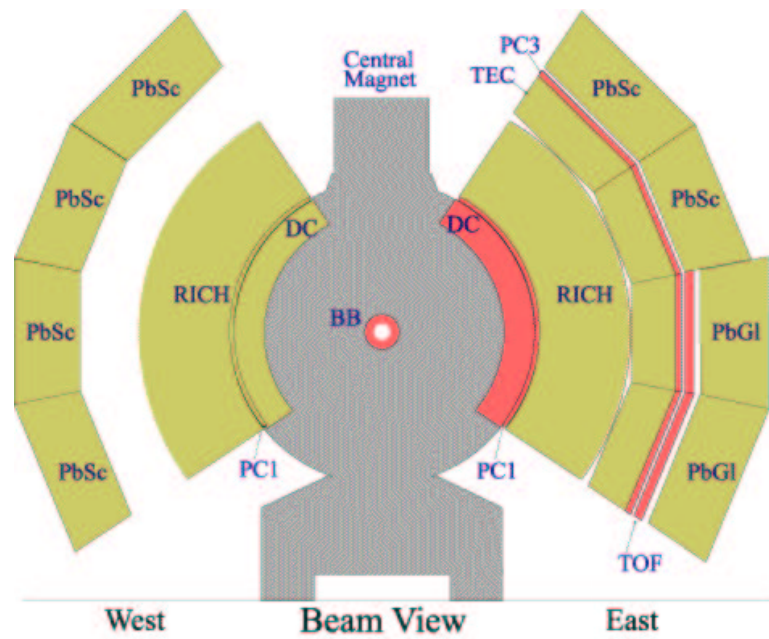


Figure 3.16: The PHENIX particle identification setup in Run 2000. The beams are perpendicular to the page. See description in the text.

ZDC limits the measurement of the most peripheral collisions due to mutual Coulomb dissociation (get reference), as the fraction of the total geometrical cross section is measured. The data reduction and centrality selection technique are described in more detail in Chapter 4.

Chapter 4

Data Reduction

In this Chapter, the steps involved in reducing the data to raw, uncorrected spectra for pions, kaons, protons, and antiprotons is described in detail. All of the events are recorded on tape during the data acquisition stage of the experiment; the detector responses are stored in PHENIX raw data format (prdf) files for each run. The PHENIX software reconstruction first determines the alignment and calibration for each detector subsystem, using a subset of the data. Then, the momentum reconstruction, track projection, and track-hit association algorithms are completed. Finally, all the reconstructed tracks and their detector-associated quantities are written to files called Data Summary Tapes (DSTs). For most analyses, only a subset of the detectors and DST information are needed. Therefore, smaller DSTs, called micro-DSTs (μ DSTs) are produced and tailored for each study. It is within these μ DSTs that the event and track selection is done. For the identified transverse momentum spectra, the following selection criteria are applied and discussed in this chapter:

- The event selection section discusses how we use BBC and ZDC correlation and a Glauber model calculation to measure event centrality and the number of participants, respectively.
- The section on global track selection discusses how drift chamber tracks are matched to the TOF detector. Global tracks based on the tracks reconstructed in the drift chamber are projected to the TOF detector. The projected points are matched with measured space points as measured in the TOF reconstruction. A 2σ momentum-dependent matching cut to the TOF detector is then applied to select tracks.
- The particle identification section describes how pions, kaons, and protons are separated as a function of momentum. The technique uses the

mass-squared width based on measured detector resolutions. Both the time and momentum measurements are described. The time measurement includes time offset calibration, time scale, and time resolution. The momentum measurement includes the momentum resolution and momentum scale. The measured mass-squared distribution is then studied. First, the centroids are determined and the n-sigma particle identification distributions are produced. An energy-loss cut made in the TOF detector reduces the background contamination in the kaons and protons.

- In the systematic uncertainties section, the random background contribution is treated as a systematic uncertainty in the data reduction. The size of the uncertainty is determined for each particle species.
- The raw transverse momentum (p_t) distributions are produced.

The raw distributions are already corrected for centrality-dependent inefficiencies that arise in high-multiplicity events during the track reconstruction. This correction and additional cuts to match simulation and data necessary to fully correct the raw spectra are described in detail in the next chapter.

4.1 Event Selection

Events are selected in PHENIX during Year-1 using the Beam-beam counter detector. The Drift Chamber is calibrated with respect to the BBC measured time of the event collision and the Drift Chamber momentum is determined with respect to the BBC measured event vertex position along the beam axis. Using the BBC value for the event vertex position along z , events with $|z| < 30$ cm along the collision axis are triggered and selected. In this section, the fraction of the measured cross section, called event centrality, is discussed in Section 4.1.1. Because PHENIX does not measure the total geometrical cross section, a model dependent calculation is used to determine the number of nucleons participating in the collisions. A Glauber model calculation is used to determine the number of participants. The resulting number of participants in each event centrality selection is discussed in Section 4.1.2.

4.1.1 Event Centrality

The events are grouped according to the measured fraction of the total geometrical cross-section of the collision between two nuclei, this is related to

the impact parameter, or centrality, of the collision. The centrality is determined by the measured correlation between the fractional charge deposited in the Beam-beam Counters (BBC) and the fractional energy deposited in the Zero-Degree Calorimeters (ZDC). The entire measured distribution of all collisions is called minimum bias.

The total geometrical cross section is the circular area of overlap between the two colliding nuclei and is transverse to the collision axis. With a nuclear radius of 6.65 fm (see the next section), the total geometrical cross section is $\sigma_{tot} = \pi R^2 = 139 fm^2$. The most central events measured have a larger overlap area and the more peripheral have a smaller overlap area. The centrality is defined as the fractional difference between the collision cross section and the total geometrical cross-section measured in PHENIX $\frac{\sigma_{tot}-\sigma}{\sigma_{tot}}$.

The more peripheral the event, the fewer the number of particles recorded in the BBCs and the more energy recorded in the ZDCs (deposited by the spectator nucleons). For the more central events it is the opposite. More particles are recorded in the beam-beam counters and the less energy that is deposited in the zero-degree calorimeters. Spectator neutrons continue in the beam direction as they are not bent by the magnet into the ZDC, while the participant nuclei produce new particles that are measured in the BBC. The more central, the fewer spectators and the more participants. The left plot in Figure 4.1.1 shows the measured correlation between the ZDC fractional energy and BBC fractional charge during Year-1. The corresponding charged track density for each type of event is shown in the plot on the right. The more central events have a larger number of tracks per event than for the more peripheral events.

In the left panel of Figure 4.1.1, the centrality angle ϕ_{cent} is determined in the charge-energy space. The angle ϕ_{cent} is the angular position of the event in the space BBC charge versus ZDC energy. Q_{max} is the maximum charge in both the BBCs and is equal to 400. E_{max} is the maximum energy deposited in both the ZDCs and is 4500 GeV. If E is the energy recorded in the event in both the ZDCs and Q is the total charge recorded in both the BBCs, then ϕ_{cent} is

$$\phi_{cent} = \tan^{-1} \left(\frac{(Q - Q_0)/Q_{max}}{E/E_{max}} \right) \quad (4.1)$$

where $Q_0 = 0.2 \cdot Q_{max}$ is the position along the BBC axis from which the angle ϕ_{cent} is determined¹. This event with ϕ_{cent} is grouped into the centrality class defined by upper and lower bounds ϕ_{min} and ϕ_{max} if $\phi_{min} < \phi_{cent} < \phi_{max}$. The resulting number of events in each ϕ bin is tabulated in Tables 4.1- 4.2.

¹J. Velkovska calculated these values.

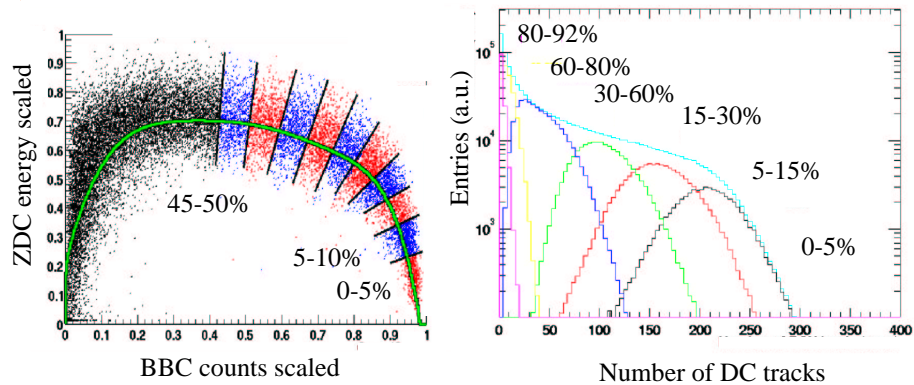


Figure 4.1: Event centrality selections using the ZDC energy fraction and BBC fraction counts (left). The charged multiplicity distributions for each centrality selection (right).

Cross Section (%)	N_{evt}	ϕ_{min} (rad)	ϕ_{max} (rad)
min. bias	139,270	-1.57	1.57
0-5	7,895	1.208	1.57
5-10	7,601	1.048	1.208
10-15	7,587	0.92	1.048
15-20	7,580	0.8112	0.92
20-25	7,689	0.712	0.8112
25-30	7,415	0.616	0.712
30-35	7,893	0.5136	0.616
35-40	7,836	0.4112	0.5136
40-45	7,395	0.312	0.4112
45-50	7,607	0.2096	0.312

Table 4.1: The number of events in each centrality class between 0 and 50% of the total measured cross section.

Cross Section (%)	N_{evt}	ϕ_{min} (rad)	ϕ_{max} (rad)
50-55	7,436	0.1136	0.2096
55-60	7,476	0.0272	0.1136
60-65	7,634	-0.0528	0.0272
65-70	7,700	-0.1264	0.0528
70-75	7,635	-0.1968	-0.1264
75-80	8,004	-0.2736	-0.1968
80-85	8,797	-0.408	-0.2736
85-92	8,090	-1.57	-0.408

Table 4.2: The number of events in each centrality class between 50 and 92% of the total measured cross section.

Cross Section (%)	Number of Events
0-5	7,895
5-15	15,188
15-30	22,684
30-60	45,643
60-92	47,860
minimum bias	139,270

Table 4.3: The centrality selections and the corresponding number of events as used in this analysis.

The centrality selections used in this analysis and the corresponding number of events are tabulated in Table 4.3. Roughly 6% of all the minimum bias events fall in the 0-5% centrality, while 34% of the events fall in the more peripheral centrality selection of 60-92%. As is evident in Figure 4.1.1, PHENIX does not measure the total geometrical cross section. In the more peripheral events, where the BBC counts tend to zero, the ZDC efficiency in measuring the energy falls to zero. Therefore, a model dependent calculation must be used in order to determine the total number of nucleons participating in the collisions as discussed in the next section.

4.1.2 Number of Participants

What is presented here is a summary of how PHENIX maps centrality to the number of participants and collisions in Reference [51]. These results are calculated by Klaus Reygers and the systematic uncertainties have improved since Reference [80]. A recent discussion of this model-dependent calculation at RHIC is in Reference [31] by D. Kharzeev.

In order to determine the number of nucleons participating in each event (and the number of collisions), a model dependent calculation is currently employed by PHENIX as only the fraction of the total cross section is measured in both the ZDC and BBC detectors. A Glauber model calculation is used with a Woods-Saxon density profile distribution for the nucleus and a value for the nucleon-nucleon inelastic cross section.[30]

The model calculates the thickness of nuclear matter that is in the direct path of each oncoming nucleon and uses the inelastic nucleon-nucleon cross section σ_{nn}^{inel} to determine whether or not a nucleon-nucleon collision occurs. What the model assumes is the following:

1. The nucleons travel in straight line paths parallel to the velocity of its respective nucleus.
2. An inelastic collision occurs if the relative distance between two nucleons is less than $\sqrt{\sigma_{nn}^{inel}/\pi}$.
3. By using the simulated detector response for both the ZDC and BBC, fluctuations are introduced.

The parameters used in a Woods-Saxon Nuclear Density distribution for each nucleus $A = 197$, and radius R are as follows:

$$\rho(r) = \frac{\rho_0}{1 + e^{\frac{r-R}{d}}}, \quad (4.2)$$

$$R = 1.19A^{1/3} - 1.61A^{-1/3} = 6.65\text{fm} \quad (4.3)$$

with $d = 0.54\text{fm}$, and $\sigma_{nn}^{inel} = 40\text{mb}$. The respective number of participants is summed accordingly².

With these parameters, the number of participants for each event centrality is tabulated in Table 4.4 and are published in Reference [80]. The uncertainties have decreased in [52] since the published results in [80].

The centrality selections correspond to the selections used in this analysis. The tracks from the minimum bias events and for the different centralities are

²The number of collisions is also determined and can be found in Reference [80].

Cross Section	Participants
0 – 5%	346.7 ± 10
5 – 15%	270.75 ± 9
15 – 30%	178.33 ± 7
30 – 60%	76 ± 7
60 – 92%	14 ± 3.5

Table 4.4: The number of participants for the centrality selections used in the analysis [80, 51, 52].

selected accordingly. Then, the one-to-one mapping between the fraction of cross section measured and the number of participants as determined by the Glauber calculation is used. In Section 4.2, the global track selection is described in more detail.

4.2 Global Track Selection

Only those tracks that are fully reconstructed in all three coordinates (three-dimensional) are selected. This is determined by selecting those tracks with Track Quality Bit > 20 . These candidate tracks are then matched within 2σ to the measured times of flights in the Time-of-Flight detector.

4.2.1 Track Reconstruction and Quality in the Drift Chambers

The track reconstruction software in the drift chambers associates hits in either X1 or X2, or both where possible, to each track. This yields the x and y position of the track in PHENIX global coordinates at the drift chamber reference radius. The algorithm³ first

- collects all the possible charged space points in ϕ in the PC1 detector for each track,
- projects the BBC vertex and the PC1 points into the xy-plane.

³The track reconstruction algorithm used in Year-1 was developed by Dr. Axel Drees of SUNY Stony Brook. Dr. Stephen Johnson, while at SUNY Stony Brook, wrote most of the pattern recognition software for the drift chambers.

X1 2^0	X2 2^1	Pc1 2^2	UV 2^3	Vertex 2^4	Quality
1	0	0	0	0	1
0	1	0	0	0	2
1	1	0	0	0	3
1	0	1	0	1	21
0	1	1	0	1	22
1	1	1	0	1	23
1	0	1	1	1	29
0	1	1	1	1	30
1	1	1	1	1	31

Table 4.5: Quality bit definitions

- fits a straight line to the drift chamber points in X1 and X2, the BBC projected vertex point, and the PC1 closest point.
- determines the PC1 point that is closest to the track.
- fits a straight line to the drift chamber points in X1 and X2, the BBC projected vertex point, and the PC1 closest point, and then
- intersects this line with a cylinder positioned at the drift chamber reference radius.

In high multiplicity events, where there is ambiguity in choosing the closest PC1 point (multiple hits available), the algorithm uses the UV points in the drift chamber (if the track has them). As a result, there are a variety of possible tracks after the track reconstruction algorithm. Therefore, each reconstructed track has assigned to it a quality bit which indicates whether or not the track has all three dimensions in coordinate space. The quality bit is set accordingly in Table 4.5.

In Figure 4.2, three groupings are observed. Each group represents a different track quality class. In the group with quality values between 0 and 3, the track is located in the xy plane only. In the second group with values between 21 and 23, the track has all three coordinates. Both the closest PC1 point and the BBC projected vertex are used to determine the beam axis position at the drift chamber reference radius. Finally, in the last group with quality values between 29 and 31, there are multiple PC1 points to choose from for these tracks. As a result, the UV information for each track is used

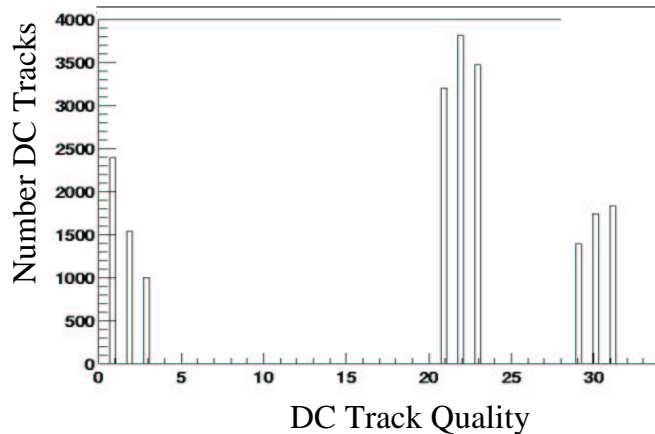


Figure 4.2: Quality variable for tracks reconstructed in run 9666, sequence 0. Three groupings are possible. See text for bit definitions.

to determine the closest PC1 point. The PC1 point and the BBC vertex are then projected into the xy-plane accordingly. The second and third groups do include z information, so full three dimensional vectors are reconstructed for these tracks. The track reconstruction default is to use the vertex and PC1 to provide z and pointing for the track; UV wire information is added where available.

4.2.2 Matching Global Tracks to the Time-of-Flight

The hit association is done using the following procedure for each arm in PHENIX:

1. Create a list of the measured hits for each detector in both ϕ_{hit} and z_{hit} .
2. Sort each list in increasing azimuthal angle ϕ_{hit} .
3. Define upper and lower bounds in both ϕ and z using the width $\Delta\phi = 0.07$ rad in azimuth and $\Delta z = 50.0$ cm.

$$\phi_{upper} = \phi_{hit} + \Delta\phi \text{ and } \phi_{lower} = \phi_{hit} - \Delta\phi.$$

$$z_{upper} = z_{hit} + \Delta z \text{ and } z_{lower} = z_{hit} - \Delta z.$$

4. Project the Drift Chamber tracks to each detector and determine ϕ_{proj} and z_{proj} , the projected position in each detector in azimuthal angle ϕ and z .
5. The detector hit is associated to the track if the projected point falls within the upper and lower bounds of the measured detector point in both ϕ and z accordingly: $\phi_{lower} < \phi_{proj} < \phi_{upper}$ and $z_{lower} < z_{proj} < z_{upper}$.

The residuals in between track projections and hits in the TOF in both ϕ and z are determined as a function of momentum. Agreement within 2σ , with σ taken from the residual distribution, is required in both ϕ and z for each track and time-of-flight pair. This is necessary in order to exclude the background contribution to the charged particle spectrum from albedo (shower particles from the central magnet) and decays (see Appendix C). A parameterization is fit to these momentum-dependent residuals and is used to determine the sigma in ϕ and z .

$$\sigma_{\phi} = Ae^{-Bp} + C, \quad (4.4)$$

where $A = 0.024568$ rad, $B = 5.6122$ rad \cdot c/GeV, $C = 0.005$ rad and

$$\sigma_z = De^{-Ep} + F, \quad (4.5)$$

where $D = 12.621$ cm, $E = 4.5384$ cm \cdot c/GeV, $F = 1.19$ cm.

The difference in z of the time-of-flight hit and the projected track, Δz is determined. The z offset in the residual distribution is $Z_0 = 0.9502$ cm and this must be taken into account in order to avoid cutting into the distribution.

$$n_Z = (\Delta Z - Z_0)/\sigma_z \quad (4.6)$$

The difference in ϕ of the time-of-flight hit and the projected track, $\Delta\phi$ is determined. The ϕ offset in the residual distribution is $\phi_0 = -1.092$ mrad and this must be taken into account in order to avoid cutting into the distribution.

$$n_{\phi} = (\Delta\phi - \phi_0)/\sigma_{\phi}; \quad (4.7)$$

The n-sigma radius is then calculated and is equal to $\sqrt{n_{\phi}^2 + n_z^2}$. The n-sigma distribution is a gaussian distribution centered at 0 with a $1\text{-}\sigma$ width equal to 1. If the n-sigma radius is greater than 2 for a given track, the track is rejected.

4.3 Particle Identification

The particle identification is determined by correlating the time-of-flight and momentum measurements. The time-of-flight measurement is discussed in Section 4.3.1, where initial time calibration, the measured time scale and resolution are described. The measured momentum scale and resolution are discussed in detail in Section 4.3.2. The particle identification technique using the calculated mass-squared width based on the time-of-flight and momentum resolution measurements is discussed in Section 4.3.3. The resulting transverse momentum distributions after the particle identification using the TOF and DC detectors is presented and discussed in Section 4.5.

4.3.1 Time-of-Flight Measurement

The total flight time for particles crossing the TOF detector is the difference between the final time as measured by the TOF detector and the initial time for the event as measured by the BBC detectors. Residual offsets and scale factors in either measurement introduce systematic shifts in the measured particle mass. Therefore, both measurements must be studied carefully and any offsets and scale factors must be calibrated before the mass is calculated. In Section 4.3.1, the residual calibrations in the initial time measured by the BBC detectors is applied and discussed. The measured time scale and resolution is described in Section 4.3.1.

Calibrating the Initial Time Measurement

The initial time is measured by the BBC detectors. The difference between this measured initial time and the time in the RHIC clock is called the global time offset. The measured global time offset is 0.6309873 ns. However, even after this global offset is taken into account, there are still two types of variation that result in time offsets. One source is the run-to-run variation of $\approx \pm 100$ ps in the time offset. This offset is determined for each run separately and then applied to all the events in each run sample (see Figure 4.3). The effect of the run offset calibration is to narrow the time resolution width by 14%. The second variation is due to the saturation of the ADC (Analog to Digital Converters) pulse-heights in the BBC detectors, which occurs in high track density events. For saturated ADC pulse-heights, the BBC slewing correction becomes inaccurate and results in a multiplicity-dependent time measurement. The measured initial time in the BBC detectors is plotted as a function of the hit density as measured in the Pad Chamber 1 for all runs in Figure 4.4. The

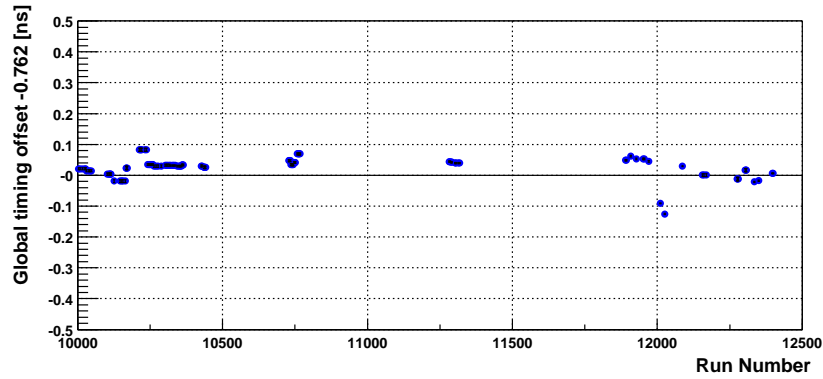


Figure 4.3: The offset in the measured initial time in the BBC detectors as a function of run number [53].

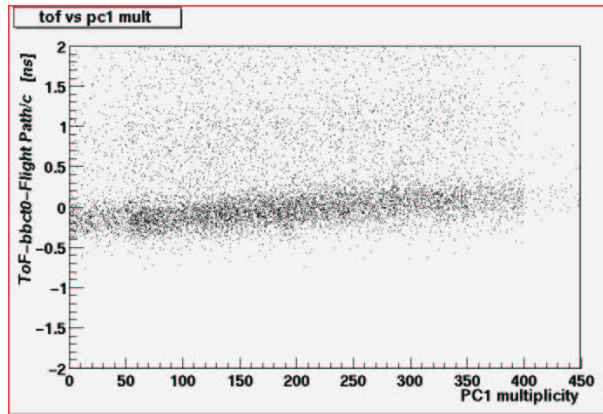


Figure 4.4: Measured initial time in the BBC detectors as a function of hit density in the Pad Chamber 1 [53].

distribution shows a linear dependence. A line is fit to this dependence and results in a slope of $m = -8.14921 \cdot 10^{-4}$ ns/count. The corrected time is then $t_{bbc} - mN$, where N is the density of Pad Chamber 1 hits and t_{bbc} is the BBC time as measured.

Time Scale and Resolution

The global time scale between the RHIC clock of 9.43 MHz and the TOF clock based on 10 MHz is determined by plotting the expected times for high-momentum pions against the measured times for these particles in the TOF detector. The expected time is the time it takes for a high-momentum pion (with $\beta \approx 1$) to travel from the event vertex at time t_{bbc} (as measured by the BBC) to the TOF detector along the trajectory with a pathlength L . Instead of applying the factor 1.06 from the clock frequency ratios, a straight line (Equation 4.8) is fit to the data to extract the scale (the slope of the line),

$$\Delta t_{exp} = At \tag{4.8}$$

, where $\Delta t_{exp} = t_{bbc} + t(L)$, and $t(L) = L/c\beta \approx L/c$ for high-momentum pions ($p_t > 1.5$ GeV/c). The measured time is plotted versus the expected time as shown in Figure 4.5 for high-momentum pions. After fitting Equation 4.8 to the points in Figure 4.5, the measured time scale is 1.046 ± 0.001 . This factor is applied to the time measurement for each particle.

The TOF resolution is determined by measuring the width of the difference between the measured time of flight and the expected time of flight for high momentum pions, typically greater than 1.0 GeV/c. In Figure 4.6, the resulting width of 115 ps is obtained.

4.3.2 Momentum Measurement

The momentum determination was described in more detail in Chapter 3. The momentum is inversely proportional to the measured angle α and directly proportional to the field-integral $K_1 = 0.3 \int l B dl / R = 87.3$ mrad GeV/c $p = K_1 / \alpha$. The momentum resolution is determined from the data by the measuring the multiple scattering of slow particles up to the Drift Chamber and the angular resolution of the Drift Chamber in measuring α . Both the momentum scale and the multiple scattering contribution are determined using a correlation measurement between the momentum and measured mass.

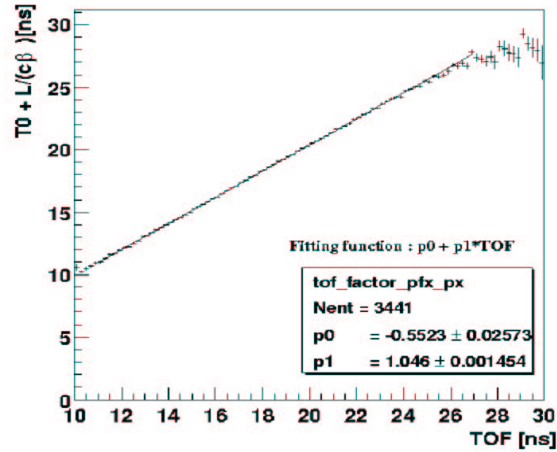


Figure 4.5: Extracting the time-of-flight scale factor by fitting a straight line to the expected total time-of-flight and the measured time-of-flight in the TOF detector [53].

Momentum Scale

The momentum scale is consistent with 1 to better than 2%. This scale is determined using the correlation between particle mass and momentum. In order to measure the momentum scale in the data, the difference between the expected mass and measured mass for each particle within the matching and PID cuts is minimized after assuming two free parameters: a momentum scale factor A and a time offset B . First, the mass-squared is written as a function M of momentum p and time of flight t :

$$m_0^2 = M(p, t) = p^2 \left(\left(\frac{ct}{L} \right)^2 - 1 \right) \quad (4.9)$$

Second, the two free parameters are assumed (a scale factor A and an offset B):

$$p \rightarrow Ap \quad (4.10)$$

$$t \rightarrow t + B \quad (4.11)$$

Third, the function M is written in terms of Ap and $t+B$:

$$M(p, t) \rightarrow M(Ap, t + B) = A^2 p^2 \left(\left(\frac{c}{L} \right)^2 \cdot (t + B)^2 - 1 \right) \quad (4.12)$$

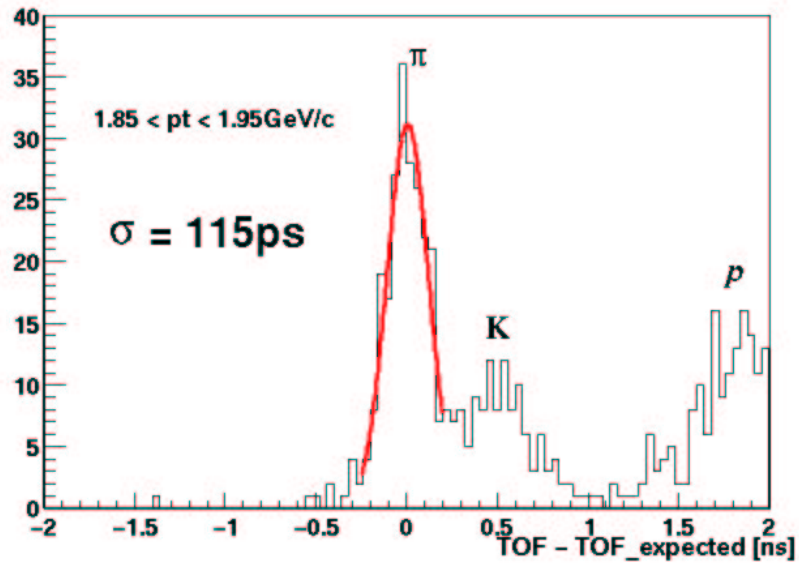


Figure 4.6: The difference of the measured and expected time for high momentum pions. The width of this residual, 115 ps, is the TOF detector resolution [55].

where, for each particle, p is its momentum, L is its flight-path length, t is its measured time-of-flight, and c is the speed of light. The measured mass $M(Ap, t + B)$ is then minimized with respect to the known particle mass. Ideally, A is 1 and B is 0.

In order to properly calculate the χ^2 , the σ_M is also determined for the current value of the parameters A and B and the known detector resolutions for both the TOF and PC detectors:

$$\sigma_M^2 = 4 \cdot M(Ap, t + B)^2 \cdot \left(\frac{\sigma_p}{p}\right)^2 + 4(Ap)^4 \left(\frac{c}{L}\right)^4 \cdot (t + B)^2 \cdot \sigma_t^2 \quad (4.13)$$

The χ^2 is calculated and minimized for each particle species:

$$\chi^2/dof = \sum \frac{(m_0^2 - M(Ap_i, t_i + B))^2}{\sigma_M^2 \cdot (N - 2)} \quad (4.14)$$

The χ^2 is minimized and the best fit parameters A and B are extracted in two different ways: (1) for each particle separately, and (2) for all particles fitted simultaneously. The 1σ χ^2 contours overlap for all six particle species in Figure 4.7 where the 1σ contours are shown for each particle species determined separately (left) and simultaneously (right). The negative particles correspond to the dashed lines (left). The vertical axis is the time-of-flight offset and the horizontal is the momentum scale. The simultaneous fit of all particles excluding the pions is also shown. The pions are excluded in the simultaneous fit as they are insensitive to the momentum scale. In the simultaneous fit, $A = 1.01 \pm 0.02$ and $B = 0.007 \pm 0.251\text{ns}$ with $\chi_{min}^2/dof = 7.7$. The $n\sigma$ contours have $\chi^2 = \chi_{min}^2 + n^2$.

There is an indication that the magnetic field map currently used in the analysis is lower by about 1.4% compared to the actual measured field map. This value is consistent with the extracted momentum scale. Therefore, the momentum scale is known within 2% systematic accuracy.

Momentum Resolution

The total momentum resolution is the combination of the angular displacement caused by the multiple Coulomb scattering of a charged particle with the materials up to the drift chamber and the inherent angular resolution of the Drift Chamber. First, the angular resolution of the drift chamber is measured from the no-field data. As a consistency check, two independent analyses that measure the resolution are discussed. One technique uses the PC3 detector and the other the TOF detector. Second, the multiple scattering

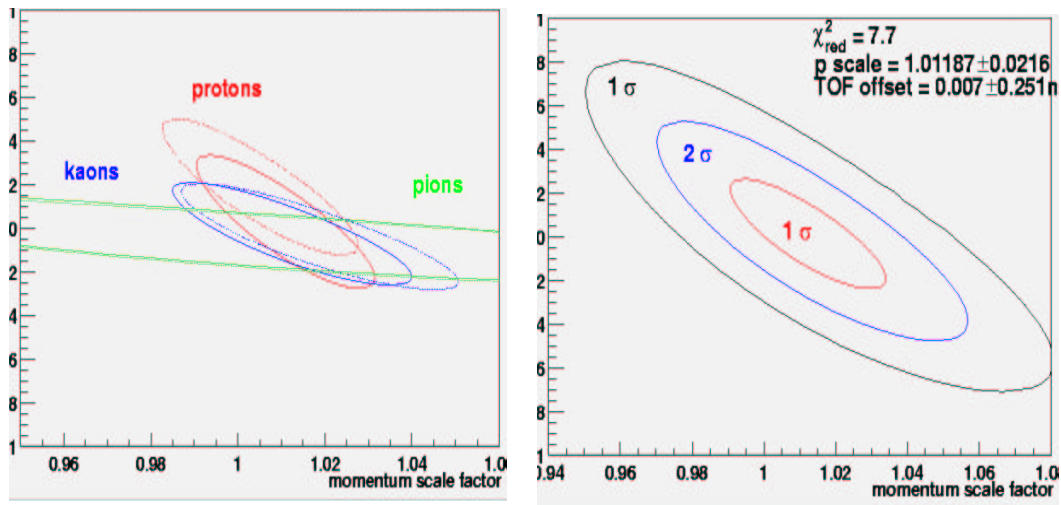


Figure 4.7: The 1σ contours for each particle species determined separately (left) and simultaneously (right). The pions are excluded in the simultaneous fit. The negative particles correspond to the dashed lines (left). The vertical axis is the time-of-flight offset and the horizontal is the momentum scale. [58]

constant is measured using a correlation measurement between the measured mass and momentum in the TOF detector.

In principle, the angular resolution is determined by the single hit resolution. The single hit resolution is the precision with which the drift distance to a single anode wire is measured. This resolution is measured to be $\sigma_{hit} = 150 \mu m$. With this intrinsic resolution and a fully functioning drift chamber, the expected resolution is $\delta p/p \approx 0.4\% p$. Experimentally, the resolution depends on the accuracy to which the wire positions in the drift chamber are known. Systematic shifts of wire groups (called nets) by a few hundred μm result in a resolution of $\delta p/p \approx 2.5\% p$ and $\delta p/p \approx 6\%$ depending on the reconstructed track quality.

The angular width can be expressed in terms of two defined variables, σ_α and σ_ϕ for the total angular resolution of a track with measured angles ϕ and α . These variables depend on how the track was reconstructed. Ideally, if the track is reconstructed partially in section X1 or X2, the $\sigma_\alpha \leq \sqrt{2}\sigma_{hit}/d$, where d is the radial width of either X1 or X2 sections in the drift chamber. For a track that is fully reconstructed in both X1 and X2 sections of the drift chamber, $\sigma_{alpha} = \sqrt{2}\sigma_\phi R/\Delta R$, where R is the reference radius, ΔR is the radial distance between the X1 and X2 sections, and $\sigma_\phi = \sigma_{hit}/(\sqrt{N_{hit}}R)$, where N_{hit} is the total number of hits associated to the track in both X1 and X2 sections.

The angular resolutions σ_α and σ_ϕ can be measured directly from fully reconstructed tracks in both X1 and X2 sections of the drift chamber ([53]). In order to minimize the residual magnetic field effects, the no-field data run (10629) is analyzed. The procedure is to determine the angles α and ϕ for X1 and X2 sections separately, denoted α_{X1} , ϕ_{X1} , α_{X2} , ϕ_{X2} , respectively. The angular resolutions can then be extracted by measuring the widths of the $\Delta\alpha = \alpha_{X1} - \alpha_{X2}$ and $\Delta\phi = \phi_{X1} - \phi_{X2}$ distributions for all the fully reconstructed tracks. The resulting widths are tabulated in Table 4.6, in the no-field data row. A similar study for simulated Monte Carlo tracks results in angular widths that are smaller by 33%.

An independent study using the Pad Chamber 3 detector and reconstructed tracks in the magnetic field results in consistent values as tabulated in Table 4.6 [59]. In this analysis, the particles tracked to PC3 are matched to the reconstructed clusters in PC3 as a function of the particle's measured momentum. The residuals in ϕ are plotted as a function of momentum for different track qualities in Figure 4.8. In this figure, the simulated Monte Carlo tracks are also shown as a comparison (triangles). The lines are the resulting fit of the function $\sigma_{phi} = \sqrt{C_{ms}^2/p^2 + \sigma_\phi^2(\sigma_{PC3}, \sigma_{DC})}$ to the data points, where

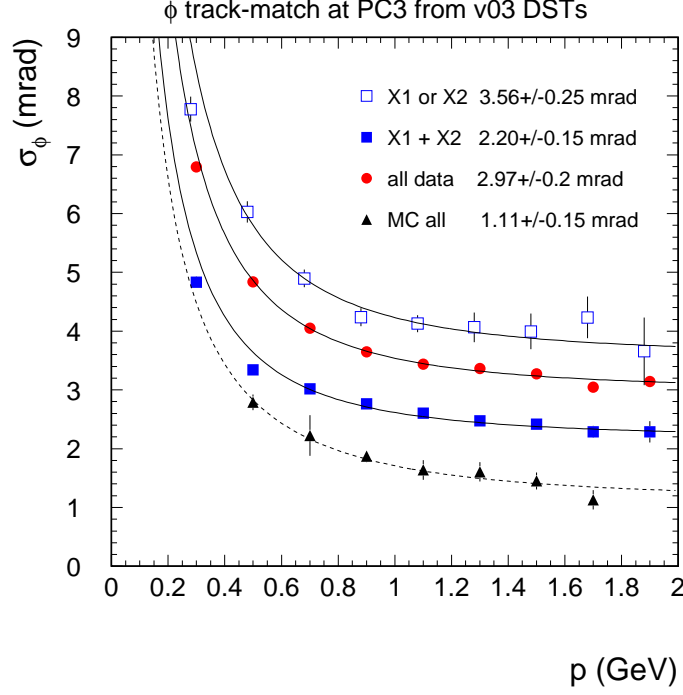


Figure 4.8: The global tracks and PC3 hit residuals in ϕ (vertical axis) as a function of momentum (horizontal) for different Drift Chamber track qualities [59].

$\sigma_\phi(\sigma_{PC3}, \sigma_{DC})$ is the total angular width for the track from the DC up to PC3 and is written in detail in Equation 4.15,

$$\sigma_\phi^2(\sigma_{PC3}, \sigma_{DC}) = \sigma_\phi^2(PC3) + w_1\sigma_\phi^2 + w_2\sigma_\alpha^2\left(\frac{r-R}{r}\right)^2 \quad (4.15)$$

where $w_1 = w_2 = 1.0$ for partially reconstructed tracks and $w_1 = 0.5$, $w_2 = 2$ for fully reconstructed tracks [59]. The track's radial position at PC3 is r . In the simulation, the extracted value of $\sigma_\phi(\sigma_{PC3}, \sigma_{DC}) = 1.1 \pm 0.2$ mrad is consistent with the expected angular resolution at PC3,

$$\sigma_{PC3} = (1.7/\sqrt{12})(1/r)\text{mrad} \quad (4.16)$$

where r is the radius in cm at PC3. Here, the size of a pixel is 1.7 cm and the width of a square distribution is $1.7/\sqrt{12}$.

	σ_α (mrad)	σ_ϕ (mrad)	σ_ϕ match (mrad)
Ideal	3.5	0.35	–
Monte Carlo (DC)	3.4	0.17	–
Monte Carlo (PC3)	3.4	0.17	1.1±0.2
No-field Data (DC)	5.1±0.5	0.28±0.03	
No-field Data (PC3)	5.8±0.5	0.28±0.2	3.0±0.2
Field Data (TOF)	–	–	3.2±0.2

Table 4.6: Angular resolutions σ_α for partially (X1 or X2) and fully (X1 and X2) reconstructed tracks in the ideal case, in simulation, and in data. [59, 58]

Another independent analysis projects DC tracks to the TOF detector by measuring and fitting a known functional form to the mass-squared width. The results from this analysis are consistent with the other measurement using the PC3 detector in Table 4.6. The total mass-squared width contains an additional term that depends on the TOF detector resolution. Without assuming the known 115 ps for the tof resolution, a three parameter fit to the measured mass-squared sigmas as a function of momentum for all particle species is made simultaneously. The parameters extracted are the angular resolution c_1 , the multiple scattering constant c_2 , and the TOF resolution, c_3 (where $K_1 = 87.3$ mrad GeV/c is the total field integral of a trajectory from the vertex to the drift chambers).

$$\frac{\sigma^2(m^2, p, t)}{4} = \left(\frac{m^2 \cdot c_1}{K_1} \cdot p\right)^2 + \left(\frac{m^2 \cdot c_2}{K_1}\right)^2 \cdot \left(1 + \frac{m^2}{p^2}\right) + \left(\frac{c_3}{t}\right)^2 \cdot (m^2 + p^2) \cdot p^2 \quad (4.17)$$

After fitting this function and extracting the multiple scattering constant, the resulting momentum resolution is obtained for pions, kaons, and protons in Figure 4.9. The extracted c_3 is 166ps. This value includes the pathlength width since the error of L is neglected in the equation for σ_{m^2} .

As a check on the simultaneous fit values, the same data are measured but separately for pions and protons in different momentum ranges. The high momentum pions are more sensitive to the TOF detector resolution, while the protons at low momenta are sensitive to multiple scattering. The angular resolution of the Drift Chamber is measured to be (3.6 – 4)% p from the simultaneous fit of the mass-squared widths for all particle species.

All particle species are sensitive to the angular resolution of the drift chamber for momenta greater than 2.5 GeV/c. For lower momenta, the detector acceptance and multiple scattering dominate. The expected contribution

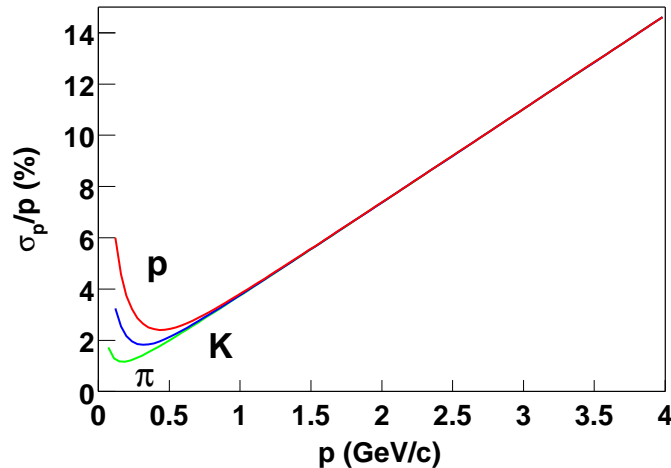


Figure 4.9: The momentum resolution using measured particle identification. The protons are more sensitive to the multiple scattering term (upper curve), while the pions are less sensitive (lower curve).

of multiple scattering to the momentum resolution is determined by calculating the angular scattering of a 1 GeV/c momentum particle as it traverses through the known materials from the collision vertex to the drift chamber. For simplicity, the particle travels in no magnetic field. The materials up to the drift chamber include the Be beam pipe, the Multiplicity Vertex Detector (MVD), air, and the mylar window of the Drift Chamber detector. The average multiple scattering angle θ_{rms} of a particle's trajectory at a radial distance r from the vertex results in an angular width $\sigma_\alpha = \theta_{rms}r/R$, where R is the drift chamber reference radius of 2.2m. For each of the materials up to the drift chamber, the θ_{rms} (planar angle) is determined. Adding each θ_{rms} results in a total multiple scattering angle of 0.53 mrad. From the m^2 width and p measurement, the multiple scattering contribution is 0.5 ± 0.05 mrad. This measured value is within 10% of the expected value.

From both the measured multiple scattering term and the angular resolution of the drift chamber, the total momentum resolution is

$$\sigma_p/p = \sqrt{(0.006 \pm 0.001)^2 + (0.026 \pm 0.003)^2 p^2} \quad (4.18)$$

for X1 and X2 tracks, and

$$\sigma_p/p = \sqrt{(0.006 \pm 0.001)^2 + (0.061 \pm 0.005)^2 p^2} \quad (4.19)$$

Material	Δr (mm)	X/X0 (%)	r (m)	$\theta_{rms}(mrad)$	σ_α (mrad)
Be beam pipe		0.3	0.04	0.58	0.01
MVD silican	0.3	0.3	0.04	0.58	0.01
MVD shell		0.4	0.4	0.69	0.13
Air	2000	0.7	1.1	0.92	0.46
DC mylar window	0.2	0.07	2.0	0.26	0.24
Total		1.77			0.53

Table 4.7: Materials positioned at radial positions r up to the drift chambers, with thicknesses Δr , and their contribution to σ_α [59].

for X1 or X2 tracks [59]. When all X sections of the drift chamber are used, the momentum resolution is

$$\sigma_p/p = 1\% \oplus 3.5\%p. \quad (4.20)$$

The measured detector resolutions and the multiple scattering constant make the particle identification possible using the calculated mass-squared width as a function of particle momentum.

4.3.3 The Mass-Squared Distribution

The light hadrons π^\pm, K^\pm, p , and \bar{p} are identified using the measured Time-of-Flight and Drift Chamber momentum. By determining the mass-squared width for each particle species as a function of momentum using the known detector resolutions⁴, the pions and kaons are separated by 2σ up to $p_t = 1.5$ GeV/c and protons are identified up to $p_t = 3.5$ GeV/c, where $|m_{meas}^2 - m_{centroid}^2| < 2\sigma_{m^2}$.

Simultaneous measurements of the particle's momentum, pathlength, and time of flight in the spectrometer provide the particle identification. The mass of the particle is calculated using Equation 4.22 and Equation 4.23. The pions, kaons, and protons are identified using the measured peak centroids of the m^2 distribution and selecting 2σ momentum, DC-resolution, TOF-resolution dependent bands as shown in Figure 4.3.3.

$$m = \frac{p}{\beta\gamma} = \frac{p\sqrt{(1-\beta^2)}}{\beta} \quad (4.21)$$

⁴For the drift chamber, Equation 4.3.2 is used.

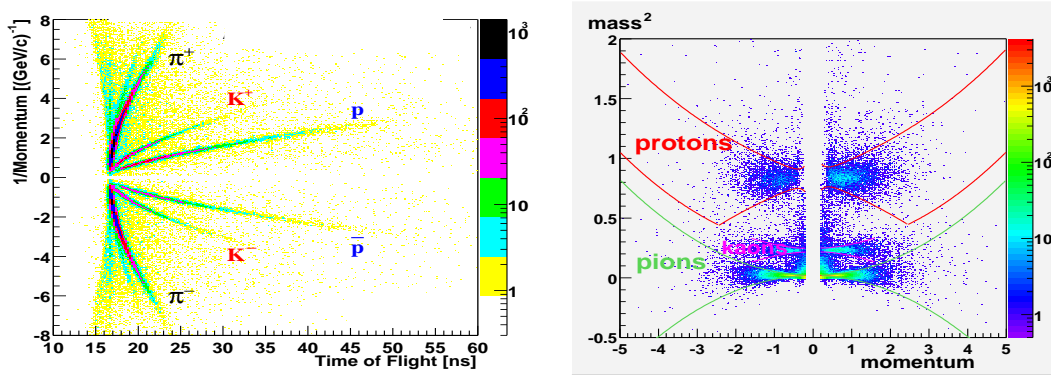


Figure 4.10: PHENIX high resolution particle identification of light hadrons (left) [56]. Particle identification bands to select pions, kaons, and protons (right) [60].

The velocity β can be expressed using the measured time of flight t_{meas} and the measured length L of the particle's trajectory where c is the speed of light (28.98 cm/ns) as expressed in Equation 4.22.

$$\beta = \frac{L}{ct_{meas}} \quad (4.22)$$

The relationship between the particle mass and the measured values can be expressed in the form convenient for use in the particle identification procedure:

$$m^2 = p^2 \left[\left(\frac{1}{\beta} \right)^2 - 1 \right] \quad (4.23)$$

The width of the mass squared peak is dependent on both the momentum and time-of-flight resolutions. An analytic form for the width of m^2 as a function of momentum resolution σ_p and time of flight resolution σ_T is determined using equation 4.23. The error in the particle's pathlength L in equation 4.22 results in a time width of 20-40 ps⁵. This width is included in the σ_t term.

$$\sigma_{m^2}^2 = 4 \frac{m^4}{p^2} \sigma_p^2 + 4p^4 \frac{1}{\beta^2} \sigma_t^2 \quad (4.24)$$

⁵The pathlength width is estimated by measuring the m^2 width of pions using the GEANT time in a Monte Carlo simulation.

The momentum resolution of the drift chambers in the PHENIX central-arm spectrometer can be expressed in the following form

$$\sigma_p^2 = \left(C_1 p \frac{1}{\beta} \right)^2 + \left(C_2 p^2 \right)^2 \quad (4.25)$$

$$C_1 = \frac{\delta\phi_{ms}}{K_1} \quad (4.26)$$

$$C_2 = \frac{\delta\phi_\alpha}{K_1} \quad (4.27)$$

where C_1 and C_2 are the multiple scattering and angular resolution terms, respectively. The units of $\delta\phi_{ms}$ are mrad·GeV/c. The constant k_1 is the amount of kick the particle gets from the magnetic field and is equal to 87.3 mrad GeV/c. The value of C_2 depends on the angular resolution of the drift chamber. The straighter the track, the higher the momentum, the larger the momentum width due to the limitations of measuring a curved trajectory in the spectrometer (the position resolution). The constant C_1 is the width due to the multiple scattering of charged particles with materials of the spectrometer up to the drift chamber's radial position of 5m from the beam axis.

Using equation 4.25 in equation 4.24 and $\beta = p/\sqrt{p^2 + m_0^2}$, where m_0 is the mass centroid of the particle's mass-squared distribution, the m^2 width for each particle is written as follows:

$$\sigma_{m^2}^2 = C_1^2 \cdot 4m^4 \left(1 + \frac{m_0^2}{p^2} \right) + C_2^2 \cdot 4 \frac{m_0^4}{p^2} + C_3^2 \cdot (4p^2(m_0^2 + p^2)) \quad (4.28)$$

$$C_3 = \frac{\sigma_t c}{L} \quad (4.29)$$

where coefficient C_3 is proportional to the ratio of the time of flight resolution σ_t and the length of the particle trajectory L squared in Equation 4.29. From the preceding sections, $C_1 = 0.006 \pm 0.001$ and $C_2 = 0.035 \pm 0.002$ c/GeV. While the TOF resolution is 115 ± 5 , the pathlength introduces a width of ≈ 20 -40 ps, so 145 ps is used in C_3 .

Measuring the Mass-Squared Centroids

Once the tracks are matched to time-of-flight hits, the centroid position of the mass-squared distribution peak is determined for each particle. This is necessary in order to avoid cutting into the distribution. A general m_0^2 cut for

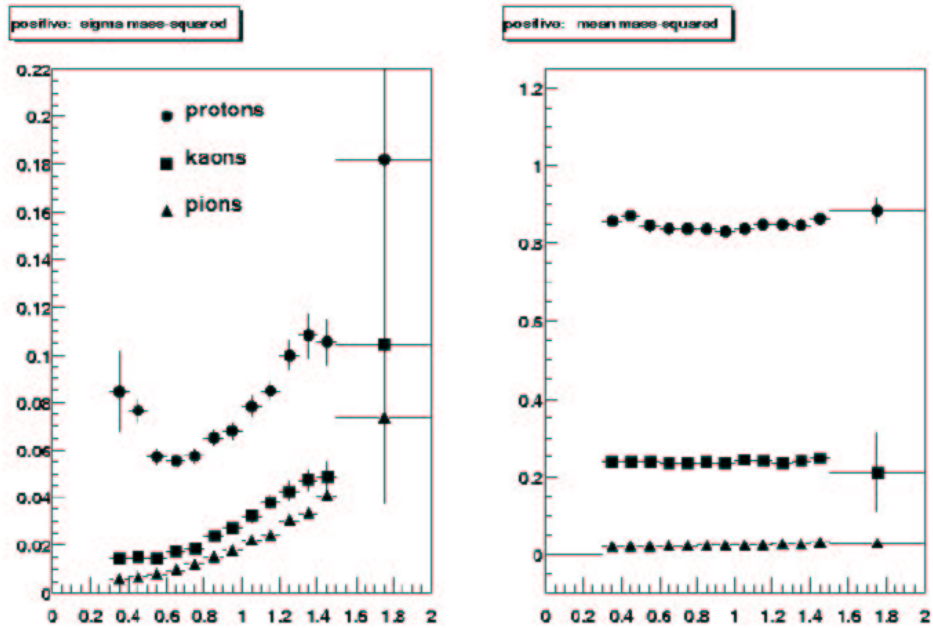


Figure 4.11: The extracted means and sigmas after fitting gaussians to the mass-squared distribution for pions, kaons, and protons in each momentum slice.

pions, kaons, protons is made. In units of GeV^2/c^4 , tracks that have a mass-squared within $-0.15 < m_0^2 < 0.15$ are initially grouped as pions; tracks with mass-squared within $0.15 < m_0^2 < 0.5$ are kaons; and tracks with $0.5 < m_0^2 < 1.25$ are protons. The same general cuts are made for the negative charged particles. The resulting mass-squared distributions (see Figure 4.12) for each particle are approximately gaussian in shape after binning the distribution into smaller momentum bins. A gaussian function is fit to the distribution in different slices of momentum, to determine the peak height, mean m_0^2 , and width σ of the mass-squared distribution. The resulting means and extracted sigmas from the gaussian fits in each momentum slice are shown in Figure 4.11.

The m_0^2 distribution that results is shown in Figure 4.12 after using

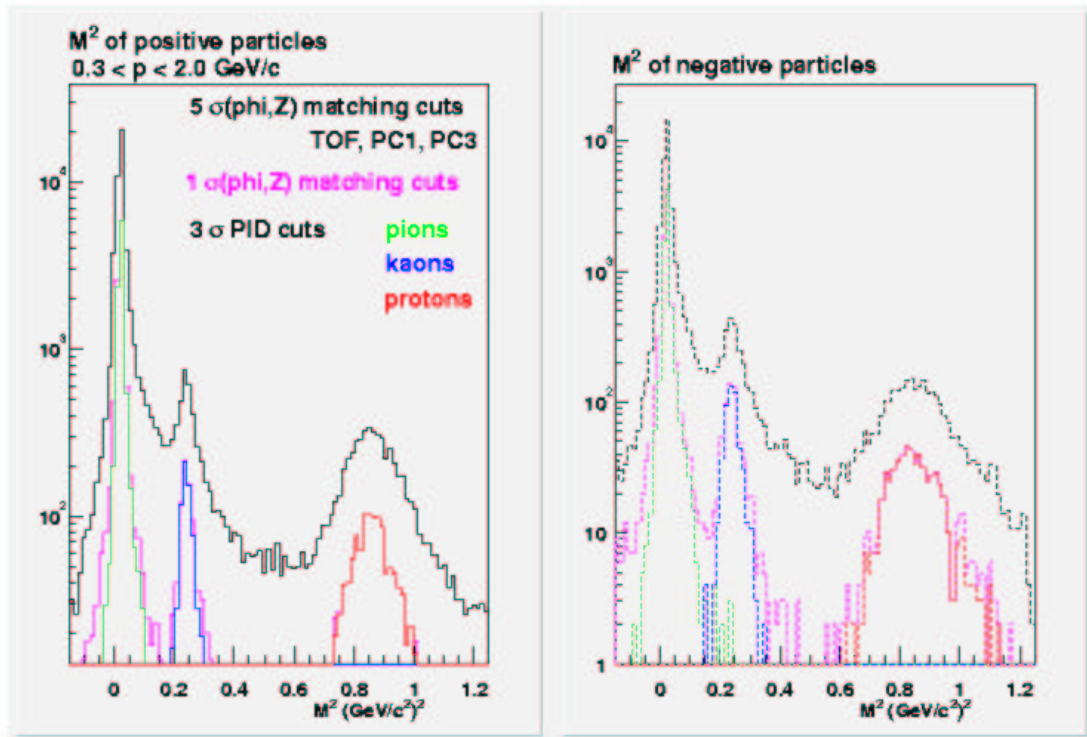


Figure 4.12: The mass-squared distribution [58].

the measured TOF and DC detector resolutions in the mass-squared width calculation, and the extracted mass-squared means for each particle species respectively.

PID n-Sigma Calibration for Pions at Low p_t

After observing a large discrepancy in the number of pions between a 2-sigma and 2.5-sigma particle identification cut, it was discovered that the n-sigma distribution at $p_t < 0.5$ GeV/c is not centered at zero and does not have a 1-sigma width of 1 as in Figure 4.13 for positive pions and Figure 4.14 for negative pions.

To calibrate the n-sigma distribution for pions, the offset and conversion factor between the fitted sigma of a gaussian and 1 are determined for each charge separately. The resulting offsets and factors are tabulated in Table 4.8, where the number of sigma n is determined by Equation 4.3.3.

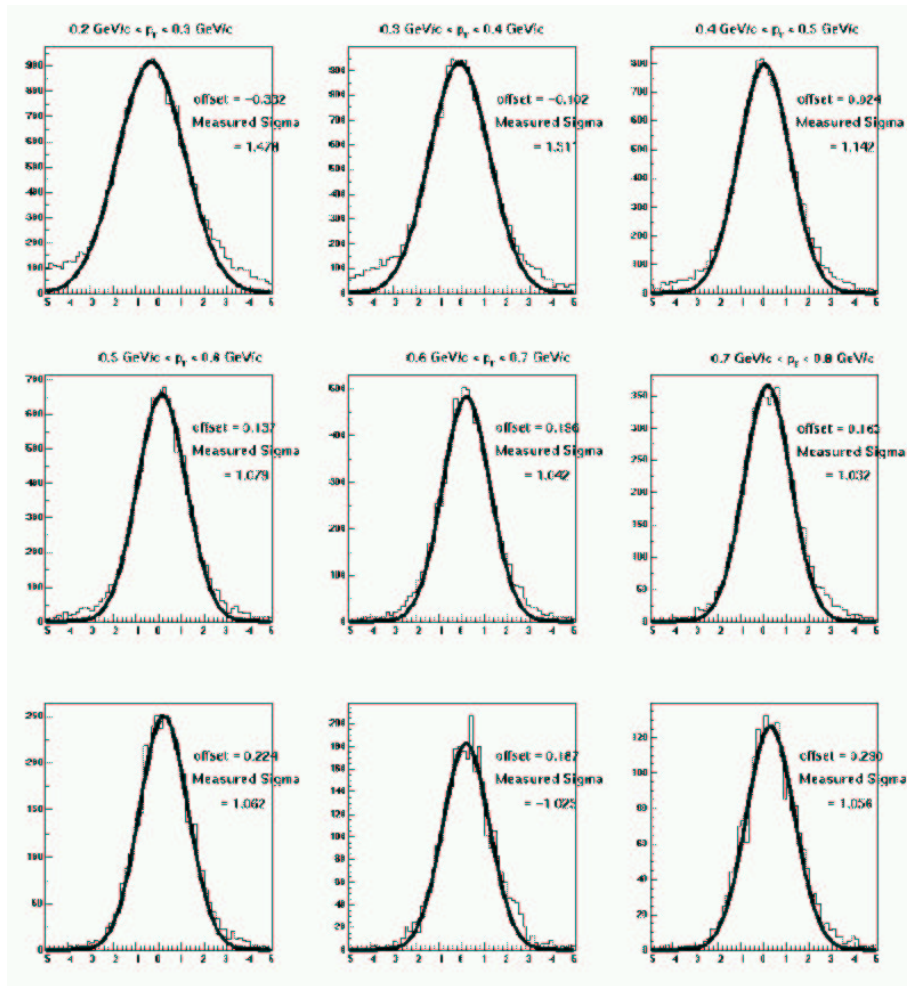


Figure 4.13: The n-sigma distribution of positive pions [57].

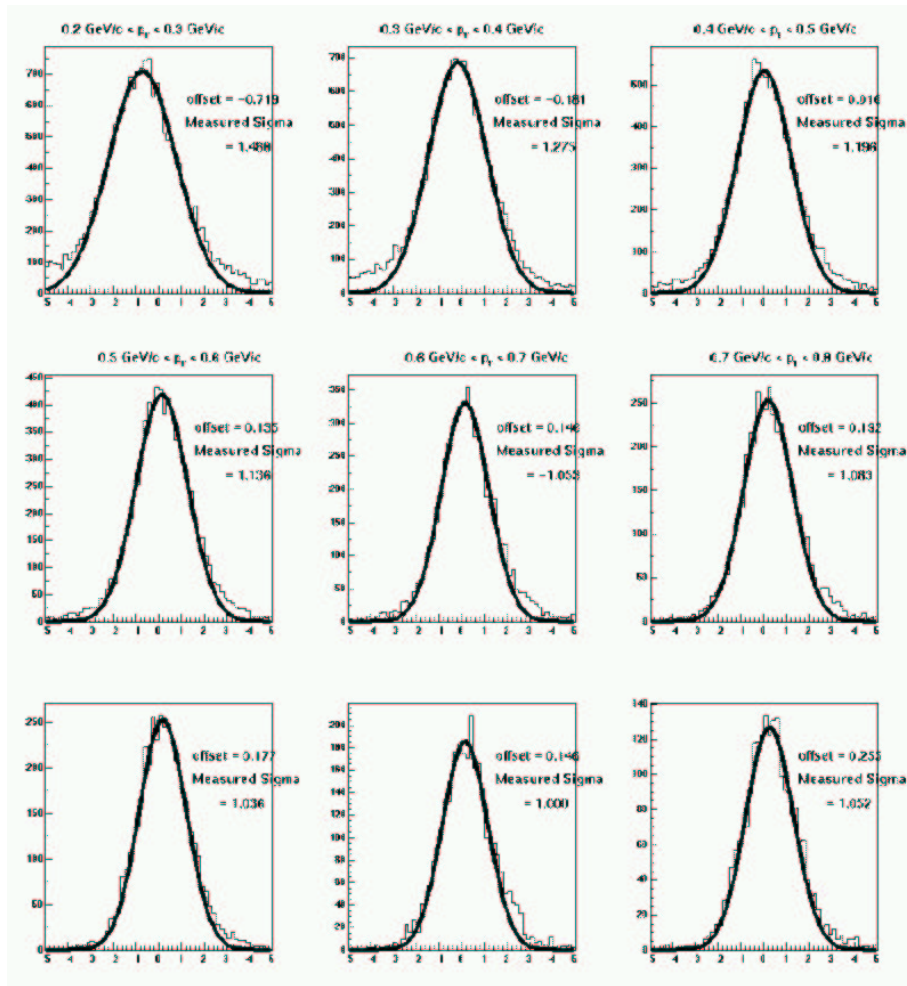


Figure 4.14: The n-sigma distribution of negative pions [57].

	p_t bin	A	B
π^+	$0.2 < p_t < 0.3$	0.42	1.47
π^+	$0.3 < p_t < 0.4$	0.13	1.47
π^-	$0.2 < p_t < 0.3$	0.73	1.47
π^-	$0.3 < p_t < 0.4$	0.18	1.27

Table 4.8: The offset A and factor B necessary to avoid cutting into the distribution of pions [57].

$$n = (n_{prev} + A)/B \quad (4.30)$$

Energy Loss Cut in the TOF

After the matching cut is made, an energy-loss cut is applied. This is to exclude those tracks that do not deposit the minimum ionizing particle energy. A β -dependent energy loss cut is used instead of a straight threshold cut of > 2 MeV, which is the ionization energy for a mip in the TOF. In Figure 4.15, the two types of cuts are shown with a scatter plot of the energy loss in the TOF slat of each particle versus $\beta = L/ct$, where L is the pathlength of the particle's trajectory from the BBC vertex to the TOF detector, t is the particle's time-of-flight, and c is the speed of light (29.98 cm/ns). As is observed in the plot, the β -dependent energy loss cut discards most of what is presumably random matches that the straight threshold cut of 2 MeV includes. The functional form is a parameterization of the Bethe-Bloch formula[7], where

$$dE/dx \approx \beta^{-5/3} \quad (4.31)$$

This form is used since the total energy loss ΔE and not the differential energy loss dE/dx is measured in the slat. The approximate Bethe-Bloch formula is scaled by a factor to fall below the data and thereby serves as a cut. The resulting equation is

$$\Delta E = A\beta^{-5/3} \quad (4.32)$$

where A is a scaling factor that allows this functional form to serve as a β -dependent threshold cut and is equal to 0.0016 GeV. This cut mainly affects the raw dN/dp_t momentum distribution of kaons and protons at low momenta (see Figure 4.16). In Table 4.9, the fraction of tracks excluded after the β -dependent energy loss cut is less than 5.5% in the data.

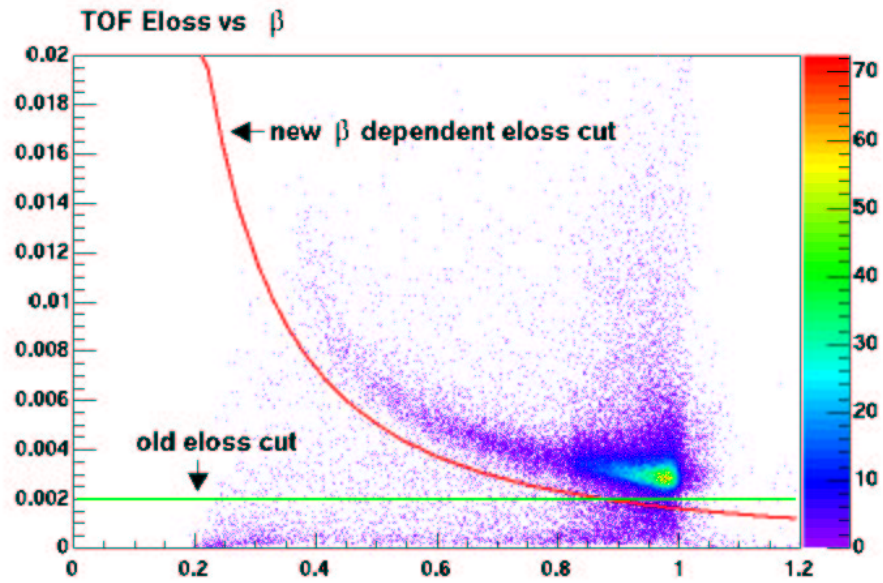


Figure 4.15: The ΔE of particles in the TOF versus β . Faster particles are to the right. Both the straight threshold cut and the new approximate Bethe-Bloch are shown. [60]

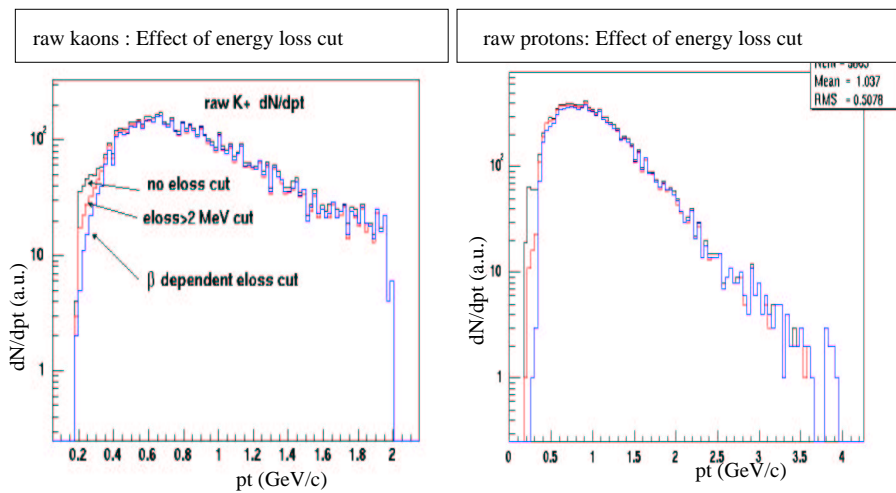


Figure 4.16: The raw dN/dp_t distribution of kaons (left) and protons (right), illustrating the effect of the two types of energy loss cuts [60].

Charge	Before Cut	After Cut	% Tracks Excluded
+ Data	97798	92837	5.1
- Data	68993	65313	5.3

Table 4.9: Positive and negative particles before and after the β -dependent energy loss cut described in the text for $p_t < 4$ GeV/c [60].

4.4 Background and Other Uncertainties in Data Reduction

Within the 2σ matching, energy-loss, and 2σ particle-identification cuts, a residual background contamination remains. The estimated contribution of the residual background for each particle is treated as a systematic uncertainty in the overall measured particle yield. The random background accepted by the particle identification cuts contribute an uncertainty of 2, 5, and 3% for pions, kaons, and protons, respectively, at $p_t < 0.6$ GeV/c [57]. These uncertainties are determined by creating a random distribution of associated tracks and hits in each detector.

To evaluate the random association probability, the track's position z along the beam axis is swapped and the hit-association between these swapped tracks and TOF detector hits is performed as described in Section 4.2.2 is performed ⁶. The swapped track's position in z is labelled here as z_{bkgd} . The swapping is done for every reconstructed track for three different cases, depending on the position of the tracks along the z axis in the drift chambers:

- For $|z| > 35.0$, $z_{bkgd} = -z$.
- For $z > 0$, $z_{bkgd} = z - 35.0$ cm.
- For $z < 0$, $z_{bkgd} = z + 35.0$ cm.

For every swapped track, all the measured detector hits are matched accordingly. The measured time and position of a real particle in the Time-of-Flight detector are associated to a swapped track. The collection of all such tracks is a random sample.

For this random sample, the same matching and energy-loss cuts as are applied in the data to evaluate the probability of a random match for unswapped

⁶This technique was developed by Y. Akiba and F. Messer

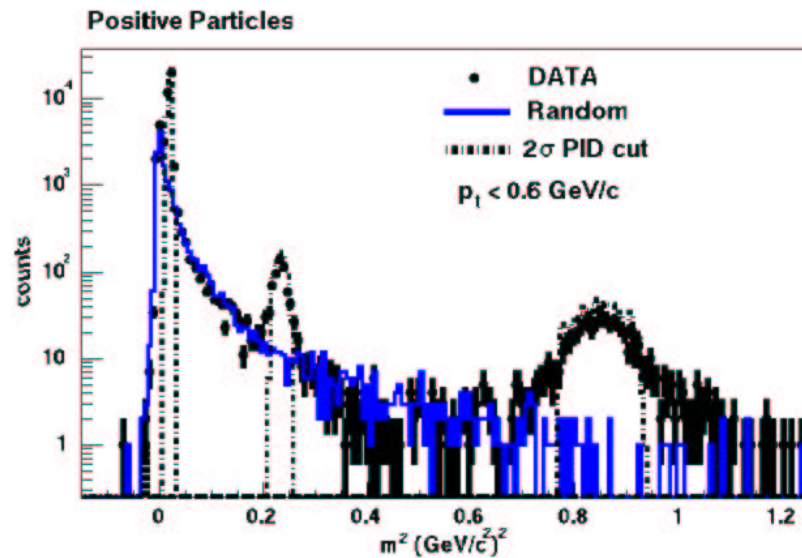


Figure 4.17: The mass-squared distribution (symbols) and the estimated random contribution (histogram). The 2σ particle-identification cuts are shown as dashed lines.

tracks. The resulting mass-squared distribution is plotted on top of the total mass-squared distribution in the time-of-flight after requiring a 2σ matching cut. In Figure 4.17, the histogram is the residual random mass-squared distribution that results. The 2σ particle-identification cuts for the unswapped tracks are shown as dashed lines. The estimated background contribution is the ratio of the integrated background contribution that falls within the dashed lines (the 2σ PID cuts) to the integrated total distribution (total = background + signal) as measured in the data. The random background is dominantly at lower momenta in the mass-squared distribution (see Figure 4.3.3 where background between the bands are primarily for $p_t < 0.6$ GeV/c).

In Figure 4.18, the mass-squared distribution in three different ranges in transverse momentum after all the particle identification cuts (the peak) are plotted with the random background distribution that also passes all cuts (falling exponentially) for positive pions (top row) and negative pions (bottom row). For positive pions, the background contamination under the peak is 4.06% in the momentum range $0.2 < p_t < 0.3$ GeV/c; 2.20% in the momentum range $0.3 < p_t < 0.4$ GeV/c; and 1.34% in the momentum range $0.4 < p_t < 0.5$ GeV/c.

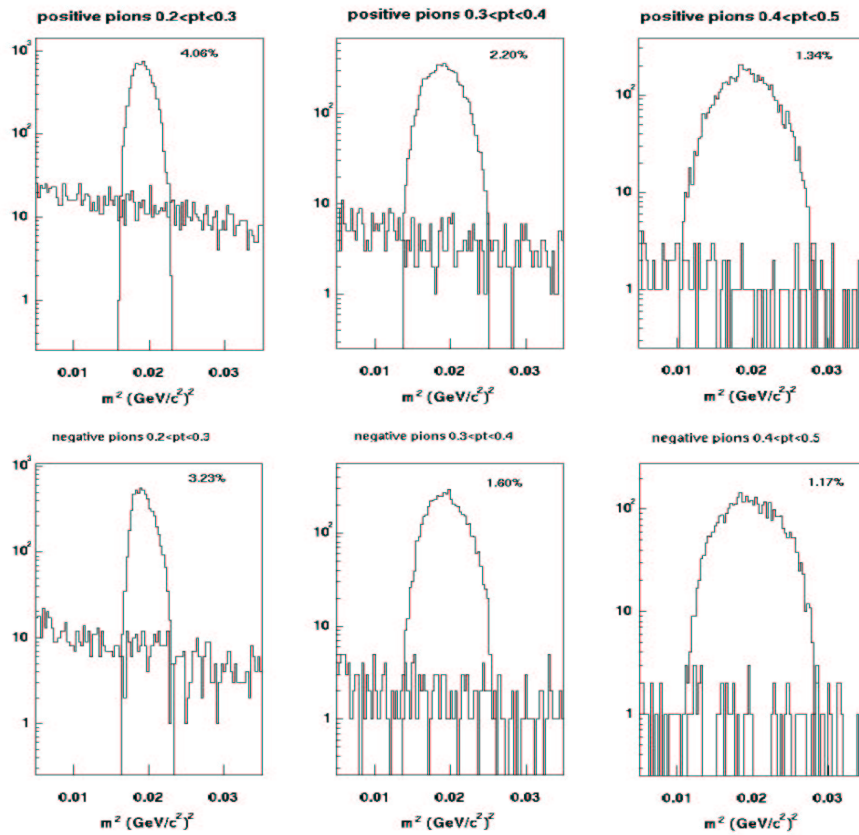


Figure 4.18: Estimating the random background contamination under the pion peaks in three different p_t ranges. Positive pions are the top row and negative pions are the bottom.

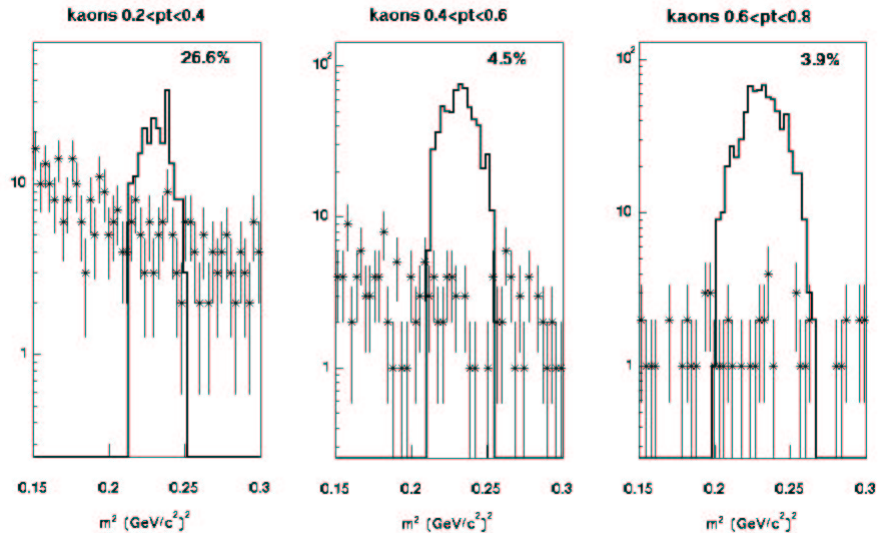


Figure 4.19: Estimating the random background contamination under the kaon peaks in three different p_t ranges.

In Figure 4.19, the equivalent distributions are plotted for kaons (both positive and negative) for slightly different ranges. The peaks are kaons (both positive and negative) that pass all PID cuts (in addition to the fiducial and energy loss cuts). The stars represent the random background contamination under each peak. The percentage is the estimated background contribution under the peak. For kaons, the background is 27% in the $0.2 < p_t < 0.4 \text{ GeV}/c$ and is why this bin is excluded in the final spectrum for both positive and negative kaons. The random background contamination is 5% in the range $0.4 < p_t < 0.6 \text{ GeV}/c$, and 4% in the range $0.6 < p_t < 0.8 \text{ GeV}/c$.

In Figure 4.20, the mass-squared distributions are plotted for both protons and anti-protons combined that pass all the particle identification cuts (peaks). The random background contribution is plotted as stars. Again, the percentage is the estimated background contribution under the peak in each momentum range selected.

In Table 4.10, the background contribution for different p_t ranges is summarized for the pion, kaon, and (anti)proton spectra. The background contribution is $\approx 30\%$ for the kaon spectra at $p_t < 0.4 \text{ GeV}/c$ and defines the low

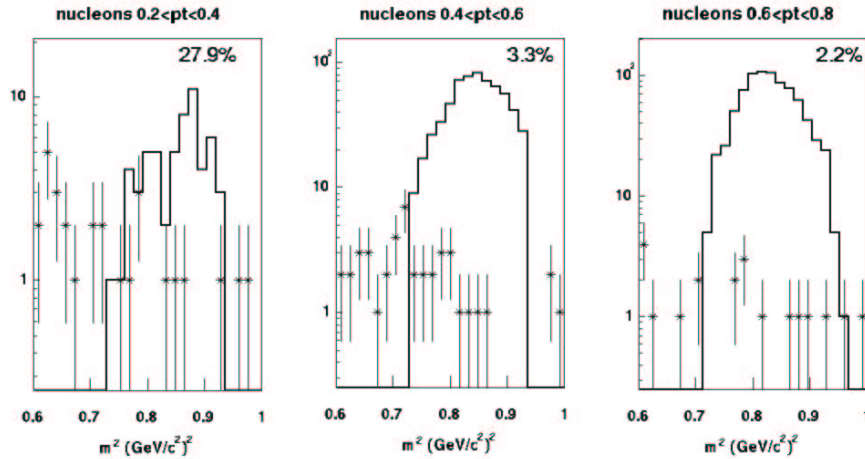


Figure 4.20: Estimating the random background contamination under the combined protons and anti-proton peaks in three different p_t ranges.

p_t limit in the spectra⁷.

4.4.1 Other Sources of Uncertainty

The momentum resolution corrections and momentum scale uncertainty are small effects. As other sources of uncertainty on the number of particles

⁷Ultimately, the best strategy is to subtract the background in order to avoid cutting off the spectrum at $p_t < 0.4$ GeV/c

Range (GeV/c)	π	K	(anti)p
0.2-0.3	4.06%	–	–
0.3-0.4	2.20%	–	–
0.4-0.5	1.34%	–	–
0.4-0.6	–	4.5%	3.3%
0.6-0.8	–	3.9%	2.2%

Table 4.10: The background contribution for different p_t ranges in the pion, kaon, and (anti)proton spectra.

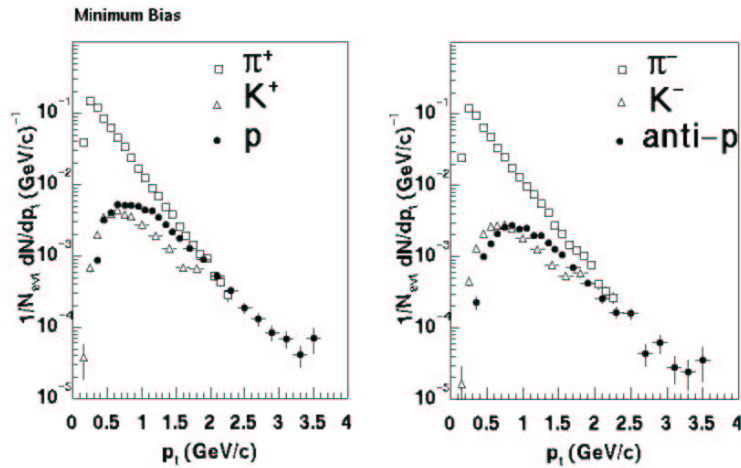


Figure 4.21: Minimum bias raw transverse momentum distributions of pions, kaons, and protons. Positive particles are plotted (left) and negative (right).

at any given momentum are much larger, they are neglected in determining the overall systematic uncertainty from the data reduction.

The background is not subtracted but is instead treated as a systematic uncertainty. The random background accepted by the particle identification cuts contribute an uncertainty of 2, 5, and 3% for pions, kaons, and protons, respectively, at $p_t < 0.6$ GeV/c. By varying the m^2 centroid and width before the particle identification cut is applied, the uncertainty in the particle identification is estimated to be 5% for all particles [57].

4.5 Raw Transverse Momentum Distributions

After the 2σ matching cut of drift chamber tracks to the TOF detector and the 2σ particle identification cuts as determined in the previous sections, the resulting raw distributions of pions, kaons, and protons for both minimum bias events and centrality selected events are made.

The minimum bias transverse momentum distributions of positive and negative pions, kaons, and protons are plotted in Figure 4.21. The vertical axis in both figures are the number of counts per p_t interval, divided by the total number of minimum bias events (see Table 4.3) as a function of p_t interval.

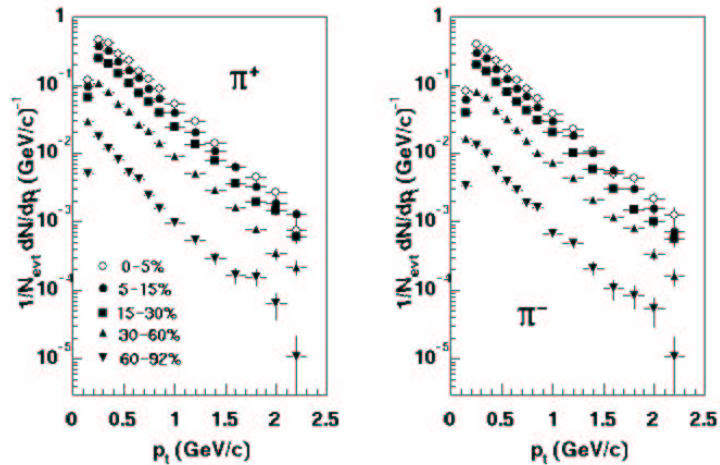


Figure 4.22: Centrality selected raw transverse momentum distributions of positive pions (left) and negative pions (right).

The centrality selected transverse momentum distributions of positive and negative pions, kaons, and protons are plotted in Figures 4.22 - 4.24. The vertical axis in all the figures is the number of counts per p_t interval, divided by the total number of minimum bias events (see Table 4.3) as a function of p_t interval.

The spectra shown here are already corrected for multiplicity inefficiencies that may result from track mis-reconstruction in high track density events using single-particles embedded into real events. The relevant fiducial cuts to match simulation and data are also applied. Factors that correct for finite geometrical acceptance; momentum resolution effects on the shape of spectra which predominantly affects the proton spectra at $p_t > 2.5\text{GeV}/c$; and the pions and kaons that decay in flight between the vertex and the TOF detector are applied next. These techniques and the additional cuts and corrections that are applied are discussed in more detail in Chapter 5.

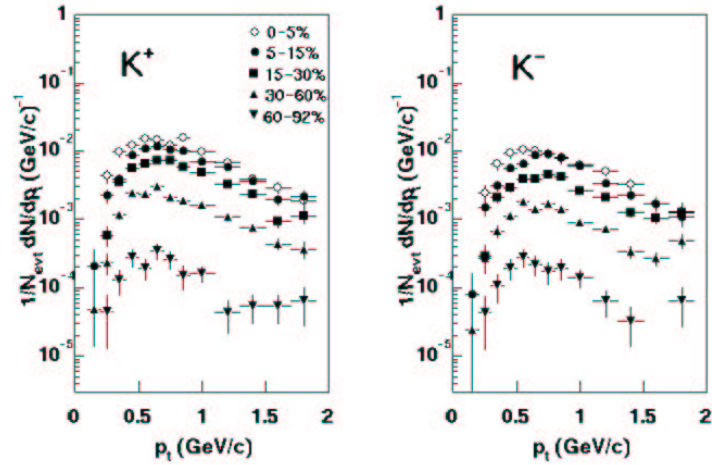


Figure 4.23: Centrality selected raw transverse momentum distributions of positive kaons (left) and negative kaons (right).

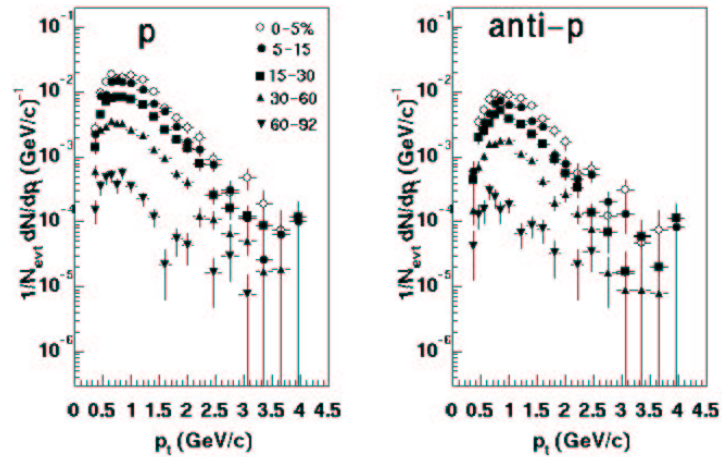


Figure 4.24: Centrality selected raw transverse momentum distributions of protons (left) and anti-protons (right).

Chapter 5

Corrections from Single Particle Monte Carlo

In this chapter, the corrections that are applied to the raw spectra are described in detail. The corrections include the finite geometrical acceptance; the detector response; the decays in flight; and the tracking inefficiencies. All of these effects are divided out of the raw spectra using single particle Monte Carlo. A known number of Monte Carlo particles are produced out to 5 GeV/c in momentum and thrown into the detector acceptance (called the input distribution). The analysis is performed in the same way as is done in the data and the number of particles reconstructed are determined (called the output distribution). The correction is the input distribution divided by the output and is calculated separately for each particle. The correction is applied bin-by-bin in p_t . The measured yield at each p_t in the spectrum, as reduced from the data in Chapter 4, is multiplied by the corresponding correction factor.

First, the simulated detector response is tuned to match the real response. This is achieved by using a wire-efficiency map, the known dead channels, and wire positions in the data in order to simulate the real detector acceptance and response. Fiducial cuts are defined in both the data and simulation to ensure the same fiducial volume. The momentum-dependent matching residuals between global tracks and the detector hits in the simulation are determined in both ϕ and z as in the data; these residuals are consistent with the measured residuals. These comparisons between Monte Carlo and data are discussed in detail in Section 5.1.4.

After the match between data and simulation is optimized, various corrections are determined. Using single particle Monte Carlo and the simulated detector response, momentum-dependent corrections are determined for geometrical acceptance, decays in flight, and detector resolution in Section 5.2.2 for each particle species separately. By embedding simulated single particles into real events, correction factors for multiplicity dependent tracking ineffi-

ciencies are determined in Section 5.3.3. The fully corrected charged particle spectra, yields, and $\langle p_t \rangle$ are presented and discussed for each particle in each centrality in Section 5.5.2.

5.1 Matching Monte Carlo and Data

In order to divide the detector response out of the raw spectra, it is essential to first match the simulated and real responses as closely as possible. In this section, the Drift Chamber and TOF simulated responses are described in detail. The vertex position as determined by the Beam-beam counter is smeared with a Gaussian distribution using a width of 2 cm, with values $-20 < z < 20$ cm. For the TOF detector, Gaussian distributions are also used with widths based on the relevant quantities as measured in the data. The drift chamber simulated response is more complicated and it is described in more detail. After all the simulated responses are tuned to match the real responses, the matching residuals between global track projections and detector hits are compared to the equivalent quantities in the data. The result is that the 2σ matching cut that is applied in the data is consistent in the simulation. Therefore, this cut can be applied in both the simulation for the corrections and in the data.

5.1.1 Drift Chamber

The objective in simulating and tuning the Drift Chamber detector is to describe the real detector as closely as possible. Charged-particle trajectories enter and leave a drift chamber drift cell as described in Chapter 3. The discussion presented here is a summary of an internal PHENIX analysis note in Reference [53].

There are two approaches to simulating the drift cell. A very detailed model would attempt to simulate the following physics processes which occur on the microscopic level:

- Determine the energy loss dE/dx of the charged-particle as it traverses the drift cell due to ionization based on the Bethe-Bloch equation.
- Simulate the electron cluster production
- Simulate the drifting of these electrons toward the anode wire (including reabsorption and diffusion in the drift cell gas).
- Close to the anode wire, simulate the avalanche region.

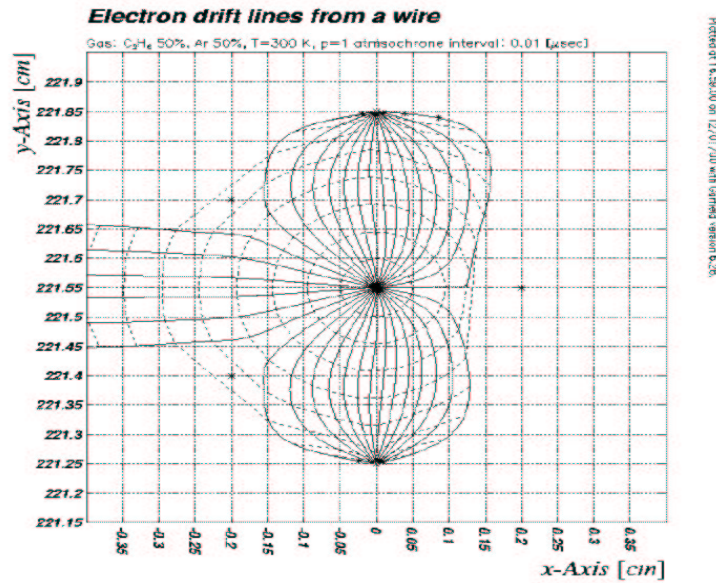


Figure 5.1: Simulation of electron drift distances (full lines) and isochrones (dashed) in one drift cell in the drift chamber. The spacing between isochrones is $0.01\mu\text{s}$. The gas mixture is 50% Ar and 50% C_2H_6 . [53].

- Simulate the amplifier response

A simpler model is based on the drift cell geometry and simply determines the resulting drift distance between the incident charged-particle position and the anode wire in Section 5.1.1. The more detailed parameters are measured from the data and the simulation is tuned accordingly. These additional parameters include the single-wire efficiency, pulse width, single-hit resolution, and the space drift-time relation as described in Section 5.1.1.

Simulating the Drift Cell

In this section, the geometrical model for the drift cell is described in detail. The geometrical description is based on the simulated drift distances between electrons and the anode wire that are generated by a program called GARFIELD. An example of such a simulation is shown in Figure 5.1.

The wire configuration in a drift cell (see Chapter 4) is used as a reference in describing the geometry. The drift lines are approximated by a circle centered around the anode wire which represents the proportional region and

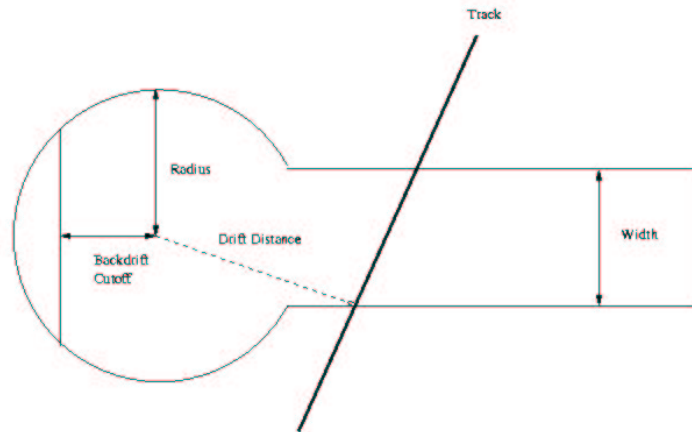


Figure 5.2: Geometrical description of a drift cell, modeled after a GARFIELD simulation of electron drift distances. A track enters the drift cell and the drift distance is calculated. [53].

a rectangle which represents the drift region for the cell as shown in Figure 5.2. The width d of the rectangle is 3 mm and corresponds to the distance between the gate wires. The radius r of the circle is 2.5 mm and represents the proportional region in the drift cell. The total length l of the drift cell is between 2 and 2.5 cm, depending on the wire plane in which the cell located. To simulate the back-drift region (between the sense/anode wire and the back wire), a back-drift cutoff b is positioned 2.0 mm from the anode wire opposite to the drift region. The drift distance is the shortest distance between a track and the anode wire within the boundaries defined by the drift cell geometry. Also shown in Figure 5.2 is a track that enters the drift cell at a particular angle. The dashed line represents how the drift distance for this track is calculated.

Tuning

The drift chamber simulated response is tuned to describe the response of the real drift chambers on the single-wire level using a non-microscopic approach using the no-field data from run 10629. The following parameters that characterize the drift chamber response are tuned accordingly:

- drift distances (tuning the drift velocity)

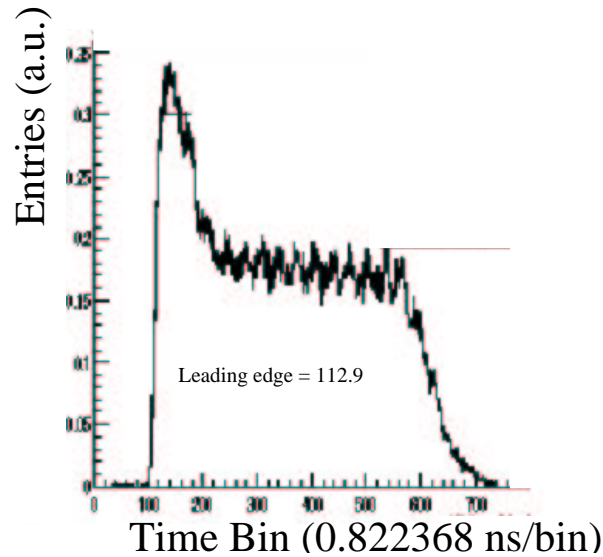


Figure 5.3: The time distribution for a pulse of electrons in a single drift cell in the drift chamber as measured in the West arm. The hit time is determined by the leading edge of the pulse (here it is 112.9). The time bin size is 0.822368 ns/bin.[61]

- pulse width (simulating its dependence on α and drift distance)
- single hit resolution (simulating its dependence on drift distance)
- single wire efficiency map, and
- wire positions which affects the detector's angular resolution

After the simulated response is tuned, the given parameter is compared to the data as a check.

In the data, the distribution of drift times is measured with a finite granularity. The time is determined by the leading edge of the measured pulse. In Figure 5.3, the time distribution pulse of electrons in a single drift cell in the drift chamber as measured in the West arm is shown. A function is fit to the distribution and the leading time bin of 112.9 is extracted from the data. The time bin size is 0.822368 ns/bin so this corresponds to a time of 92.8 ns. In order to determine the drift distance, a linear relation is assumed between drift distance and time with a constant drift velocity which is obtained by

calibrating the data. In Year-1, the drift velocity is $4.36 \text{ cm}/\mu\text{s}$ in the East drift chamber and $4.29 \text{ cm}/\mu\text{s}$ in the West drift chamber.

In the simulation, the geometrical model determines the distribution of drift distances for a charged track entering a drift cell; however, these distances are not produced with a finite granularity. The simulated response uses an assumed drift velocity in order to produce the leading edge of the simulated pulse. It also uses the same time binning as in data during calibration; this ensures that the time resolution between simulation and data are identical. After the simulated time distributions are determined, the simulated times are calibrated and the resulting “tuned” drift distances are produced. The simulation uses a drift velocity of $5 \text{ cm}/\mu\text{s}$ to determine the time distributions and is within 14% of the measured drift velocity in the data for the East arm and 16% of the West arm measured drift velocity.

In Figure 5.4, the distribution of the tuned drift distances as determined in the simulation is compared to the drift distances as measured in the data. The vertical axis is the number of entries per drift distance bin in cm. The horizontal axis is the drift distance. (The simulated histogram is above the measured in the range 0.5-2 cm). The measured and simulated drift distances are consistent; however, discrepancies exist close to the edge of the drift region and in the proportional region. The simple assumption of a linear space drift-time relation may not be correct for these regions.

The pulse width is the distance between the leading and trailing edges in the distribution of times for the electrons as they travel toward the anode wire. The pulse width depends on both the drift distance in the proportional region and on the angle α as observed in the measured data. If a track enters the drift cell perpendicularly at $\alpha = 0$, the pulse width is a minimum. If the track enters the drift cell at a grazing angle at $\alpha = \pi/2$, then the pulse width is a maximum. This angular dependence is simulated by using the maximum drift distance in the drift cell. If the difference between the minimum and maximum distances to the anode wire is greater than the pulse width, then this difference becomes the pulse width (within the drift cell boundaries). The pulse width dependence on the angle α in both data and simulation is shown in Figure 5.5. The points are data and the histogram is simulated. The pulse width dependence on drift distance is also extracted from the data and parameterized in the simulation, as shown in Figure 5.6.

In order to produce the same hit position resolution as measured in the data, the drift distance is smeared. It then becomes the leading edge of a hit in the drift chamber. The hit resolution depends on the drift distance; the resolution is worse close to the proportional region and at the edge of the drift region. The measured hit resolution as measured in the data as a function of

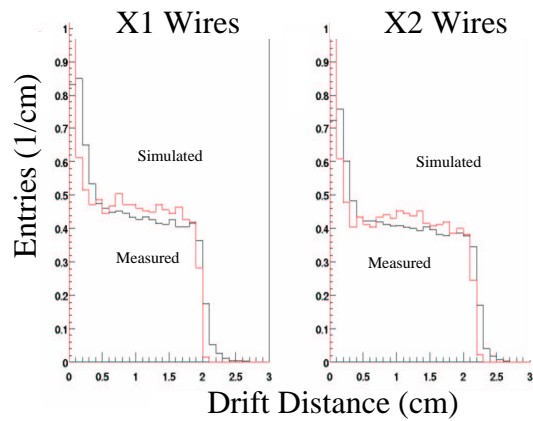


Figure 5.4: Measured and simulated distributions of the drift distances for all X1 (left) and X2 (right) wire nets in the drift chamber.[53]

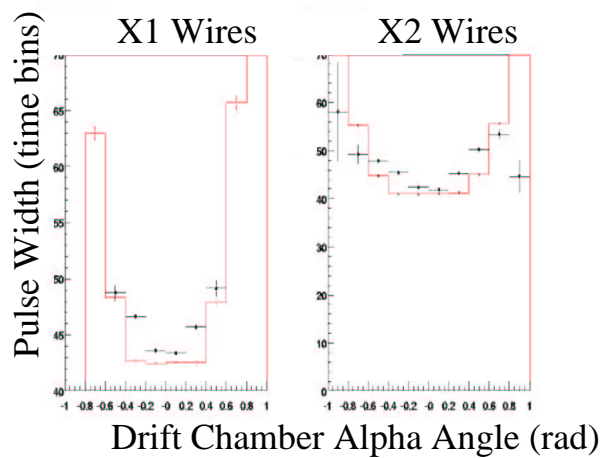


Figure 5.5: The width of the time distribution (pulse width) depends on the angle α both in data (points) and, after tuning, in simulation (histogram).[53].

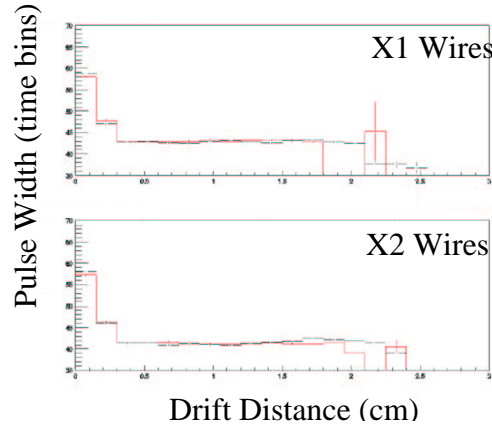


Figure 5.6: The width of the time distribution (pulse width) as a function of the drift distance in the drift cell.[53]

drift distance is shown (left) in Figure 5.7. The line is a parameterization of this curve that is used to tune the simulation which results in the plot on the right in Figure 5.7. Excellent agreement is obtained.

In Year-1, large fractions of the drift chambers, especially of DC East, could not be operated at nominal high voltages. As a result, there are large inactive areas with an inhomogeneous distribution of single-wire efficiencies in neighboring wire nets. It is therefore essential to measure single-wire efficiency map and use this map in the simulation.

The measurement of the efficiency in a single wire is determined as follows. A track defined by two hits in two drift cells determines whether or not in a third drift cell a hit should or should not be observed. Averaged over many events, and for each wire, an individual efficiency is obtained. In Figure 5.8, the resulting wire efficiencies in both data (left) and simulation (right) are shown for the drift chamber in the East arm. The X wires are assigned a plane number (the vertical axis) up to 40 and the drift cells in each wire plane (the horizontal axis) are numbered up to 80. Each X section has 12 wires, while the UV together have 8 for a total of 40 wires. As can be seen in this figure, the simulated and measured wire efficiencies are similar. A precise determination of single-wire efficiency requires large statistics in the data.

In order to simulate the detector resolution as measured in the data in Chapter 4, the angular resolution is smeared by randomizing the wire posi-

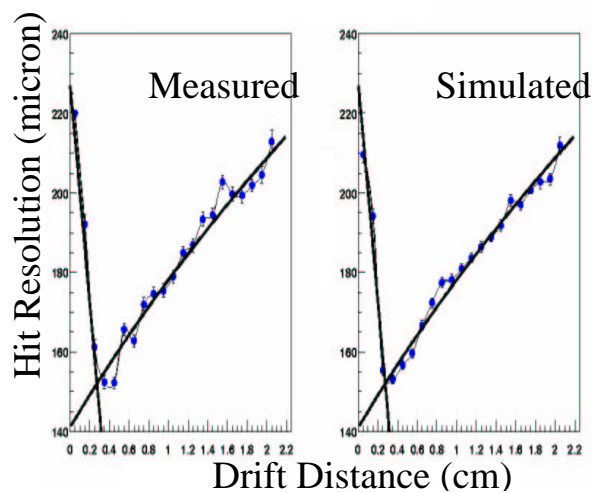


Figure 5.7: The hit resolution depends on the drift distance as measured in the data (left) and parameterized in the simulation (right).[53]

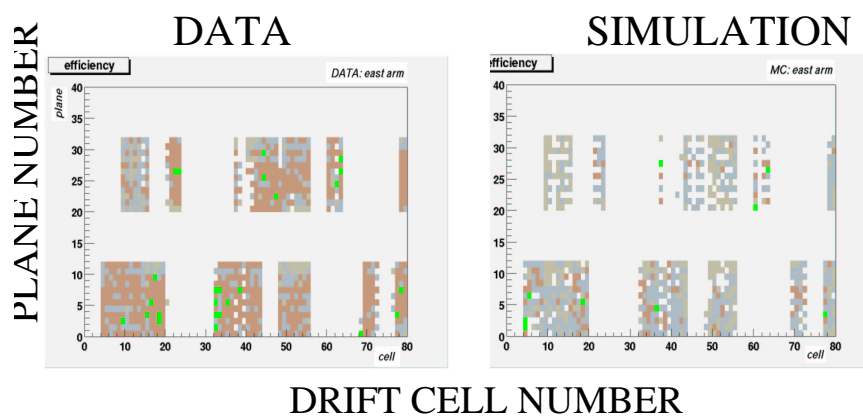


Figure 5.8: The single wire efficiency as measured in the data (left) and as mapped in the simulation (right) for the drift chamber in the East arm.[53]

tions. The hit resolution is not affected. Two random rotations of the X nets are done: (1) a rotation of the wire net around the beam axis which affects the ϕ resolution, and (2) a rotation of the wire net around its center which affects the α resolution. The resulting simulated angular resolutions are $\sigma_\alpha = 5.1 \pm 0.3$ mrad and $\sigma_\phi = 0.37 \pm 0.02$ mrad in excellent agreement with the measured results.

The simple geometrical model of the drift cell in the drift chamber is sufficient to describe the parameters observed in the data; namely, the drift distance distribution, the pulse width, the single wire efficiency, and the detector resolution.

5.1.2 Time-of-Flight

The Time-Of-Flight response is simulated by smearing the GEANT time using a Gaussian distribution with a width as measured in the data. The GEANT time and y-position are smeared using σ_t of 145 ps, and $\sigma_y = \sqrt{2}v_t\sigma_t$, where v_t is the speed of signals in the scintillator = 14 cm/ns. (The y-position in the TOF slat is determined by measuring the time difference across the slat and using v_t . The x and z positions in the TOF are the slat positions.) The simulated mass-squared versus momentum scatter plot shows a π/K separation up to 1.5 GeV/c which is the same as is observed in the data (see Figure 5.9). In this figure, the simulated mass after smearing the TOF GEANT time (left) is compared to data (right two plots). The data plots correspond to before and after the $2\sigma_{m^2}$ PID cuts, respectively. The particle identification is determined using the GEANT id and requiring that the reconstructed momentum is within $5\sigma_p$ of the expected resolution ($\sigma_p/p = 1\% \oplus 3.5\%p$).

5.1.3 Matching Global Tracks to TOF Hits

The same momentum-dependent matching cuts are made in the TOF simulation as is done in the data. In Figure 5.10, the matching sigmas are compared between data and simulation. A 2σ match that is momentum-dependent in both ϕ and z is consistent for both data and simulation. Table 5.1, lists the simulated σ_ϕ and σ_z values used in the functional fit shown in Figure 5.10. The functional form used is an exponential and a constant.

The matching residuals in the TOF in both ϕ and z are determined as a function of momentum so that the same 2σ matching cut in the simulation as is done in the data can be applied.

$$\sigma_\phi = Ae^{-Bp} + C, \quad (5.1)$$

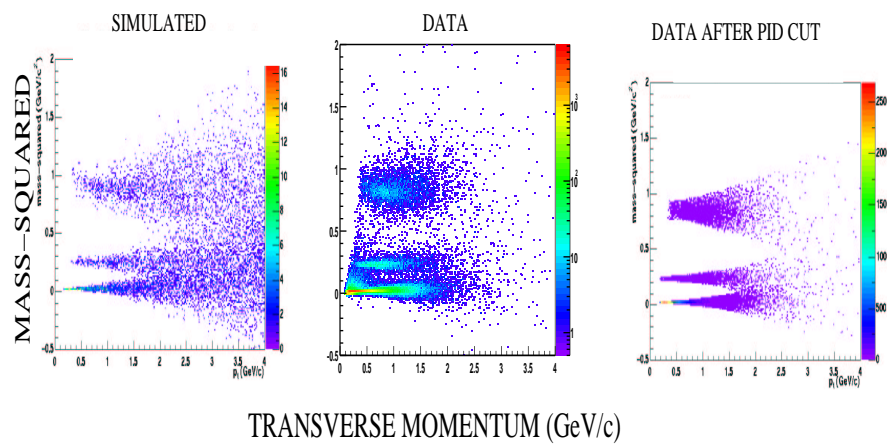


Figure 5.9: The simulated mass after smearing the TOF GEANT time (left) compared to data (right two plots). The data plots correspond to before and after the $2\sigma_{m^2}$ PID cuts, respectively.

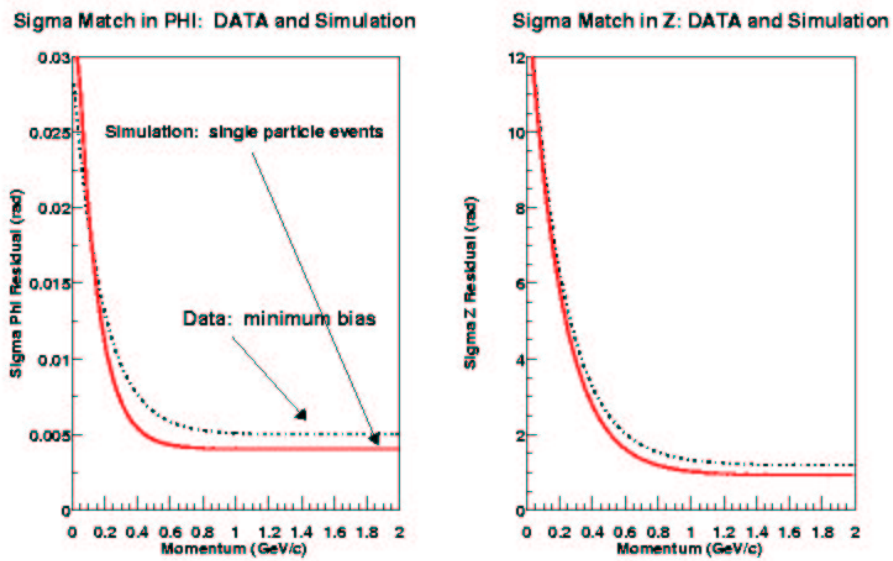


Figure 5.10: Comparison of the momentum-dependent residuals of DC tracks matched to TOF hits in ϕ (left) and z (right) between data (dashed) and simulation (line). (The residuals in the data were determined by F. Messer of the PHENIX Collaboration.)

p	σ_ϕ (rad)	σ_z (cm)
0.10	0.014809 ± 0.001187	7.351827 ± 0.487912
0.30	0.007151 ± 0.000117	3.941753 ± 0.030380
0.50	0.005117 ± 0.000052	2.046872 ± 0.011089
0.70	0.004628 ± 0.000037	1.480159 ± 0.007443
0.90	0.004341 ± 0.000036	1.255459 ± 0.006363
1.10	0.004258 ± 0.000035	1.121560 ± 0.006070
1.30	0.004191 ± 0.000037	1.062325 ± 0.006079
1.50	0.004133 ± 0.000037	1.029622 ± 0.005962
1.70	0.004047 ± 0.000038	0.993370 ± 0.005910
1.90	0.004069 ± 0.000039	0.982388 ± 0.005972

Table 5.1: The simulated matching sigmas depend on momentum in both ϕ and z .

where $A = 0.0109377$ rad, $B = 4.4915$ rad \cdot c/GeV, $C = 0.00411304$ rad and

$$\sigma_z = De^{-Ep} + F, \quad (5.2)$$

where $D = 9.91449$ cm, $E = 4.32516$ cm \cdot c/GeV, $F = 1.00645$ cm. The constants are determined after fitting these functional forms to the values tabulated in Table 5.1. The matching residuals both in ϕ and z are well simulated when compared to the data. Therefore, the same 2σ matching cut made in the data is applied in the simulation.

5.1.4 Fiducial Cuts

Once the simulated global tracks are matched to the TOF detector, the phase space coverage in the detector is compared to the coverage in the data. Inconsistencies are handled by using a fiducial cut in both the simulation and in the data to ensure the same fiducial volume. In Year-1, the inconsistencies include detector edges in both the TOF and Drift Chamber detectors. Such inconsistencies arise from imperfect geometry information leading to a mismatch between Monte Carlo and data, and run-dependent wire inefficiencies which are not fully described in the Monte Carlo. What follows is a detailed description of how these detector edges are determined. When a cut has a momentum dependence, diagonal lines in the $q/p - \phi$ space are made to parameterize the edges. It is important to find the cause of the discrepancy in order to cut on

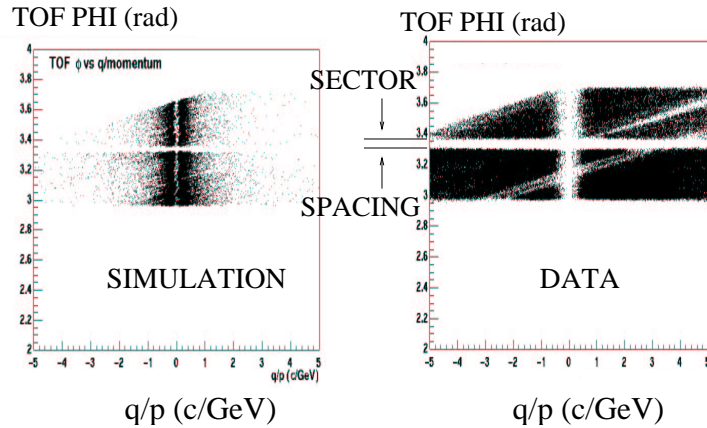


Figure 5.11: The TOF sector spacing in simulation (left) is too small when compared to data (right). The arrow indicates the gap which is the geometrical space between the sectors in the TOF.

the appropriate variable. First, the cuts made in the TOF detector are described. Then the Drift Chamber edges cuts are defined after a detailed study. This cut minimizes the fraction of tracks cut and minimizes the effects due to edges from dead regions. Low momentum particles are especially sensitive to such edge effects and large discrepancies can cause systematic differences in the acceptance on the order of 20%.

TOF Detector Edges

In the TOF detector, the main discrepancy between data and simulation is geometry. The spacing between Sector 0 and Sector 1 in the TOF detector is larger in the data than the simulation (see Figure 5.11, where the vertical axis is the azimuthal position of the track in the TOF and the horizontal is the charge divided by the momentum in the Drift Chamber). Since the sector spacing is larger in the data than in the simulation, this fiducial should remove more simulated tracks than real tracks. The TOF sector spacing is visible as a gap in the projection of q/p versus ϕ_{TOF} , where q is the particle's charge, p is its momentum, and ϕ_{TOF} is the azimuthal angle of the track in the TOF detector. As the gap is independent of momentum, a straight ϕ cut is made to exclude those tracks both in the simulation and in the data (to be consistent). Edge cuts are made to ensure that the Monte Carlo and data are consistent in the space ϕ_{TOF} - q/p (refer to Figure 5.11). The cuts that are made on the

Charge	Before Cuts	After Cuts	% Tracks Excluded
+ Data	97798	95238	2.7
- Data	68993	67044	2.8
+ Monte Carlo	10034	9038	9.9
- Monte Carlo	9002	7760	1.4

Table 5.2: Positive and negative particles before and after fiducial cuts are made in the TOF detector. The fraction of tracks cut is greatest for positive Monte Carlo tracks.

ϕ variable in the TOF detector are mostly momentum independent. Tracks in the TOF that meet the following criteria are excluded:

- $3.3 \leq \phi_{TOF} \leq 3.38$ rad.
- $\phi_{TOF} < 2.98$ rad.
- $\phi_{TOF} > 3.691$ rad (positive particles)
- $\phi_{TOF} > -0.06/p + 3.7$ rad, where p is the track momentum from the Drift Chamber (negative particles).

After these cuts are made, approximately 3% of the tracks are excluded, as tabulated in Table 5.2. The largest fraction of tracks cut are for the positive Monte Carlo tracks, corresponding to 10%.

Additional cuts in the variables x and z in the TOF detector are all momentum independent. They are made based on the TOF Sector. All tracks that meet the following criteria are excluded:

- Sector 1: $|z_{TOF}| > 175$ cm
- Sector 0: $|z_{TOF}| > 50$ cm, $x_{TOF} > -400$ or $x_{TOF} < -495$ cm

The next step is to study the dead areas in the drift chamber and apply the appropriate cuts to match the fiducial volume between simulation and data accordingly.

Drift Chamber Dead Areas

In addition to the cuts described above, fiducial cuts in the Drift Chamber are made in order to better match the acceptance between the simulation and data. This is due to the fact that in time, the dead regions in the drift chamber increased during the run in Year-1, while in the simulation, the no-field dead channel map of Run 10629 is used. Enough statistics must be generated in order to study the edge effects of the dead areas in the Drift Chamber between Monte Carlo and data. In the Drift Chamber, there are three gross features that are not consistently described in the Monte Carlo and data.

One main feature that contributes mostly to the systematic difference between positive and negative particles is the size of a dead channel region that is larger in the data than in the simulation. In Figure 5.12, the ϕ distribution for high momentum particles in both simulation and data are shown for both the North and South regions of the drift chamber in the East arm. The right panel is the North East section and the arrows point to the dead region that is not as large as is observed in the data. This is due to the fact that the dead channel map from Run 10629 is a snapshot in time of the chamber. This hole is run-dependent, so the Monte Carlo only describes this region for a small subset of runs around the dead-channel map. (The left panel shows a dead region that is described.)

In Figure 5.13, two example fiducial cuts for the North East section are shown in the q/p - ϕ_{DC} plane. The fiducial cut on the left panel cuts out less tracks than the larger cut on the right.

Another gross feature is an edge difference between Monte Carlo and data that is approximately 1/2 a keystone in phi width (see Figure 5.14). This edge difference is not likely to be the geometrical difference due to misalignment in the data (the misalignment is known to be several mrad and not as large as is observed). This edge difference is most likely caused by the drift chamber in the simulation. The perfect tracker which does not use the Combinatorial Hough Transform but instead fits a line to the GEANT hits to get ϕ and α covers this region.

The last feature is the known large dead region on the other side of the drift chamber also in the East arm (the left panel in Figure 5.12). This hole is well described in the Monte Carlo, but edge effects are created especially in a small triangular region where the Monte Carlo and data differ (see Figure 5.15).

To create a consistent description, fiducial cuts are defined from the measured hole dimensions in the data in both the Monte Carlo and the data. In order to minimize edge effects, the size of the fiducial cuts described above are

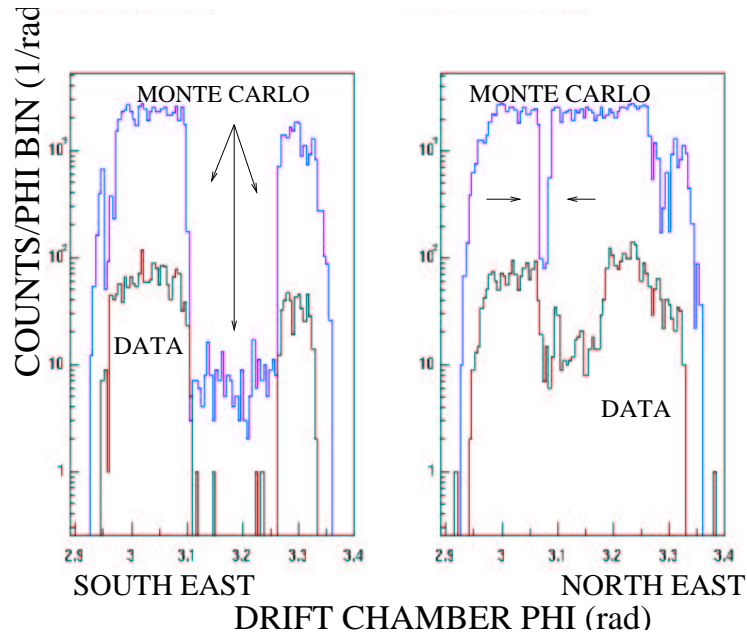


Figure 5.12: The ϕ distribution of tracks with $p_t > 1.5$ GeV/c in the each drift chamber for both Monte Carlo and data. The dead channel region in the south (left) is well describe while the north (right) Monte Carlo is too small.

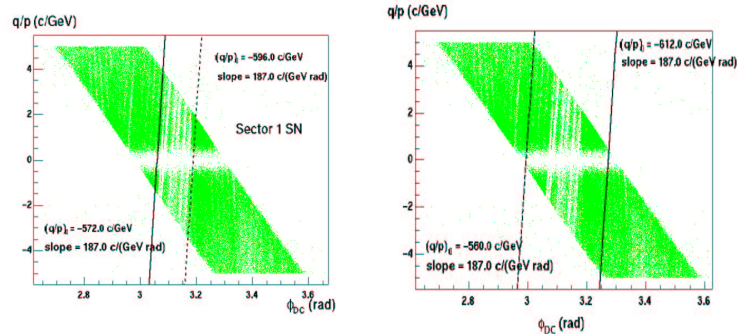


Figure 5.13: The North East dead channel region in the Drift Chamber (left). The lines indicate an example of a p-dependent fiducial cut in the q/p - ϕ_{DC} space (left). An example of a larger fiducial cut is also shown (right).

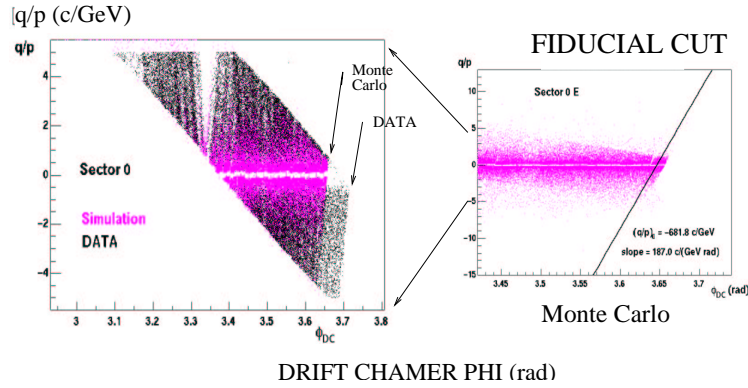


Figure 5.14: The edge in the Monte Carlo that is approximately 1/2 a keystone short of the data (left). The line indicates the p-dependent fiducial cut in the q/p - ϕ_{DC} space (right) and is applied both in the Monte Carlo and in the raw data.

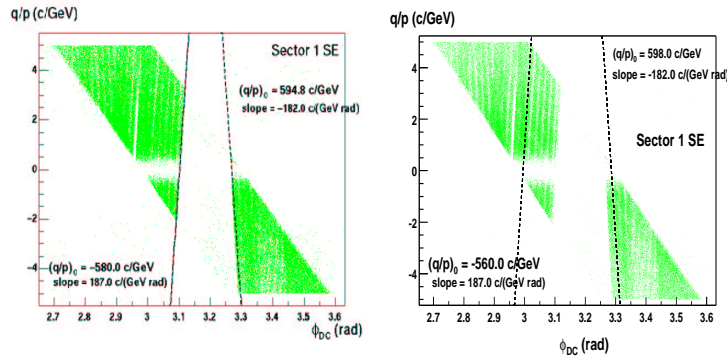


Figure 5.15: The known hole in the South East part of the Drift Chamber (left). The lines indicate an example of a p-dependent fiducial cut in the q/p - ϕ_{DC} space. The figure on the right is the same region, but with a wider cut that excludes the triangular region on the lower left-hand side that is not well described by the Monte Carlo.

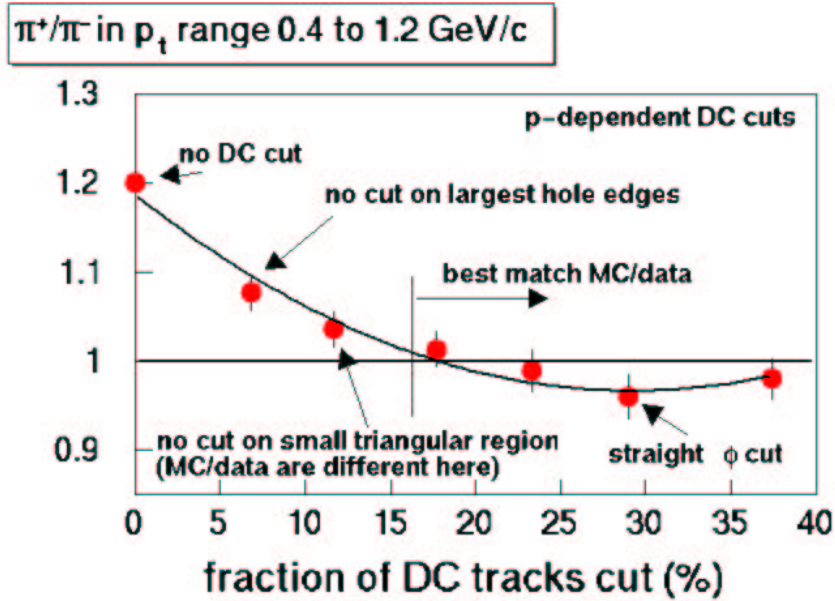


Figure 5.16: A study of how the negative to positive pion ratio changes as a fraction of drift chamber tracks cut in each fiducial cut in $q/p - \phi_{DC}$ space.

increased accordingly. The cut that minimizes both the fraction of tracks cut and the edge effects is used.

To determine the appropriate cut, a fiducial cut study is performed. In this study, the match between simulation and data improves until a region of stability in the cuts is found. The observable is the positive to negative ratio of pions at low momenta. Since low momentum pions curve more in the magnetic field, they are sensitive to the edges. In Figure 5.16, all the fiducial cuts are studied by observing the ratio of fully corrected pions at low momenta (positive to negative) as a function of the fraction of Drift Chamber tracks cut. In Table 5.2, the point labeled “No DC cut” means no additional fiducial cut beyond the 3% as described in Section 5.1.4.

The systematic difference between positive and negative particles decreases from 20% to 5% as the match between simulation and data improves and the fraction of DC tracks cut increases. Also shown in this figure is the result of a straight cut in ϕ_{DC} in the drift chamber instead of a p-dependent fiducial cut. The fiducial cut that is consistent with the region of stability (to the right of the line) and that minimizes the number of tracks cut (to maximize the statistics) is chosen. The fiducial cuts are tabulated in Table 5.3. In

Cut	DC Side	TOF Sector	m_1	b_1	m_2	b_2
1	South	1	187	-560	-182	598
2	North	1	187	-572	187	-596
3	Both	0	187	-681.8	-	-

Table 5.3: The three main momentum-dependent fiducial cuts that are made using the Drift Chamber ϕ variable. These cuts are used in both the simulation and in the raw data are defined according to TOF Sector and DC Side accordingly.

In addition to the TOF fiducial cuts described above, the fiducial cuts described below are applied consistently to both data and simulation.

The cuts that are made on the ϕ variable in the drift chamber are all momentum dependent. These cuts are defined by lower and upper bounds in ϕ , called ϕ_1 and ϕ_2 respectively.

$$\phi_1 = (\text{charge}/p - b_1)/m_1 \quad (5.3)$$

$$\phi_2 = (\text{charge}/p - b_2)/m_2 \quad (5.4)$$

The selection is such that all tracks that have $\phi_1 < \phi < \phi_2$ are excluded as defined in Equations 5.1.4 and 5.1.4, with cuts defined in Table 5.3. These bounds are determined differently for both the TOF sectors and for the side of the Drift Chamber. For Cut 3, the tracks with ϕ in the Drift Chamber greater than this calculated boundary are excluded.

An additional cut is the edge in z in the drift chamber. All tracks with $|z_{DC}| > 75.0$ cm are excluded.

The systematic uncertainty in these fiducial cuts is determined by comparing the deviation of the ratio for all the “best matching” fiducial cuts (to the right of the line in Figure 5.16). The systematic uncertainty in these fiducial cuts is approximately 5%.

5.2 Correcting for Geometrical Acceptance, Decays in Flight, and Detector Response

The raw data are corrected for the finite geometrical acceptance of the detector; decays in flight for pions and kaons; and momentum resolution which affects the spectra shape, primarily for protons, after 2.5 GeV/c. It is important to have reasonable Monte Carlo statistics (especially at low p_t) in order to obtain corrections that can be used bin-by-bin in transverse momentum for each particle species. The alternative approach is to fit arbitrary functions to the resulting correction factors; but this may introduce systematic errors which are hard to quantify. The statistical errors from the correction factors after a bin correction is applied are added in quadrature to the statistical errors in the data.

5.2.1 How much Monte Carlo statistics is enough ?

Single particles are generated for pions, kaons, and protons (including the negatives) using a particle generator called EXODUS.[62] EXODUS generates particles and their decays to produce a simulated phase-space distribution¹. The input parameters for EXODUS include the particle's identity, four-momentum, and decay properties. Weight factors adjust the relative production cross sections. EXODUS can generate a distribution of single particles or a realistic event with different particle species.

The particles are distributed with a flat distribution in rapidity y , flat azimuthal angle ϕ in the TOF acceptance, and weighted with an exponential and constant in p_t . This is necessary in order for the MC statistics at low- p_t and high- p_t to be comparable. A flat p_t distribution in the Monte Carlo is not optimal since acceptance and tracking efficiency deplete significantly the low p_t part of the reconstructed spectra.

In order to determine the total statistics necessary to correct the raw spectra pt-bin by pt-bin, the relative error is calculated for both simulation and raw data. Using the strategy that the relative error in the data should dominate the error from the correction, 4 million pions, 2 million kaons, and 2 million protons single particle MC tracks were produced. Figure 5.17 shows the relative error as a function of p_t for both simulation and raw data for pions.

¹The decay machine in EXODUS is based on the decay algorithms in the GENESIS package. GENESIS simulated the invariant mass distribution of lepton pairs produced in p+Be at 450 GeV/c in the CERES experiment.[63]

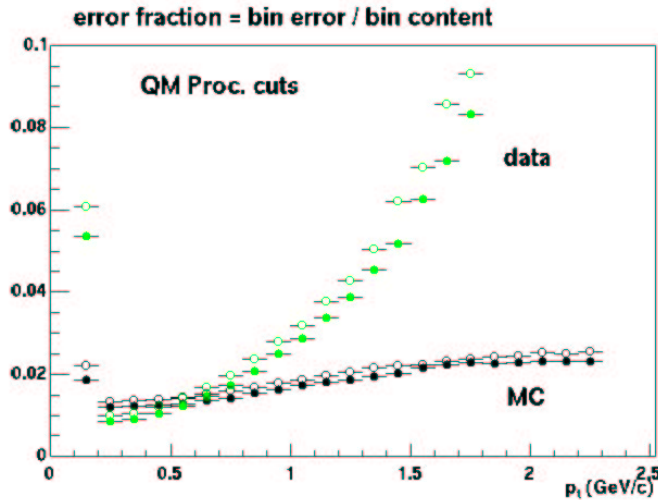


Figure 5.17: Relative error comparison of Monte Carlo and raw data for π^+ (solid) and π^- (open). The relative error in the data dominates above 1 GeV/c and is comparable to the simulation at low p_t .

5.2.2 Corrections

The corrections are determined using the Perfect Tracker and the Evaluator tools [64]. The Perfect Tracker reproduces the original generated track without the pattern recognition step². The momentum as given by EXODUS is assigned to the track. The Evaluator uses a dominant contributor method to associate a perfect track to a track that is reconstructed using the same pattern recognition step as used in the data (called a reconstructed track for brevity). The dominant contributor of a reconstructed track is defined as the Monte Carlo particle which contributes more hits to the track than any other Monte Carlo particle. In order to evaluate the tracking performance, the following information is used:

- The number of X and UV hits contributed to the reconstructed track.
- The total number of Monte Carlo contributors.
- The calculated differences between the Monte Carlo contributor and reconstructed tracking parameters. These include α , ϕ , β , and z .

²The pattern recognition uses a Combinatorial Hough Transform to determine ϕ and α as described in Chapter 3.

- The calculated differences between the Monte Carlo contributor and reconstructed momentum as determined by the track model. These include ϕ_0 , θ_0 , and momentum.
- If no Monte Carlo contributor is found for a given reconstructed track, the tracking parameters that characterize this contributor can be used to evaluate why.

This information is all that is required in order to study both the geometrical acceptance and the track reconstruction efficiency in the drift chambers. Evaluations that go beyond tracking in the drift chambers include the efficiency in projecting and matching tracks to the outer detector hits. The Evaluator also contains all the relevant information concerning the track's positions in the Pad Chambers, RICH, and EMCAL detectors:

- The projected points to PC1/3, TOF and EmCal as determined by the track model.
- The coordinates of reconstructed hits or clusters that are associated to the track by the hit association algorithm in the PC1/3, TOF, and EMCAL. Other quantities include the time and energy loss in the TOF.
- The original Monte Carlo particles that produced the associated hits in the other detectors. All the relevant GEANT information that describes the particle is recorded for each detector. In the TOF, this includes the GEANT time and hit position. Both the identity and the history of the particle are recorded (for instance, if the particle is a primary from the event vertex or decay secondary).
- The hits or clusters in the other detectors that are not associated to the reconstructed track but are identified as coming from the main contributor of the track.
- If a RICH ring and its relevant information matches the reconstructed track.

With this information, it is possible to duplicate the tracking, matching, and acceptance for different types of analyses as is done in the raw data reduction.

Particles can be accepted and/or reconstructed as according to the following criteria. A particle is accepted in the drift chambers if: (1) a perfect track exists for this particle (at least one GEANT hit is found in the drift chambers); and (2) this particle is a primary particle from the event vertex (not a secondary from decay). For example, a primary particle which decays

before it reaches the drift chambers is not counted as an accepted particle. The particle is reconstructed in the drift chambers if it falls within the 2σ matching, energy-loss, and fiducial cuts (as is done in the data). The simulated particle identification is made using the Monte Carlo contributor particle identity and by requiring the reconstructed momentum to be within 5σ of the expected momentum resolution of the drift chambers.

The simulated distributions are generated uniformly in p_t , ϕ , and y . The maximum value in p_t is 5.0 GeV/c. In rapidity, the coverage is 1.2 units. All particles subtend 160 degrees in azimuth. The distribution of the number of particles generated in each p_t slice, dN/dp_t is called the input distribution. This is the distribution before the detector response and track reconstruction. The input dN/dp_t distribution for each particle is normalized to 2π and 1 unit of rapidity by multiplying each dN/dp_t value by the factor $360/160 \cdot 1/1.2$. After the detector response, the reconstructed track distribution in the number of particles generated in each p_t , dN/dp_t is called the output distribution. The phase-space coverage (y versus p_t) for both input (top) and output (bottom) distributions is shown in Figure 5.18. The three panels in the figure correspond to the phase space distributions of the single particle protons for three types of distributions: (1) the top panel is the input distribution from EXODUS, (2) the middle panel is the distribution of accepted protons in the drift chambers, and (3) the bottom panel is the distribution of reconstructed tracks. The top panel corresponds to a detector which covers 2π in azimuth and 180 degrees in polar angle. Since the drift chambers subtend 90 degrees in azimuth and between 70 and 110 degrees in polar angle, the rapidity acceptance decreases with decreasing momentum (middle panel). The acceptance is smaller still for reconstructed tracks (bottom) based on the track quality requirement (refer to Chapter 3).

The final corrections are determined after an iterative weighting procedure [66]. In order to do this last step, the EXODUS weighting function used to generate the input particle distributions must be divided out in order to create flat distributions in p_t for both the input and output distributions. First, the flat input and output distributions are weighted by exponential functions for all particles using an inverse slope of 300 MeV. The iterative procedure is then as follows:

1. Once the dN/dp_t distributions are obtained determine the ratio of input to output as a function of momentum and bin correct the raw data.
2. The corrected data are fitted with exponentials for kaons and protons, and a power-law for the pions.

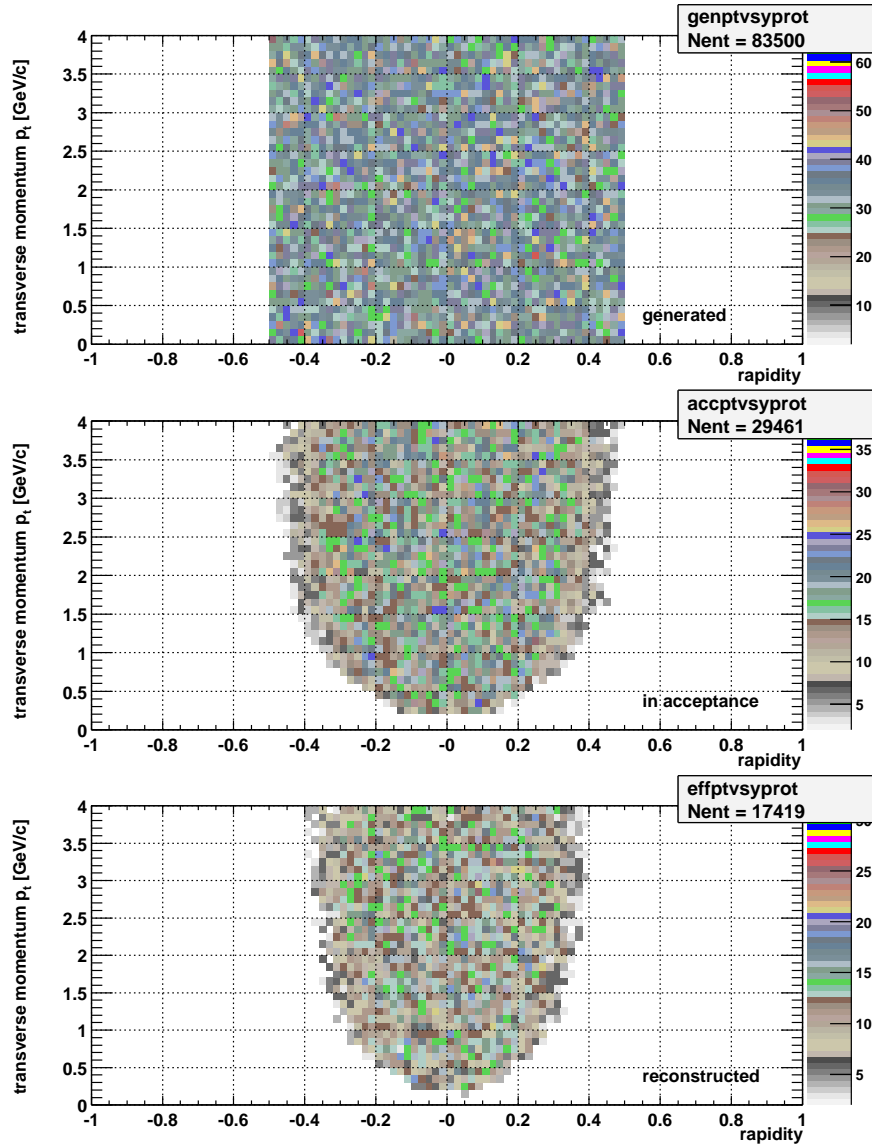


Figure 5.18: The phase space coverage for the single protons. The vertical axis is p_t and the horizontal is y . The top panel are the EXODUS input particles, the middle are the protons in the drift chamber acceptance, and the bottom are the protons reconstructed with x , y , and z information in coordinate space. [53]

3. The original flat input and output distributions are weighted by exponential functions for kaons and protons, and a power-law for the pions.
4. Repeat until the functions remain constant in their parameters.

The final weighting function for kaons and nucleons is:

$$dN/dp_t \approx p_t \cdot e^{B \cdot p_t} \quad (5.5)$$

where $B = -2.95098 \text{ c/GeV}$ for protons and -3.03047 for \bar{p} ; -3.54952 for K^+ and -3.8674 for K^- . The final power-law function used to weight both the positive and negative pion dN/dp_t input and output distributions is:

$$dN/dp_t \approx p_t \cdot \left(\frac{p_0}{p_0 + p_t} \right)^n \quad (5.6)$$

where $p_0 = 1.41891 \text{ GeV/c}$ and $n = 10.9563$. The single pion, kaon, and proton dN/dp_t input and output distributions after the iterative weighting procedure are shown in Figure 5.19. The top three curves in each panel are the input dN/dp_t distributions and the bottom three curves are the reconstructed output dN/dp_t distributions. The left panel corresponds to positive particles while the right negative. Due to the small TOF acceptance and the DC dead regions, there is an asymmetry in the number of positive and negative particles. There is a smaller yield of negative particles relative to positive; hence, the corrections are larger for negative. The input and output distributions of each particle are divided to produce acceptance correction factors. Where the corrections vary rapidly with p_t after low momenta in Figure 5.20 corresponds to the geometrical acceptance of the detector for each particle species.

The corrections are systematically larger for the negative particles than for the positive particles because of the different acceptance for each charge. The corrections are larger for kaons due to the decays in flight.

The correction values are tabulated in Tables 5.4 - 5.6 for pions through protons respectively. The binning in p_t corresponds to the minimum bias binning in the raw data.

The raw spectra are corrected bin by bin in p_t by the corresponding factor. The statistical error in determination of the correction factor is added in quadrature to the statistical error in the data.

5.3 High Track-Density Efficiency Correction

In this section, the overall track reconstruction efficiency as a function of centrality is determined for particles identified using the TOF detector.

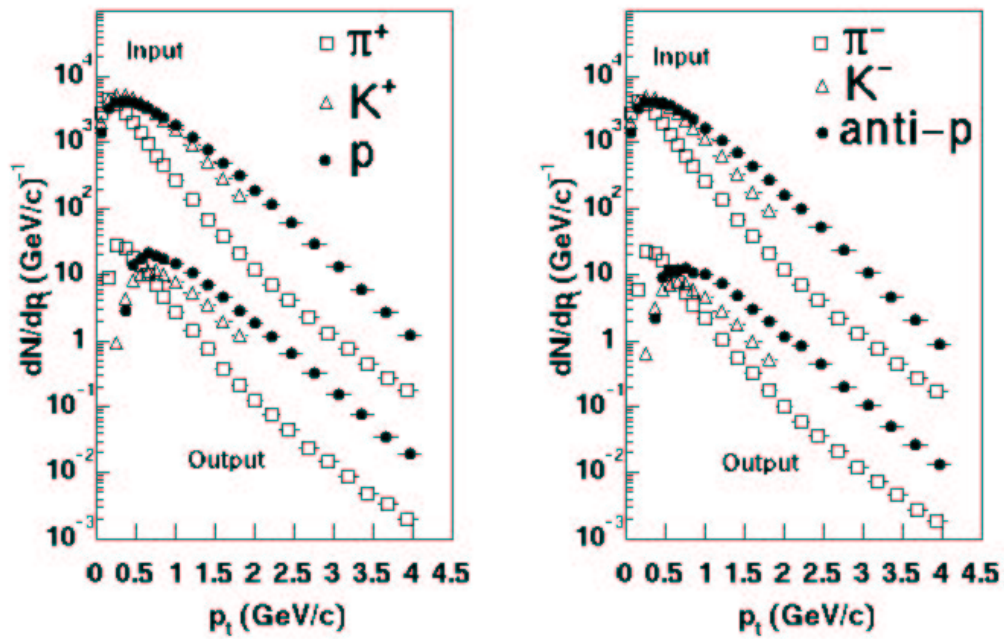


Figure 5.19: The pion, kaon, and proton dN/dp_t input (top three curves in each panel as labeled) and output (bottom three curves in each panel as labeled) distributions for positive (left panel) and negative (right panel) single particle Monte Carlo.

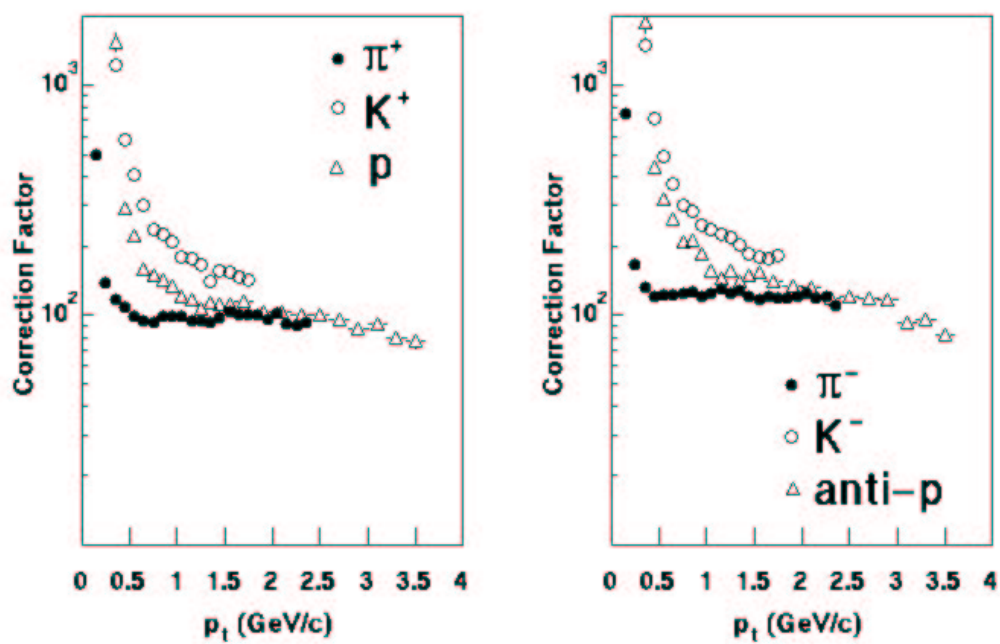


Figure 5.20: Corrections for positive (left) and negative (right) particles using single particle Monte Carlo.

p_t (GeV/c)	π^+	π^-
0.15	496 ± 13	754 ± 24
0.25	137 ± 2	166 ± 3
0.35	116 ± 2	132 ± 2
0.45	108 ± 2	121 ± 2
0.55	99 ± 2	121 ± 2
0.65	94 ± 2	121 ± 2
0.75	93 ± 2	123 ± 3
0.85	98 ± 2	125 ± 3
0.95	98 ± 2	121 ± 3
1.05	99 ± 2	125 ± 3
1.15	94 ± 2	129 ± 4
1.25	94 ± 2	124 ± 3
1.35	93 ± 2	127 ± 4
1.45	96 ± 3	119 ± 4
1.55	104 ± 3	116 ± 4
1.65	100 ± 3	121 ± 4
1.75	100 ± 3	118 ± 4
1.85	100 ± 3	118 ± 4
1.95	96 ± 3	121 ± 4
2.05	101 ± 3	124 ± 5
2.15	92 ± 3	118 ± 4
2.25	89 ± 3	119 ± 5
2.35	93 ± 3	110 ± 4

Table 5.4: Pion correction factors from single particle Monte Carlo.

p_t (GeV/c)	K^+	K^-
0.25	5902 ± 769	7866 ± 1173
0.35	1232 ± 77	1499 ± 104
0.45	576 ± 27	718 ± 37
0.55	406 ± 17	488 ± 23
0.65	300 ± 12	370 ± 16
0.75	236 ± 9	300 ± 13
0.85	223 ± 9	283 ± 12
0.95	209 ± 8	245 ± 11
1.05	179 ± 7	237 ± 11
1.15	174 ± 7	223 ± 10
1.25	166 ± 7	219 ± 11
1.35	140 ± 6	200 ± 10
1.45	155 ± 7	183 ± 9
1.55	154 ± 7	178 ± 9
1.65	146 ± 7	175 ± 9
1.75	141 ± 7	181 ± 10

Table 5.5: Kaon correction factors from single particle Monte Carlo.

p_t (GeV/c)	p	\bar{p}
0.35	1543 ± 138	1880 ± 184
0.45	289 ± 12	441 ± 22
0.55	220 ± 8	317 ± 15
0.65	157 ± 6	259 ± 12
0.75	149 ± 5	208 ± 9
0.85	142 ± 5	210 ± 10
0.95	133 ± 5	184 ± 9
1.05	120 ± 5	155 ± 7
1.15	116 ± 5	145 ± 7
1.25	106 ± 4	156 ± 8
1.35	112 ± 5	140 ± 7
1.45	112 ± 5	148 ± 8
1.55	111 ± 5	153 ± 8
1.70	115 ± 4	141 ± 6
1.90	103 ± 4	134 ± 6
2.10	103 ± 4	131 ± 6
2.30	99 ± 4	118 ± 5
2.50	100 ± 4	121 ± 6
2.70	96 ± 4	118 ± 6
2.90	87 ± 4	116 ± 6
3.10	91 ± 5	92 ± 5
3.30	80 ± 4	95 ± 6
3.50	77 ± 5	82 ± 5

Table 5.6: Proton and anti-proton correction factors from single particle Monte Carlo.

Both the track reconstruction efficiency in the drift chamber and the mis-reconstruction of particle mass for slow particles in the TOF are determined. Due to a mismatch in the UV wire efficiency between the simulated and real response, an additional correction is applied to the efficiency correction for the most central events.

5.3.1 Drift Chamber Efficiency

The main loss of tracks is when the drift chamber cannot reconstruct the tracks in high multiplicity events. The tracking efficiency decreases as the track density increases. Tracks are mis-reconstructed when hits are incorrectly associated.

Mis-reconstruction occurs when the two-track spacing in the drift chamber is smaller than the combinatorial hough space grid in ϕ and α , or when there is more than one PC1 point possible. In the first case, the direction vector in the azimuth prevents the track from pointing properly to the PC1 detector and the correct hit cannot be associated. In the second case, the track is reconstructed properly in ϕ and α , but there are two possible PC1 points. If no UV hits are found, then the wrong PC1 point can be associated to the track and the track's z coordinate is mis-reconstructed. In both of these cases, the track falls outside the 2σ matching cut to the TOF detector and is lost.

The efficiency of the drift chamber UV-wires is better in the simulated response than in the real response. A correction factor that matches the UV efficiency in both simulation and data is applied. Two factors are calculated. One is the efficiency of the UV wires as a function of centrality and the other is the probability for a track to have more than one PC1 point. For the most central events, the resulting correction is 6%.

5.3.2 Time-of-Flight Efficiency

In high track density events, even within a 2σ matching cut, tracks may point to more than one slat in the TOF, or in a small fraction of cases when two particles hit the same TOF slat at different times. The measured time for these tracks may be wrong and the mass can be mis-reconstructed.

The slower particle gets the faster particle's time. Since the pathlength is unaffected, the speed for the particle increases. Since the momentum from the drift chamber is unaffected, the mass decreases.

In some cases, this incorrectly measured mass will fall outside the particle identification cuts (the resulting measured energy loss is higher and is therefore included in the energy loss cut). As an example, the simulated

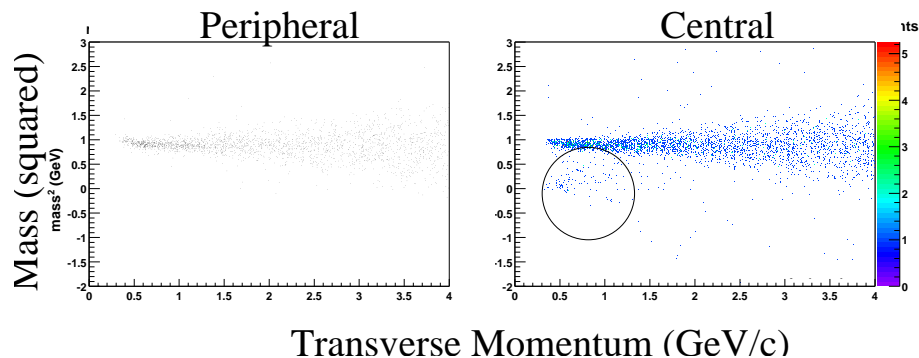


Figure 5.21: The resulting mass-squared distribution of anti-protons reconstructed after embedding into peripheral events (left) and central events (right), before the 2σ particle identification cut. The circle shows the region where particles have the wrong mass reconstructed in the higher track density environment. [57]

mass-squared distribution of anti-protons that are reconstructed in two different track-density environments, peripheral and central, are shown in Figure 5.21. In this figure, the 2σ particle identification cut was not applied. The circle in the right panel shows the region where the mass is mis-reconstructed due to the higher-track density environment in the TOF.

5.3.3 Efficiency Correction

In order to correct for such inefficiencies, it is necessary to quantify the fraction of tracks that are lost by both the matching and particle identification cuts for all types of events, from the most peripheral to the most central. The efficiency correction is determined using a technique that uses single particles from Monte Carlo simulation embedded into real events [65]. For each simulated particle, its simulated hit from the detector response is merged with the raw detector hits in the data. The data simulate the variation in track density and serve as background for the simulated particles. To determine the efficiency correction, simulated π^- and \bar{p} are merged into the data before track reconstruction. Since the kaons, being heavier than the pions, suffer from a similar mass inefficiency as the anti-protons, the correction obtained for anti-protons is used to correct the kaons. Two distributions are produced for each particle. Each distribution is the number of particles that successfully meet

the following criteria for each type of event:

- The particle is a primary, or first generation particle and not a secondary from decay.
- Both the particle's direction vector in all three coordinates and momentum are reconstructed properly in the drift chamber.
- The particle is within the 2σ matching and acceptance cuts in the TOF detector.
- The particle deposits an energy in the TOF higher than the mip energy. This is the same β -dependent energy loss cut that is made in the data.
- The particle is accepted in a 2σ particle identification cut in the m^2 vs p space.

The input distribution is simply the number of simulated particles that are reconstructed without any background and pass these criteria. After these particles are embedded into the data, the track reconstruction produces an output distribution. This output distribution is the number of particles that pass these criteria in each centrality selection, using the BBC and ZDC measured centrality. For each centrality selection, the reconstruction efficiency is determined by calculating the ratio of output and input distributions.

The correction factor for each reconstructed particle in the raw transverse momentum distribution is applied as a weight and depends on the type of particle (pion, kaons, or proton), the track quality (fully or partially reconstructed), and the event centrality. The final efficiency corrections are shown in Figure 5.22. The centrality is expressed in increments of 5% in bin number. The most central and peripheral bins are labeled accordingly. The fully (X1&X2) and partially (X1||X2) reconstructed track corrections are different.

The systematic uncertainty in the TOF multiplicity efficiency correction is determined by varying the size of the particle identification cut and studying the change in the efficiency correction. The overall systematic uncertainty is 9% in applying the multiplicity efficiency correction.

5.4 Systematic Uncertainties from the Corrections

The systematic uncertainties from the single particle Monte Carlo corrections include the fiducial cuts, the single particle corrections, and the multiplicity efficiency correction. The residual uncertainties on the multiplicity

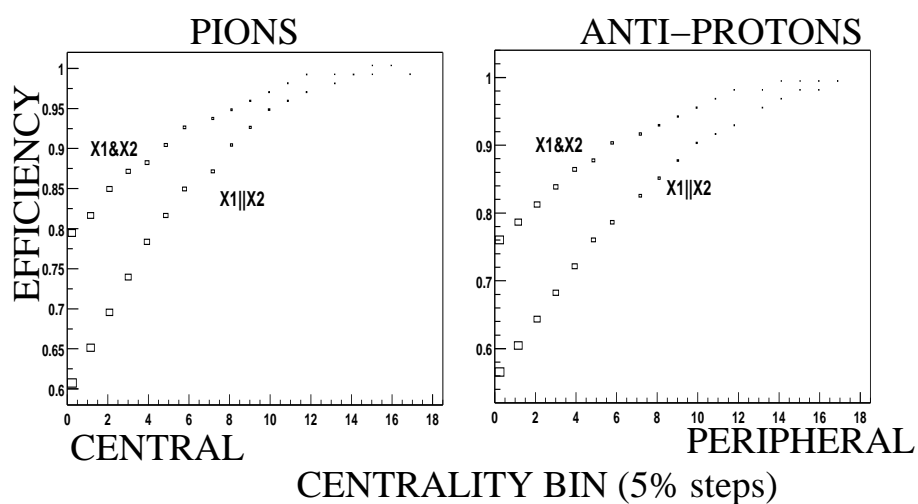


Figure 5.22: Final efficiency correction as a function of centrality for pions (left) and anti-protons (right). The centrality is expressed in increments of 5% in bin number. The most central and peripheral bins are labeled accordingly. The fully (X1&X2) and partially (X1||X2) reconstructed track corrections are different and labeled accordingly. [57]

dependence of the efficiency corrections is 9%. The statistical errors on the Monte Carlo corrections are less than the statistical error of the raw data and are added in quadrature. The systematic uncertainty in the spectra from the PHENIX acceptance is 5%.

5.5 The Identified Particle Spectra

The single particle corrections are applied to the raw spectra. The p_t binning is the same for both the single particle corrections and the raw data. The final distributions are scaled by p_t ; divided by the number of events for the corresponding centrality selection; normalized to the area of a full Gaussian distribution as the 2σ particle identification is applied in the data (a factor of 1.0455); the bin width in p_t with a factor of $1/(0.100 \text{ GeV}/c)$; and then normalized to 2π with the factor $1/2\pi$. What results are fully normalized spectra.

The fully normalized minimum bias identified spectra are shown in Figure 5.23 and the fully normalized centrality selected are shown in Figures 5.24-5.26. The spectra are tabulated in Appendix A.

5.5.1 Systematic Uncertainties in the Spectra

The systematic uncertainty in the spectra is the combined systematic uncertainty from the data reduction and the corrections. The multiplicity efficiency correction and the particle identification uncertainties, result in 11% for all particles. The random background contribution, results in 2% for pions, 5% for kaons, and 3% for protons, respectively [57]. The uncertainty from the single particle corrections is added in quadrature to the statistical error in the raw spectra. The systematic uncertainty is therefore 11% for pions, 12% for kaons, and 11% for protons.

5.5.2 Truncated Mean Transverse Momentum and Yield

The truncated mean transverse momentum $\langle p_t \rangle$ and data yield dN/dy are determined in the measured p_t range. The errors are the statistical errors from the spectra alone (with the single particle correction errors added in quadrature).

The pions have a measured $\langle p_t \rangle$ that decreases from 0.5 to 0.45 from the most central to the most peripheral events. The measured yields decrease

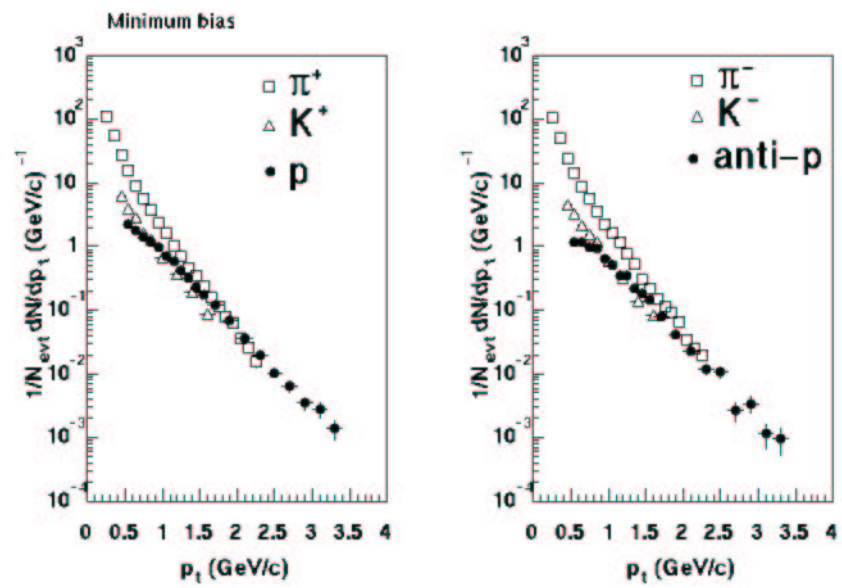


Figure 5.23: The spectra of positive particles (left) and negative (right) in minimum bias events at 130 GeV.

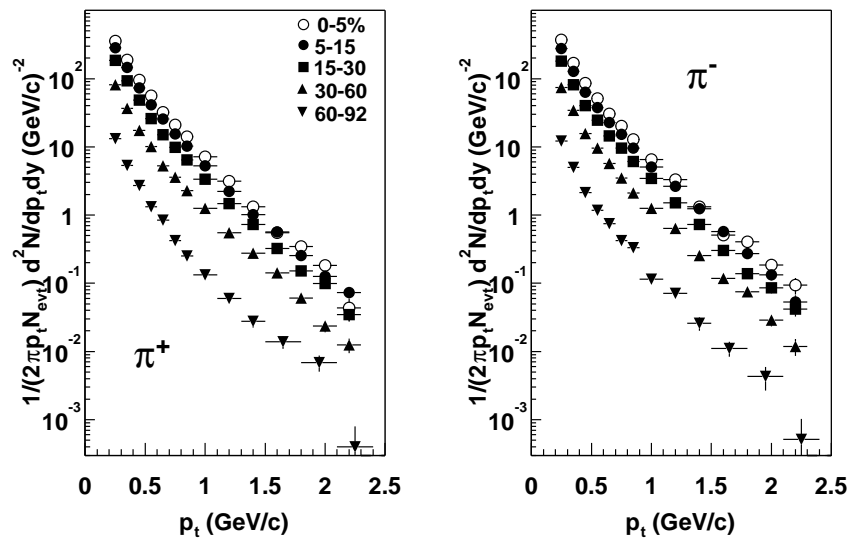


Figure 5.24: The spectra of π^+ (left) and π^- (right) for five centralities from the most central 0-5% to the most peripheral 60-92% at 130 GeV.

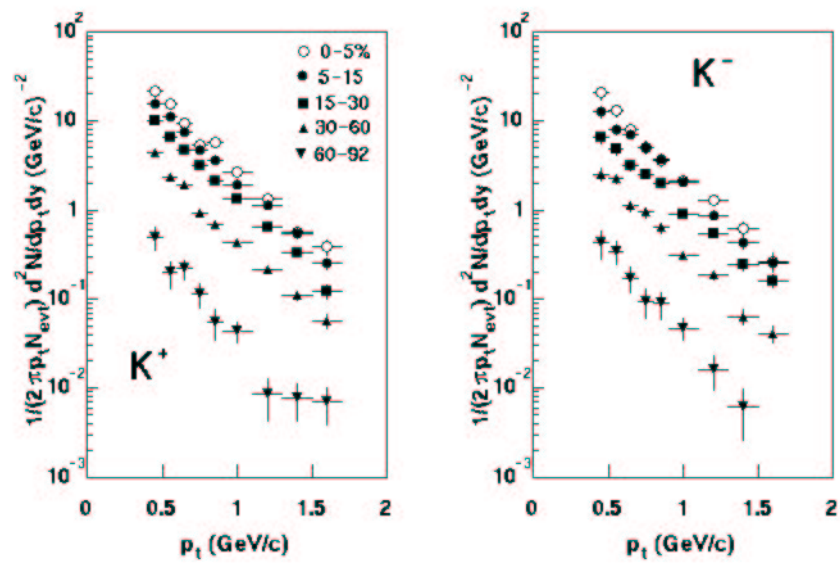


Figure 5.25: The spectra of K^+ (left) and K^- (right) for five centralities from the most central 0-5% to the most peripheral 60-92% at 130 GeV.

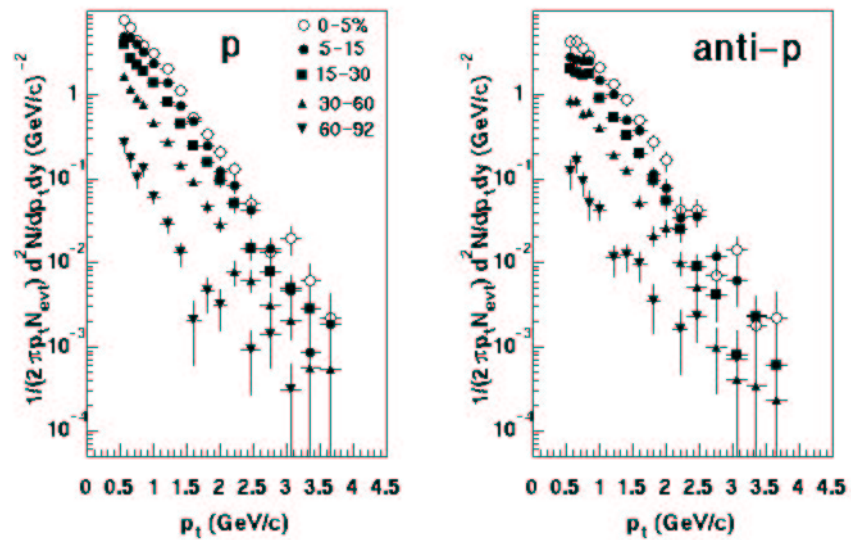


Figure 5.26: The spectra of p (left) and \bar{p} (right) for five centralities from the most central 0-5% to the most peripheral 60-92% at 130 GeV.

Centrality (%)	p_t (GeV/c)	$\langle p_t \rangle$ (GeV/c)	dN/dy
0-5	0.25-2.2	0.498 ± 0.006	193 ± 2
5-15	0.25-2.2	0.494 ± 0.005	149 ± 1
15-30	0.25-2.2	0.491 ± 0.005	95.7 ± 0.9
30-60	0.25-2.2	0.477 ± 0.005	37.7 ± 0.4
60-92	0.25-2.2	0.45 ± 0.01	5.5 ± 0.1

Table 5.7: The $\langle p_t \rangle$ and yield as measured from the data for positive pions. The measured ranges in p_t are indicated.

Centrality (%)	p_t (GeV/c)	$\langle p_t \rangle$ (GeV/c)	dN/dy
0-5	0.25-2.2	0.496 ± 0.007	184 ± 2
5-15	0.25-2.2	0.503 ± 0.006	139 ± 2
15-30	0.25-2.2	0.497 ± 0.006	89 ± 1
30-60	0.25-2.2	0.488 ± 0.006	35.4 ± 0.4
60-92	0.25-2.2	0.45 ± 0.01	5.0 ± 0.1

Table 5.8: The $\langle p_t \rangle$ and yield as measured from the data for negative pions. The measured ranges in p_t are indicated.

from almost 200 to 5 pions from the most central to the most peripheral events.

The kaons have measured $\langle p_t \rangle$ that are almost constant as a function of centrality (within errors). The measured yields decrease by 98% from 25 – 30 to less than 1 from the most central to the most peripheral events.

The protons have a measured $\langle p_t \rangle$ that decreases by 12% from 1.07 ± 0.04 to 0.94 ± 0.08 from the most central to the most peripheral. The measured yields decrease by 98% from 21.6 to 0.46 from the most central to the most peripheral events.

In the next chapter, functions are fit to the spectra to extract the relevant physics quantities. Functions that extrapolate the spectra at low p_t are used to determine the total particle yield and $\langle p_t \rangle$, not just the truncated mean and yield over the measured range as is presented here. Another function based on hydrodynamics assumptions is fit simultaneously to the spectra and the expansion parameters are extracted.

Centrality (%)	p_t (GeV/c)	$\langle p_t \rangle$ (GeV/c)	dN/dy
0-5	0.45-1.6	0.75 ± 0.03	28 ± 1
5-15	0.45-1.6	0.76 ± 0.03	21.1 ± 0.8
15-30	0.45-1.6	0.75 ± 0.03	13.1 ± 0.5
30-60	0.45-1.6	0.73 ± 0.03	4.8 ± 0.2
60-92	0.45-1.6	0.70 ± 0.08	0.48 ± 0.06

Table 5.9: The $\langle p_t \rangle$ and yield as measured from the data for positive kaons. The measured ranges in p_t are indicated.

Centrality (%)	p_t (GeV/c)	$\langle p_t \rangle$ (GeV/c)	dN/dy
0-5	0.45-1.6	0.74 ± 0.04	24 ± 1
5-15	0.45-1.6	0.77 ± 0.03	18.7 ± 0.8
15-30	0.45-1.6	0.78 ± 0.03	9.7 ± 0.5
30-60	0.45-1.6	0.74 ± 0.04	3.6 ± 0.2
60-92	0.45-1.4	0.69 ± 0.08	0.50 ± 0.06

Table 5.10: The $\langle p_t \rangle$ and yield as measured from the data for negative kaons. The measured ranges in p_t are indicated.

Centrality (%)	Measured p_t (GeV/c)	$\langle p_t \rangle$ (GeV/c)	dN/dy
0-5	0.55-3.65	1.07 ± 0.04	21.6 ± 0.7
5-15	0.55-3.65	1.06 ± 0.03	16.0 ± 0.5
15-30	0.55-3.35	1.04 ± 0.03	9.7 ± 0.3
30-60	0.55-3.65	1.00 ± 0.03	3.6 ± 0.1
60-92	0.55-3.05	0.94 ± 0.08	0.46 ± 0.04

Table 5.11: The $\langle p_t \rangle$ and yield as measured from the data for protons. The measured ranges in p_t are indicated.

Centrality (%)	Measured p_t Range (GeV/c)	$\langle p_t \rangle$ (GeV/c)	dN/dy
0-5	0.55-3.65	1.09 ± 0.05	15.1 ± 0.7
5-15	0.55-3.35	1.08 ± 0.04	10.4 ± 0.4
15-30	0.55-3.65	1.04 ± 0.04	6.7 ± 0.3
30-60	0.55-3.65	1.01 ± 0.04	2.6 ± 0.1
60-92	0.55-3.05	1.0 ± 0.1	0.32 ± 0.04

Table 5.12: The $\langle p_t \rangle$ and yield as measured from the data for anti-protons. The measured ranges in p_t are indicated.

Chapter 6

Results

In this chapter, the physics results of fully normalized and corrected identified hadron spectra produced in $\sqrt{s_{NN}} = 130$ GeV are presented for centrally selected events. For the most central, mid-central, and the most peripheral events, the invariant cross section of pions, kaons, and (anti)protons are shown. We observe a new feature in the spectra: the crossing of the nucleon spectra over the pion spectra that appears to be dependent on the number of participants. The shape, normalization, particle dependence, and centrality dependence of the spectra are sensitive to the collision dynamics. A possible explanation for this crossing is discussed in Chapter 7.

The shape of the spectra is sensitive to the radial expansion generated in the collisions. Using an empirical expression used previously at CERN-SPS energies in Reference [99], the freeze-out temperature T_{fo} and radial expansion velocity $\langle \beta_t \rangle$ are determined. As this expression is non-relativistic, the pions should be excluded from the fit; however, this would result in zero degrees of freedom. In order to improve upon simple analyses, and to better constrain the parameters from the dynamics, a hydrodynamics-based parameterization is fit to all particle spectra simultaneously. The parameters extracted from the fit are quantitative measures of the expansion duration and size. It is assumed that

- all particles decouple kinematically on the freeze-out hypersurface at the same freeze-out temperature T_{fo} ,
- the particles collectively expand with a velocity profile that is linear with the radial position,
- the average radial flow velocity $\langle \beta_t \rangle$ is the geometrical average and is equal to $2/3$ the maximum velocity β_t , and
- the particle density distribution is independent of the radial position.

Boost invariance is also assumed as discussed in more detail in Chapter 1 where the functional form is derived.

For all centralities, the yield dN/dy and $\langle p_t \rangle$ for each particle are determined by integrating the measurement and extrapolating fitted functions to low and high p_t where there is no measurement. The extrapolated integrals are added to the measured quantities from the data (as presented in Chapter 5). The overall systematic uncertainties in the measured quantities include the uncertainties inherent in extrapolations, the background contribution as described in Chapter 4, and the point-to-point systematic uncertainty in the spectra.

The particle ratios reflect the hadron chemistry, and are presented as a function of participant number. Ultimately, the particle ratios are also used to tune chemical models that extract the chemical freeze-out temperature (when the particle production stops) and baryon chemical potential. The p/\bar{p} ratio is used to tune hydrodynamic models with a specified equation of state and initial conditions to extract the initial energy density and maximum kinetic temperature. The measured total multiplicity dN/dy as a function of both the number of participants and the number of collisions are used to tune hydrodynamic models. From the measured total particle yields, the initial energy densities $\langle \epsilon_0 \rangle$ for all centralities are determined assuming a formation time of 1 fm/c and using Bjorken's formula as derived in Chapter 1.

At low p_t , the spectra are dominated by late-collision dynamics which include soft collective effects (radial flow) and resonances. High p_t spectra are sensitive to the parton dynamics generated in the early part of the collision (hard or semi-hard processes). Based on the analysis and results presented here, which is predominantly in the soft process regime, Chapter 7 includes a discussion of the transition region between hard and soft physics.

6.1 Particle Spectra

The transverse momentum spectra of pions, kaons, (anti)protons for the most central (top), mid-central (center), and most peripheral (bottom) are shown in Figure 6.1. The nucleon spectra cross the pion spectra at smaller p_t for more central collisions. The dominant contribution of protons relative to the pions in the more central collisions can indicate radial flow and is discussed in Chapter 7.

The particle source expands longitudinally close to the velocity of light, so we use cylindrical symmetry. In this cylindrical symmetry, the longitudinal

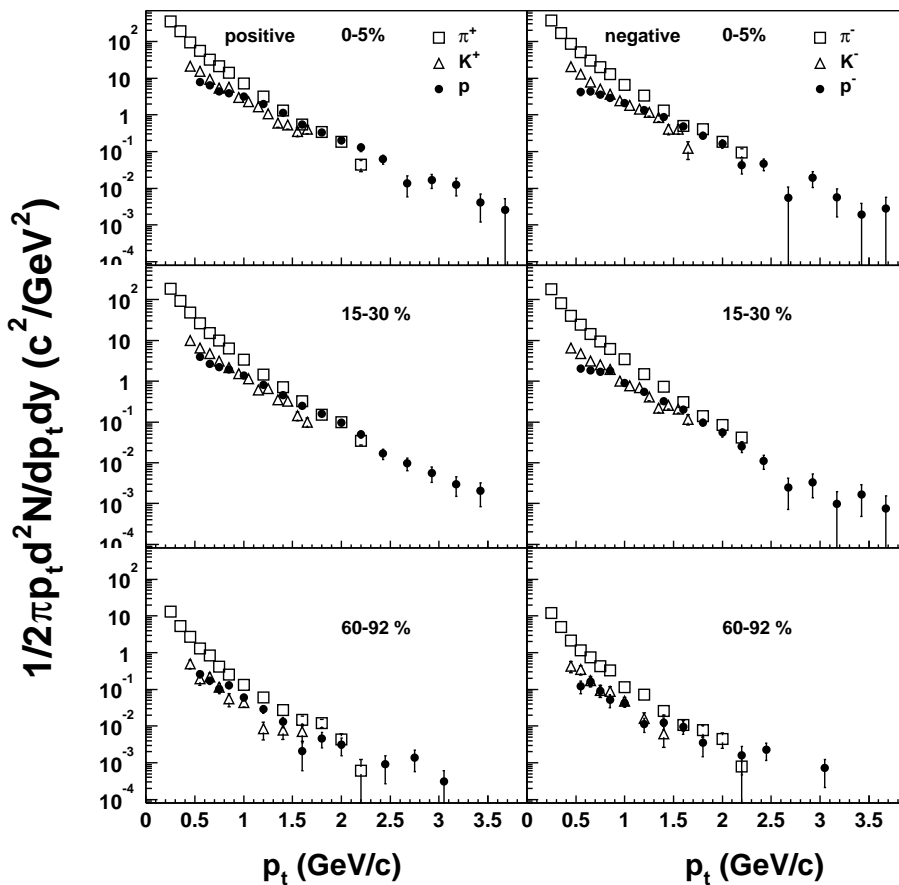


Figure 6.1: The transverse momentum spectra of pions, kaons, protons and antiprotons for the most central (top), mid-central (center), and most peripheral (bottom) collisions. In both the positive particles (left) and negative particles (right) the crossing point of nucleons and pions decreases with increasing impact parameter [68].

motion is aligned with the cylinder axis and the transverse motion is the cylinder circle. In Reference [69], it was pointed out that the longitudinal flow can be measured from the data. The particles experience a longitudinal boost, and a radial boost (or flow) is also predicted. The shape of the transverse momentum spectra is sensitive to the radial expansion. As is observed at CERN SPS energies (Ref. [69]), a static thermal source does not describe the measured rapidity distribution, which is determined by the longitudinal motion generated in the collision. A boosted thermal source describes both the rapidity distribution and the transverse momentum spectra, a strong indication that radial flow exists.

Based on the idea of a hydrodynamically behaving boosted source, a parameterization is fitted simultaneously to all the particle spectra to determine the magnitude of the radial flow, as a function of collision centrality. The particles are assumed to decouple from the expanding source at the same temperature, called the freeze-out temperature T_{fo} . The freeze-out temperature is the point in the expansion when the particles decouple from the system and are no longer interacting. This occurs when the mean free path of the particles is comparable to the source size at freeze-out¹. The radial flow velocity is the collective boost in the transverse direction. As a comparison, a full hydrodynamical model calculation is also compared to both the data and the parameterization.

This section is organized as follows:

- Static Thermal Source;
- Boosted Thermal Source; and
- β_t and T_{fo} from the data.

6.1.1 Static Thermal Source

On the freeze-out surface the entropy density is constant but the number density is changing. The chemical potential μ is by definition the change in the internal energy per mole of substance added (or removed) from a system at constant entropy and volume²[70]. If the particles are emitted from a static source of volume dV with temperature T such that $T \gg \mu - E$, then

¹The source radius at freeze-out is $\geq 6-7$ fm from HBT measurements[12, 11]

²The chemical potential μ includes the baryon (B) and strangeness (S) potentials μ_B and μ_S .

the Fermi-Dirac or Bose-Einstein distributions approach a Maxwell-Boltzmann distribution³. The volume in phase-space is

$$gd\Sigma = gdp^3d^3\sigma/(2\pi)^3 = gdp^3dV/(2\pi)^3 \quad (6.1)$$

where the surface is fixed in time. The number of particles d^3N per unit of phase space follows the Maxwell-Boltzmann distribution

$$\frac{d^3N}{gd\Sigma} = e^{(\mu-E)/T} \quad (6.2)$$

and the resulting invariant momentum distribution is

$$E \frac{d^3N}{dp^3} = \frac{gdV}{(2\pi)^3} E e^{(\mu-E)/T} \quad (6.3)$$

As shown in Chapter 1, the invariant momentum distribution can also be written in terms of transverse energy and rapidity as

$$E \frac{d^3N}{dp^3} = \frac{d^3N}{m_t dm_t d\phi dy} \quad (6.4)$$

After assuming azimuthal symmetry and integrating from 0 to 2π in ϕ with $dV = r dr d\phi dy = 2\pi r dr dy$) the double differential spectrum becomes

$$\frac{d^2N}{m_t dm_t dy} = \frac{gr dr dy}{(2\pi)^2} E e^{(\mu-E)/T} \quad (6.5)$$

Using $E = m_t \cosh(y)$ as defined in Chapter 1 results in

$$\frac{d^2N}{m_t dm_t dy} = \frac{gr dr dy}{(2\pi)^2} m_t \cosh(y) e^{(\mu - m_t \cosh(y))/T} \quad (6.6)$$

The integrand $\cosh y e^{-m_t \cosh y/T}$ vanishes for $|y| > 2$. Therefore, the integration over rapidity is generally taken to be from $-\infty$ to $+\infty$ using the modified K_1 Bessel function:

$$K_1(m_t/T) = \int \cosh(y) e^{-m_t \cosh(y)/T} dy \quad (6.7)$$

The single differential is therefore

$$\frac{dN}{m_t dm_t} = \frac{gr dr}{(2\pi)^2} e^{\mu/T} m_t K_1(m_t/T) \quad (6.8)$$

³Indistinguishable particles with degeneracy factor g are assumed for a single particle spectrum[71]. The units used are $c = k = \hbar = 1$.

The source is static so the momentum distribution is independent of the source radius. After integrating over the source radius R , and grouping the μ exponential with the other constants results in a value that affects the normalization of the distribution:

$$A = \int_0^R \frac{r dr}{(2\pi)^2} e^{\mu/T} = \frac{R^2}{8\pi^2} e^{\mu/T} \quad (6.9)$$

since it is independent of m_t . This constant is related to the number of particles produced in the source with radius R at chemical freeze-out when the particle production stops.

Since the energy of the particles is much greater than the source temperature, the Bessel function K_1 can be approximated as:

$$K_1(m_t/T) \approx \sqrt{\frac{\pi T}{2m_t}} e^{-m_t/T} \quad (6.10)$$

and the single differential spectrum becomes

$$\frac{dN}{m_t dm_t} = A \sqrt{m_t} e^{-m_t/T}, \quad (6.11)$$

The Equation 6.11 is called a Boltzmann distribution for the duration of this analysis. Because $m_t \gg T$, this distribution can also be approximated as an exponential in m_t in Equation 6.12

$$\frac{dN}{m_t dm_t} = A e^{-m_t/T} \quad (6.12)$$

as used in an equivalent analysis in Reference [99]⁴. The limit $m_t > T$ is true for all the measured data points so this approximation holds.

It is simple to produce the transverse kinetic energy distributions from the transverse momentum distributions since the particle mass for each hadron is known. From these distributions, effective temperatures can be extracted after fitting a thermal functional form to each particle species separately.

The transverse energy spectrum is determined by calculating the transverse mass in Equation 1.2.2 as defined in Chapter 1 for each particle with mass m_0 for each measured p_t in the spectrum. What immediately follows after taking the derivative of Equation 1.2.2 with respect to p_t is Equation 6.1.1

$$\frac{dN}{p_t dp_t} = \frac{dN}{m_t dm_t} \quad (6.13)$$

⁴In the yields analysis in the next section, both Equation 6.11 and Equation 6.12 are within 2%.

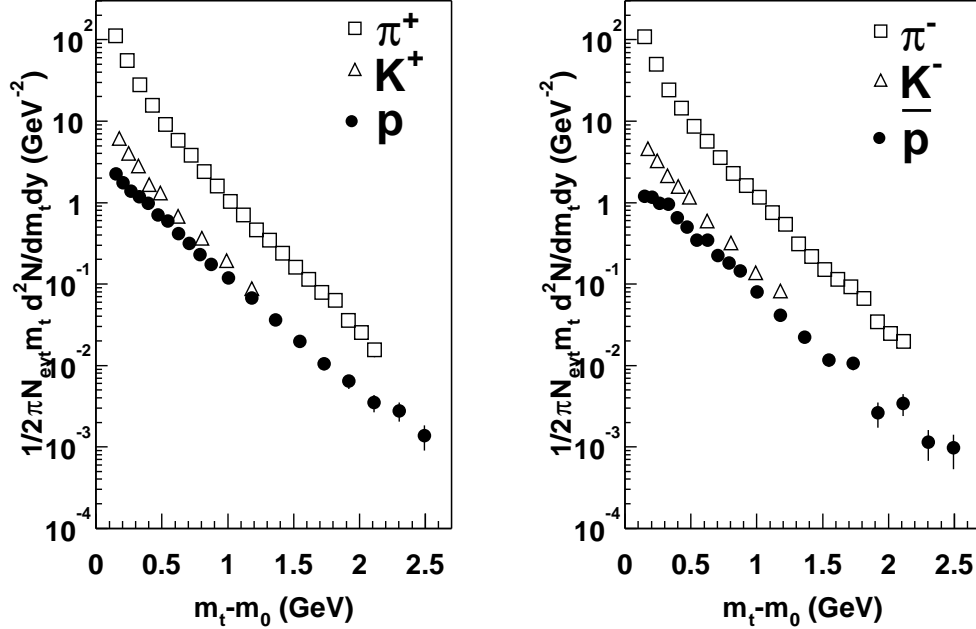


Figure 6.2: Transverse mass distributions of π^+ , K^+ , and p (left) in minimum bias events and the equivalent for negative particles (right).

since $dm_t/dp_t = p_t/m_t$. The invariant cross section on the vertical axis at each p_t does not change. The total transverse kinetic energy

$$E_t = K_t + m_0 = m_t \quad (6.14)$$

is equal to the transverse kinetic energy and the rest mass for the particle. Typically the transverse kinetic energy is $(m_t - m_0)$ is used to plot particles with different masses on the same scale (since the minimum energy starts at m_0 , each particle spectrum starts at m_0).

In Figure 6.2, the transverse energy distribution for minimum bias events is shown for all positive particles (left) and negative (right). The pion spectra appear to be exponential for $0.3 < (m_t - m_0) < 1.0$ in shape while the kaons and protons appear exponential for all measured kinetic energy. The same is true for the negative particles in the right panel; however, the antiprotons have more curvature for $(m_t - m_0) < 0.5$.

The equivalent transverse energy distributions for all measured centralities

are studied next. As the transverse energy distributions are exponential for $(m_t - m_0) < 1$ GeV, thermal fits are applied and effective temperatures are extracted.

6.1.2 Effective Temperature

The effective temperature is extracted by using a thermal Boltzmann distribution (Equation 6.11), where the units are such that $k = 1$ and T is in GeV. In this analysis, T is called the effective temperature T_{eff} .

$$\frac{d^2N}{2\pi N_{evt} m_t dm_t dy} = A e^{-m_t/T_{eff}} \quad (6.15)$$

The normalization is not relevant as only the slope of the spectrum is required to determine T_{eff} . Taking the log of this function on both sides results in:

$$\ln\left(\frac{d^2N}{2\pi N_{evt} m_t dm_t dy}\right) = -m_t/T_{eff} + \ln(A) \quad (6.16)$$

where $1/T_{eff}$ is the local inverse slope. It is called local as the spectrum may not be exponential over the measured m_t range, as it is the case for pions. The local inverse slope is an effective temperature because the system may not be in thermal equilibrium.

As central collisions produce more particles, collective effects should be stronger, and heavier particles should be boosted to higher transverse momenta. This flattening of the spectra causes T_{eff} to increase with particle mass. We extract T_{eff} by fitting exponentials of the form Equation 6.12 to the transverse mass spectra in the range $(m_t - m_0) < 1$ GeV. This range is chosen in order to both minimize the contributions from hard processes and to fit particles with the same transverse kinetic energy. Caution must be taken when comparing T_{eff} results as the local slope of the transverse mass spectra varies over m_t especially for pions and antiprotons as measured in PHENIX.

The resulting thermal fits for pions, kaons, and (anti)protons are shown in Figures 6.3 - 6.5. The fitted equation is then extrapolated to higher values of transverse kinetic energy. In comparing the extrapolated thermal fit to the spectra, one notes that pion spectra are not exponential over the entire range of $(m_t - m_0)$. The kaon and (anti)proton spectra are exponential over the measured range. The resulting values of T_{eff} for all particles and centralities are tabulated in Tables 6.1- 6.6 in units of MeV.

The effective temperature in each centrality is plotted against the average number of participants in Figure 6.6. The effective temperature appears to

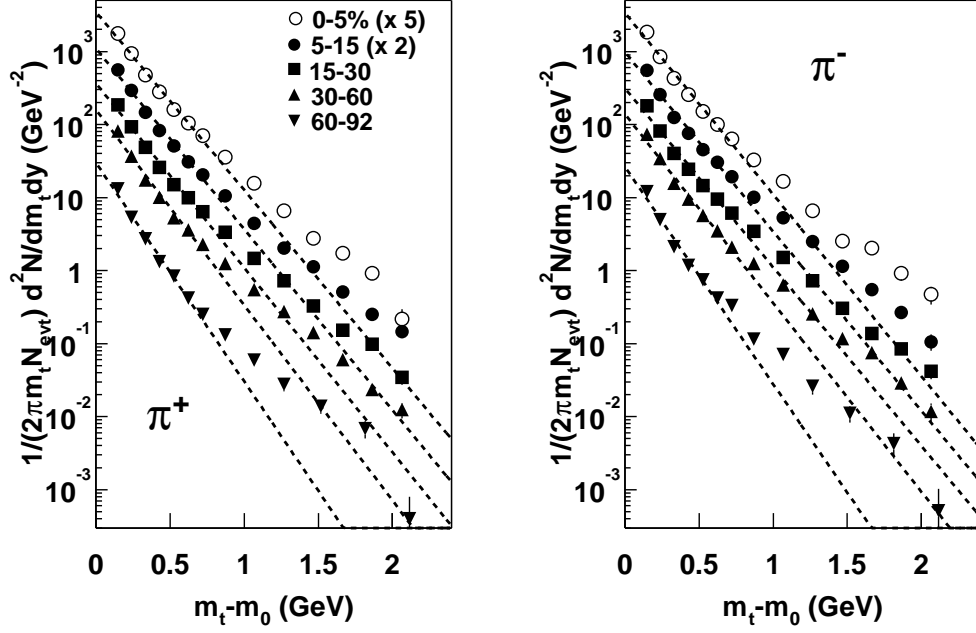


Figure 6.3: The transverse energy spectra of positive pions (left) and negative pions (right). Thermal fits in the range $(m_t - m_0) < 1$ GeV are extrapolated over the entire transverse kinetic energy range for comparison to the data. The pions are not exponential over the measured range.

Centrality (%)	χ^2/dof	local slope	T_{eff} (MeV)
0-5	120.9/6	-5.61 ± 0.07	178 ± 2
5-15	181.4/6	-5.70 ± 0.06	175 ± 2
15-30	218.1/6	-5.82 ± 0.06	172 ± 2
30-60	319.0/6	-6.15 ± 0.07	163 ± 2
60-92	58.8/6	-6.9 ± 0.2	145 ± 4

Table 6.1: The resulting effective temperatures of positive pions after fitting a thermal function to $m_t - m_0 < 1$ GeV in all centralities.

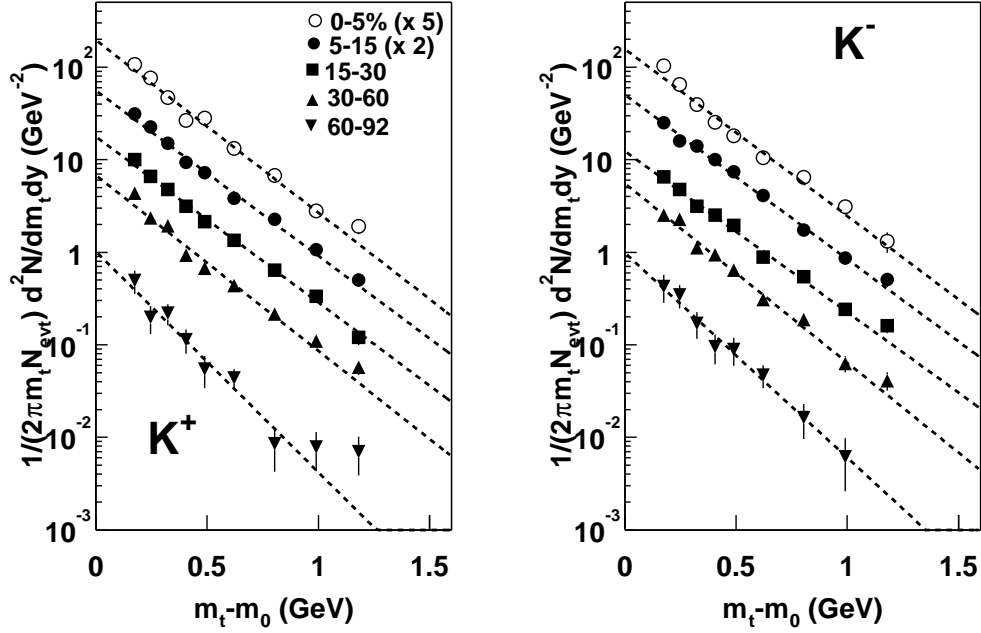


Figure 6.4: The transverse energy spectra of positive kaons (left) and negative kaons (right). Thermal fits in the range $(m_t - m_0) < 1$ GeV are extrapolated over the entire transverse kinetic energy range for comparison to the data. The kaons are exponential over the measured range.

Centrality (%)	χ^2/dof	local slope	T_{eff} (MeV)
0-5	149.4/6	-5.72 ± 0.08	175 ± 2
5-15	225.4/6	-5.65 ± 0.07	177 ± 2
15-30	263.1/6	-5.63 ± 0.07	178 ± 2
30-60	243.6/6	-5.95 ± 0.08	168 ± 2
60-92	74.8/6	-6.8 ± 0.2	147 ± 4

Table 6.2: The resulting effective temperatures of negative pions after fitting a thermal function to $m_t - m_0 < 1$ GeV in all centralities.

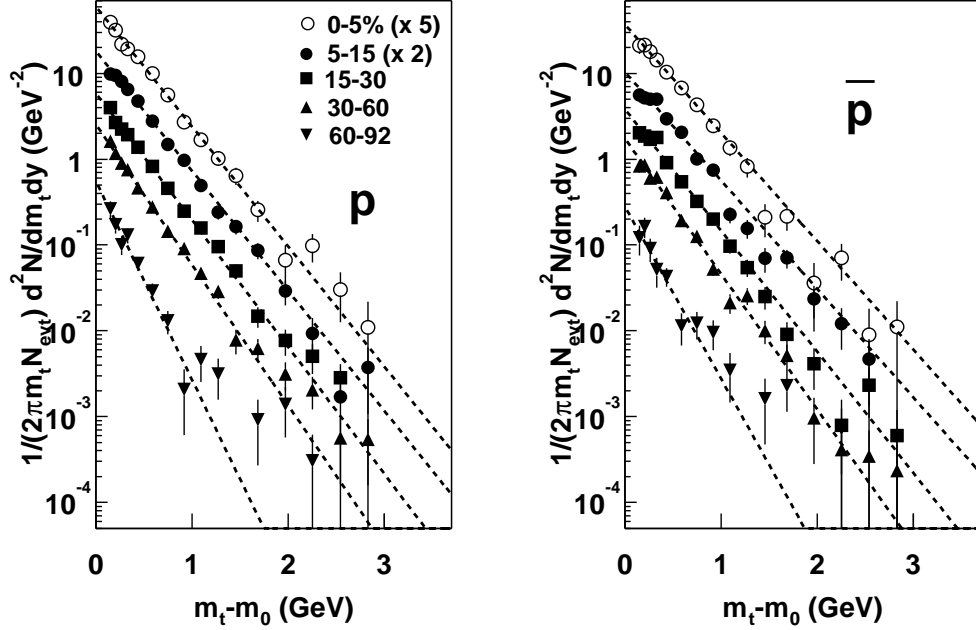


Figure 6.5: The transverse energy spectra of protons (left) and antiprotons (right). Thermal fits in the range $(m_t - m_0) < 1$ GeV are extrapolated over the entire transverse kinetic energy range for comparison to the data. The protons are exponential over the measured range, while the thermal extrapolation diverges slightly from the measured antiproton data.

Centrality (%)	χ^2/dof	local slope	T_{eff} (MeV)
0-5	9.34/6	-4.3 ± 0.2	233 ± 11
5-15	8.67/6	-4.1 ± 0.2	244 ± 12
15-30	4.12/6	-4.1 ± 0.2	244 ± 12
30-60	17.6/6	-4.4 ± 0.2	227 ± 10
60-92	5.29/6	-5.5 ± 0.6	182 ± 20

Table 6.3: The resulting effective temperatures of positive kaons after fitting a thermal function to $m_t - m_0 < 1$ GeV in all centralities.

Centrality (%)	χ^2/dof	local slope	T_{eff} (MeV)
0-5	8.33/6	-4.2 ± 0.3	238 ± 17
5-15	2.92/6	-4.1 ± 0.2	244 ± 12
15-30	4.25/6	-4.0 ± 0.2	250 ± 13
30-60	6.63/6	-4.5 ± 0.2	222 ± 10
60-92	1.65/6	-5.1 ± 0.6	196 ± 23

Table 6.4: The resulting effective temperatures of negative kaons after fitting a thermal function to $m_t - m_0 < 1$ GeV in all centralities.

Centrality (%)	χ^2/dof	local slope	T_{eff} (MeV)
0-5	6.18/6	-3.2 ± 0.2	313 ± 20
5-15	3.95/6	-3.2 ± 0.1	313 ± 10
15-30	3.63/6	-3.4 ± 0.1	294 ± 9
30-60	3.71/6	-3.8 ± 0.2	263 ± 14
60-92	7.26/6	-5.3 ± 0.4	189 ± 14

Table 6.5: The resulting effective temperatures of protons after fitting a thermal function to $m_t - m_0 < 1$ GeV in all centralities.

Centrality (%)	χ^2/dof	local slope	T_{eff} (MeV)
0-5	7.42/6	-2.9 ± 0.2	345 ± 24
5-15	7.54/6	-2.9 ± 0.2	345 ± 24
15-30	7.38/6	-3.3 ± 0.2	303 ± 18
30-60	7.45/6	-3.6 ± 0.2	278 ± 15
60-92	7.67/6	-4.6 ± 0.7	217 ± 33

Table 6.6: The resulting effective temperatures of antiprotons after fitting a thermal function to $m_t - m_0 < 1$ GeV in all centralities.

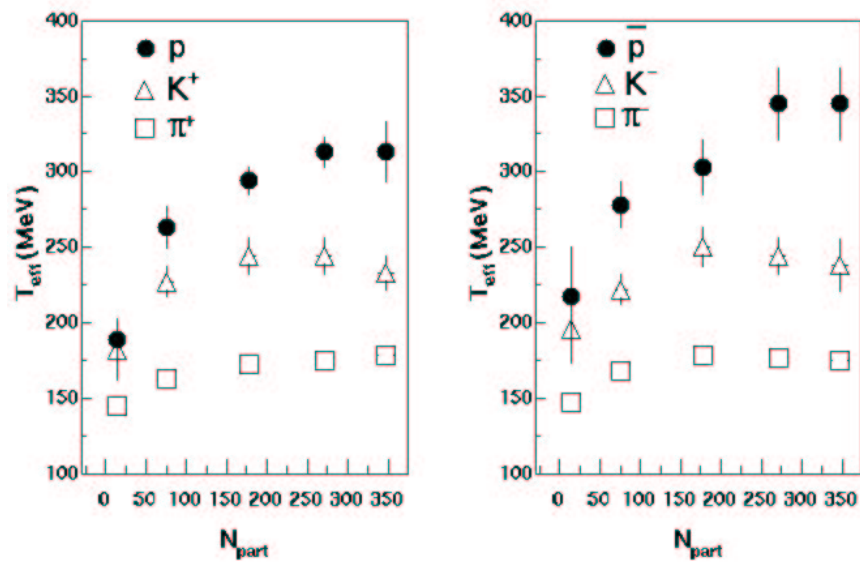


Figure 6.6: The effective temperature in each centrality is plotted against the average number of participants for each particle. Positive particles are plotted (left) and negative (right). The errors are statistical only from the thermal fit to the particle transverse energy spectra in the range $(m_t - m_0) < 1$ GeV.

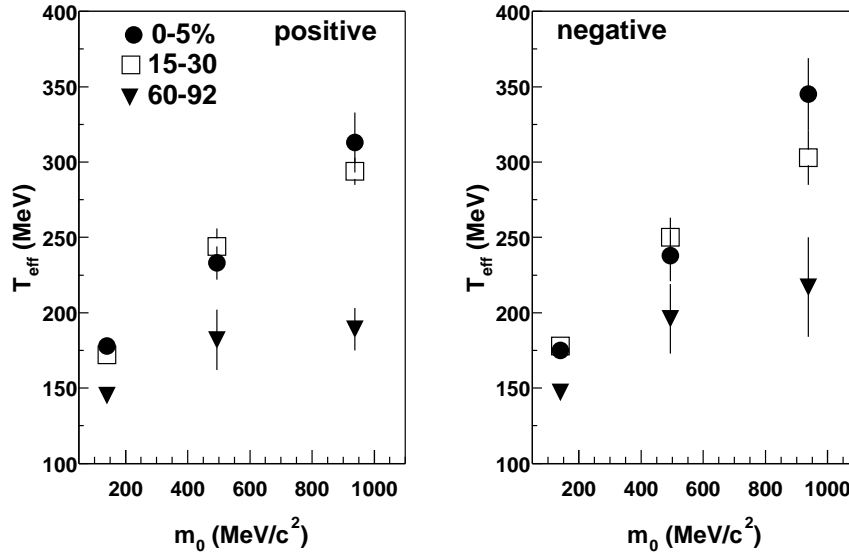


Figure 6.7: T_{eff} versus m_0 for the most central and most peripheral data.

increase steadily to a constant value for all particles except for the antiprotons for the top two centralities. The effective temperature increases by 40% from the 5 – 15% centrality to the most central collisions. The increase is 14% between the 15 – 30% to the 5 – 15% centralities. The effective temperature in all other centralities for the antiprotons is comparable to the protons.

The effective temperature T_{eff} for π , K, and p/p_{bar} for two different centralities, 0 – 5% and 60 – 92% are plotted against the particle mass m_0 in Figure 6.7. The dependence of the T_{eff} on both mass and centrality is what would be expected for radial expansion. The dependence of the effective temperature on both mass and the number of participants is indicative of radial expansion. The effective temperature includes the local temperature of a small piece of matter and its collective velocity (for motion in two dimensions, the classical $T = 1/2m_0 \langle v_x \rangle^2 + 1/2m_0 \langle v_y \rangle^2 = m_0 \langle v \rangle^2$, where $\langle v \rangle = \langle v_x \rangle = \langle v_y \rangle$ in circular coordinates). The simple exponential fit of Equation 6.11 or Equation 6.12 treats each particle spectrum as a static thermal source and a collective expansion velocity cannot be extracted reliably from a single particle spectrum. By using the information from all the particles, the expansion velocity can be inferred. For example, NA44 attempted in

Centrality (%)	χ^2/dof	T_{fo}	slope	$\langle \beta_t \rangle$
0-5	0.12	155 ± 4	0.16 ± 0.02	0.40 ± 0.05
	0.38	146 ± 4	0.20 ± 0.03	0.45 ± 0.07
15-30	1.98	150 ± 3	0.16 ± 0.01	0.40 ± 0.03
	1.17	154 ± 4	0.17 ± 0.02	0.41 ± 0.05
60-92	0.69	137 ± 5	0.06 ± 0.02	0.24 ± 0.08
	0.43	133 ± 7	0.10 ± 0.04	0.3 ± 0.1

Table 6.7: The fitted freeze-out temperature T_{fo} and averaged transverse flow velocity $\langle \beta_t \rangle$ for three different centralities: most central, mid-central, and most peripheral using the empirical expression Equation 6.1.2 as is done in [99]. The first line in each centrality corresponds to positive particles and the second to negative.

Reference [99],

$$T_{eff} = T_{fo} + m_0 \langle \beta_t \rangle^2 \quad (6.17)$$

to separate the effective temperature into the two respective contributions (thermal and collective motion). This function is fit to each centrality curve in Figure 6.7 with results tabulated in Table 6.7. Equation 6.1.2 assumes that the flow velocity $\langle \beta_t \rangle$ is independent of particle mass m_0 (all particles collectively travel at the same radial velocity). It also assumes that the pions, kaons, and protons have the same freeze-out temperature T_{fo} . If the flow velocity is zero, then all the particles are emitted from a static thermal source. As the number of participants decreases from the most central to the more peripheral events, the flow velocity decreases from $\approx 0.4c$ to $0.2c$. The freeze-out temperature also decreases from ≈ 155 MeV to 137 MeV.

The Equations 6.11 or 6.12 describe the kaon and proton spectra in the most central events; however, it does not describe the pion spectra for $(m_t - m_0) > 1$ GeV/c. The pion spectra are more concave in shape, with the extrapolated functional fit falling below the spectra. The functional form does not describe the (anti)proton spectra in the most peripheral events, corresponding to the 60 – 92% centrality. Here too, the fit⁵ falls below the data for $p_t > 2$ GeV/c. Based on these observations, the (anti)protons are not thermal over the entire range in $m_t - m_0$ for the most peripheral events.

⁵In extracting the particle yields, it is necessary to fit each spectrum in the low p_t range. The measured data yield is added to the function extrapolated yield at low p_t only.

6.1.3 Resonances

Equation 6.11 does not include particles arising from resonance and weak decays. Relevant resonances and decays are both mesonic and baryonic.

- Mesonic resonances and weak decays include: $\rho \rightarrow \pi^+\pi^-$, $\omega \rightarrow \pi^+\pi^0\pi^-$, $\eta \rightarrow \pi^+\pi^0\pi^-$, $\eta' \rightarrow \pi^+\pi^-\eta$, $K_s^0 \rightarrow \pi^+\pi^-$, $K^* \rightarrow K\pi$
- Baryon resonances and weak decays include: $\Delta \rightarrow N\pi^-$, $\Lambda \rightarrow p\pi^-$, $\bar{\Lambda} \rightarrow \bar{p}\pi^+$, $\Sigma^+ \rightarrow p\pi^0$, $n\pi^+$.

From a calculation by Derek Teaney, the resonance contribution is determined for the pions and protons. In Figure 6.8, the resonances in the pion spectra affect the shape for $p_t < 0.5$ GeV/c. The resonances in the proton spectra mostly affect the yield, since the spectra are quite flat at low p_t .

In Reference [69], the inclusion of resonances improves the fit of Equation 6.11 to the measured S+S data at CERN SPS energies; however, the longitudinal description is not consistent with the data. A static thermal source yields a fairly narrow Gaussian rapidity distribution, in disagreement with the data. PHOBOS measures the charged particle pseudorapidity distribution to be flat over 2 units of pseudorapidity [84]. Thus a static source is not appropriate at RHIC.

Even if Equation 6.1.2 were used, it is not relativistic and is inappropriate for the pions, which are relativistic. All the particle species are fit simultaneously to extract the radial expansion parameters using a relativistic function that is based on hydrodynamics assumptions. A boosted thermal source is used.

6.1.4 A Boosted Thermal Source

A static thermal source is boosted in both the longitudinal and transverse directions. The transverse surface velocity $\beta_r(r)$ of the source is parameterized as a function of the radius.

The following assumptions are made:

1. All the particles decouple at a freeze-out temperature T_{fo} ; and
2. The source has an infinite length in the longitudinal direction (boost-invariance).

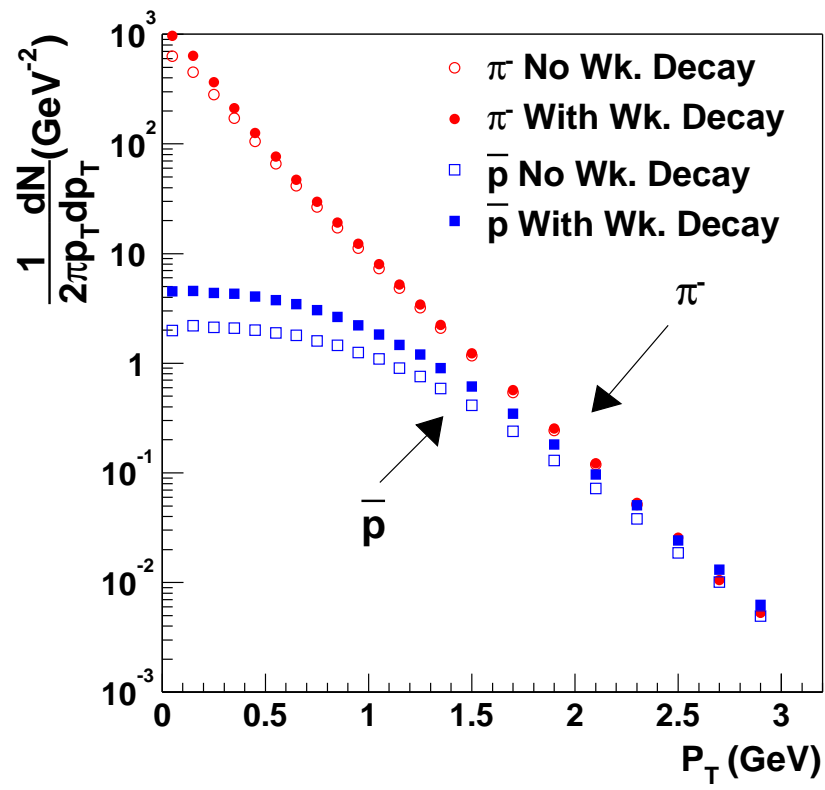


Figure 6.8: The resonance contribution in the pion and anti-proton spectra at RHIC energies [73].

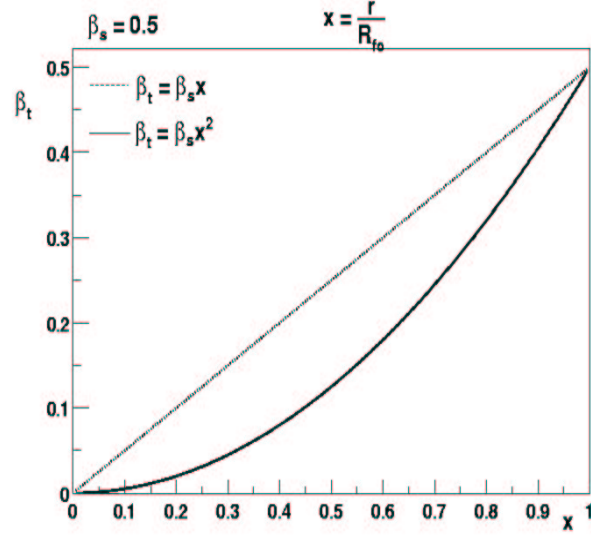


Figure 6.9: Transverse velocity profiles as a function of ξ .

6.1.5 Measuring β_t and T_{fo} from the Data

We use a hydrodynamics parameterization from U. Heinz et. al., derived in Reference [69]. The derivation was described in Chapter 1. A flat particle density distribution $f(\xi) = \text{const}$ is assumed. The transverse velocity profile (Figure 6.9) is parameterized in Equation 6.18 where $\xi = \frac{r}{R}$, and R is the maximum radius of the expanding source at freeze-out ($0 < \xi < 1$) [72].

$$\beta_t(\xi) = \beta_s \xi^n. \quad (6.18)$$

The geometrical average of the transverse velocity is equal to Equation 6.19, where β_s is the maximum surface velocity.

$$\langle \beta_t \rangle = \frac{\int \beta_s \xi^n \xi d\xi}{\int \xi d\xi} = \frac{2}{2+n} \beta_s \quad (6.19)$$

Each fluid element is locally thermalized and is given a transverse kick ρ that depends on the radial position in Equation 6.20:

$$\rho = \tanh^{-1}(\beta_t(\xi)). \quad (6.20)$$

$$\frac{dN}{m_t dm_t} = A \int m_t \cdot f(\xi) \cdot K_1 \left(\frac{m_t \cosh(\rho)}{T_{fo}} \right) \cdot I_0 \left(\frac{p_t \sinh(\rho)}{T_{fo}} \right) \xi d\xi. \quad (6.21)$$

The parameters in Equation 6.21 are the freeze-out temperature T_{fo} , the normalization A , and the maximum surface velocity β_t . The normalization A is determined by fitting Equation 6.21 to an m_t spectrum for all possible pairs of β_t and T_{fo} in the region $(m_t - m_0) < 1.0$ GeV in order to minimize contributions from hard processes. This equation can be fit simultaneously to all particle spectra or individually. First, the results of individual fits to each particle independently is discussed. Then, a simultaneous fit is performed and the results are presented.

Contours of Individual Particle Fits

Before attempting a simultaneous fit, it is important to study the contours that result after individually fitting a single particle spectrum. The interplay between T_{fo} and β_t was noted first in Reference [19]. If the contours do not overlap, then a simultaneous fit will not work. The T_{fo} versus β_t contours are produced for each particle separately. Figure 6.10 shows that the pions fix T_{fo} , while the protons determine β_t . The pions are quite relativistic and an additional boost does not change their effective temperature. The protons are heavier and are not travelling as fast; they are thus more sensitive to a velocity boost, which increases their effective temperature. The contours obtained from the fit to each particle separately suggest that an overlap region exists.

Contours of Simultaneous Particle Fits

The individual fits to the particle spectra indicate that a region of overlap in the parameter space T_{fo} and the maximum surface velocity β_t , should result from a simultaneous fit. Alternatively, the individual contours can be overlayed to produce an overlap region; however, the errors are more easily determined from the 1σ χ^2 contour after a simultaneous fit.

In Figure 6.11, the χ^2 contours are shown after a simultaneous fit to the particle spectra in the 5% most central events. The vertical axis shows T_{fo} and the horizontal axis β_t . The χ^2 contours show the anti-correlation of the two parameters. If the freeze-out temperature decreases, the flow velocity increases. The minimum χ^2 is 34 and the total number of degrees of freedom (dof) is 40. The parameters that correspond to this minimum are $T_{fo} = 121 \pm 4$ MeV and $\beta_t = 0.70 \pm 0.01$. The n-sigma contours are labeled up to 8σ . Within 3σ , the T_{fo} range is 106 – 141 MeV and the β_t range is 0.75 – 0.64.

As a linear velocity profile is assumed, the geometrical average flow velocity in the transverse plane is $\langle \beta_t \rangle = 2/3\beta_t$. If a different particle density distribution (for instance, a Gaussian) is used, then the average should be

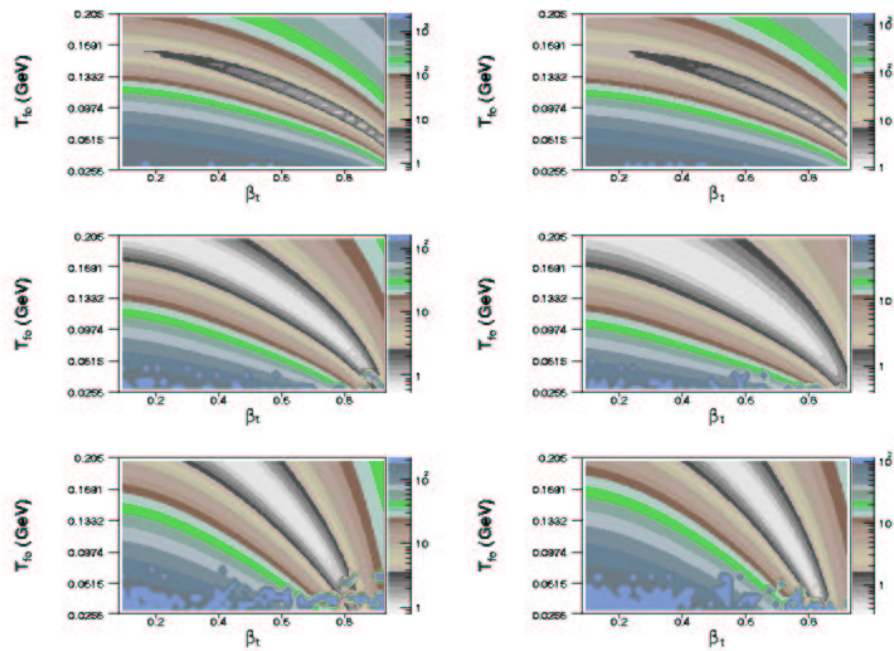


Figure 6.10: Individual particle contours of the parameter space T_{fo} and β_t for pions (top), kaons (middle), and protons (bottom). The left column are positive particles and the right are negative particles.

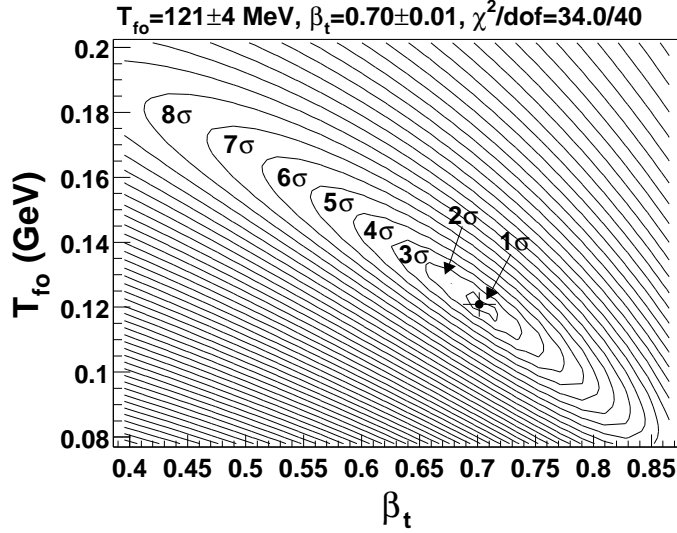


Figure 6.11: The χ^2 contours in the parameter space T_{fo} and β_t that result after simultaneously fitting pions, kaons, and (anti)protons for 0 – 5% centrality. The minimum χ^2/dof is 34.0/40 with parameters corresponding to the point as shown. The n-sigma contours are labeled accordingly.

determined after weighting accordingly as stated in Reference [72]. The equivalent contours for other centralities are shown below in Figures 6.12 - 6.15. The errors quoted on each figure are the 1σ contour widths of $\Delta\beta_t$ and ΔT_{fo} , respectively. The extracted radial flow parameters in the other centralities are determined in the same way as for the most central. The resulting fits are plotted with the spectra for all centralities in Figures 6.16- 6.18. The fits describe the spectra better than the simple exponential.

The T_{fo} and β_t values corresponding to each centrality are tabulated with the minimum χ^2 in Table 6.8. The best fit parameters are determined by averaging all parameter pairs within the 1σ χ^2 contour. The errors correspond to the standard deviation of the parameter pairs within the 1σ χ^2 contour. In Figure 6.19, the resulting parameters are shown as a function of the number of participants for T_{fo} (top) and $\langle \beta_t \rangle$ (bottom). There is a slight decrease of T_{fo} , while β_t increases and saturates at 0.70 with increasing N_{part} . Equivalent values obtained from hydrodynamics calculations are also shown for comparison [74]. The equation of state used and the initial assumptions are discussed in more detail in Chapter 7. The flow velocity decreases to 0.2 and the freeze-out temperature increases from values around 120 to 161 MeV.

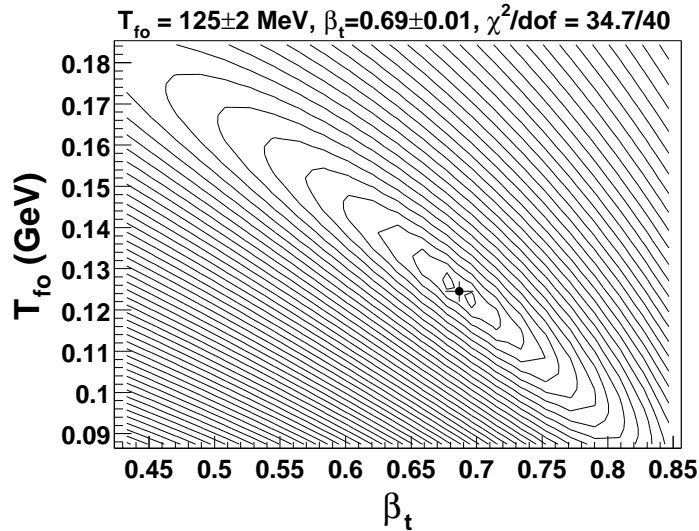


Figure 6.12: The χ^2 contours in the parameter space T_{fo} (vertical axis) and β_t (horizontal) that result after simultaneously fitting pions, kaons, and protons for 5 – 15% centrality. The minimum χ^2/dof is 34.7/40 with parameters corresponding to the point as shown.

Centrality (%)	χ^2/dof	T_{fo} (MeV)	β_t	$\langle \beta_t \rangle$
0-5	34.0/40	121 ± 4	0.70 ± 0.01	0.47 ± 0.01
5-15	34.7/40	125 ± 2	0.69 ± 0.01	0.46 ± 0.01
15-30	36.2/40	134 ± 2	0.58 ± 0.01	0.43 ± 0.01
30-60	68.9/40	140 ± 4	0.49 ± 0.01	0.39 ± 0.01
60-92	36.3/40	$161 \pm_{12}^{19}$	$0.24 \pm_{0.2}^{0.16}$	$0.16 \pm_{0.2}^{0.16}$

Table 6.8: The minimum χ^2 and the parameters T_{fo} and β_t for each of the five centrality selections. The best fit parameters are determined by averaging all parameter pairs within the 1σ contour. The errors correspond to the standard deviation of the parameter pairs within the 1σ χ^2 contour.

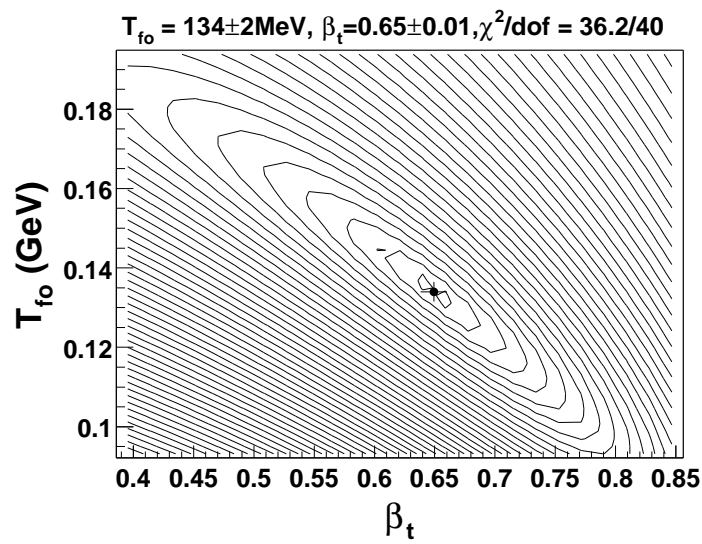


Figure 6.13: The χ^2 contours in the parameter space T_{fo} and β_t that result after simultaneously fitting pions, kaons, and (anti)protons for 15 – 30% centrality. The minimum χ^2/dof is 36.2/40 with parameters corresponding to the point as shown.

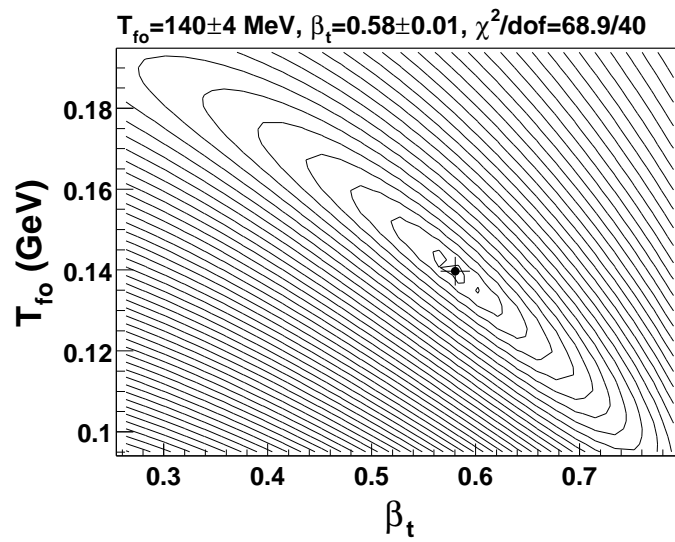


Figure 6.14: The χ^2 contours in the parameter space T_{fo} and β_t that result after simultaneously fitting pions, kaons, and (anti)protons for 30 – 60% centrality. The minimum χ^2/dof is 68.9/40 with parameters corresponding to the point as shown.

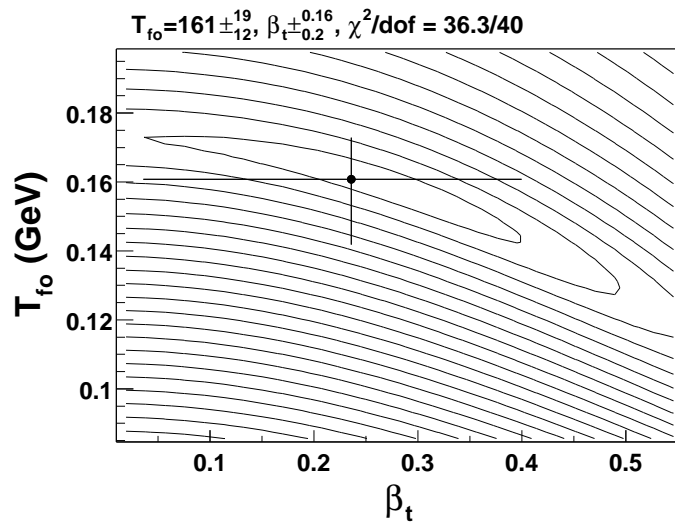


Figure 6.15: The χ^2 contours in the parameter space T_{fo} and β_t that result after simultaneously fitting pions, kaons, and (anti)protons for 60 – 92% centrality. The minimum χ^2/dof is 36.3/40 with parameters corresponding to the point as shown.

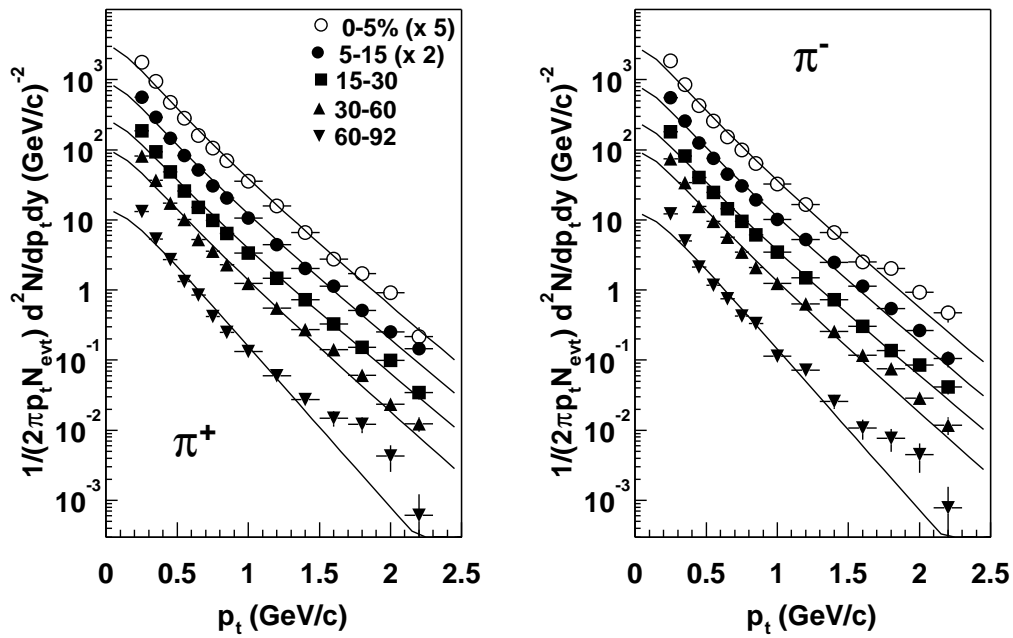


Figure 6.16: The parameterization and the π^+ (left) and π^- (right) data for all five centrality selections.

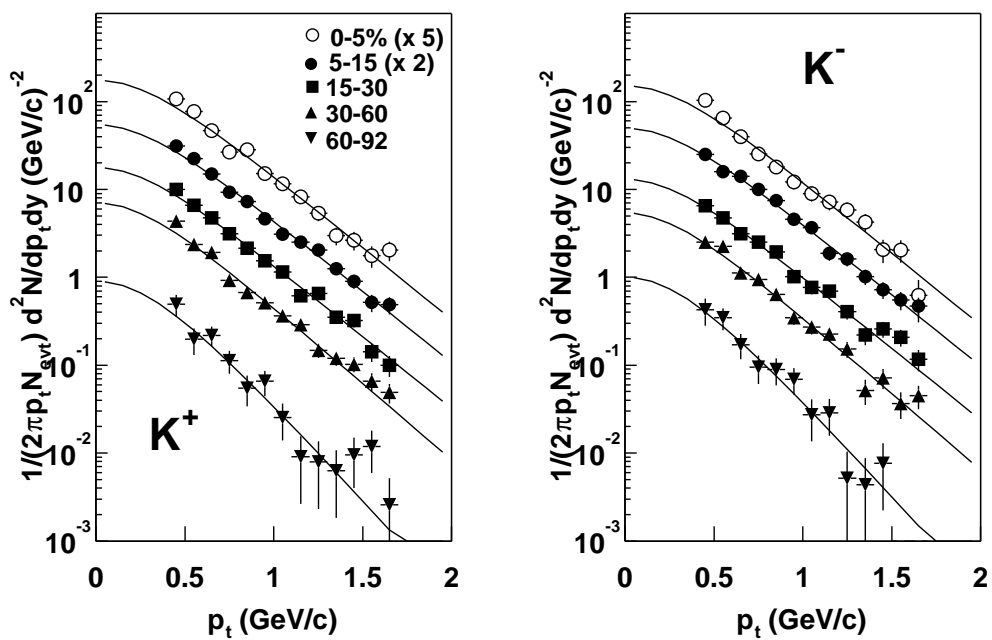


Figure 6.17: The parameterization and the K^+ (left) and K^- (right) data for all five centrality selections.

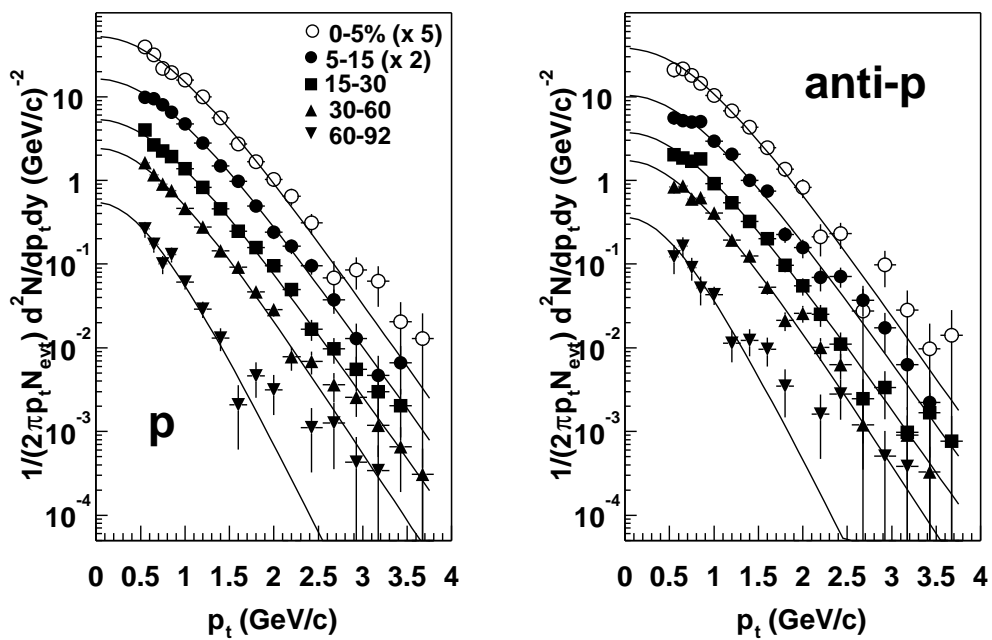


Figure 6.18: The parameterization and the proton (left) and anti-proton (right) data for all five centrality selections.

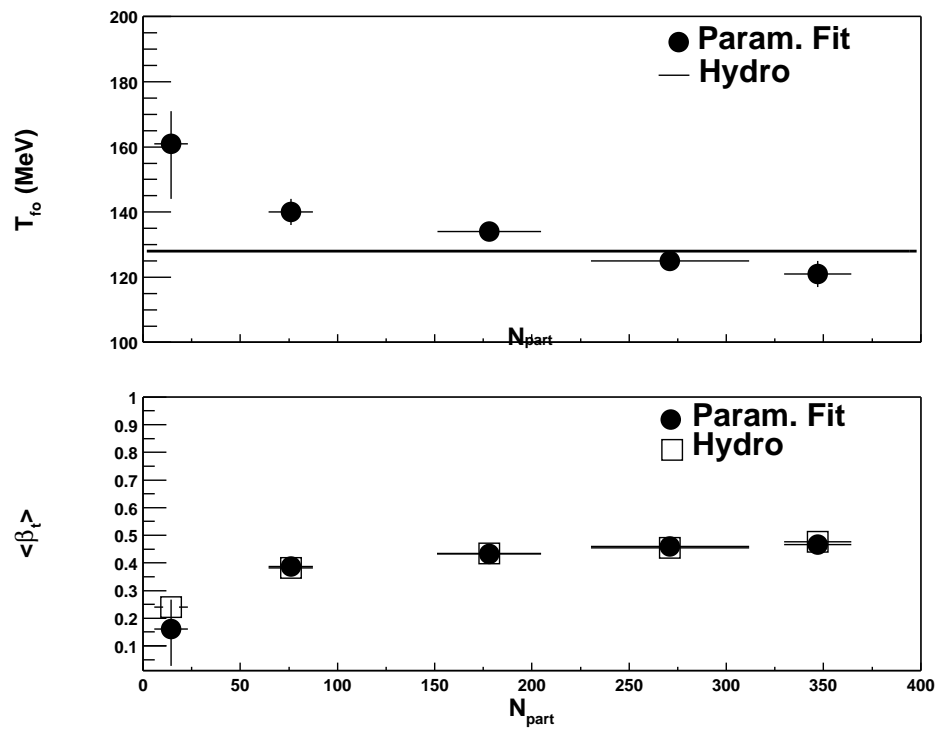


Figure 6.19: The expansion parameters T_{fo} and β_t as a function of the number of participants.

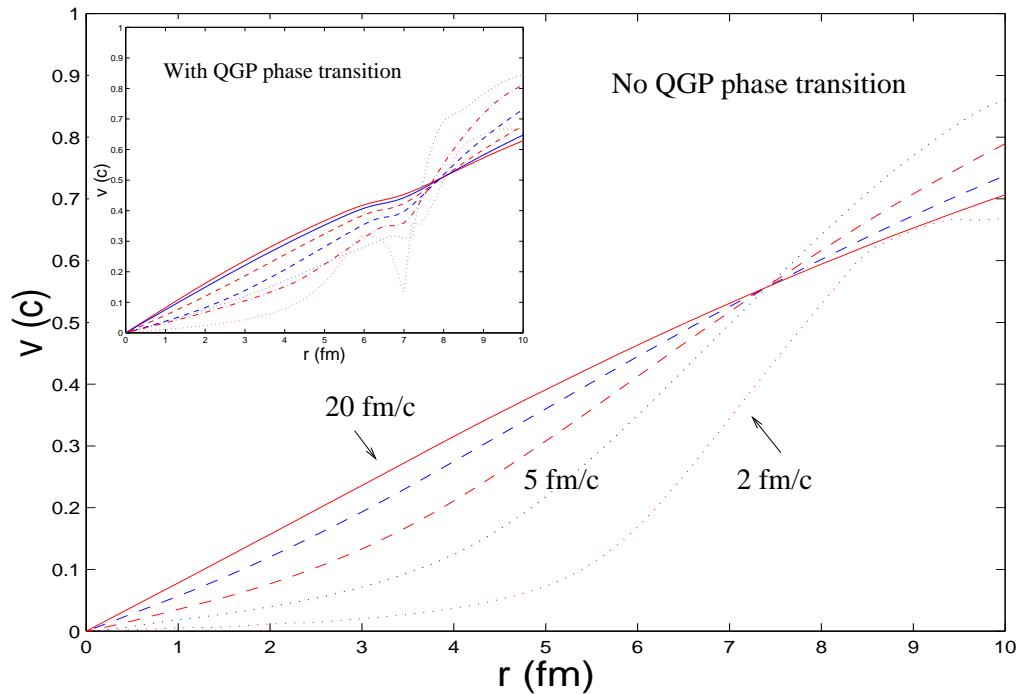


Figure 6.20: The velocity profiles as generated by hydrodynamics [75]. The vertical axis is the velocity of a fluid element and the horizontal axis is the radial position on the expanding surface. Each contour represents a different proper time in the expansion. The inset shows the velocity profiles when the system undergoes a QGP phase transition.

The analysis presented here is repeated using a parabolic velocity profile. In Reference [75], it is strongly suggested to use a linear velocity profile, based on the velocity profiles from hydrodynamics. In Figure 6.20 produced by Peter Kolb, at each “snapshot” in time during the expansion, there is a distribution of velocities that depend on the radial position r . The inset shows the velocity profiles when the system undergoes a QGP phase transition. Most of the proper-time contours close to freeze-out resemble linear velocity profiles. Parabolic velocity profiles seem to be more appropriate for earlier times. The effect of using a parabolic profile is to increase β_t by 13%. The effect on T_{fo} is marginal as expected increasing by 5%. Appendix B includes the analysis results after using a parabolic profile. With or without a QGP phase transition, a linear velocity profile is a reasonable parameterization for the later proper

times at freeze-out. The results after using a linear velocity profile are used consistently in the comparisons in Chapter 7.

As analyzed in Reference [69], the effect of fitting in the region where resonances affect the pion shape is to reduce the freeze-out temperature. For the most central events, the value of T_{fo} changes by 20% between the two pion fit ranges, while the β_t remains unchanged in the simultaneous fit.

6.2 Measured Yields and Average Transverse Momentum

The yield dN/dy and the average transverse momentum $\langle p_t \rangle$ are determined simultaneously for each particle. Instead of integrating a functional fit to the spectrum from zero to infinity, the total dN/dy and $\langle p_t \rangle$ are determined as follows:

1. Determine the dN/dy and $\langle p_t \rangle$ as measured from the data (including the statistical errors for each quantity, respectively),
2. Fit appropriate functional forms to different ranges in p_t and record the χ^2/dof . Integrate from zero to the first data point. Integrate from the last data point to infinity. Determine the value of the integrals needed to calculate dN/dy and $\langle p_t \rangle$ for each region,
3. Sum the data and extrapolated yields. Sum the p_t weighted integrals and divide by the total yield to get the $\langle p_t \rangle$,
4. After evaluating all possible fit ranges, choose the pair that has the best χ^2 and the maximum number of fit points for each function, and
5. Take the average between the upper and lower bounds to get dN/dy and $\langle p_t \rangle$. The statistical error is determined from the data and the systematic uncertainty is taken as 1/2 the difference between the upper and lower bounds.

For pions, a power-law in p_t (Equation 6.22) and an exponential in m_t (Equation 6.12) are fit to the data. For kaons and (anti)protons, two exponentials, one in p_t (Equation 6.23) and the other in m_t are used. The p_t exponential is an upper limit for a systematic estimate for the spectral shape in the extrapolation which is most important for the (anti)protons. After fitting a Boltzmann distribution (Equation 6.11) and an m_t exponential (Equation 6.12), the extracted yields are found to be within 2%; however, they both

have the same shape at low p_t . Therefore, the systematics are determined by comparing an exponential in p_t . (Refer to the data tables in Appendix D). The power-law function has three parameters labeled A, p_0 , and n in Equation 6.22. The exponentials have two parameters, A and T.

$$\frac{d^2 N}{2\pi N_{evt} p_t dp_t dy} = A \left(\frac{p_0}{p_0 + p_t} \right)^n \quad (6.22)$$

$$\frac{d^2 N}{2\pi N_{evt} p_t dp_t dy} = A e^{-p_t/T} \quad (6.23)$$

The fits for each centrality are shown in Figures 6.21 - 6.25. The top row in each figure are for pions, the middle for kaons, and the bottom for protons. The left column shows positive particles, and the right for negative particles. The power-law fit for the pions is dashed. The p_t exponentials for both the kaons and protons are dashed. The solid lines are m_t exponentials for all particles. The fit range in p_t , χ^2 , and functional form results are tabulated in Appendix A. Based on these tables, the dN/dy and $\langle p_t \rangle$ are determined for the 0 - 5% most central to the 60 - 92% most peripheral by selecting the fit range in p_t that results in the minimum χ^2 and maximum degrees of freedom.

As the function used to fit the invariant momentum distribution is dependent on p_t , it can be written as some function⁶ of p_t called $f(p_t)$

$$\frac{d^2 N}{2\pi N_{evt} dp_t dy} = f(p_t) \quad (6.24)$$

Two integrals are determined over the same fit range in p_t , called I_1 and I_2 ,

$$I_1 = \int_{p_t^{min}}^{p_t^{max}} p_t f(p_t) dp_t \quad (6.25)$$

$$I_2 = \int_{p_t^{min}}^{p_t^{max}} f(p_t) dp_t \quad (6.26)$$

where p_t^{min} and p_t^{max} are the minimum and maximum p_t in the fit range. The mean transverse momentum $\langle p_t \rangle$ is the ratio of I_1 to I_2

$$\langle p_t \rangle = \frac{I_1}{I_2} \quad (6.27)$$

and the yield dN/dy is determined by I_2

$$\frac{dN}{dy} = 2\pi I_2 \quad (6.28)$$

⁶To simplify the integrals, p_t is multiplied on both sides.

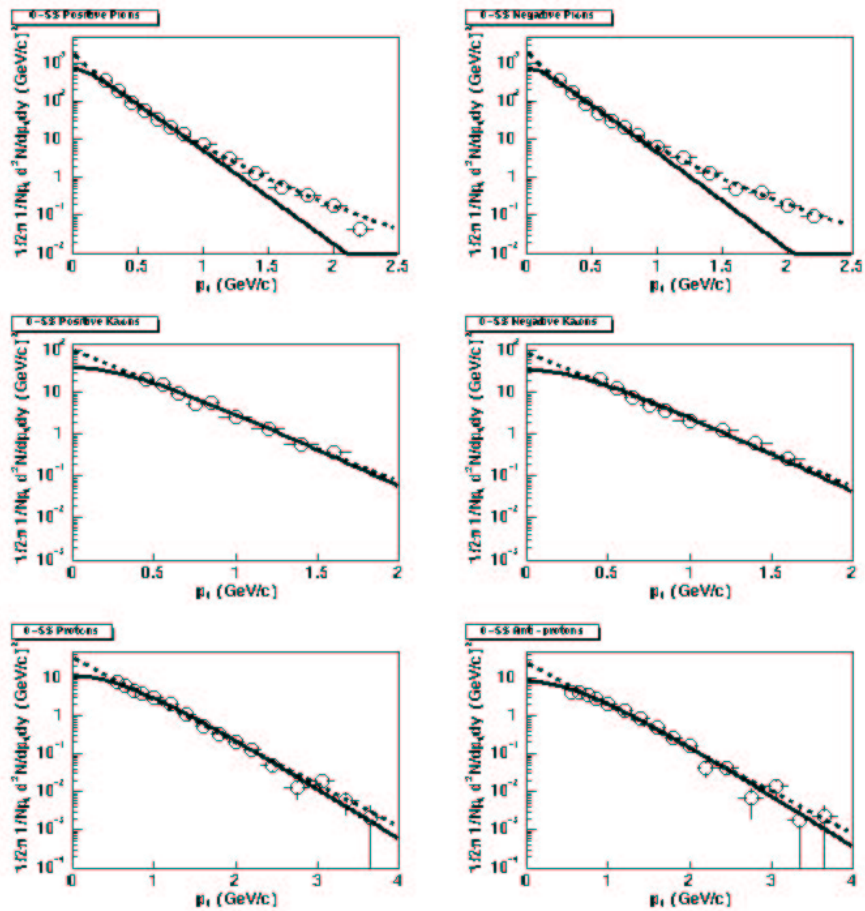


Figure 6.21: The 5% central events. Pions are the top row, kaons the middle, and protons the bottom. Positive particles are left and negative right.

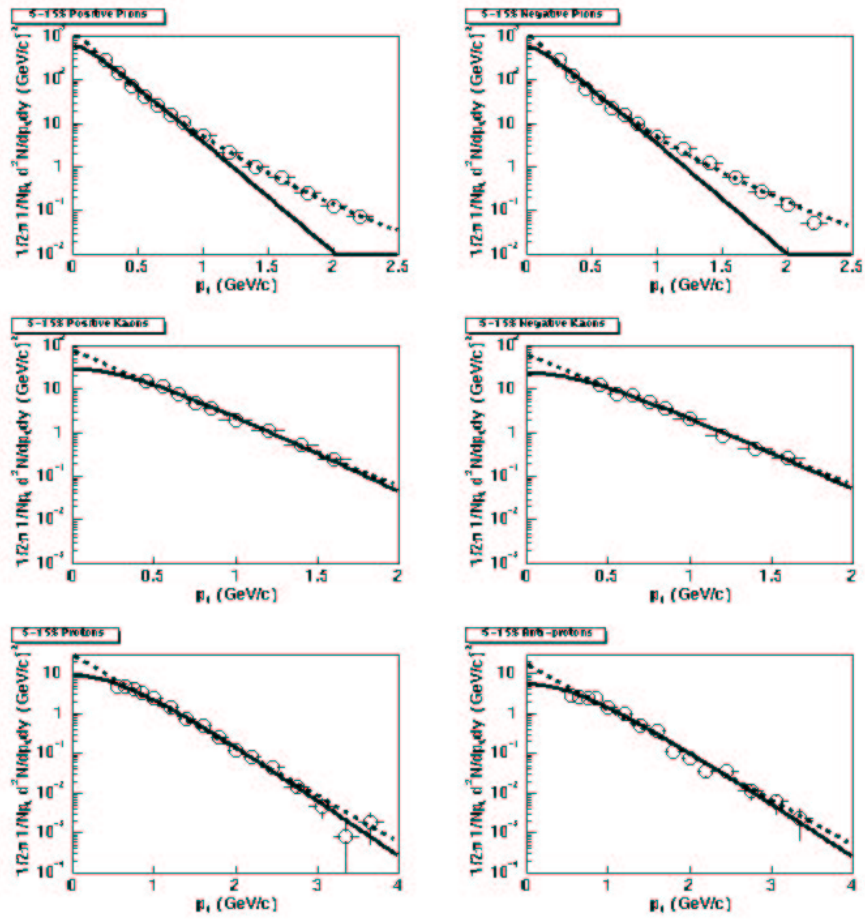


Figure 6.22: The 5-15% event centrality selection. Pions are the top row, kaons the middle, and protons the bottom. Positive particles are left and negative right.

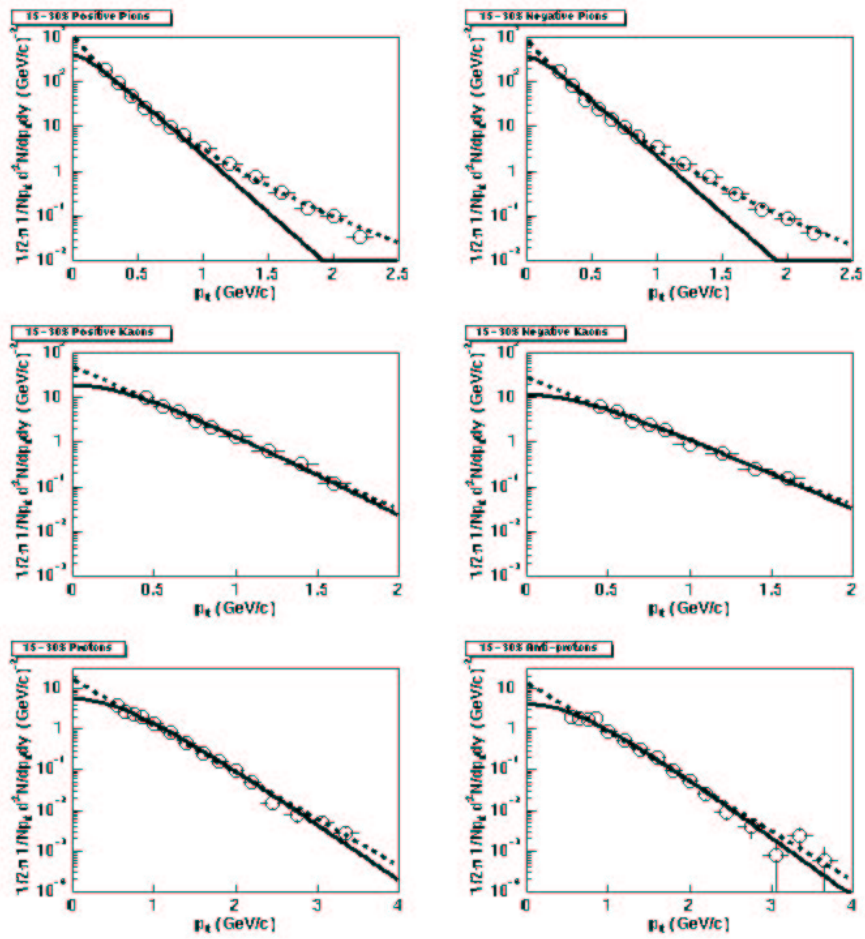


Figure 6.23: The 15-30% event centrality selection. Pions are the top row, kaons the middle, and protons the bottom. Positive particles are left and negative right.

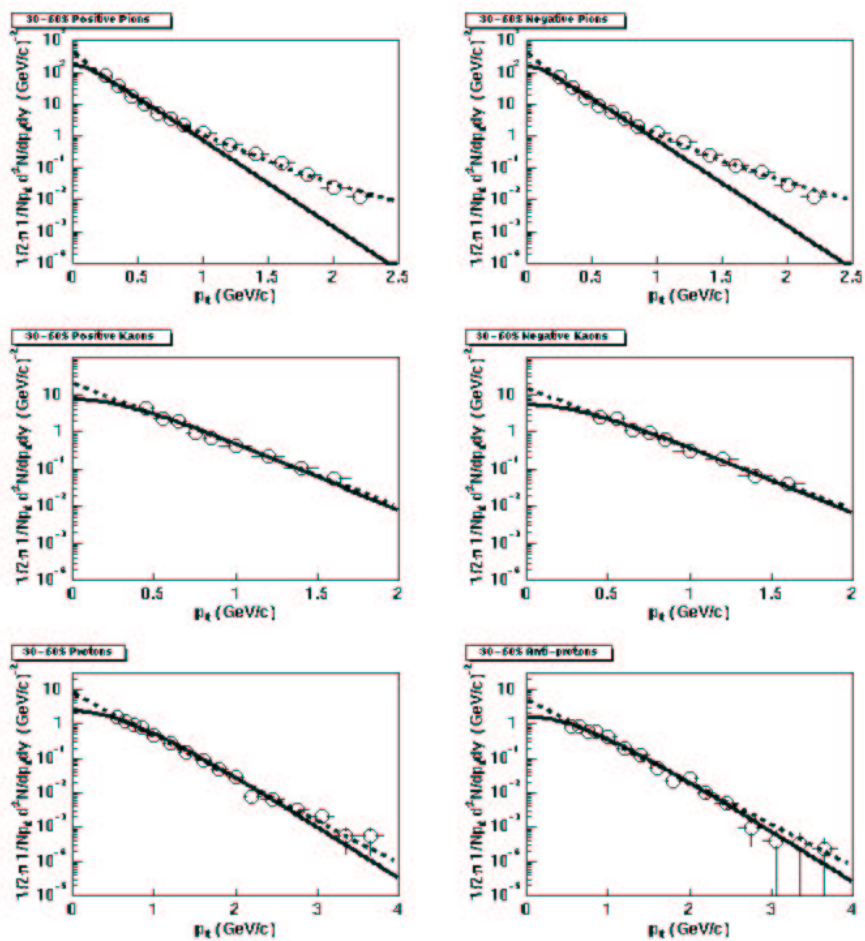


Figure 6.24: The 30-60% event centrality selection. Pions are the top row, kaons the middle, and protons the bottom. Positive particles are left and negative right.

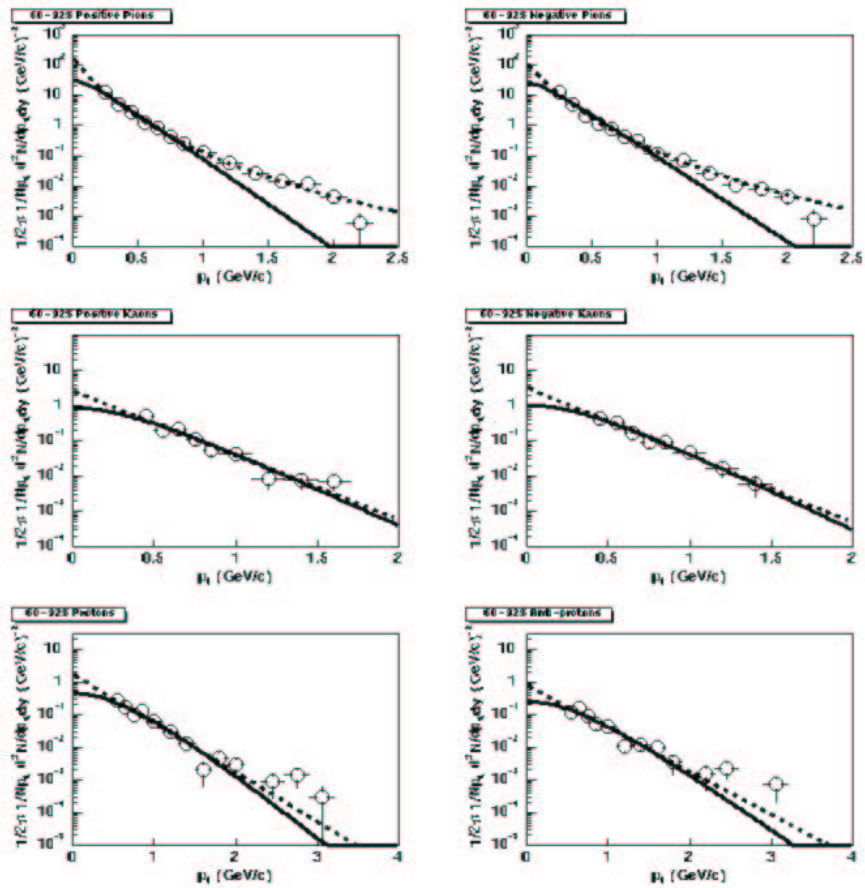


Figure 6.25: The 60-92% event centrality selection. Pions are the top row, kaons the middle, and protons the bottom. Positive particles are left and negative right.

The extrapolated $\langle p_t \rangle$ and dN/dy are determined in two sets of p_t ranges. The first p_t range is $[0, p_t^i]$, where p_t^i is the first measured p_t in the spectrum. The second p_t range is $[p_t^f, \infty]$, where p_t^f is the last measured p_t .

The average transverse momentum of the combined extrapolations and measured range are determined by summing the corresponding I_1 integrals for each p_t range. The integrals are I_1^i and I_1^f , for the lower and upper parts of the extrapolated spectrum respectively. The integral over the measured range is determined by replacing the integral in Equation 6.25 by a summation sign Σ and labeled as I_1^{if} . The average transverse momentum is

$$\langle p_t \rangle = \frac{I_1^i + I_1^{if} + I_1^f}{I_2^i + I_2^{if} + I_2^f} \quad (6.29)$$

The total yield is calculated by first determining the integrals for each end of the spectrum, labeled as I_2^i and I_2^f for each p_t range, respectively. The integral as measured in the data in Chapter 5 corresponds to the measured range $[p_t^i, p_t^f]$ and is determined by replacing the integral in Equation 6.26 by a summation sign Σ , labeled as I_2^{if} . The total yield dN/dy is therefore

$$dN/dy = 2\pi(I_2^i + I_2^{if} + I_2^f) \quad (6.30)$$

This procedure is repeated for all the centralities. The yield dN/dy and average transverse momentum $\langle p_t \rangle$ that result are tabulated in Tables 6.9 to 6.13. The systematic uncertainties are discussed next.

Particle	$dN/dy \pm \text{stat} \pm \text{syst}$	$\langle p_t \rangle \pm \text{stat} \pm \text{syst}$
π^+	$276 \pm 2 \pm 16$	$0.39 \pm 0.006 \pm 0.01$
π^-	$270 \pm 2 \pm 17$	$0.38 \pm 0.007 \pm 0.02$
K^+	$48 \pm 1 \pm 4$	$0.56 \pm 0.03 \pm 0.03$
K^-	$40 \pm 1 \pm 2$	$0.57 \pm 0.04 \pm 0.03$
p	$28.7 \pm 0.7 \pm 0.3$	$0.88 \pm 0.04 \pm 0.005$
\bar{p}	$20.1 \pm 0.7 \pm 0.2$	$0.898 \pm 0.05 \pm 0.006$

Table 6.9: The 5% central dN/dy and $\langle p_t \rangle$ for all measured particles.

6.2.1 Systematic Uncertainties

The hadron yields and $\langle p_t \rangle$ values include an additional uncertainty arising from the fitting function used for extrapolation at low and high p_t .

Particle	dN/dy \pm stat \pm syst	$\langle p_t \rangle \pm$ stat \pm syst
π^+	$216 \pm 2 \pm 13$	$0.38 \pm 0.005 \pm 0.01$
π^-	$200 \pm 2 \pm 10$	$0.39 \pm 0.006 \pm 0.01$
K^+	$35 \pm 1 \pm 3$	$0.58 \pm 0.03 \pm 0.02$
K^-	$31 \pm 1 \pm 3$	$0.59 \pm 0.03 \pm 0.03$
p	$21.6 \pm 0.5 \pm 0.2$	$0.867 \pm 0.03 \pm 0.005$
\bar{p}	$13.8 \pm 0.4 \pm 0.1$	$0.889 \pm 0.04 \pm 0.006$

Table 6.10: The 5-15% central dN/dy and $\langle p_t \rangle$ for all measured particles.

Particle	dN/dy \pm stat \pm syst	$\langle p_t \rangle \pm$ stat \pm syst
π^+	$141.5 \pm 0.9 \pm 9.7$	$0.375 \pm 0.005 \pm 0.016$
π^-	$129 \pm 1 \pm 7$	$0.383 \pm 0.005 \pm 0.012$
K^+	$21.9 \pm 0.5 \pm 1.6$	$0.57 \pm 0.03 \pm 0.02$
K^-	$15.5 \pm 0.5 \pm 1.0$	$0.61 \pm 0.03 \pm 0.02$
p	$13.2 \pm 0.3 \pm 0.1$	$0.85 \pm 0.03 \pm 0.005$
\bar{p}	$9.21 \pm 0.27 \pm 0.09$	$0.84 \pm 0.04 \pm 0.005$

Table 6.11: The 15-30% central dN/dy and $\langle p_t \rangle$ for all measured particles.

Extrapolating with several functional forms consistent with the data results in extrapolating $30 \pm 6\%$ of the spectrum for pions, $40 \pm 8\%$ for kaons, and $25 \pm 7.5\%$ for protons [57]. The systematic uncertainty in the yield is taken as 1/2 the difference between two functional forms.

In Table 6.14, the sources of systematic uncertainties in both $\langle p_t \rangle$ and dN/dy are tabulated. The three sources of uncertainty include the extrapolation; the background; and the Monte Carlo corrections and cuts. The uncertainty in the corrections and cuts is 11% and includes: the multiplicity efficiency correction of 9%; the particle identification cut of 5%; and the fiducial cuts of 5%. The uncertainty in the correction functions is already added in quadrature to the statistical error in the data (refer to Chapter 5). The background contribution is treated as a systematic uncertainty and is most significant for $p_t < 0.6$ GeV/c in the spectra (refer to Chapter 4). Added in quadrature to the systematic uncertainties from the spectra, the overall uncertainty on dN/dy is 13%, 15% and 14% for pions, kaons, and protons, respectively. Uncertainties on $\langle p_t \rangle$ depend on the extrapolation and background uncertainties; the uncertainties are 7%, 10% and 8% for pions, kaons,

Particle	dN/dy \pm stat \pm syst	$\langle p_t \rangle \pm$ stat \pm syst
π^+	$57.0 \pm 0.4 \pm 3.5$	$0.359 \pm 0.005 \pm 0.014$
π^-	$53.3 \pm 0.4 \pm 3.5$	$0.368 \pm 0.006 \pm 0.015$
K^+	$8.2 \pm 0.2 \pm 0.6$	$0.55 \pm 0.03 \pm 0.024$
K^-	$6.3 \pm 0.2 \pm 0.6$	$0.55 \pm 0.04 \pm 0.03$
p	$5.1 \pm 0.1 \pm 0.04$	$0.80 \pm 0.03 \pm 0.004$
\bar{p}	$3.6 \pm 0.1 \pm 0.03$	$0.82 \pm 0.04 \pm 0.004$

Table 6.12: The 30-60% central dN/dy and $\langle p_t \rangle$ for all measured particles.

Particle	dN/dy \pm stat \pm syst	$\langle p_t \rangle \pm$ stat \pm syst
π^+	$9.8 \pm 0.1 \pm 1.6$	$0.31 \pm 0.01 \pm 0.03$
π^-	$8.4 \pm 0.1 \pm 1.1$	$0.32 \pm 0.01 \pm 0.02$
K^+	$0.96 \pm 0.06 \pm 0.11$	$0.47 \pm 0.08 \pm 0.03$
K^-	$1.04 \pm 0.06 \pm 0.13$	$0.46 \pm 0.08 \pm 0.03$
p	$0.725 \pm 0.037 \pm 0.006$	$0.707 \pm 0.076 \pm 0.003$
\bar{p}	$0.472 \pm 0.036 \pm 0.003$	$0.782 \pm 0.111 \pm 0.003$

Table 6.13: The 60-92% central dN/dy and $\langle p_t \rangle$ for all measured particles.

and protons, respectively [57].

A Monte Carlo simulation is used to estimate the probability for reconstructing protons from Λ decays as prompt protons. Within the PHENIX acceptance, this probability is $\approx 50\%$. Taking into account the branching ratio of $\Lambda \rightarrow p + \pi^-$ of 64.1% and $\frac{\Lambda}{p} = 1$ as an upper limit, an estimated $\approx 32\%$ is the upper limit of weak decay contribution to the proton and anti-proton spectra and yields [57].

6.3 Particle Yields

The resulting yields are shown in Figure 6.26 for each number of participants for positive (left) and negative (right) hadrons. The pion yield is linear with increasing number of participants. For the largest number of participants, pions are dominant when compared to the kaons and protons. The yield of antiprotons is comparable to that of the protons. Both kaon and (anti) proton yields depend nonlinearly on the number of participants, but on this scale it

	π (%)	K (%)	(anti)p (%)
Extrapolation	6	8	7.5
Background ($p_t < 0.6$ GeV/c)	2	5	3
$\langle p_t \rangle$	7	10	8
Corrections and cuts	11	11	11
dN/dy	13	15	14

Table 6.14: The sources of systematic uncertainties in $\langle p_t \rangle$ and dN/dy [57].

is not as apparent.

In Figure 6.27, the particle yield dN/dy per participant nucleon pair for positive particles (left) and negative particles (right) are plotted as a function of the average number of participants N_p . The errors on the points include both statistical errors from the measured data and systematic errors. The dashed lines about the pions are the systematic errors in determining N_p from the Glauber calculation, which increases for the most peripheral collisions. The yields for kaons, protons, and antiprotons are scaled by a factor of 2 for plotting purposes. The yield per participant pair for pions is independent of the number of participants. The particle production of pions therefore scales with the number of participant pairs. Both the kaon and (anti)proton yields per participant pair increase with participant number, which suggests that the yield also depends on the number of nucleon-nucleon binary collisions.

The particle yields determined at mid-rapidity are sensitive to the initial energy density, which is estimated in the next section.

6.3.1 Estimating the Initial Energy Density

The initial energy density using Bjorken's formula in Chapter 1 is determined from the measured yields of all particles produced in the most central collisions. Bjorken's formula [14] is used to determine the initial energy density in a relativistic collision using (1) a value for the hadron formation time of 1 fm/c; (2) the transverse radius of the nucleus (R); and (3) the measured transverse energy (dE_t/dy). The average energy per particle is 0.8 GeV/fm³ (or approximately 1 GeV/fm³) [76]. Therefore, the expression $dE_t/dy = dE_t/dN \cdot dN/dy = 1 \text{ GeV/fm}^3 \cdot dN/dy$ can be used once the multiplicity dN/dy is measured. Assuming a parton formation time of 1.0 fm/c,

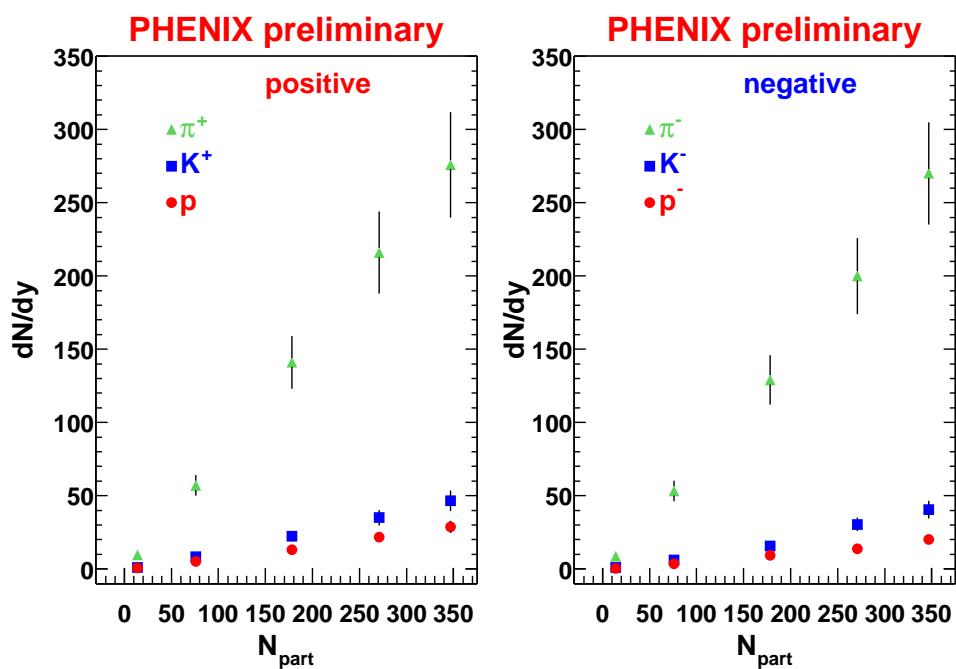


Figure 6.26: The particle yield dN/dy for positive particles (left) and negative particles (right) as a function of the average number of participants N_p . The errors on the points include both statistical errors from the measured data and systematic errors.

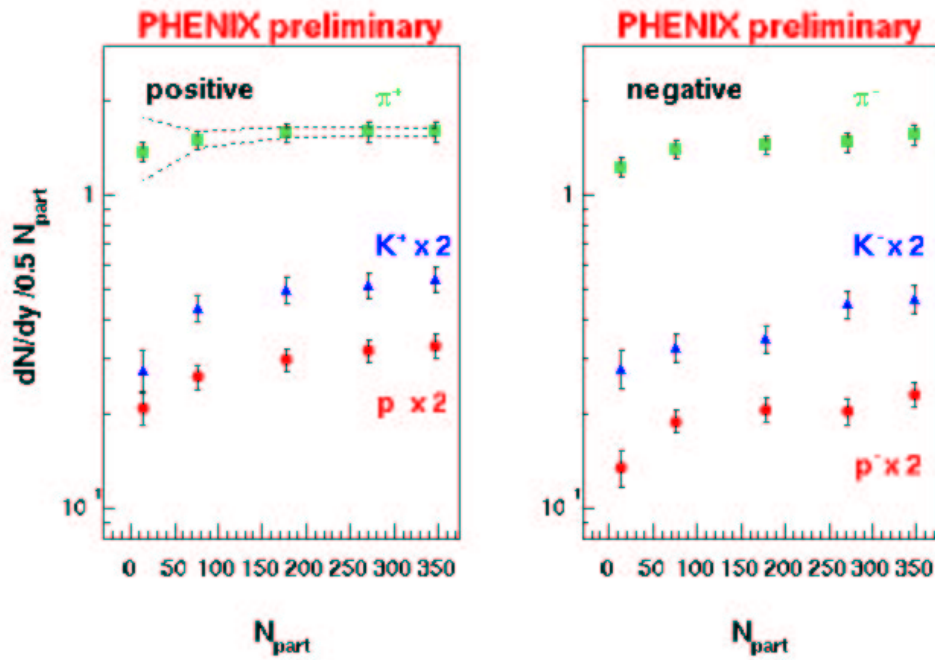


Figure 6.27: The particle yield dN/dy per participant nucleon pair for positive particles (left) and negative particles (right) as a function of the average number of participants N_p . The errors on the points include both statistical errors from the measured data and systematic errors. The dashed lines about the pions are the systematic errors in determining N_p from the Glauber calculation. The yields for kaons, protons, and antiprotons are scaled by a factor of 2 for clarity.[68]

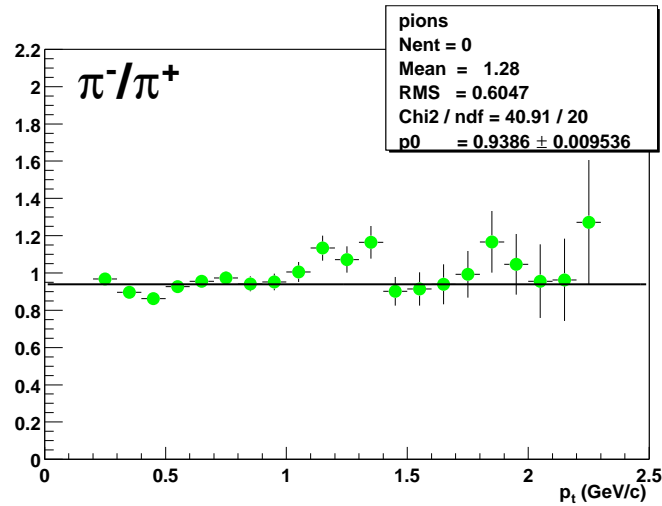


Figure 6.28: Negative pions divided by positive pions in each p_t bin. The fit is a constant fit and results in 0.94.

and using $\pi R^2 = 139 \text{ fm}^2$ for the area transverse to the beam axis⁷, the initial energy density is calculated for the most central events using Equation 1.10 and is equal to $4.9 \pm 0.2 \text{ GeV}/\text{fm}^3$.

6.3.2 Particle Ratios

The particle ratios of different species in both p_t and dN/dy are sensitive to the chemistry of the collisions. The value of π^-/π^+ is independent of p_t in Figure 6.28. After fitting a constant through these points, the result is 0.94. The K^-/K^+ ratio is also independent of p_t with a constant fit of 0.83 ± 0.03 (see Figure 6.29). The \bar{p}/p ratio is 0.67 ± 0.02 and is also constant in p_t . The π^-/π^+ ratio is independent of the number of participants N_p as shown in Figure 6.31. This is also true for K^-/K^+ and \bar{p}/p in Figure 6.32 and Figure 6.33.

In Figure 6.34, the ratio \bar{p}/π^- is independent of the number of participants, while p/π^+ increases. The kaon ratios K^-/π^- and K^+/π^+ both increase (see Figure 6.35). Pions are independent of the number of participants, so there is no hard binary collision dependence in their production. Pions are produced by pair production, weak decays, resonances, string fragmentation, etc..

⁷The radius used is the same as was used to determine N_p and N_c in Chapter 3.

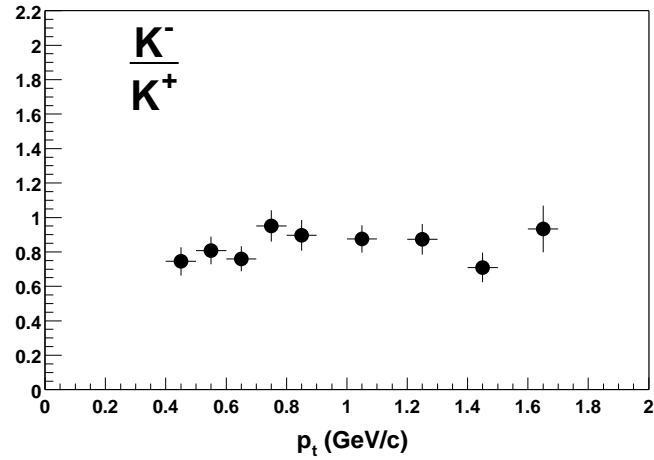


Figure 6.29: The K^-/K^+ ratio is independent of p_t in the measured range [54].

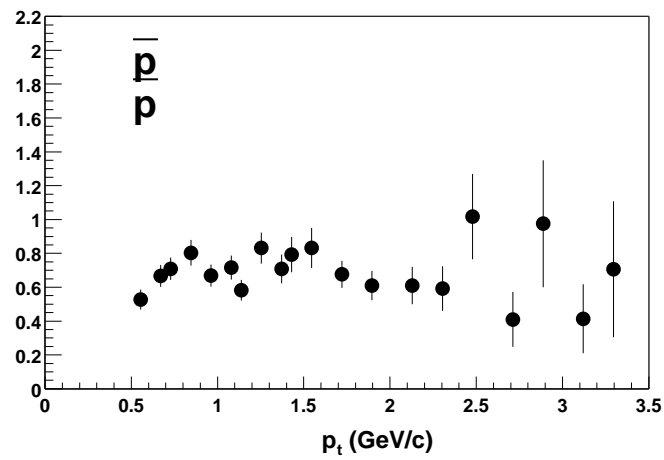


Figure 6.30: The \bar{p}/p ratio is independent of p_t in the measured range [54].

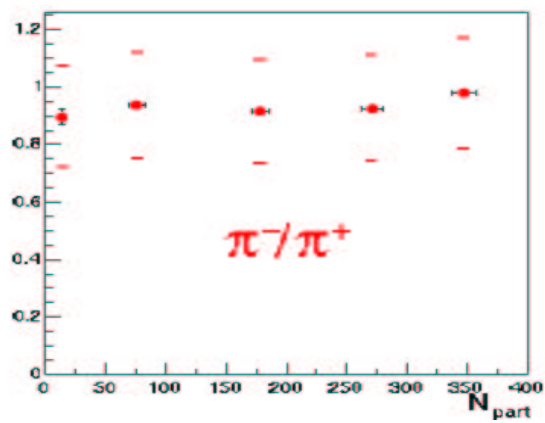


Figure 6.31: The π^-/π^+ ratio does not depend on the number of participants [54].

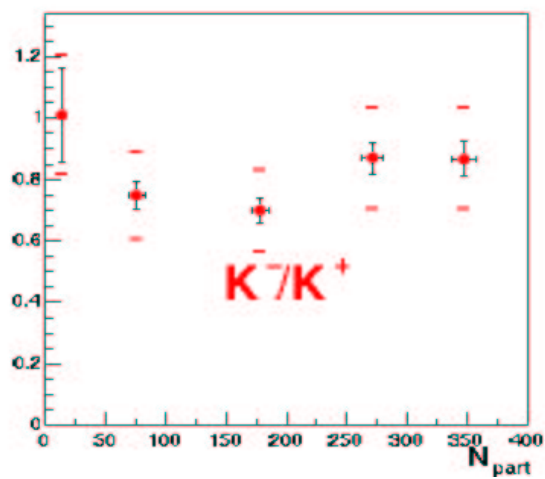


Figure 6.32: The K^-/K^+ ratio plotted against the number of participants [54].

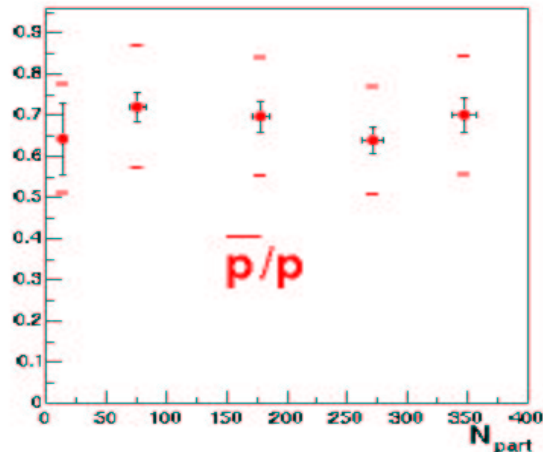


Figure 6.33: The \bar{p}/p ratio plotted against the number of participants [54].

Unlike for pions, the increase in both the K/π and p/π ratios with participant number is most likely due to the high energy contribution. Because there is a dependence on the number of binary collisions, there is enough center-of-mass energy to produce $s\bar{s}$ and baryon-antibaryon pairs.

6.4 Mean Transverse Momentum

In Figure 6.36, the average transverse momentum for positive (left) and negative (right) particles corresponding to the number of participating nucleons N_p in each event centrality is shown. The $\langle p_t \rangle$ increases monotonically with smaller impact parameters for the nucleons, while pions and kaons show a strong dependence only for the most peripheral. As a comparison, the average transverse momentum of particles produced in $p\bar{p}$ collisions interpolated to 130 GeV are shown as open symbols [67].

The results presented here are compared to previously published results from RHIC, and to lower center-of-mass energies at the CERN-SPS and BNL-AGS accelerators in the next chapter, Chapter 7. In addition, the equivalent results from a hydrodynamic model calculation by Peter Kolb and Ulrich Heinz are compared to the measured quantities. Implications of the results will be discussed.

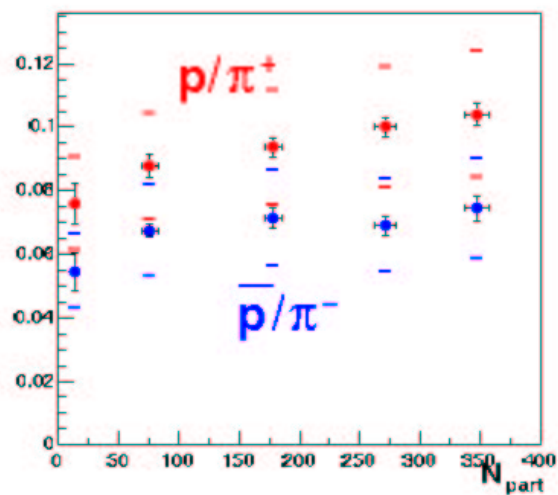


Figure 6.34: The p/π^+ and \bar{p}/π^- ratios plotted against the number of participants [54].

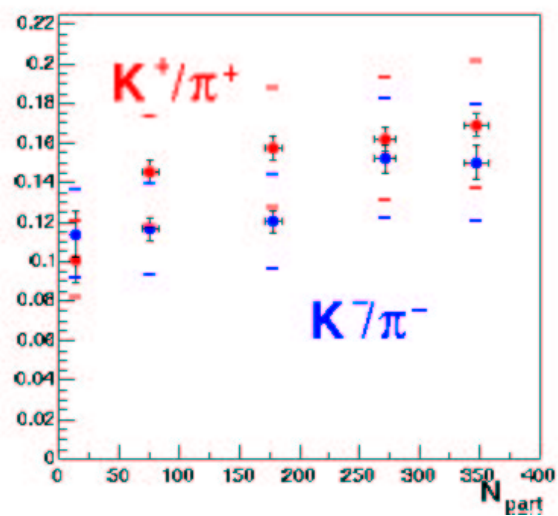


Figure 6.35: The K^+/π^+ and K^-/π^- ratios plotted against the number of participants [54].

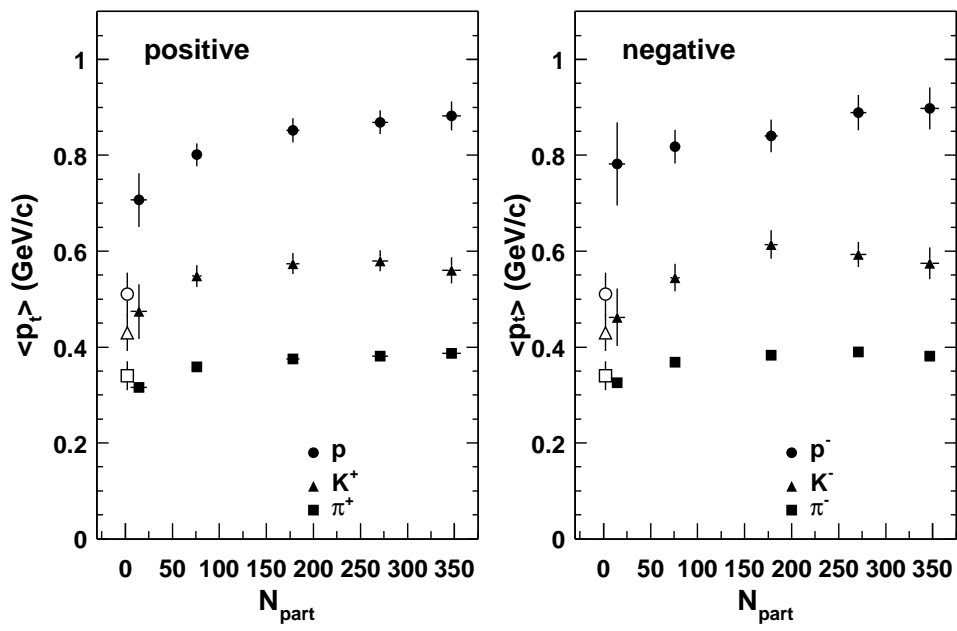


Figure 6.36: Average transverse momentum for positive (left) and negative (right) particles corresponding to the number of participating nucleons N_p in each event centrality [68].

Chapter 7

Discussion and Conclusion

A discussion of the results in Chapter 6 is presented. Comparisons are made to similar measurements at both CERN-SPS and RHIC energies. First, the transition region in p_t between hard and soft components is discussed. In Pb+Pb collisions at CERN-SPS energies, both pQCD and hydrodynamic calculations describe the spectra. A radial flow analysis at CERN-SPS energies for different collision systems is described. From the measured hadron spectra, it is unclear where the transition between hard and soft components occurs. At RHIC energies, the measured initial energy density is well above the threshold for a QGP phase transition and the data indicate both soft and hard components. In the collisions with the highest initial energy density, the transition region in the spectra between soft and hard processes is determined by comparing the radial flow analysis in Chapter 6 and the high p_t hadron data[81] also measured in PHENIX.

Finally, a full hydrodynamics model calculation is compared to the data. A hydrodynamic model calculation with an equation of state that simulates a mixed phase transition between a hadron gas and a relativistic gas of quarks and gluons (QGP) is tuned to RHIC energies. The calculated spectra of π^- and \bar{p} are compared to the measured spectra for five different collision centralities.

7.1 Radial Flow

Radial flow arises from the collective expansion of the hadron gas produced in relativistic heavy-ion collisions. Collective transverse flow adds a momentum-independent velocity boost to the motion of the hadrons. Without such a boost, the transverse mass distribution of hadrons from a static, thermally equilibrated source are all independent of mass.

Just after hadronization, the particles are unable to leave the hadronic medium as the system size is approximately 1 fm. The multiple rescattering of

the hadrons builds up pressure in the system and causes the hadrons to expand collectively at a transverse flow velocity β_t . As the system expands radially and cools, the mean-free path of the pions increases until they decouple from the system. This occurs at a temperature, T_{fo} called the freeze-out temperature. HBT source radii at the CERN SPS and RHIC energies are of the order $\approx 6-7$ fm at the time of freeze-out [12, 11]. The hadrons then stream freely without additional rescattering to the detectors.

7.2 What is Measured at CERN-SPS Energies?

What follows is a radial flow analysis of the CERN SPS data. A variety of collision systems Pb+Pb, S+Pb, S+S, and p+A are studied in the same manner. The p+A collisions are used as a reference as the particles are produced after multiple initial scattering of the partons produced early in the collision. The p+A collisions are not expected to be described hydrodynamically. The study is motivated by the statement in Reference [78] that the hadron spectra measured out to 3 GeV/c cannot be described hydrodynamically. The hadron p_t distributions are sensitive to both soft and hard processes. After comparing pQCD calculations and measured data at CERN SPS experiments at $\sqrt{s} = 17$ GeV, there is little evidence of energy loss [78].

From [99], Equation 6.21 is fit to identified pions, kaons, and (anti)protons with average transverse flow velocities and freeze-out temperatures that are consistent with the empirical analysis using Equation 6.1.2. Using published effective temperatures that result after fitting Equation 6.12 to the transverse energy spectra, Equation 6.1.2 is used to determine T_{fo} and $\langle \beta_t \rangle$ for a variety of collision systems at the same \sqrt{s} energy. The radial flow parameters are then compared to overlapping χ^2 contours of T_{fo} and β_t as measured in Reference [79]. These parameters are then used in Equation 6.21 and the normalization is adjusted to obtain the best fit to the pion data in the region $(m_t - m_0) < 1$ GeV.

7.2.1 Effective Temperatures

The published effective temperatures T_{eff} of the invariant momentum distributions produced at midrapidity from simple m_t exponential fits in the region $(m_t - m_0) < 1.2$ GeV/c² are listed in Table 7.1 and Table 7.2 for a variety of collision systems.

System	Particle	T_{eff} (MeV)	Reference
Pb+Pb	π^+	156 ± 6	[99]
	K^+	234 ± 6	[99]
	p	289 ± 7	[99]
	Λ	293 ± 10	[101]
	$\bar{\Lambda}$	288 ± 15	[101]
S+Pb	π^+	156 ± 8	[100]
	K^+	206 ± 6	[100]
	p	242 ± 3	[100]
S+S	π^+	148 ± 4	[99]
	K^+	180 ± 8	[99]
	p	208 ± 8	[99]

Table 7.1: The effective temperature of hadrons for S+S, S+Pb, Pb+Pb colliding systems at CERN energies. Errors are statistical only.

In the p+Pb system, the proton effective temperature is adjusted by a model dependent correction factor that accounts for Λ resonances. In all collision systems, pion resonances are excluded in the exponential fits by excluding the measured points below $(m_t - m_0) < 0.3$ GeV [97].

The effective temperatures for each particle mass are shown in Figure 7.2.1 for positive hadrons. The left panel is for symmetric systems (A+A), while the right is for asymmetric systems (A+B and p+A). The effective temperatures of particles within each collision system depends on the particle mass. Error bars are statistical only. As the effective temperature shows a mass dependence, radial flow is assumed and Equation 6.1.2 is fit to the curves in Figure 7.2.1 for each collision system. The freeze-out temperature T_{fo} and flow velocity that result are tabulated in Table 7.3 for charged particles separately. The values of T_{fo} for all systems fluctuate about 140 MeV, while the radial flow varies when the parameters are plotted versus the system size on a semi-log plot in Figure 7.2. Here, the system size is A·B, where the beam nucleon number is A and the target nucleon number is B.

The average radial flow velocities are used to determine the surface velocity β_t by calculating $3/2 \langle \beta_t \rangle$ in Table 7.3. The radial flow velocity and freeze-out temperature are used in the hydrodynamical parameterization in Equation 6.21 in order to calculate the boosted hadron spectrum out to 3 GeV/c in p_t . The function is then scaled to match the normalization of the neutral pion spectra in the range $0.3 < (m_t - m_0) < 1$ GeV. The neutral pion

System	Particle	T_{eff} (MeV)	Reference
p+Pb	π^+	145 ± 3	[98]
	K^+	172 ± 9	[98]
	p	203 ± 6	[97]
	Λ	203 ± 9	[104]
	$\bar{\Lambda}$	180 ± 15	[104]
p+S	π^+	139 ± 3	[100]
	K^+	163 ± 14	[100]
	p	175 ± 30	[100]
p+Be	π^+	148 ± 3	[100]
	K^+	154 ± 8	[100]
	p	156 ± 4	[100]
p+p	π^+	139 ± 13	[102], [103]
	K^+	139 ± 15	[102], [103]
	p	148 ± 20	[102], [103]

Table 7.2: The effective temperatures of hadrons produced in p+p and p+nucleus colliding systems at CERN and ISR energies. Errors are statistical only.

Colliding system	T_{fo}^+ (MeV)	$\langle v_T \rangle^+(c)$	T_{fo}^- (MeV)	$\langle v_T \rangle^-(c)$
Pb+Pb	145 ± 6	0.39 ± 0.01	150 ± 8	0.37 ± 0.02
S+Pb	149 ± 8	0.31 ± 0.01	139 ± 7	0.28 ± 0.02
S+S	140 ± 5	0.26 ± 0.02	143 ± 5	0.23 ± 0.02
p+Pb	136 ± 4	0.26 ± 0.02	142 ± 4	0.15 ± 0.03
p+S	133 ± 4	0.22 ± 0.03	139 ± 4	0.05 ± 0.10
p+Be	147 ± 4	0.10 ± 0.03	—	—
p+p	136 ± 15	0.09 ± 0.15	140 ± 10	0.12 ± 0.09

Table 7.3: The freeze-out temperature T_{fo} and radial flow velocity $\langle \beta_t \rangle$ for both positive and negative hadrons produced at CERN energies in a variety of collision systems.

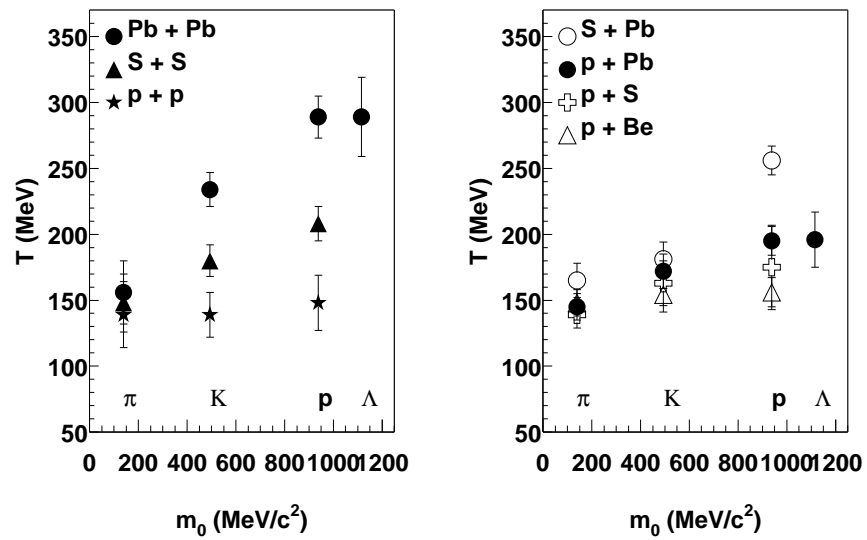


Figure 7.1: The effective temperatures are plotted against particle mass for positive particles produced in symmetric (A+A) collisions (left) and asymmetric (p+A and A+B) collisions (right) at CERN energies. Error bars are statistical only.

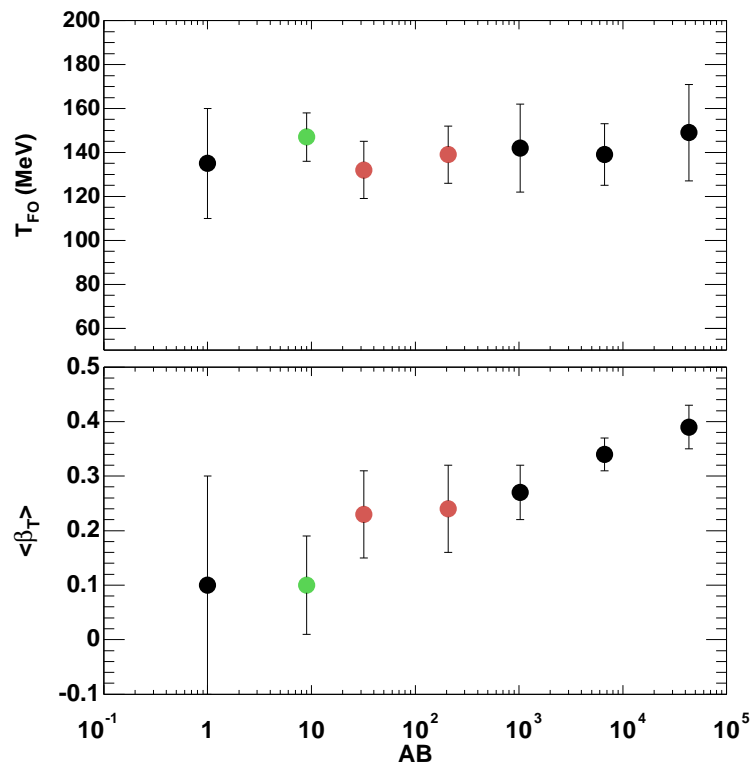


Figure 7.2: The freeze-out temperature T_{fo} (top) and radial flow velocity $\langle \beta_t \rangle$ (bottom) plotted for each system in terms of system size AB at CERN energies.

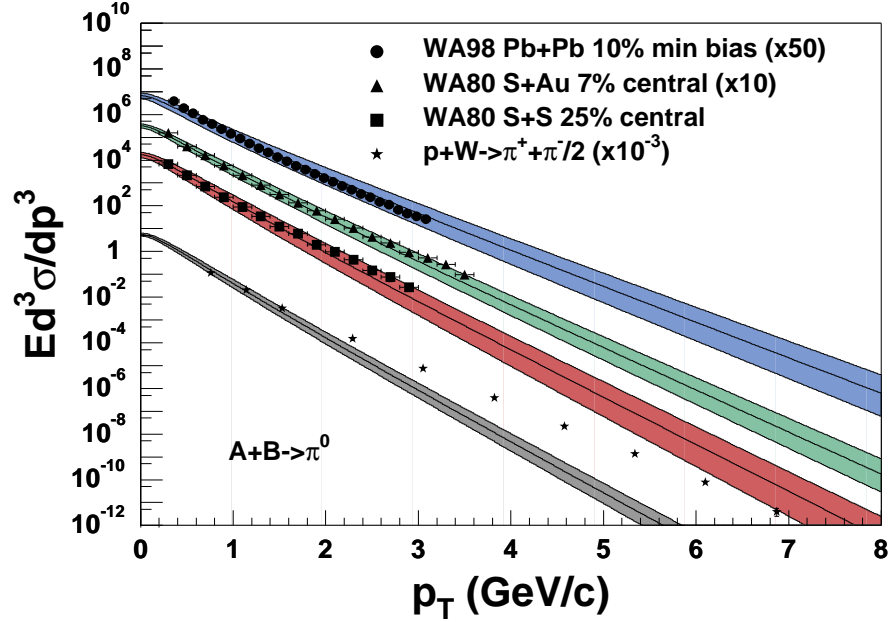


Figure 7.3: Results of calculating the p_t distribution using a hydrodynamics based parameterization for pions measured out to ≈ 3 GeV produced in a variety of collision systems.

spectra produced in the most central Pb + Pb collisions are measured out to p_t of ≈ 3 GeV/c by the WA98 collaboration [105]. The analysis is repeated for the WA80 central S + Au, measured out to ≈ 3.5 GeV/c and 25% central S + S measured out to ≈ 3 GeV/c [106]. The $p + W \rightarrow (\pi^+ + \pi^-)/2$ data is used as a control for the boosted extrapolations [107].

The resulting boosted spectra compared to highest available hadron data at CERN energies for the four different collision systems are in Figure 7.3. The error bands correspond to the errors in T_{fo} and β_t , after adding in quadrature the systematic and statistical uncertainties in the effective temperatures for each collision system. The parameters are anticorrelated, so the bands are determined as $T_{fo} \pm \Delta T_{fo}$ and $\beta_t \mp \Delta \beta_t$ accordingly. For all heavy-ion collisions, the spectra can be described hydrodynamically up to the measured p_t ranges. The pions produced in p+W clearly deviate from the hydrodynamic parameterization at $p_t > 2$ GeV/c. The long tail in the p+W spectra is caused

by the Cronin effect¹ and hard processes such as high p_t jets. In order to see the effects of hard processes in the heavy-ion hadron data, measurements out to 5 GeV/c need to be made.

The radial flow velocity and freeze-out temperature used to extrapolate the boosted spectrum for the most central Pb+Pb collisions are compared to an independent measurement of these values, also made at CERN. In Reference [79], a parameterization by Chapman et al. is used to fit the single particle transverse mass distribution for central Pb+Pb collisions. This parameterization uses the same source function as used in their HBT pion correlation analysis². Fitting both the hadrons, deuterons, and using the m_t dependence of the measured HBT source radii, overlapping χ^2 contours result in the range $T_{fo} = 120 \pm 12$ MeV and $\beta_t = 0.55 \pm 0.12$.

No correction is made for the resonance contribution, which results in a smaller freeze-out temperature[69]. The difference in T_{fo} between Reference [79] and the present analysis is due to the pion resonance contribution which dominates the pion spectra for $m_t - m_0 < 0.3$. Assuming a linear velocity profile, the extracted value of $\beta_t = 3/2 < \beta_t > = 3/2(0.39) = 0.55$ for positive particles in Pb+Pb collisions, from published NA44 effective temperatures, is consistent with Reference [79].

The result of the analysis is that the CERN data can be described hydrodynamically, contrary to the assertion made in Reference [78]. These are the highest p_t nuclear data available at CERN energies. In order to observe the onset of hard processes in the most central collisions, it is necessary to repeat the analysis for hadron distributions produced in nuclear collisions at 10 times the center-of-mass energy³, or measure out to 5 GeV/c at CERN energies. A similar analysis that is based on the hydrodynamic results presented in Chapter 6 is compared to the high p_t hadron distributions measured at RHIC energies in PHENIX [81].

¹The Cronin effect is caused by the multiple initial scattering of partons in the nucleus[96].

²The HBT analysis measures the Bose-Einstein correlations between π^+ and π^- pairs. A parameterization that simulates both longitudinal and transverse expansion is fit to the measured radius as a function of the mean transverse momentum of the pion pairs.

³The higher the \sqrt{s} , the higher the p_t of produced hadrons.

7.3 Comparison to High p_t Hadron Spectra

Transverse momentum spectra of both charged hadrons and neutral pions in the range $1 < p_t < 5$ GeV/c are also measured in PHENIX at the same energy and reported in Reference [81]. The hydrodynamic results are compared to the charged hadron spectra as measured from the particle data in Chapter 6, as was done previously at CERN energies in Section 7.2. There is no evidence for hard processes in the measured p_t range at CERN energies. By performing the same comparison at RHIC energies, the p_t where hard processes start to dominate the spectra is determined.

Before the comparison can be made, a simple conversion must be made for consistency. The charged hadrons are measured in η and not y , because the particle mass is not known. The hydrodynamic fits to the particle spectra are converted to units of η . The conversion mostly affects low momentum.

The difference between pseudorapidity and rapidity is important when comparing identified particles to unidentified charged particles. In Figure 7.4, the factor y/η is plotted at each value of p_t for pions, kaons, and protons. The factor is greatest at low momentum for protons. The pions are more relativistic at these momenta and the factor is smaller accordingly. For each particle, the transverse momentum spectrum $d^2N/p_t dp_t dy$ is multiplied by the momentum-dependent conversion in Figure 7.4 to produce $d^2N/p_t dp_t d\eta$.

In Figure 7.5, the fit results assuming radial flow from the $\pi K p$ spectra are compared to the high p_t hadron spectra in the most central events (5% of the total inelastic cross section). In the left panel, the total charged hadron spectrum is calculated based on a hydrodynamic fit to the particle spectra produced in 5% central Au+Au collisions in Chapter 6. Each curve below the total is the contribution from $K^+ + K^-$, $\pi^+ + \pi^-$, and $p + \bar{p}$. The right panel is the comparison of the total curve determined from the left panel to the measured charged hadrons $h^+ + h^-$. No fit is made to the charged hadrons, the total curve is compared absolutely. The data differ from the hydrodynamic extrapolation at $\approx 2.5 - 3$ GeV/c in p_t . The deviation is dominated by soft physics. To study jet quenching, hadrons should be measured above 3 GeV/c in p_t .

A plausible explanation for the protons crossing the pions is that the high p_t pions suffer from jet-quenching, which decreases the p_t of the pion spectrum measured for $p_t > 2.5$ GeV/c, while the (anti)proton spectrum is broadened in p_t due to the radial flow. The spectra therefore appear to cross. The crossing region of \bar{p}/π^- also increases with decreasing number of participants as predicted in [2].

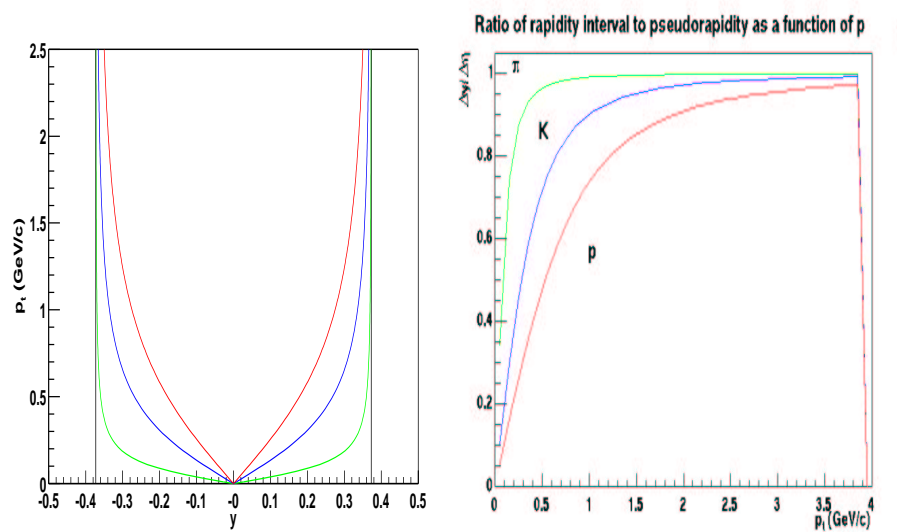


Figure 7.4: The phase space boundaries for pions, kaons, and protons. The vertical axis is p_t and the horizontal axis is y . The vertical lines correspond to the acceptance in η . On the right panel, the factor y/η (vertical) is plotted for each value of p_t .

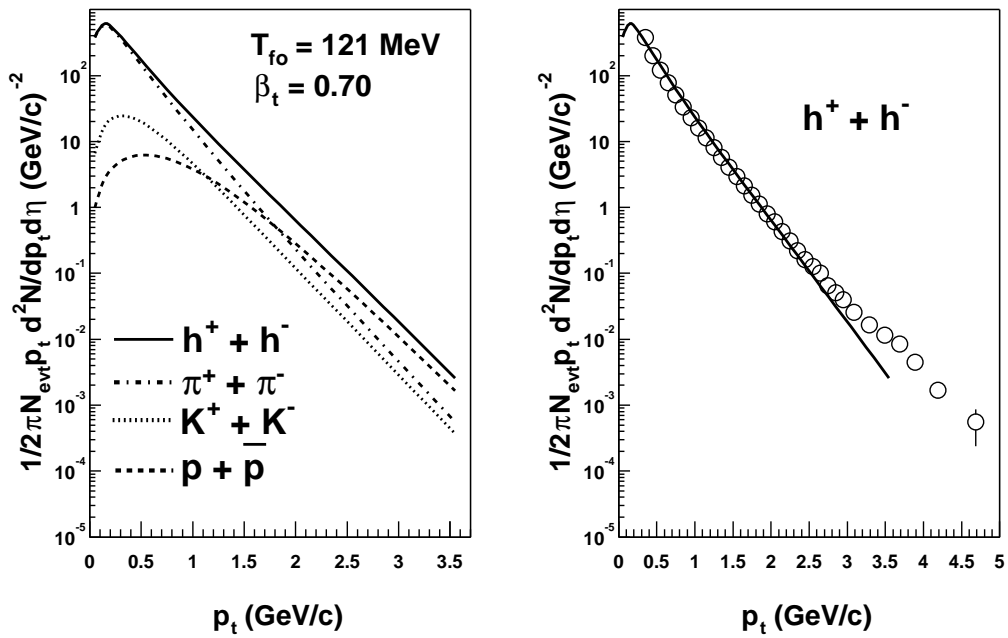


Figure 7.5: The high p_t hadron spectra in Reference [81] compared to the fit results assuming radial flow from the $\pi K p$ spectra in the most central events.

7.4 HIJING: pQCD Model Prediction at RHIC Energies

A model based on perturbative QCD (pQCD) calculations at RHIC energies is called HIJING (Heavy Ion Jet Interacting Generator) [95]. The HIJING model is first tuned to reproduce the p+p and p+A invariant cross section data at CERN energies. For p+A collisions, the parton distributions of protons and neutrons are scaled by a nuclear modification factor $S_{a/A}(x, b)$ that depends on the impact parameter b of the nucleus A

$$f_{a/A}(x, Q^2, b) = S_{a/A}(x, b) \left[\frac{Z}{A} f_{a/p}(x, Q^2) + \left(1 - \frac{Z}{A}\right) f_{a/n}(x, Q^2) \right] \quad (7.1)$$

where $f_{a/p}(x, Q^2)$ and $f_{a/n}(x, Q^2)$ are the proton and neutron structure functions, respectively. The variable x is the momentum fraction of the parton and Q^2 is the momentum transfer given to the parton. Folded with the structure functions, this simulates the probability of scattering two quarks. Using the Woods-Saxon distribution for the thickness function, the A+A particle cross sections are estimated. The invariant cross sections of particles produced in Au+Au collisions at RHIC energies are calculated reliably down to a few GeV in p_t .

In Figure 7.6, the multiplicity distribution of charged particles is used to determine the 10% most central events and 85% most peripheral events from minimum bias HIJING events. Unlike what is observed in data in Section 6.1, Chapter 6, the proton spectra do not cross the pion spectra (see Figure 7.7). Instead, the (anti)proton spectra cross the kaon spectra at about 1.5 GeV/c in p_t for the 10% central Au+Au events in HIJING.

For comparison to the observed effective temperature dependence on particle mass in the data, the effective temperatures are extracted from the predicted particle distributions generated from HIJING calculations. The m_t distributions of the resulting 10% most central events for pions, kaons, and protons are shown in Figure 7.8. The thermal fits are m_t exponentials as in Equation 6.12 that are fit over the range $(m_t - m_0) < 1$ GeV. For the 85% most peripheral events, equivalent fits are made to the m_t spectra. The effective temperatures are independent of particle mass and are similar to those from a static hadron-emitting thermal source as shown in Figure 7.9. In summary, HIJING cannot predict the suppressed pion spectrum and the broadened proton spectrum as observed in the data (see Section 6.1, Chapter 6). Also, the effective temperatures are consistently flat with varying particle mass. Since there is no multiple rescattering, the pressure does not increase

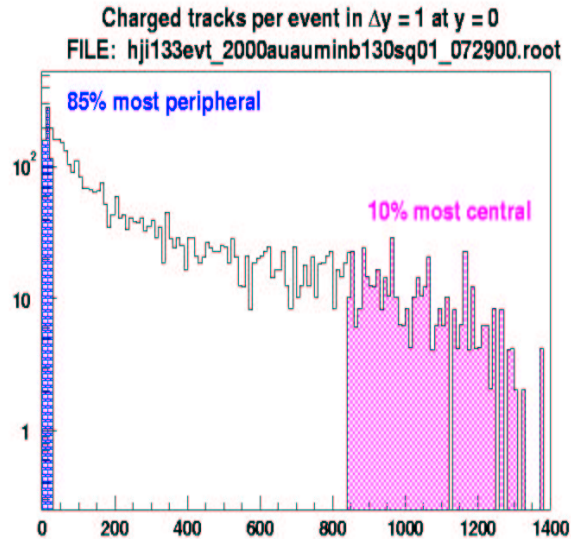


Figure 7.6: The multiplicity distribution of charged particles produced in HIJING.

and the hadrons do not collectively flow. Even though HIJING is tuned to reproduce the p+p data and scaled by a nuclear enhancement factor, it cannot predict the cross-over for the most central events.

7.5 Multiplicity Dependence on Centrality

The measured particle production (multiplicity) dependence on the number of participant nucleons is compared to the equivalent published values. As the differential number of charged particles per pseudorapidity interval, $dN_{ch}/d\eta$ is measured as the masses are unknown, the particle spectra are first converted to η components using the procedure described in Section 7.3. The same procedure used to determine dN/dy is performed to obtain $dN/d\eta$ as described in Chapter 6. For each centrality, the total $dN/d\eta$ is determined by summing the $dN/d\eta$ for each particle. The $dN/d\eta$ in each centrality is then scaled by $0.5N_p$. The result (solid points) is compared to the published total charged multiplicity (open points) for each centrality as a function of the number of participants in Figure 7.10. The agreement is excellent. The dashed lines represent the parameterization described in Reference [80]. As a comparison, the PHOBOS and STAR values for $dN_{ch}/d\eta$ are shown for the top centrality 0 – 5%. The values of $dN_{ch}/d\eta$ as presented here for π Kp are

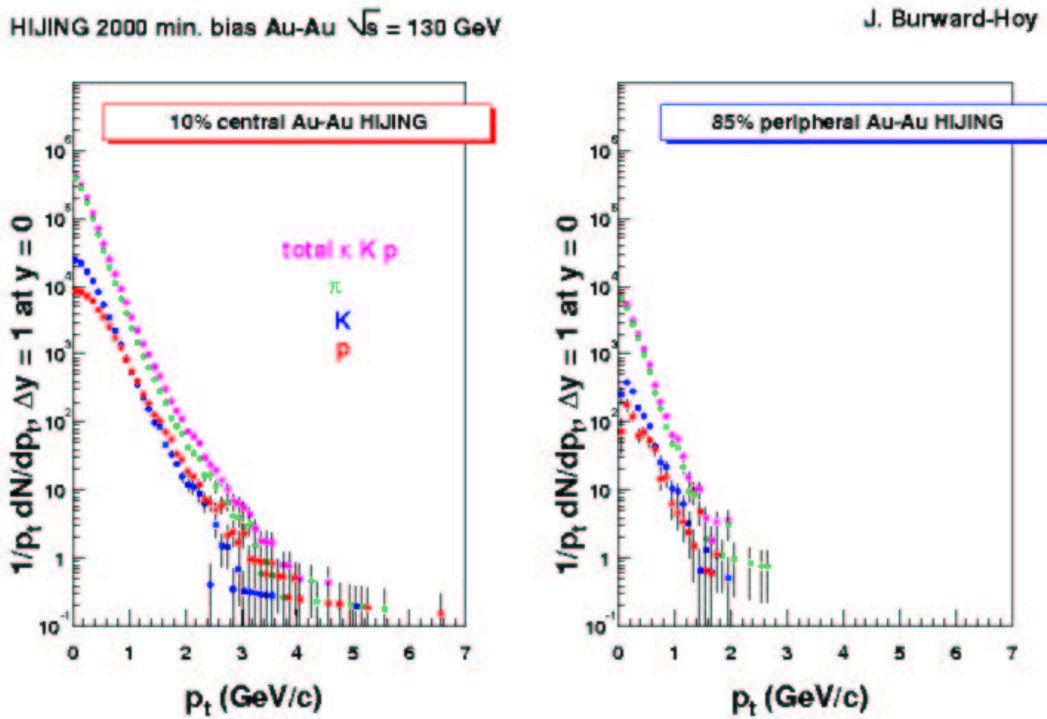


Figure 7.7: The p_t distributions of hadrons in HIJING events for the 10% central (left) and 85% centrality (right). The proton spectra cross the kaon spectra and not the pion spectra as is observed in data.

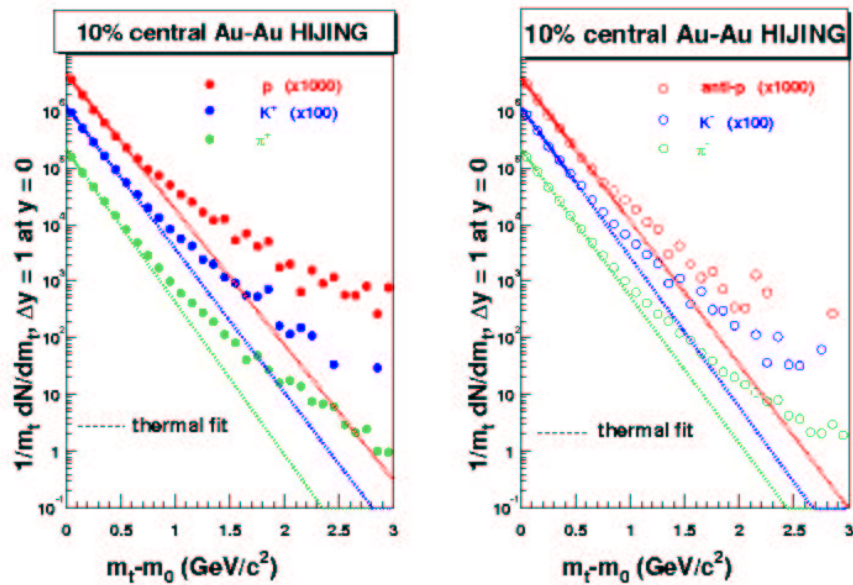


Figure 7.8: The $m_t - m_0$ distributions of pions, kaons, and protons in 10% central HIJING events at RHIC energies. The dotted lines are simple exponential fits in the range $m_t - m_0 < 1$ GeV.

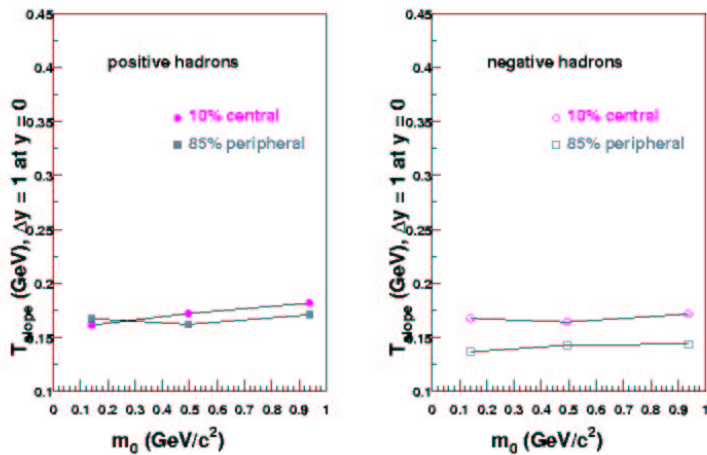


Figure 7.9: The effective temperatures of pions, kaons, and protons at $m_t - m_0 < m_0$ are independent of particle mass in both central and peripheral HIJING events at RHIC energies.

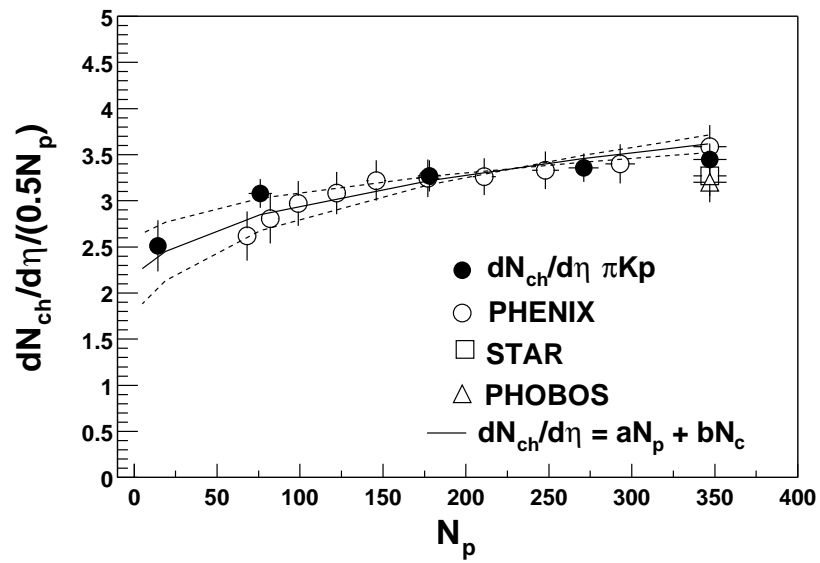


Figure 7.10: Both the total charged multiplicity (open) in References [80, 83, 84] and the total identified charged multiplicity (closed) scaled by the number of participant pairs are plotted together as a function of the number of participants.

	0-5%	5-15%	15-30%	30-60%	60-92%
π Kp	598 ± 30	455 ± 21	291 ± 15	117 ± 6	18 ± 2
PHENIX[80]	622 ± 41				
STAR[83]	567 ± 38				
PHOBOS[84]	555 ± 37				

Table 7.4: The $dN_{ch}/d\eta$ as determined from summing the yields for π , K, and $(\bar{p})p$ respectively. Published values that are measured in the 0-5% centrality are shown as a comparison. The errors include both statistical and systematic uncertainties.

tabulated in Table 7.4. The line is the parameterization of $dN_{ch}/d\eta$ in terms of the number of collisions and the number of participants,

$$dN_{ch}/d\eta = (aN_p + bN_c) \quad (7.2)$$

where $a = 0.88 \pm 0.28$ and $b = 0.34 \pm 0.12$ as determined in Reference [80]. The first term is the number of particles that are produced by the participant nucleons (wounded nucleons), while the second is the high energy contribution to particle production which is proportional to the number of binary collisions. In comparison to SPS energies, the multiplicity scales linearly with the number of participants as N_p^α , where $\alpha \approx 1.08$ as measured by WA98 [108]. At RHIC energies, the second term is the particle production that results at high energy [86].

7.6 Hydrodynamic Model Comparison

In the discussion that follows, a hydrodynamics model by Peter Kolb and Ulrich Heinz is compared to the data for different centralities. What is written here summarizes the analysis by Peter Kolb and the unpublished results are obtained by private communication. References are made to relevant publications that describe the model in more detail.

Ideally, a model will have only a few parameters. First, the parameters that are tuned to predict the spectra at RHIC energies are described and then the resulting spectra are compared to both the data and the parameterized fit as described in Chapter 6.

7.6.1 Initial Parameter Tuning

The initial parameters in the calculation are tuned to reproduce the shape of the transverse momentum spectra in the p_t range 0.3 – 2.0 GeV/c for the

most central events (the 0-5% centrality).

The following initial conditions are used in the hydrodynamics model at RHIC energies. The initial parameters are the entropy density s_0 , baryon number density n_0 , the equilibrium time τ_0 , and the freeze-out temperature T_{fo} which controls the duration of the expansion. As these are preliminary results, the parameters have an uncertainty of 10%. These parameters are adjusted to the following values and are explained in more detail in [87] and [88]:

- $s_0 = 85 \text{ fm}^{-3}$. This corresponds to $\epsilon_0 = 21.28 \text{ GeV/fm}^3$ and $T_{max} = 327.7 \text{ MeV}$,
- $n_0 = 0.19 \text{ fm}^{-3}$ such that $\bar{p}/p \approx 0.6$ when $T_c = 165 \text{ MeV}$,
- $\tau_0 = 0.6 \text{ fm/c}$. This is the time just after the produced particles have thermalized, and
- $T_{fo} = 128 \text{ MeV}$.

The variable T_c is defined to be the chemical freeze-out temperature when particle production stops. The initial entropy(energy) density $s_0(\epsilon_0)$ and maximum temperature T_{max} are fixed to match the measured multiplicity for the most central collisions with the relation

$$s(s_p, s_c) = 0.75s_p + 0.25s_c, \quad (7.3)$$

where s_p and s_c are the number densities for the number of participants and the number of collisions, respectively. This parameterization is tuned to produce the measured $dN_{ch}/d\eta$ dependence on both N_p and N_c . The calculated maximum initial energy density and maximum temperature for each of the centrality selections measured in PHENIX are shown in Table 7.5⁴. An additional tuning is the re-scaling of both the proton and anti-proton spectra after the model is run. Both the proton and anti-proton spectra are scaled by factors that fix the ratio $\bar{p}/\pi^- = 0.074$ as is observed at the chemical freeze-out temperature. The resulting factors are 3.09 and 4.72 for protons and antiprotons, respectively.

⁴Courtesy of Peter Kolb.

Centrality (%)	Impact Parameter (%)	ϵ_{max} (GeV/fm ³)	T_{max} (MeV)
0-5%	0	21.28	327.7
5-15%	5	18.49	316.2
15-30%	7	15.70	303.3
30-60%	9.5	10.59	274.0
60-92%	12.5	2.747	190.4

Table 7.5: Peter Kolb’s calculated maximum initial energy density and maximum temperature for a variety of impact parameters in the transverse plane. The initial energy density is determined using both wounded nucleons and the number of binary collisions.

7.6.2 The Comparison

The hydrodynamic model spectra are shown in Figure 7.11 for pions and Figure 7.12 for protons as dashed lines. The solid lines are the simultaneous fit results from the hydrodynamic parameterization. The model includes resonances. The parameterization is fit in the range $0.5 < p_t < 1.13$ GeV/c for pions to avoid the resonance contribution. Both the parameterization and model agree for most of the centralities. The hydrodynamic model for the two most peripheral events (the bottom two curves) tend to overpredict the data in both the proton and anti-proton spectra; however the uncertainties are still 10% in the initial parameters.

The average initial energy density $\langle \epsilon_0 \rangle$ is 4.8 GeV/fm³ at a proper time $\tau = 1$ fm/c for collisions with impact parameter zero (the most central)[86]. The measured average from the data in Chapter 6 is 4.9 GeV/fm³. Both the model and data are in excellent agreement. In the model, the $\langle p_t \rangle$ of π^- is systematically higher by 16% than the measured values. This is most likely due to the extrapolation in the experimental value to zero (see Chapter 6) using a functional form that curves up at low p_t compared to the spectrum shape from the model. The average radial flow velocities are within 5%, in excellent agreement. The values are tabulated in Table 7.6. A hydrodynamic model is powerful if it can describe other measurements that are consistent with hydrodynamic assumptions. These measurements include elliptic flow [88] and the HBT source radii [11].

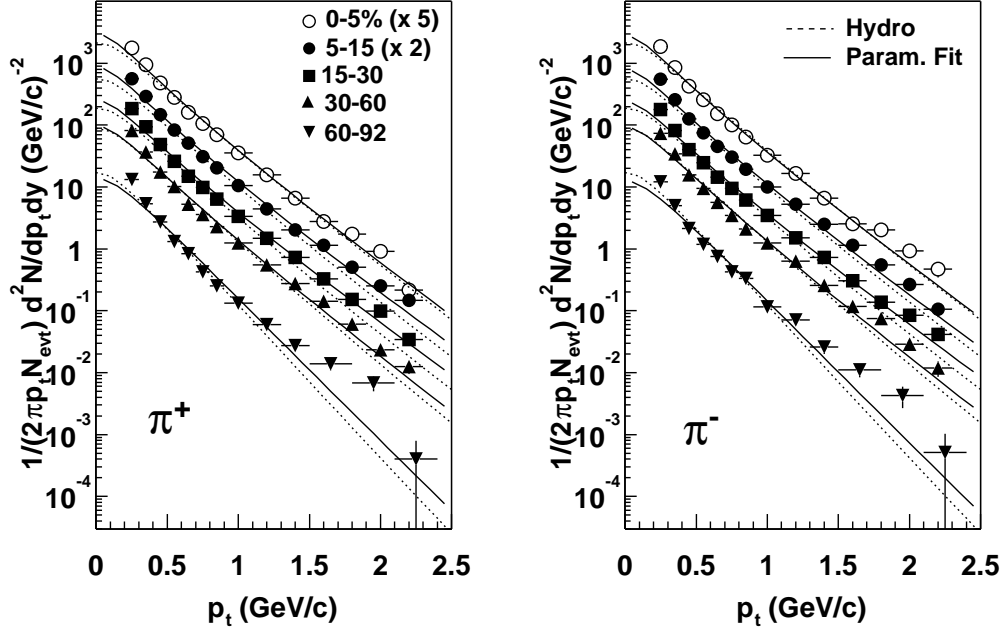


Figure 7.11: The hydrodynamics calculation with initial parameters tuned to match the most central spectra in the p_t range 0.3 – 2.0 GeV/c.

	0-5%	5-15%	15-30%	30-60%	60-92%
Hydro $\langle \beta_t \rangle$	0.476	0.4546	0.4334	0.3811	0.2407
Data $\langle \beta_t \rangle$	0.47	0.46	0.43	0.39	0.16
Hydro $\langle p_t \rangle$	0.4561	0.4537	0.4482	0.4314	0.3749
Data $\langle p_t \rangle$	0.38 ± 0.02	0.39 ± 0.01	0.38 ± 0.01	0.36 ± 0.02	0.32 ± 0.02

Table 7.6: The $\langle \beta_t \rangle$ as measured from the data compared to the hydrodynamics values. The values are within 5%. The $\langle p_t \rangle$ are also compared for negative pions.

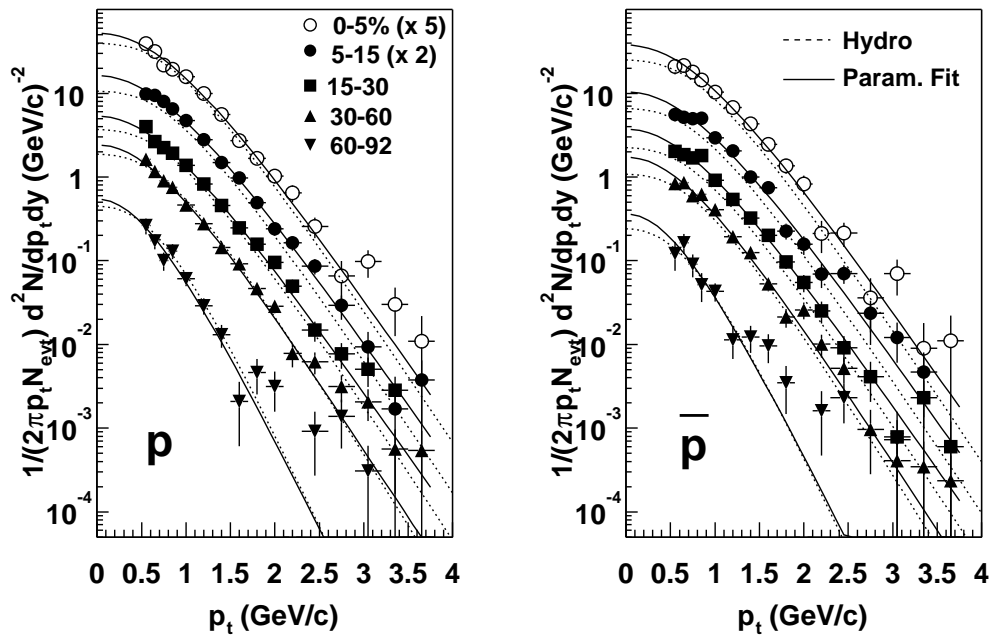


Figure 7.12: The hydrodynamics calculation with initial parameters tuned to match the most central spectra.

7.7 Particle Yields and Ratios

The kaon to pion ratios for both positive and negative particles are dependent on the number of participants. This is also true for the proton to pion ratios. The \bar{p}/π^- is independent on the number of participants. While pair production may be the dominant mechanism for the \bar{p}/π^- , the K/π and p/π^+ ratios suggest a dependence on the number of nucleon-nucleon binary collisions. The increase in production of strange quarks relative to u and d quarks is due to hard processes between the partons in the incident colliding nucleons.

In Figure 7.13, the K^+/π^+ ratios for different center of mass energies are compared for both heavy-ion and pp collisions. The experimental values are taken from References [89, 90, 91, 92, 93]. In pp collisions at ISR energies, soft hadrons are the decay products of fireballs generated by partonic interactions of the colliding hadrons, according to Reference [94]. Between 20 GeV and 200 GeV, the K^+/π^+ ratio is independent of energy. The strangeness production at RHIC for the most peripheral events (60-92%) is comparable to pp collisions.

Strangeness production in heavy-ion collisions is systematically higher than in pp collisions. The K^+/π^+ produced in the most central events at RHIC follows the heavy-ion trend, which increases dramatically at AGS energies and saturates at CERN SPS energies. The increase in the ratio between Pb+Pb at 17 GeV to Au+Au at 130 GeV is less than 2%.

The pion yields are linearly dependent on the number of participants N_p ; they are independent of N_p when scaled by the number of participant pairs. This suggests that the pions do not have a hard contribution to their yield.

The observed increase in the initial energy density of 70% when compared to CERN SPS energies is most likely due to the increase in the number of particles produced and not in the increase of energy per particle. This is also consistent with the measured transverse energy as a function of participant number (cite reference).

The \bar{p}/p ratio is 10% higher than the experimental values measured in Pb+Pb collisions at CERN energies [77]. Because the net number of protons is close to zero, most of the baryons are produced pairs. This is very different from Pb+Pb collisions at $\sqrt{s} = 17$ GeV, where $\bar{p}/p \approx 0.07$. In Au+Au collisions at $\sqrt{s} = 4.5$ GeV, the \bar{p}/p is 0.02%. There is not enough energy at 4.5 GeV for proton and antiproton pair production. In heavy-ion collisions at AGS and CERN SPS energies, most of the protons are stopped at midrapidity. At RHIC energies, protons from the incident nuclei are transported over 2 rapidity units[84]. The ratio of K^-/K^+ ratio is 0.87 ± 0.20 at RHIC energies for the most central Au+Au events is 50% higher than what is measured in

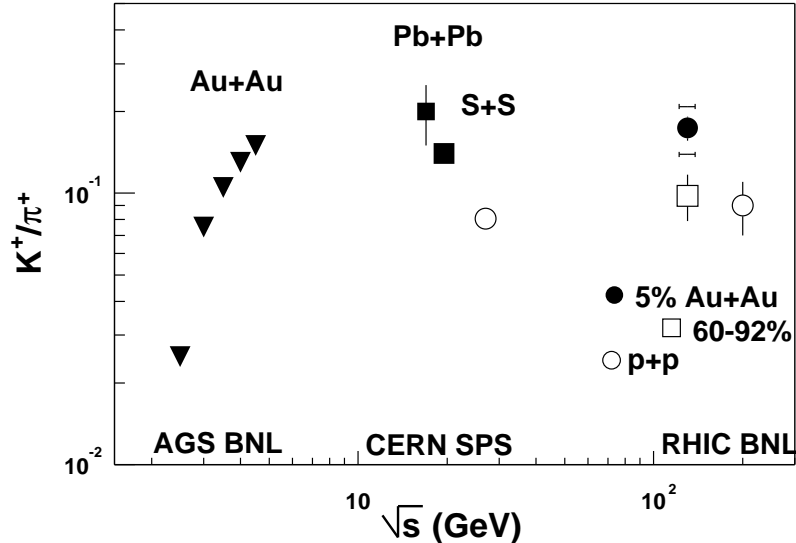


Figure 7.13: The K^+/π^+ ratio for different center of mass energies.

the most central Pb+Pb collisions at CERN [90] and 83% higher than what is measured at AGS energies [89] for the most central Au+Au collisions.

7.8 Conclusion and Outlook

The first new feature we observe is the crossing of the proton spectra and pion spectra in the region $1.5 - 2.0$ GeV/c in p_t . This crossing is not predicted in HIJING perturbative QCD calculations. Possible explanations include the radial expansion which is dominant in the proton spectra and the jet quenching of the pions [2, 3]. The crossing region of \bar{p}/π^- increases with decreasing number of participants as is predicted in [3].

The data indicate both soft and hard physics contributions in the measured cross sections. In collisions with the highest initial energy density, the transition region in the spectra occurs in the range $p_t \approx 2.5 - 3$ GeV/c. In order to measure jet quenching, the hadron spectra should be measured for $p_t > 3$ GeV/c. At CERN SPS energies, the spectra need to be measured for $p_t > 5$ GeV/c.

The total produced yields are in excellent agreement with charged parti-

cle yields from three independent measurements from PHOBOS, STAR, and PHENIX. The initial energy density is 70% higher than what is measured in Pb+Pb collisions at the CERN SPS. This increase is most likely due to an increase in particle production.

In Year-2, the full event rate at RHIC will result in higher statistics for the hadron spectra. This will enable a π K separation out to 5 GeV/c in p_t and the crossing of protons and pions will be measured with larger statistics. The RICH detectors will be used for electron and pion rejection for high $p_t > 5$ GeV/c pions. Other hadron spectra, such as the Λ and $\bar{\Lambda}$ spectra will be measured. Ultimately, the resonance and weak-decay contributions will be measured in the spectra. Additional comparisons will be made between PHENIX results and the other experiments.

At RHIC energies, the measured initial energy density is well above the threshold for a QGP phase transition; however, additional measurements of hadron and lepton observables will be necessary in order to experimentally confirm the predicted phase transition. Once this is accomplished, increasing the energy density may be necessary in order to test QCD further. The Large Hadron Collider at CERN will be a factor of 10 higher in center of mass energy than at RHIC energies with a physics program beginning in the year 2005.

Bibliography

- [1] Xin-Nian Wang, Phys. Rev. C 58 (1998) 2321.
- [2] Jet Quenching and the $\bar{p} \geq \pi^-$ Anomaly at RHIC, Ivan Vitev and Miklos Gyulassy, nucl-th/0104066, 22 Apr 2001.
- [3] Explanation of the RHIC p_t -spectra in a thermal model with expansion, Wojciech Broniowski and Wojciech Florkowski, nucl-th/0106050, 21 Jun 2001, Long Island, New York, January 2001.
- [4] Testing the Friedman Equation: The Expansion of the Universe During Big-Bang Nucleosynthesis, Sean Carroll et al, astro-ph/01018002, submitted to Phys.Rev.D.
- [5] From the early universe to large scale structure, Peter Anninos, gr-qc/0108083, appearing in Living Reviews in Relativity.
- [6] "Quarks and Leptons," Francis Halzen and Alan D. Martin, John-Wiley and Sons, Inc., New York, USA, 1984.
- [7] The European Physical Journal C, Review of Particle Physics 3, Number 1-4, 1998.
- [8] E.V. Shuryak, Phys. Rept. 61, 71 (1980).
- [9] Equation of state, radial flow, and freeze-out in high energy heavy ion collisions, C.M. Hung and E. Shuryak, Phys. Rev. C 57 (1998) 1891.
- [10] S.A. Bass, M. Gyulassy, H Stocker, and W. Greiner, J. Phys. G: Nucl. Part. Phys. (1998).
- [11] Two-Particle Correlations in Relativistic Heavy-Ion Collisions, U. Heinz and Barbara V Jacak, Ann. Rev. Nucl. Part. Sci 49 (1999) 529-579.

- [12] First Measurements of Pion Correlations by the PHENIX Experiment, S.C. Johnson, for the PHENIX Collaboration, Contribution to Quark Matter 2001, Long Island, New York, Jan. 15-20, 2001.
- [13] G.E. Brown and M. Rho, *Phys. Rev. Lett.* 66, (1991).
- [14] Highly relativistic nucleus-nucleus collisions: The central rapidity region, J.D. Bjorken, *Phys. Rev. D* 27, Number 1, (1983).
- [15] F. Weber, *J. Phys. G: Nucl. Part. Phys.* 25 (1999), R195-R229.
- [16] Figure courtesy of Federica Messer, Ph.D. thesis.
- [17] F. Cooper and G. Frye, *Phys. Rev. D* 10, 186 (1974).
- [18] R. Venugopalan and M. Prakash, *Nucl. Phys. A* 546 (1992) 718.
- [19] R. Venugopalan and M. Prakash, *Phys. Rev. Lett.* 41 (1990) 221.
- [20] W.A. Zajc, Heavy ion collider detectors, *Nuclear Instruments and Methods in Physics Research Section A* 453 (1-2) (2000) pp. 25-31.
- [21] The Relativistic Heavy Ion Collider Design Manual (unpublished).
- [22] Photograph obtained from the Relativistic Heavy Ion Collider website.
- [23] Diagram obtained from the Collider-Accelerator Department website.
- [24] Relativistic Heavy Ion Collider (to appear in *Nuclear Instruments and Methods in Physics Research Section A* in 2001).
- [25] W. Wajc for the PHENIX Collaboration, Quark Matter 2001 Proceedings.
- [26] M. Chiu, J. Nagle, S. White, A. Franz, et. al. (unpublished).
- [27] Picture courtesy of Richard Hutter.
- [28] J. Mitchell, Brookhaven National Laboratory.
- [29] Jiangyoung Jia, State University of New York at Stony Brook.
- [30] R. J. Glauber in: *Lectures in Theoretical Physics* eds., W.E. Brittin and L.G. Dunham (Interscience, New York, 1959).

- [31] Hadron production in nuclear collisions at RHIC and high density QCD, nucl-th/0012025, 11 Apr 2001.
- [32] Online monitoring figure by Dr. Steve Adler, the PHENIX Collaboration (figure obtained from PHENIX website).
- [33] Tracking Chambers at RHIC, Julia Velkovska, SUNY Stony Brook, contributed talk, Application of Accelerators in Research and Industry, Sixteenth Int'l Conf., American Institute of Physics, 2001 (227).
- [34] Master Thesis (1999), Tassilo Christ, SUNY Stony Brook.
- [35] D.P. Morrison for the PHENIX Collaboration, Nucl. Phys. A 638 (1998) 565c.
- [36] N. Saito, Spin physics with the PHENIX detector system, Nuclear Physics A 638 (1-2) (1998) pp. 575-578.
- [37] Plot obtained from the PHENIX web page.
- [38] K. Ikematsu et al., Nuclear Instruments and Methods in Physics Research Section A 411 (1998) 238-248.
- [39] C. Adler, A. Denisov, E. Garcia, M. Murray, H. Stroebele, S. White. nucl-ex/0008005 (2000).
- [40] M.J. Bennett et al., The PHENIX multiplicity and vertex detector, Nuclear Physics A 661 (1-4) (1999) pp. 661-664. J.S. Kapustinsky et al., A double-metal silicon pad design for the PHENIX multiplicity/vertex detector, Nuclear Instruments and Methods in Physics Research Section A 409 (1-3) (1998) pp. 173-175.
- [41] V.G. Riabov, Drift chambers for the PHENIX central tracking system, Nuclear Instruments and Methods in Physics Research Section A 419 (2-3) (1998) pp. 363-369.
- [42] Plots courtesy of S.C. Johnson, PHENIX Collaboration.
- [43] J. Barrette et al., The pixel readout system for the PHENIX pad chambers, Nuclear Physics A 661 (1-4) (1999) pp. 665-668.
- [44] K. Barish et al., The PHENIX time expansion chamber, Nuclear Physics A 661 (1-4) (1999) pp. 669-672.

- [45] Y. Akiba, J. Burward-Hoy, et al, Nuclear Instruments and Methods in Physics Research A, 433 (1-2) (1999) pp. 143-148. Y. Akiba et al., Nuclear Instruments and Methods in Physics Research Section A 453 (1-2) (2000) pp. 279-283.
- [46] Y. Tanaka et al., Front-end readout system for PHENIX RICH, Nuclear Instruments and Methods in Physics Research Section A 455 (3) (2000) pp. 576-588.
- [47] Y. Miake, American Inst. Phys. 340 (1995) 78-89; L. Carlen et al., Nucl. Instr. and Meth. A 431 (1999) 123-133.
- [48] W. Klempt, Nuclear Instruments and Methods in Physics Research Section A 433 (1-2) (1999) 542-553.
- [49] Event Reconstruction in the PHENIX Central Arm Spectrometers, J.T. Mitchell, et. al, submitted to Nuclear Instruments and Methods in Physics Research Section A (OASIS NIMA 41226) (2000).
- [50] The robust fitting algorithm is based on the routine used by the CERES experiment at the CERN SPS (A. Drees, F. Messer et al).
- [51] M. Chiu, J. Nagle, D. Morrison, S. Mioduszewski, K. Reygers, Internal PHENIX Analysis Note 18 (2000).
- [52] K. Reygers, Internal PHENIX Analysis Note 78 (2001).
- [53] R. Auerbeck, A. Drees, J. Jia, F. Messer, F. Muehlbacher, J. Velkovska, PHENIX Internal Analysis Note 50 (2001).
- [54] Plot courtesy of Hiroaki Ohnishi, PHENIX Collaboration.
- [55] Plot courtesy of Tatsuya Chujo, PHENIX Collaboration.
- [56] H. Hamagaki for the PHENIX Collaboration, Quark Matter 2001 Proceedings.
- [57] R. Auerbeck, J. Burward-Hoy, A. Drees, T. Hemmick, B. Jacak, J. Jia, A. Kiyomichi, H. Ohnishi, J. Velkovska, Internal PHENIX Analysis Note 80 (2001).
- [58] J. M. Burward-Hoy, Internal PHENIX Analysis Note 35 (2000).

- [59] R. Averbeck, J. Burward-Hoy, T. Chujo, A. Drees, A. Kiyomichi, F. Messer, F. Muehlbacher, H. Ohnishi, J. Velkovska, Internal PHENIX Analysis Note 37 (2001).
- [60] R. Averbeck, J. Burward-Hoy, A. Drees, H. Hemmick, B. Jacak, J. Jia, H. Ohnishi, J. Velkovska, Internal PHENIX Analysis Note 74 (2001).
- [61] Plot courtesy of F. Messer, PHENIX Collaboration.
- [62] Written by R. Averbeck, State University of New York, Stony Brook.
- [63] G. Agakichiev et. al., Eur. Phys. Jour. C4 (1998) 231.
- [64] The Perfect Tracker and Evaluator algorithms were written by S.C. Johnson (now at Lawrence Livermore National Laboratory) and R. Averbeck, State University of New York, Stony Brook.
- [65] The simulated single particle embedding package is written by J. Jia, PHENIX Collaboration, SUNY Stony Brook.
- [66] F. Ceretto (Messer) (1998), Ph.D. thesis.
- [67] A. Drees, Internal PHENIX Analysis Note 67 (2001).
- [68] Identified charged hadron production at RHIC, PHENIX Collaboration, to be published in Physics Review Letters (2001).
- [69] Ekkard Schnedermann, Josef Sollfrank, and Ulrich Heinz, Phys. Rev. C 48, No. 5, 2462 (1993).
- [70] Thermodynamics, Kinetic Theory, and Statistical Thermodynamics, Sears and Salinger, Addison-Wesley Publishing Company, Reading Massachusetts (1986).
- [71] Statistical Physics, L.D. Landau and E.M. Lifshitz, Butterworth-Heinemann, Oxford (1951).
- [72] S. Esumi, S. Chapman, H. van Hecke, and Nu Xu, Physical Review C 55, No. 5 (1997).
- [73] Plot courtesy of D. Teaney, SUNY Stony Brook.
- [74] The hydrodynamics points and spectra are presented here courtesy of Peter Kolb.

- [75] Private communication with Peter Kolb.
- [76] Measurement of the mid-rapidity transverse energy distribution from $\sqrt{s_{NN}} = 130$ GeV Au+Au collisions at RHIC, PHENIX Collaboration, Phys. Rev. Lett (2001).
- [77] NA44 Collaboration, Phys. Letters B 388 (1996) 431-436.
- [78] Xin Nian Wang, Phys. Rev. Letters 81, Number 13, 2655 (1998).
- [79] NA49 Collaboration, Eur. Phys. J. C 2, 661-670 (1998).
- [80] PHENIX Collaboration, Phys. Rev. Lett. 86, 3500 (2001).
- [81] Suppression of Hadrons with Large Transverse Momentum in Central Au-Au Collisions at $\sqrt{s_{NN}} = 130$ GeV, The PHENIX Collaboration, August 22, 2001 (submitted to Phys. Rev. Lett.); Quark Matter 2001 Proceedings.
- [82] Equation of state, radial flow, and freeze-out in high energy heavy ion collisions, C.M. Hung and E. Shuryak, Phys. Rev. C 57, Number 4, April 1998.
- [83] STAR Collaboration, Quark Matter 2001 Proceedings.
- [84] Charged-particle pseudorapidity density distribution from Au+Au collisions at $\sqrt{s_{NN}} = 130$ GeV, PHOBOS Collaboration, nucl-ex/0106006, 6 Jun 2001.
- [85] J. Harris, STAR Collaboration, Talk presented at Quark Matter Conference 2001, Stony Brook, January 2001.
- [86] Hydrodynamic flow at RHIC, Peter F. Kolb, Proc. 17th Winter Workshop on Nuclear Dynamics, Park City, Utah, USA (2001).
- [87] Anisotropic transverse flow and the quark-hadron phase transition, Peter F. Kolb, Josef Sollfrank, and Ulrich Heinz, Phys. Rev. C 62 (2000).
- [88] Elliptic Flow at SPS and RHIC: From Kinetic Transport to Hydrodynamics, P.F. Kolb, P. Huovinen, U. Heinz, and H. Heiselberg, hep-ph/0012137, Phys. Letters B, in press.
- [89] Review of nuclear reactions at the AGS, C. Ogilvie, Quark Matter 2001 Proceedings (and references therein).

- [90] NA44 Collaboration, Phys. Letters B 471 (1999) 6-12.
- [91] NA35 Collaboration, Z. Phys. C 58 (1993) 367.
- [92] LEBC-EHS Collaboration, Z. Phys. C 50 (1991) 405.
- [93] UA5 Collaboration, Nucl. Phys. B 328 (1989) 36.
- [94] Eur. Phys. J. C 18(2001) 563-576.
- [95] Xin-Nian Wang, Phys. Rev. D 43 (1991) 104.
- [96] D. Antreasyan, J.W. Cronin, H.J. Frisch, M.J. Shochet, L. Kluberge, P.A. Piroue, and R.L. Sumner, Phys. Rev. D 19 (1979) 764.
- [97] NA44 Collaboration, Phys. Rev. C 57 (1998) 837.
- [98] NA44 Collaboration, Phys. Rev. C 59 (1999) 328.
- [99] NA44 Collaboration, Phys. Rev. Letters 78, No. 11 (1997).
- [100] NA44 Collaboration, Nucl. Phys. A 590 (1995) 523c.
- [101] NA49 Collaboration, Nucl. Phys. A 610 (1996) 188c.
- [102] ISR, Nucl.Phys. B 100 (1975) 237.
- [103] ISR, Nucl.Phys. B 116 (1976) 77.
- [104] WA97 Collaboration, Phys. Lett. B 433, Issue 1-2 (1998) 209.
- [105] WA98 Collaboration, M.M. Aggarwal et al., Phys. Rev. Lett. 81 (1998) 4087-4091.
- [106] WA80 Collaboration, R. Albrecht et al., Eur. Phys. J. C 5 (1998) 255-267.
- [107] Cronin et al., Phys. Rev. D 11, No. 11 (1975).
- [108] WA98 Collaboration, M.M. Aggarwal, et al., Eur. Phys. J C 18 (2001) 651.

Appendix A

Tables of Invariant Cross Sections

The invariant cross section is the double differential in transverse momentum and rapidity variables:

$$\frac{d^2N}{2\pi N_{evt} p_t dp_t dy} \quad (\text{A.1})$$

expressed in units of c^2/GeV^2 . For each of the following tables, the errors include the statistical error from the data and the systematic uncertainty from the bin correction. Positive and negative particles with the same mass are tabulated together.

p_t	π^+	π^-
0.25	112.403381±1.880760	108.724174 ± 2.008756
0.35	55.686600 ± 0.957232	49.865032 ± 0.928933
0.45	27.981390 ± 0.522599	24.115091 ± 0.491539
0.55	15.699497 ± 0.314688	14.560169 ± 0.330541
0.65	9.077192 ± 0.200005	8.673667 ± 0.220801
0.75	5.802424 ± 0.14164	5.645314 ± 0.160719
0.85	3.795581 ± 0.105970	3.574268 ± 0.114851
0.95	2.400232 ± 0.075427	2.283496 ± 0.081152
1.05	1.605748 ± 0.056668	1.613605 ± 0.064098
1.15	1.028164 ± 0.040360	1.165465 ± 0.051738
1.25	0.706376 ± 0.031083	0.757289 ± 0.037462
1.35	0.464375 ± 0.023162	0.540930 ± 0.030179
1.45	0.345790 ± 0.019290	0.311731 ± 0.020296
1.55	0.237678 ± 0.015678	0.217263 ± 0.015805
1.65	0.160162 ± 0.011982	0.150416 ± 0.012839
1.75	0.114363 ± 0.009690	0.113465 ± 0.010595
1.85	0.078846 ± 0.007775	0.092009 ± 0.009316
1.95	0.063192 ± 0.006596	0.066122 ± 0.007622
2.05	0.035725 ± 0.004831	0.034131 ± 0.005346
2.15	0.025519 ± 0.003813	0.024580 ± 0.004298
2.25	0.015466 ± 0.002849	0.019674 ± 0.003695

Table A.1: Invariant cross section for positive and negative pions produced in minimum bias events. The errors include the statistical error from the data and the systematic uncertainty from the bin correction.

p_t	K^+	K^-
0.45	6.145813 ± 0.429140	4.576652 ± 0.395962
0.55	4.009192 ± 0.259180	3.239306 ± 0.246768
0.65	2.826578 ± 0.170301	2.147586 ± 0.159324
0.75	1.661132 ± 0.103360	1.579896 ± 0.113719
0.85	1.304979 ± 0.084993	1.169340 ± 0.088428
1.00	0.675819 ± 0.038873	0.591414 ± 0.040688
1.20	0.366657 ± 0.023994	0.320291 ± 0.025257
1.40	0.193754 ± 0.014648	0.137424 ± 0.012952
1.60	0.087417 ± 0.008289	0.081584 ± 0.008878

Table A.2: Invariant cross section for positive and negative kaons produced in minimum bias events. The errors include the statistical error from the data and the systematic uncertainty from the bin correction.

p_t	p	\bar{p}
0.55	2.253295 ± 0.138411	1.189064 ± 0.110466
0.65	1.750277 ± 0.096512	1.166351 ± 0.094183
0.75	1.380516 ± 0.078194	0.979152 ± 0.073558
0.85	1.181093 ± 0.067957	0.949184 ± 0.070883
0.95	0.979109 ± 0.057372	0.654602 ± 0.051189
1.05	0.702205 ± 0.042934	0.503017 ± 0.038599
1.15	0.596906 ± 0.037599	0.347985 ± 0.029042
1.25	0.413912 ± 0.027637	0.344296 ± 0.029868
1.35	0.316000 ± 0.023306	0.223672 ± 0.020994
1.45	0.228625 ± 0.018625	0.181462 ± 0.018644
1.55	0.174744 ± 0.015497	0.145356 ± 0.016125
1.70	0.118620 ± 0.008392	0.080207 ± 0.007469
1.90	0.067746 ± 0.005503	0.041304 ± 0.004776
2.10	0.036215 ± 0.003757	0.022088 ± 0.003258
2.30	0.019733 ± 0.002567	0.011693 ± 0.002100
2.50	0.010436 ± 0.001746	0.010610 ± 0.001939
2.70	0.006394 ± 0.001282	0.002620 ± 0.000894
2.90	0.003487 ± 0.000847	0.003401 ± 0.001016
3.10	0.002768 ± 0.000739	0.001144 ± 0.000474
3.30	0.001370 ± 0.000469	0.000969 ± 0.000439

Table A.3: Invariant cross section for protons and antiprotons produced in minimum bias events. The errors include the statistical error from the data and the systematic uncertainty from the bin correction.

p_t	π^+	π^-
0.25	354.678253 ± 8.870661	370.790314 ± 9.974777
0.35	188.297409 ± 4.915118	169.201447 ± 4.886657
0.45	95.470909 ± 2.832097	85.738220 ± 2.847889
0.55	56.149567 ± 1.831556	51.342472 ± 1.955462
0.65	32.130817 ± 1.208998	30.401445 ± 1.352175
0.75	21.074289 ± 0.897326	20.043797 ± 1.019591
0.85	14.028296 ± 0.701180	12.791404 ± 0.755836
1.00	7.139374 ± 0.319851	6.528771 ± 0.341583
1.20	3.157450 ± 0.185953	3.313038 ± 0.223188
1.40	1.319694 ± 0.108373	1.317090 ± 0.124481
1.60	0.552899 ± 0.067645	0.506440 ± 0.070455
1.80	0.345117 ± 0.051278	0.404215 ± 0.060224
2.00	0.182570 ± 0.033894	0.184480 ± 0.039068
2.20	0.043494 ± 0.015531	0.094209 ± 0.025532

Table A.4: Invariant cross section for positive and negative pions produced in the 0-5% centrality. The errors include the statistical error from the data and the systematic uncertainty from the bin correction.

p_t	K^+	K^-
0.45	21.460285 ± 2.910133	20.579514 ± 3.243572
0.55	15.372856 ± 1.854499	13.015769 ± 1.888413
0.65	9.348874 ± 1.110120	7.915579 ± 1.171795
0.75	5.335274 ± 0.687584	5.062783 ± 0.768727
0.85	5.659477 ± 0.672608	3.615072 ± 0.585431
1.00	2.658314 ± 0.272636	2.097209 ± 0.269170
1.20	1.344369 ± 0.166017	1.296232 ± 0.186873
1.40	0.558529 ± 0.090836	0.619106 ± 0.110966
1.60	0.382781 ± 0.070605	0.262133 ± 0.064893

Table A.5: Invariant cross section for positive and negative kaons produced in the 0-5% centrality. The errors include the statistical error from the data and the systematic uncertainty from the bin correction.

p_t	p	\bar{p}
0.55	7.880279 ± 0.962818	4.204628 ± 0.840803
0.65	6.339887 ± 0.675603	4.297285 ± 0.697454
0.75	4.366022 ± 0.499065	3.574926 ± 0.539169
0.85	3.868814 ± 0.440195	2.879245 ± 0.458818
1.00	3.142257 ± 0.244346	2.078044 ± 0.229175
1.20	2.002548 ± 0.168224	1.358032 ± 0.159363
1.40	1.118864 ± 0.115497	0.860341 ± 0.115611
1.60	0.541775 ± 0.073670	0.492069 ± 0.080052
1.80	0.335851 ± 0.053768	0.272646 ± 0.055176
2.00	0.204428 ± 0.037861	0.164940 ± 0.042142
2.20	0.129057 ± 0.029574	0.042131 ± 0.017478
2.45	0.051301 ± 0.014009	0.043098 ± 0.013996
2.75	0.013236 ± 0.006682	0.007177 ± 0.005217
3.05	0.019634 ± 0.007114	0.014105 ± 0.006459
3.35	0.006039 ± 0.003535	0.001805 ± 0.001807
3.65	0.002190 ± 0.002193	0.002221 ± 0.002224

Table A.6: Invariant cross section for protons and antiprotons produced in the 0-5% centrality. The errors include the statistical error from the data and the systematic uncertainty from the bin correction.

p_t	π^+	π^-
0.25	282.078644 ± 6.061248	275.380066 ± 6.518840
0.35	146.285217 ± 3.280852	128.141113 ± 3.191878
0.45	73.535576 ± 1.862933	62.884819 ± 1.790531
0.55	41.363132 ± 1.160002	37.721771 ± 1.224918
0.65	25.642372 ± 0.798581	22.607384 ± 0.846591
0.75	15.382240 ± 0.557308	15.325456 ± 0.645343
0.85	10.276505 ± 0.431052	9.621212 ± 0.471111
1.00	5.290095 ± 0.196036	5.043291 ± 0.214139
1.20	2.210896 ± 0.109291	2.637686 ± 0.141561
1.40	1.013316 ± 0.066874	1.246218 ± 0.087070
1.60	0.566848 ± 0.048930	0.571077 ± 0.052751
1.80	0.254853 ± 0.029735	0.273799 ± 0.034271
2.00	0.125791 ± 0.019488	0.133144 ± 0.022570
2.20	0.073247 ± 0.013793	0.053113 ± 0.013440

Table A.7: Invariant cross section for positive and negative pions produced in the 5-15% centrality. The errors include the statistical error from the data and the systematic uncertainty from the bin correction.

p_t	K^+	K^-
0.45	15.637797 ± 1.741157	12.551521 ± 1.744714
0.55	11.260056 ± 1.114792	7.958909 ± 1.025840
0.65	7.483896 ± 0.727727	7.008992 ± 0.782413
0.75	4.648152 ± 0.469713	4.986730 ± 0.554055
0.85	3.641411 ± 0.381575	3.724235 ± 0.436070
1.00	1.912274 ± 0.164325	2.051577 ± 0.191157
1.20	1.137383 ± 0.108574	0.866852 ± 0.105607
1.40	0.534800 ± 0.062366	0.432668 ± 0.063987
1.60	0.251185 ± 0.039416	0.254543 ± 0.044288

Table A.8: Invariant cross section for positive and negative kaons produced in the 5-15% centrality. The errors include the statistical error from the data and the systematic uncertainty from the bin correction.

p_t	p	\bar{p}
0.55	4.901357 ± 0.533467	2.783103 ± 0.478789
0.65	4.708341 ± 0.414342	2.588809 ± 0.386785
0.75	4.006443 ± 0.351171	2.502131 ± 0.316258
0.85	3.259707 ± 0.291802	2.507218 ± 0.303908
1.00	2.373570 ± 0.153971	1.477835 ± 0.135544
1.20	1.393580 ± 0.099979	1.023421 ± 0.097878
1.40	0.744873 ± 0.066088	0.502885 ± 0.061320
1.60	0.487384 ± 0.050094	0.372548 ± 0.049793
1.80	0.246384 ± 0.032289	0.113494 ± 0.024275
2.00	0.120152 ± 0.020683	0.078263 ± 0.019426
2.20	0.081918 ± 0.015915	0.034826 ± 0.011205
2.45	0.043132 ± 0.008831	0.035301 ± 0.008737
2.75	0.014561 ± 0.004686	0.011828 ± 0.004874
3.05	0.004683 ± 0.002374	0.006082 ± 0.003066
3.35	0.000850 ± 0.000851	0.002342 ± 0.001670
3.65	0.001871 ± 0.001337	–

Table A.9: Invariant cross section for protons and antiprotons produced in the 5-15% centrality. The errors include the statistical error from the data and the systematic uncertainty from the bin correction.

p_t	π^+	π^-
0.25	186.076965 ± 3.904568	179.813110 ± 4.173567
0.35	93.467865 ± 2.060555	81.856361 ± 1.999121
0.45	48.465652 ± 1.195200	40.107689 ± 1.119559
0.55	26.036377 ± 0.720550	24.548098 ± 0.776498
0.65	15.010371 ± 0.473632	14.512262 ± 0.530157
0.75	9.893822 ± 0.350256	9.537067 ± 0.396370
0.85	6.401269 ± 0.266796	6.123549 ± 0.294376
1.00	3.351424 ± 0.121959	3.448246 ± 0.138930
1.20	1.470903 ± 0.069841	1.505393 ± 0.082489
1.40	0.723165 ± 0.044638	0.723754 ± 0.051581
1.60	0.325510 ± 0.028389	0.304363 ± 0.029644
1.80	0.152171 ± 0.017931	0.137812 ± 0.018756
2.00	0.098554 ± 0.013638	0.085190 ± 0.014213
2.20	0.034495 ± 0.007257	0.041570 ± 0.009165

Table A.10: Invariant cross section for positive and negative pions produced in the 15-30% centrality. The errors include the statistical error from the data and the systematic uncertainty from the bin correction.

p_t	K^+	K^-
0.45	10.022571 ± 1.095717	6.549067 ± 0.972691
0.55	6.578553 ± 0.670772	4.762258 ± 0.615808
0.65	4.742712 ± 0.445502	3.124552 ± 0.401325
0.75	3.124560 ± 0.297783	2.506989 ± 0.302215
0.85	2.135251 ± 0.225121	1.951316 ± 0.241651
1.00	1.338092 ± 0.108042	0.885104 ± 0.096268
1.20	0.640326 ± 0.062306	0.545914 ± 0.066301
1.40	0.333462 ± 0.038081	0.242411 ± 0.037208
1.60	0.120284 ± 0.021058	0.160967 ± 0.027174

Table A.11: Invariant cross section for positive and negative kaons produced in the 15-30% centrality. The errors include the statistical error from the data and the systematic uncertainty from the bin correction.

p_t	p	\bar{p}
0.55	3.980795 ± 0.380126	2.031382 ± 0.318395
0.65	2.665342 ± 0.242032	1.857176 ± 0.254930
0.75	2.242063 ± 0.202983	1.695511 ± 0.206447
0.85	1.930207 ± 0.174142	1.793970 ± 0.203620
1.00	1.369577 ± 0.090722	0.909540 ± 0.083401
1.20	0.823462 ± 0.059650	0.541992 ± 0.054828
1.40	0.455696 ± 0.040310	0.322705 ± 0.038074
1.60	0.247961 ± 0.027303	0.200973 ± 0.027862
1.80	0.157787 ± 0.020028	0.097006 ± 0.017669
2.00	0.095474 ± 0.014288	0.054771 ± 0.012534
2.20	0.049824 ± 0.009662	0.024971 ± 0.007313
2.45	0.014793 ± 0.004007	0.009114 ± 0.003470
2.75	0.007743 ± 0.002606	0.004134 ± 0.002078
3.05	0.005039 ± 0.001921	0.000789 ± 0.000789
3.35	0.002825 ± 0.001279	0.002313 ± 0.001342
3.65	–	0.000601 ± 0.000602

Table A.12: Invariant cross section for protons and antiprotons produced in the 15-30% centrality. The errors include the statistical error from the data and the systematic uncertainty from the bin correction.

p_t	π^+	π^-
0.25	81.497780 ± 1.71413	73.905998 ± 1.752676
0.35	36.624748 ± 0.835743	34.308941 ± 0.851634
0.45	17.455591 ± 0.460742	15.661615 ± 0.454633
0.55	10.107584 ± 0.293980	9.560963 ± 0.315925
0.65	5.262456 ± 0.181490	5.688040 ± 0.217633
0.75	3.581926 ± 0.137542	3.475468 ± 0.155921
0.85	2.291283 ± 0.104109	2.099744 ± 0.111952
1.00	1.250822 ± 0.049237	1.248351 ± 0.054828
1.20	0.550560 ± 0.028283	0.633263 ± 0.035685
1.40	0.274864 ± 0.018298	0.255661 ± 0.020140
1.60	0.141429 ± 0.012572	0.117562 ± 0.012300
1.80	0.060361 ± 0.007550	0.075014 ± 0.009216
2.00	0.023467 ± 0.004396	0.028780 ± 0.005495
2.20	0.012417 ± 0.002944	0.011877 ± 0.003312

Table A.13: Invariant cross section for positive and negative pions produced in the 30-60% centrality. The errors include the statistical error from the data and the systematic uncertainty from the bin correction.

p_t	K^+	K^-
0.45	4.338284 ± 0.481166	2.525620 ± 0.395222
0.55	2.351272 ± 0.263579	2.255347 ± 0.284241
0.65	1.930917 ± 0.190744	1.119026 ± 0.156259
0.75	0.927482 ± 0.105986	0.940233 ± 0.120824
0.85	0.672480 ± 0.082557	0.640113 ± 0.090156
1.00	0.435287 ± 0.040291	0.307653 ± 0.037340
1.20	0.213873 ± 0.023939	0.187931 ± 0.025324
1.40	0.110126 ± 0.014392	0.063124 ± 0.012596
1.60	0.057055 ± 0.009834	0.041075 ± 0.009098

Table A.14: Invariant cross section for positive and negative kaons produced in the 30-60% centrality. The errors include the statistical error from the data and the systematic uncertainty from the bin correction.

p_t	p	\bar{p}
0.55	1.626821 ± 0.162052	0.837310 ± 0.135219
0.65	1.172411 ± 0.106518	0.859043 ± 0.115971
0.75	0.903796 ± 0.084641	0.599128 ± 0.080564
0.85	0.753814 ± 0.071549	0.618349 ± 0.078007
1.00	0.463549 ± 0.034159	0.409084 ± 0.036972
1.20	0.278651 ± 0.022636	0.193478 ± 0.021460
1.40	0.144540 ± 0.014931	0.125648 ± 0.015721
1.60	0.091476 ± 0.010902	0.052561 ± 0.009257
1.80	0.046671 ± 0.007250	0.021164 ± 0.005373
2.00	0.028748 ± 0.005203	0.025741 ± 0.005736
2.20	0.007777 ± 0.002481	0.010051 ± 0.003063
2.45	0.006216 ± 0.001820	0.005175 ± 0.001749
2.75	0.003152 ± 0.001123	0.000967 ± 0.000686
3.05	0.002058 ± 0.000846	0.000410 ± 0.000411
3.35	0.000564 ± 0.000401	0.000346 ± 0.000346
3.65	0.000543 ± 0.000385	0.000236 ± 0.000236

Table A.15: Invariant cross section for protons and antiprotons produced in the 30-60% centrality. The errors include the statistical error from the data and the systematic uncertainty from the bin correction.

p_t	π^+	π^-
0.25	13.155022 ± 0.499267	12.117185 ± 0.523969
0.35	5.333086 ± 0.240932	5.011864 ± 0.247994
0.45	2.720976 ± 0.144620	2.128696 ± 0.133987
0.55	1.316177 ± 0.085894	1.176475 ± 0.089716
0.65	0.843434 ± 0.061323	0.747923 ± 0.065516
0.75	0.421674 ± 0.039888	0.423077 ± 0.045961
0.85	0.250568 ± 0.029551	0.332797 ± 0.038659
1.00	0.132499 ± 0.013966	0.114597 ± 0.014463
1.20	0.059546 ± 0.008319	0.071362 ± 0.010615
1.40	0.027559 ± 0.005233	0.025931 ± 0.005825
1.65	0.013873 ± 0.002907	0.011129 ± 0.002793
1.95	0.006864 ± 0.001841	0.004295 ± 0.001627
2.25	0.000399 ± 0.000400	0.000511 ± 0.000511

Table A.16: Invariant cross section for positive and negative pions produced in the 60-92% centrality. The errors include the statistical error from the data and the systematic uncertainty from the bin correction.

p_t	K^+	K^-
0.45	0.493662 ± 0.138850	0.427218 ± 0.144129
0.55	0.196951 ± 0.066191	0.345398 ± 0.097133
0.65	0.218676 ± 0.055342	0.171229 ± 0.054673
0.75	0.113181 ± 0.032951	0.094847 ± 0.033771
0.85	0.054888 ± 0.020861	0.089192 ± 0.029990
1.00	0.043570 ± 0.011318	0.047058 ± 0.013137
1.20	0.008496 ± 0.004256	0.016271 ± 0.006665
1.40	0.007830 ± 0.003511	0.006188 ± 0.003579
1.60	0.007031 ± 0.003154	–

Table A.17: Invariant cross section for positive and negative kaons produced in the 60-92% centrality. The errors include the statistical error from the data and the systematic uncertainty from the bin correction.

p_t	p	\bar{p}
0.55	0.263399 ± 0.057081	0.121989 ± 0.046462
0.65	0.171840 ± 0.035602	0.164110 ± 0.044482
0.75	0.101002 ± 0.024779	0.090536 ± 0.027584
0.85	0.130525 ± 0.026087	0.051480 ± 0.019605
1.00	0.060631 ± 0.010854	0.042981 ± 0.010518
1.20	0.028986 ± 0.006384	0.011358 ± 0.004653
1.40	0.013088 ± 0.003969	0.012282 ± 0.004366
1.60	0.002079 ± 0.001472	0.009567 ± 0.003637
1.80	0.004601 ± 0.002065	0.003486 ± 0.002018
2.00	0.003142 ± 0.001576	–
2.20	–	0.001614 ± 0.001143
2.45	0.000922 ± 0.000653	0.002295 ± 0.001152
2.75	0.001384 ± 0.000814	–
3.05	0.000307 ± 0.000307	0.000729 ± 0.000517

Table A.18: Invariant cross section for protons and antiprotons produced in the 60-92% centrality. The errors include the statistical error from the data and the systematic uncertainty from the bin correction.

Appendix B

Parabolic Velocity Profile

A parabolic velocity profile used in the hydrodynamics parameterization as described in Chapter 6 increases the β_t by $\approx 13\%$. The T_{fo} also increases slightly by $\approx 5\%$. In Table B.1, using a parabolic velocity profile, the T_{fo} and β_t that result after fitting the hydrodynamic parameterization to the single particle spectra for each centrality is shown. The χ^2 contours of β_t versus T_{fo} are also shown for each centrality.

Centrality (%)	T_{fo}	β_t	χ^2/dof
0-5	124 ± 4	0.79 ± 0.01	36.0/40
5-15	133 ± 4	0.76 ± 0.01	50.0/40
15-30	137 ± 4	0.75 ± 0.01	36.2/40
30-60	141 ± 6	0.68 ± 0.02	66.8/40
60-92	$162 \pm_{17}^{10}$	$0.27 \pm_{0.27}^{0.2}$	36.3/40

Table B.1: The T_{fo} and β_t that result after fitting the hydrodynamic parameterization to the particle spectra simultaneously. A parabolic velocity profile is used.

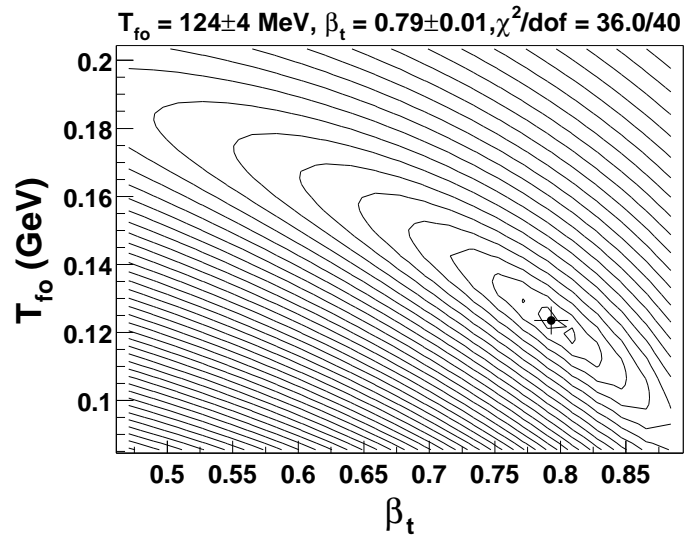


Figure B.1: The χ^2 contours of β_t versus T_{fo} after a simultaneous fit to the 0-5% particle spectra. A parabolic profile is used.

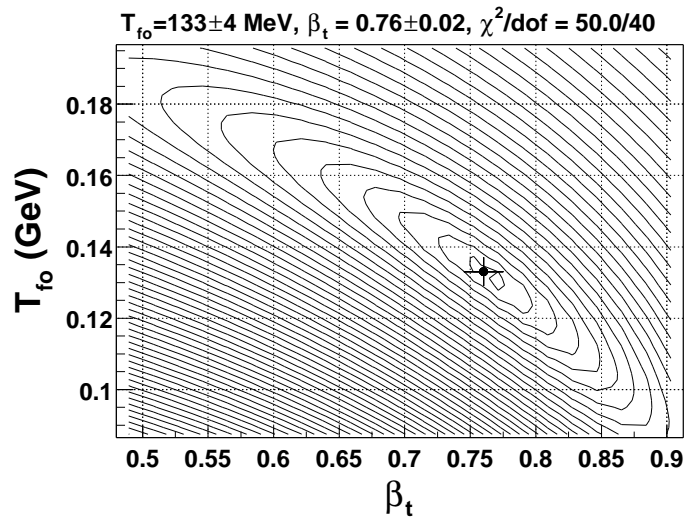


Figure B.2: The χ^2 contours of β_t versus T_{fo} after a simultaneous fit to the 5-15% particle spectra. A parabolic profile is used.

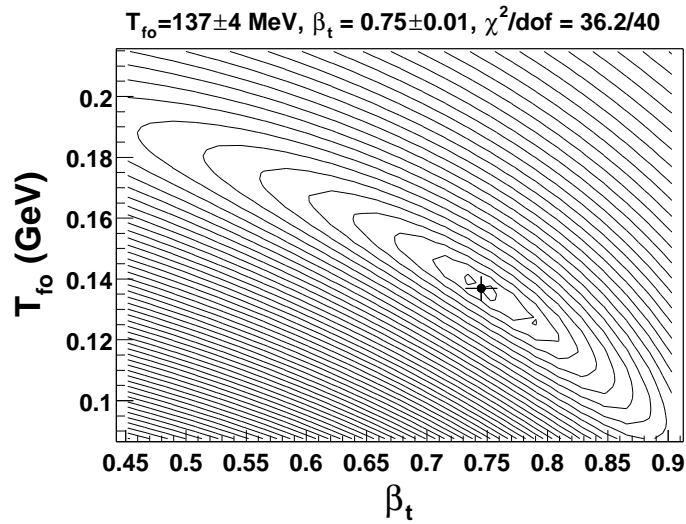


Figure B.3: The χ^2 contours of β_t versus T_{fo} after a simultaneous fit to the 15-30% particle spectra. A parabolic profile is used.

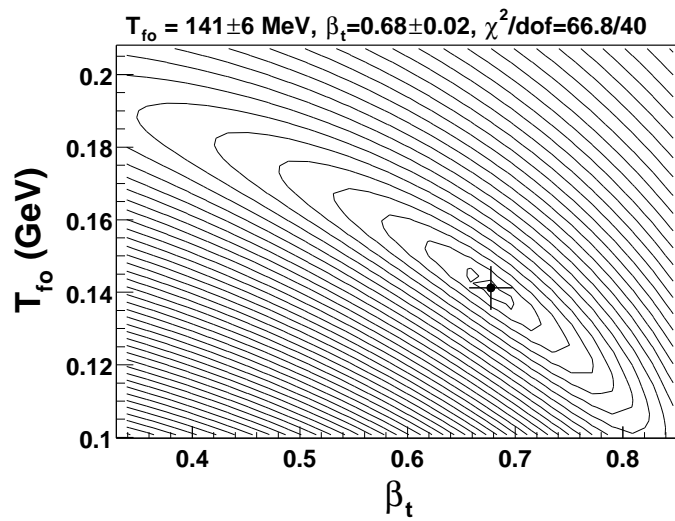


Figure B.4: The χ^2 contours of β_t versus T_{fo} after a simultaneous fit to the 30-60% particle spectra. A parabolic profile is used.

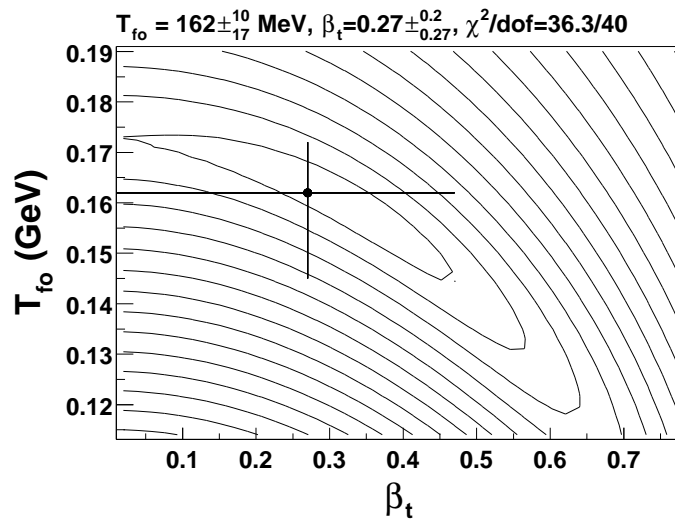


Figure B.5: The χ^2 contours of β_t versus T_{fo} after a simultaneous fit to the 60-92% particle spectra. A parabolic profile is used.

Appendix C

Background from Albedo and Decays

The momentum and track reconstruction assumes that all particles originate at the collision vertex. The background particles from albedo (shower particles from the central magnet) and decays are misreconstructed as high- p_t particles. Monte Carlo is used to study this misreconstruction.

The particles produced in HIJING events are used with the GEANT simulation of the PHENIX detector. In Figure C.1, the parent information from GEANT is used to produce the p_t distributions for primary and secondary particles for both the input Monte Carlo (left) and reconstructed Monte Carlo (right) spectra. The tail in the reconstructed spectrum is due to the particles that do not originate from the event vertex. In Figure C.2, the contribution of misreconstructed decays and albedo is not large below 2.5 GeV/c.

From GEANT, the decay vertices from albedo and decays with $70 < \theta < 100^\circ$ are excluded. The reconstructed spectrum (closed) is shown in Figure C.3; the p_t spectrum of the particles from albedo and decays that are excluded in the cut are shown as stars. As a comparison, the primary particles from Monte Carlo are shown as open points. The signal to background at $p_t > 3$ GeV/c is much improved after cutting on the decay vertices.

Therefore, any analysis of the charged particle p_t spectrum above 3 GeV/c in p_t requires a method that rejects the background from albedo and decays due to misreconstruction. The method used in Year-1 requires the projected point of a reconstructed track to fall within 2σ of a measured space point in one of the outer detectors. Such detectors include: Pad Chamber 3, Time-of-Flight, Time-Expansion Chamber, or the Electromagnetic Calorimeter. The misreconstructed tracks are excluded in the detector matching cuts as described in Chapter 4.

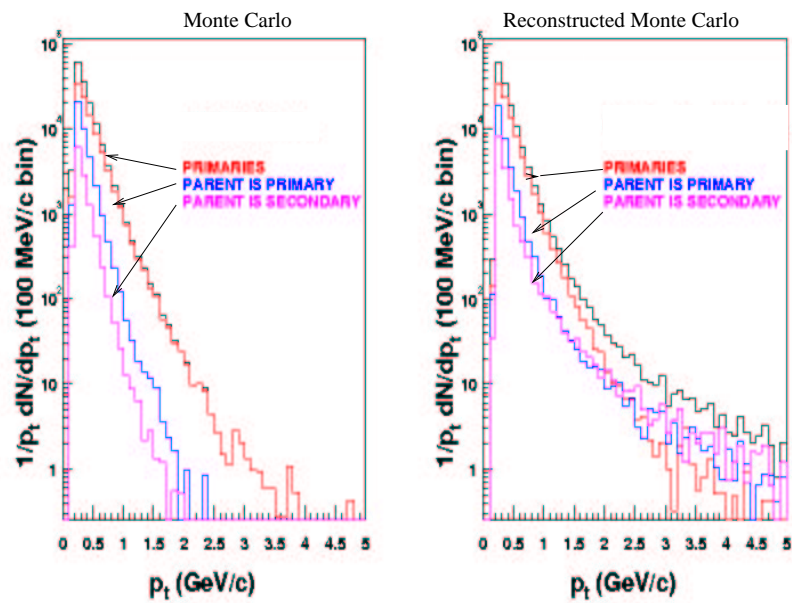


Figure C.1: Monte Carlo (left) and reconstructed Monte Carlo (right) p_t distributions.

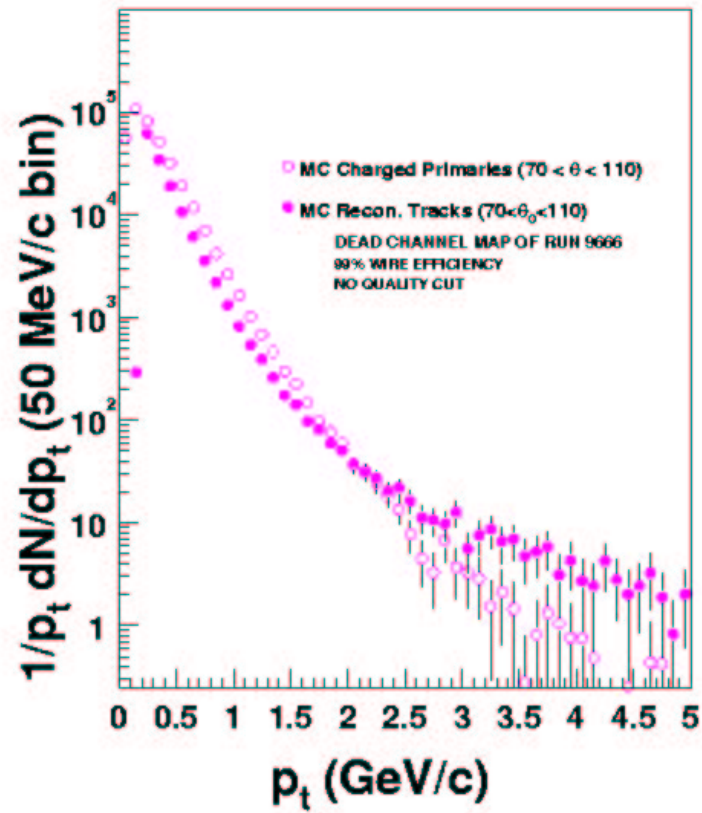


Figure C.2: Monte Carlo input distribution of charged primary particles (before reconstruction, left) compared to the reconstructed distribution (right).

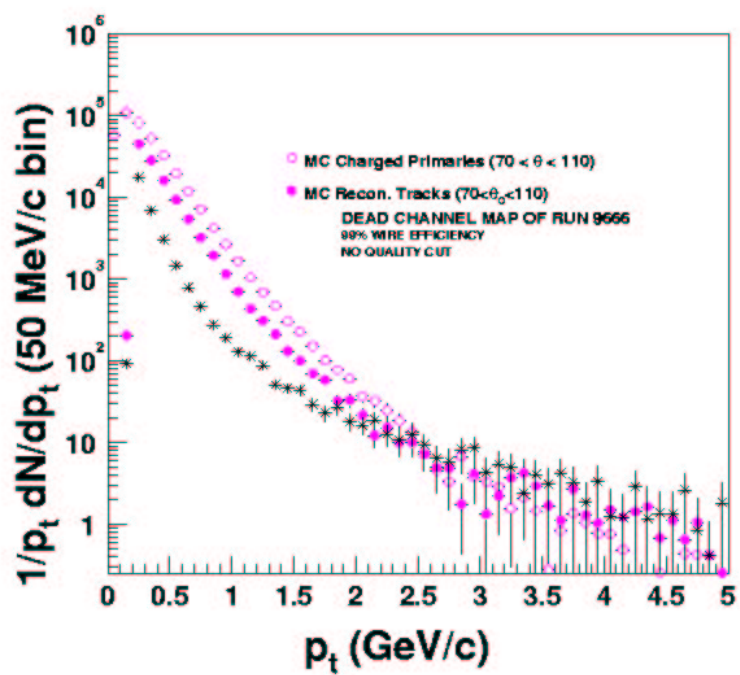


Figure C.3: Same as in Figure C.2 but with decay vertex cut (exclude all decays and albedo outside of 70 and 110 degrees theta). Decays and albedo excluded in the cut are shown as black stars.

Appendix D

Tables of Extrapolated Yields and $\langle p_t \rangle$

The extrapolated values that are used to determine the total integrated yield and average transverse momentum for each particle are tabulated here. The tables are organized by event centrality. A single table corresponds to a single particle. In each table, the fit range in p_t , the number of fitted points, the type of function, the χ^2/dof , the yield dN/dy from zero to the first measured data point (and from the last data point to infinity), and the average transverse momentum $\langle p_t \rangle$ are included. For more detail on how this is done, refer to Chapter 6. The maximum number of points and the smallest χ^2/dof are the criteria that determine which fit range to use for each function. The extrapolated values are added to the integrated data (in Chapter 5) and are tabulated in Chapter 6.

Range (GeV/c)	Eqn	χ^2/dof	dN/dy	$\langle p_t \rangle$ (GeV/c)
0.20-2.20(13)	power-law	23.69/10	291.741012	0.373023
0.20-2.20(13)	m_t exp	550.44/11	243.608612	0.420962
0.20-1.20(8)	power-law	6.43/ 5	324.013229	0.366140
0.20-1.20(8)	m_t exp	130.28/ 6	258.799594	0.402691
0.20-0.95(7)	power-law	6.62/ 4	338.361222	0.370297
0.20-0.95(7)	m_t exp	88.24/ 5	260.529040	0.400791

Table D.1: Extrapolated yield and average transverse momentum after fitting functions to the 0-5% positive pion spectra. The power-law is Equation 6.22 and the m_t exponential is Equation 6.12.

Range (GeV/c)	Eqn	χ^2/dof	dN/dy	$\langle p_t \rangle$ (GeV/c)
0.20 - 2.20(13)	power-law	46.25/10	286.501200	0.366638
0.20 - 2.20(13)	m_t exp	626.50/11	234.659393	0.417642
0.20 - 1.20(8)	power-law	8.04/ 5	330.425391	0.359467
0.20 - 1.20(8)	m_T exp	175.42/ 6	251.413637	0.397147
0.20 - 0.95(7)	power-law	2.10/ 4	356.745564	0.372248
0.20 - 0.95(7)	m_t exp	136.76/ 5	253.337257	0.395019

Table D.2: Extrapolated yield and average transverse momentum after fitting functions to the 0-5% negative pion spectra. The power-law is Equation 6.22 and the m_t exponential is Equation 6.12.

Range (GeV/c)	Eqn	χ^2/dof	dN/dy	$\langle p_t \rangle$ (GeV/c)
0.40-1.65(12)	p_t exp	8.98/10	51.293667	0.535098
0.40-1.65(12)	m_t exp	11.86/10	43.763588	0.587798
0.40-1.20(8)	p_t exp	8.03/ 6	50.884232	0.539093
0.40-1.20(8)	m_t exp	10.63/ 6	44.422034	0.579599
0.40-0.95(5)	p_t exp	7.43/ 3	51.758080	0.530505
0.40-0.95(5)	m_t exp	8.55/ 3	45.762874	0.563665

Table D.3: Extrapolated yield and average transverse momentum after fitting functions to the 0-5% positive kaon spectra. The p_t exponential is Equation 6.23 and the m_t exponential is Equation 6.12.

Range (GeV/c)	Eqn	χ^2/dof	dN/dy	$\langle p_t \rangle$ (GeV/c)
0.40-1.65(12)	p_t exp	6.87/10	42.358656	0.552406
0.40-1.65(12)	m_t exp	11.52/10	36.885703	0.597233
0.40-1.20(8)	p_t exp	2.52/ 6	45.033683	0.521604
0.40-1.20(8)	m_t exp	4.74/ 6	38.987057	0.565875
0.40-0.95(5)	p_t exp	0.35/ 3	49.301831	0.485609
0.40-0.95(5)	m_t exp	0.76/ 3	42.124188	0.533852

Table D.4: Extrapolated yield and average transverse momentum after fitting functions to the 0-5% negative kaon spectra. The p_t exponential is Equation 6.23 and the m_t exponential is Equation 6.12.

Range (GeV/c)	Eqn	χ^2/dof	dN/dy	$\langle p_t \rangle$ (GeV/c)
0.40-4.00(16)	p_t exp	22.53/14	33.622445	0.793153
0.40-4.00(16)	m_t exp	12.65/14	28.922261	0.878829
0.40-2.00(9)	p_t exp	11.99/ 7	32.811663	0.807408
0.40-2.00(9)	m_t exp	6.75/ 7	29.251920	0.871903
0.40-1.20(5)	p_t exp	3.42/ 3	31.835401	0.827493
0.40-1.20(5)	m_t exp	5.89/ 3	29.849428	0.859782

Table D.5: Extrapolated yield and average transverse momentum after fitting functions to the 0-5% proton spectra. The p_t exponential is Equation 6.23 and the m_t exponential is Equation 6.12.

Range (GeV/c)	Eqn	χ^2/dof	dN/dy	$\langle p_t \rangle$ (GeV/c)
0.40 - 3.50(15)	m_t exp	12.37/13	20.275042	0.892245
0.40 - 3.50(15)	p_t exp	27.13/13	23.840210	0.798592
0.40 - 2.00(9)	m_t exp	1.02/ 7	19.971349	0.902083
0.40 - 2.00(9)	p_t exp	4.13/ 7	22.075740	0.846789
0.40 - 1.00(4)	p_t exp	0.53/ 2	20.979729	1.064982
0.40 - 1.00(4)	m_t exp	0.43/ 2	19.533237	0.927215

Table D.6: Extrapolated yield and average transverse momentum after fitting functions to the 0-5% antiproton spectra. The p_t exponential is Equation 6.23 and the m_t exponential is Equation 6.12.

π^+				
Range (GeV/c)	Eqn	χ^2/dof	dN/dy	$\langle p_t \rangle$ (GeV/c)
0.20-2.20(13)	power-law	28.89/10	228.523304	0.367271
0.20-2.20(13)	m_t exp	985.73/11	188.868469	0.417095
0.20-1.20(8)	power-law	6.12/ 5	254.740244	0.355345
0.20-1.20(8)	m_t exp	196.06/ 6	201.715559	0.397549
0.20-0.95(7)	power-law	5.83/ 4	261.807974	0.355967
0.20-0.95(7)	m_t exp	128.00/ 5	203.238218	0.395447
π^-				
Range (GeV/c)	Eqn	χ^2/dof	dN/dy	$\langle p_t \rangle$ (GeV/c)
0.20-2.20(13)	power-law	85.11/10	210.052338	0.378464
0.20-2.20(13)	m_t exp	972.32/11	175.955954	0.424289
0.20-1.20(8)	power-law	12.17/ 5	252.851433	0.369202
0.20-1.20(8)	m_t exp	269.08/ 6	188.359903	0.403489
0.20-0.95(7)	power-law	4.52/ 4	274.945999	0.387557
0.20-0.95(7)	m_t exp	205.93/ 5	189.864172	0.401218

Table D.7: Extrapolated yield and average transverse momentum after fitting functions to the 5-15% pion spectra. The power-law is Equation 6.22 and the m_t exponential is Equation 6.12.

K^+				
Range (GeV/c)	Eqn	χ^2/dof	dN/dy	$\langle p_t \rangle$ (GeV/c)
0.40 - 1.65(9)	p_t exp	4.52/ 7	37.433469	0.557460
0.40 - 1.65(9)	m_t exp	10.68/ 7	32.590988	0.603466
0.40 - 1.30(7)	p_t exp	4.11/ 5	37.860415	0.550667
0.40 - 1.30(7)	m_t exp	7.90/ 5	33.313398	0.587824
0.40 - 0.95(5)	p_t exp	1.18/ 3	38.772000	0.537427
0.40 - 0.95(5)	m_t exp	1.49/ 3	34.256749	0.571893
K^-				
Range (GeV/c)	Eqn	χ^2/dof	dN/dy	$\langle p_t \rangle$ (GeV/c)
0.40 - 1.65(9)	p_t exp	6.11/ 7	32.492689	0.580195
0.40 - 1.65(9)	m_t exp	4.88/ 7	28.269027	0.628726
0.40 - 1.30(7)	p_t exp	6.15/ 5	31.914485	0.594366
0.40 - 1.30(7)	m_t exp	3.30/ 5	28.386647	0.624718
0.40 - 0.95(5)	p_t exp	1.21/ 3	30.722573	0.645474
0.40 - 0.95(5)	m_t exp	1.42/ 3	28.022360	0.641830

Table D.8: Extrapolated yield and average transverse momentum after fitting functions to the 5-15% kaon spectra. The p_t exponential is Equation 6.23 and the m_t exponential is Equation 6.12.

p				
Range (GeV/c)	Eqn	χ^2/dof	dN/dy	$\langle p_t \rangle$ (GeV/c)
0.40 - 3.50(15)	p_t exp	42.39/13	26.165266	0.761977
0.40 - 3.50(15)	m_t exp	8.96/13	21.896537	0.859617
0.40 - 2.50(12)	p_t exp	24.08/10	25.340453	0.778744
0.40 - 2.50(12)	m_t exp	6.50/10	21.777276	0.862823
0.40 - 1.50(7)	p_t exp	11.11/ 5	23.787876	0.818571
0.40 - 1.50(7)	m_t exp	4.60/ 5	21.646888	0.866596
\bar{p}				
Range (GeV/c)	Eqn	χ^2/dof	dN/dy	$\langle p_t \rangle$ (GeV/c)
0.40 - 3.50(15)	p_t exp	37.56/13	16.569013	0.787909
0.40 - 3.50(15)	m_t exp	23.32/13	13.976177	0.883960
0.40 - 2.00(9)	p_t exp	29.78/ 7	15.726749	0.820595
0.40 - 2.00(9)	m_t exp	18.00/ 7	13.937862	0.886014
0.40 - 1.00(4)	p_t exp	0.07/ 2	157.583502	7.635982
0.40 - 1.00(4)	m_t exp	0.08/ 2	64.094558	5.169059

Table D.9: Extrapolated yield and average transverse momentum after fitting functions to the 5-15% (anti)proton spectra. The p_t exponential is Equation 6.23 and the m_t exponential is Equation 6.12.

π^+				
Range (GeV/c)	Eqn	χ^2/dof	dN/dy	$\langle p_t \rangle$ (GeV/c)
0.20 - 2.20(13)	power-law	33.37/10	151.176671	0.359128
0.20 - 2.20(13)	m_t exp	1311.05/11	121.671618	0.414382
0.20 - 1.20(8)	power-law	7.56/ 5	173.634800	0.344952
0.20 - 1.20(8)	m_t exp	238.42/ 6	130.645279	0.393472
0.20 - 0.95(7)	power-law	8.81/ 4	179.437414	0.345260
0.20 - 0.95(7)	m_t exp	150.35/ 5	131.761846	0.391130
π^-				
Range (GeV/c)	Eqn	χ^2/dof	dN/dy	$\langle p_t \rangle$ (GeV/c)
0.20 - 2.20(13)	power-law	91.77/10	135.953548	0.370593
0.20 - 2.20(13)	m_t exp	902.00/11	113.364498	0.417964
0.20 - 1.20(8)	power-law	7.01/ 5	171.871581	0.367587
0.20 - 1.20(8)	m_t exp	315.57/ 6	121.143712	0.398212
0.20 - 0.95(7)	power-law	5.15/ 4	177.842659	0.374830
0.20 - 0.95(7)	m_t exp	221.08/ 5	122.380473	0.395367

Table D.10: Extrapolated yield and average transverse momentum after fitting functions to the 15-30% pion spectra. The power-law is Equation 6.22 and the m_t exponential is Equation 6.12.

K^+				
Range (GeV/c)	Eqn	χ^2/dof	dN/dy	$\langle p_t \rangle$ (GeV/c)
0.40 - 1.65(9)	p_t exp	3.20/ 7	23.824327	0.542821
0.40 - 1.65(9)	m_t exp	5.28/ 7	20.518740	0.592498
0.40 - 1.30(7)	p_t exp	1.02/ 5	23.728841	0.544647
0.40 - 1.30(7)	m_t exp	4.18/ 5	20.838464	0.582363
0.40 - 0.95(5)	p_t exp	0.18/ 3	24.233017	0.533094
0.40 - 0.95(5)	m_t exp	0.34/ 3	21.407376	0.567467
K^-				
Range (GeV/c)	Eqn	χ^2/dof	dN/dy	$\langle p_t \rangle$ (GeV/c)
0.40 - 1.65(9)	p_t exp	6.44/ 7	16.466579	0.600060
0.40 - 1.65(9)	m_t exp	9.15/ 7	14.531036	0.642535
0.40 - 1.30(7)	p_t exp	4.78/ 5	16.497657	0.598722
0.40 - 1.30(7)	m_t exp	4.73/ 5	14.725588	0.627851
0.40 - 0.95(5)	p_t exp	0.82/ 3	16.111762	0.627673
0.40 - 0.95(5)	m_t exp	1.28/ 3	14.680984	0.631917

Table D.11: Extrapolated yield and average transverse momentum after fitting functions to the 15-30% kaon spectra. The p_t exponential is Equation 6.23 and the m_t exponential is Equation 6.12.

p				
Range (GeV/c)	Eqn	χ^2/dof	dN/dy	$\langle p_t \rangle$ (GeV/c)
0.40 - 3.50(15)	p_t exp	21.79/13	15.601014	0.762854
0.40 - 3.50(15)	m_t exp	12.59/13	13.300736	0.848742
0.40 - 2.50(12)	p_t exp	19.24/10	15.601690	0.762825
0.40 - 2.50(12)	m_t exp	7.42/10	13.409638	0.843875
0.40 - 1.50(7)	p_t exp	4.38/ 5	14.937394	0.789112
0.40 - 1.50(7)	m_t exp	4.45/ 5	13.524940	0.838744
\bar{p}				
Range (GeV/c)	Eqn	χ^2/dof	dN/dy	$\langle p_t \rangle$ (GeV/c)
0.40 - 3.50(15)	p_t exp	34.25/13	11.308898	0.732578
0.40 - 3.50(15)	m_t exp	12.78/13	9.293335	0.835318
0.40 - 2.50(12)	p_t exp	25.31/10	11.140342	0.739782
0.40 - 2.50(12)	m_t exp	9.62/10	9.286765	0.835703
0.40 - 1.50(7)	p_t exp	11.62/ 5	10.123799	0.792987
0.40 - 1.50(7)	m_t exp	8.44/ 5	9.131380	0.845354

Table D.12: Extrapolated yield and average transverse momentum after fitting functions to the 15-30% (anti)proton spectra. The p_t exponential is Equation 6.23 and the m_t exponential is Equation 6.12.

π^+				
Range (GeV/c)	Eqn	χ^2/dof	dN/dy	$\langle p_t \rangle$ (GeV/c)
0.20 - 2.20(13)	power-law	111.99/10	60.513528	0.345393
0.20 - 2.20(13)	m_t exp	1666.30/11	48.982918	0.397128
0.20 - 1.20(8)	power-law	9.04/ 5	82.757857	0.306815
0.20 - 1.20(8)	m_t exp	377.32/ 6	52.891164	0.376129
0.20 - 0.95(7)	power-law	9.31/ 4	84.598489	0.306037
0.20 - 0.95(7)	m_t exp	248.42/ 5	53.528897	0.373045
π^-				
Range (GeV/c)	Eqn	χ^2/dof	dN/dy	$\langle p_t \rangle$ (GeV/c)
0.20 - 2.20(13)	power-law	76.18/10	56.856115	0.353550
0.20 - 2.20(13)	m_t exp	1179.44/11	45.516575	0.408579
0.20 - 1.20(8)	power-law	12.86/ 5	68.746287	0.328978
0.20 - 1.20(8)	m_t exp	282.82/ 6	49.149567	0.386595
0.20 - 0.95(7)	power-law	13.89/ 4	66.604614	0.329852
0.20 - 0.95(7)	m_t exp	184.53/ 5	49.795535	0.383101

Table D.13: Extrapolated yield and average transverse momentum after fitting functions to the 30-60% pion spectra. The power-law is Equation 6.22 and the m_t exponential is Equation 6.12.

K^+				
Range (GeV/c)	Eqn	χ^2/dof	dN/dy	$\langle p_t \rangle$ (GeV/c)
0.40 - 1.65(9)	p_t exp	13.74/ 7	8.916600	0.522651
0.40 - 1.65(9)	m_t exp	25.44/ 7	7.677747	0.570434
0.40 - 1.30(7)	p_t exp	11.57/ 5	9.590403	0.491989
0.40 - 1.30(7)	m_t exp	18.37/ 5	8.157557	0.541160
0.40 - 1.16(6)	p_t exp	9.57/ 4	10.135642	0.472695
0.40 - 1.16(6)	m_t exp	13.66/ 4	8.527782	0.524663
K^-				
Range (GeV/c)	Eqn	χ^2/dof	dN/dy	$\langle p_t \rangle$ (GeV/c)
0.40 - 1.65(9)	p_t exp	7.59/ 7	6.680511	0.530315
0.40 - 1.65(9)	m_t exp	9.29/ 7	5.688631	0.583087
0.40 - 1.30(7)	p_t exp	5.92/ 5	6.660047	0.532009
0.40 - 1.30(7)	m_t exp	6.95/ 5	5.780877	0.573484
0.40 - 0.95(5)	p_t exp	3.69/ 3	6.716814	0.527808
0.40 - 0.95(5)	m_t exp	3.79/ 3	5.904568	0.562057

Table D.14: Extrapolated yield and average transverse momentum after fitting functions to the 30-60% kaon spectra. The p_t exponential is Equation 6.23 and the m_t exponential is Equation 6.12.

		p			
Range (GeV/c)	Eqn	χ^2/dof	dN/dy	$\langle p_t \rangle$ (GeV/c)	
0.40 - 3.50(15)	p_t exp	12.16/13	6.130482	0.705660	
0.40 - 3.50(15)	m_t exp	20.05/13	5.107484	0.796471	
0.40 - 2.50(12)	p_t exp	10.73/10	6.213037	0.699638	
0.40 - 2.50(12)	m_t exp	9.95/10	5.173960	0.789985	
0.40 - 1.00(4)	p_t exp	0.60/ 2	5.853902	0.728332	
0.40 - 1.00(4)	m_t exp	1.10/ 2	5.392609	0.769616	
		\bar{p}			
Range (GeV/c)	Eqn	χ^2/dof	dN/dy	$\langle p_t \rangle$ (GeV/c)	
0.40 - 3.50(15)	p_t exp	27.67/13	4.431485	0.707933	
0.40 - 3.50(15)	m_t exp	17.09/13	3.613673	0.810341	
0.40 - 2.00(9)	p_t exp	21.88/ 7	4.347682	0.716543	
0.40 - 2.00(9)	m_t exp	10.69/ 7	3.660249	0.803669	
0.40 - 1.00(4)	p_t exp	1.69/ 2	3.709751	1.028015	
0.40 - 1.00(4)	m_t exp	1.73/ 2	3.419277	0.855285	

Table D.15: Extrapolated yield and average transverse momentum after fitting functions to the 30-60% (anti)proton spectra. The p_t exponential is Equation 6.23 and the m_t exponential is Equation 6.12.

		π^+		
Range (GeV/c)	Eqn	χ^2/dof	dN/dy	$\langle p_t \rangle$ (GeV/c)
0.20 - 2.20(13)	power-law	6.13/10	12.013109	0.269193
0.20 - 2.20(13)	m_t exp	378.42/11	7.365536	0.367916
0.20 - 1.20(8)	power-law	5.39/ 5	11.007486	0.282401
0.20 - 1.20(8)	m_t exp	67.25/ 6	8.101618	0.345060
0.20 - 0.95(7)	power-law	6.04/ 4	10.707168	0.286724
0.20 - 0.95(7)	m_t exp	47.42/ 5	8.225494	0.341629
		π^-		
Range (GeV/c)	Eqn	χ^2/dof	dN/dy	$\langle p_t \rangle$ (GeV/c)
0.20 - 2.20(13)	power-law	29.62/10	9.108901	0.305164
0.20 - 2.20(13)	m_t exp	253.69/11	6.808083	0.368403
0.20 - 1.20(8)	power-law	16.73/ 5	11.224313	0.281740
0.20 - 1.20(8)	m_t exp	106.83/ 6	7.337376	0.350285
0.20 - 0.95(7)	power-law	5.95/ 4	668.500215	0.017415
0.20 - 0.95(7)	m_t exp	101.08/ 5	7.369600	0.349267

Table D.16: Extrapolated yield and average transverse momentum after fitting functions to the 60-92% pion spectra. The power-law is Equation 6.22 and the m_t exponential is Equation 6.12.

K^+				
Range (GeV/c)	Eqn	χ^2/dof	dN/dy	$\langle p_t \rangle$ (GeV/c)
0.40 - 1.65(9)	p_t exp	8.52/ 7	0.965167	0.472119
0.40 - 1.65(9)	m_t exp	9.27/ 7	0.787985	0.532501
0.40 - 1.16(6)	p_t exp	3.45/ 4	1.066707	0.442261
0.40 - 1.16(6)	m_t exp	3.88/ 4	0.871740	0.498621
0.40 - 0.96(5)	p_t exp	2.77/ 3	1.180858	0.415609
0.40 - 0.96(5)	m_t exp	2.80/ 3	0.941145	0.476859
K^-				
Range (GeV/c)	Eqn	χ^2/dof	dN/dy	$\langle p_t \rangle$ (GeV/c)
0.40-1.50(8)	p_t exp	1.49/6	1.073389	0.454906
0.40-1.50(8)	m_t exp	1.70/6	0.868696	0.513688
0.40-1.20(6)	p_t exp	1.38/4	1.047096	0.463616
0.40-1.20(6)	m_t exp	1.75/4	0.881340	0.507899
0.40-0.95(5)	p_t exp	1.10/3	1.099673	0.446001
0.40-0.95(5)	m_t exp	1.18/3	0.918048	0.492520

Table D.17: Extrapolated yield and average transverse momentum after fitting functions to the 60-92% kaon spectra. The p_t exponential is Equation 6.23 and the m_t exponential is Equation 6.12.

Range (GeV/c)	Eqn	P χ^2/dof	dN/dy	$\langle p_t \rangle$ (GeV/c)
0.40 - 2.20(10)	p_t exp	15.96/ 8	0.939591	0.600481
0.40 - 2.20(10)	m_t exp	15.20/ 8	0.731128	0.703474
0.40 - 2.00(9)	p_t exp	12.80/ 7	0.977306	0.586640
0.40 - 2.00(9)	m_t exp	10.34/ 7	0.749499	0.693372
0.40 - 1.00(4)	p_t exp	3.39/ 2	0.851073	0.639011
0.40 - 1.00(4)	m_t exp	3.82/ 2	0.757887	0.688803

Range (GeV/c)	Eqn	\bar{p} χ^2/dof	dN/dy	$\langle p_t \rangle$ (GeV/c)
0.40 - 2.00(9)	p_t exp	7.67/ 7	0.573220	0.688682
0.40 - 2.00(9)	m_t exp	9.57/ 7	0.475085	0.779204
0.40 - 2.00(9)	p_t exp	7.67/ 7	0.573220	0.688682
0.40 - 2.00(9)	m_t exp	9.57/ 7	0.475085	0.779204
0.40 - 1.00(4)	p_t exp	2.19/ 2	0.614737	0.657630
0.40 - 1.00(4)	m_t exp	1.92/ 2	0.526504	0.731000

Table D.18: Extrapolated yield and average transverse momentum after fitting functions to the 60-92% (anti)proton spectra. The p_t exponential is Equation 6.23 and the m_t exponential is Equation 6.12.